

PEER REVIEW PAPER

This paper has been peer-reviewed and published in a special edition of Traffic Injury Prevention 24(S1), by Taylor & Francis Group. The complete paper will be available on the Traffic Injury Prevention website soon. To access ESV Peer-reviewed papers click the link below
<https://www.tandfonline.com/toc/gcpi20/24/sup1?nav=toCList>

PEER REVIEW PAPER

This paper has been peer-reviewed and published in a special edition of Traffic Injury Prevention 24(S1), by Taylor & Francis Group. The complete paper will be available on the Traffic Injury Prevention website soon. To access ESV Peer-reviewed papers click the link below
<https://www.tandfonline.com/toc/gcpi20/24/sup1?nav=toCList>

PEER REVIEW PAPER

This paper has been peer-reviewed and published in a special edition of Traffic Injury Prevention 24(S1), by Taylor & Francis Group. The complete paper will be available on the Traffic Injury Prevention website soon. To access ESV Peer-reviewed papers click the link below
<https://www.tandfonline.com/toc/gcpi20/24/sup1?nav=toCList>

A NOVEL POWERED TWO-WHEELER RIDER DUMMY; SPECIFICATIONS AND INITIAL TESTING

Jolyon Carroll

Autoliv Research
Sweden

Bernard Been

Mark Burleigh

Humanetics
The Netherlands and UK, respectively

Paper Number 23-0132

ABSTRACT

Powered Two and Three-Wheelers (PTWs) are a popular means of transport. Fully electric PTWs can be operated locally emission-free and, therefore, may support sustainable transport options. However, in terms of the safety offered to PTW riders there is still a long way to go compared with other means of transportation. As such, PTW riders are a vulnerable road user group that stands to benefit from improved protection. Primarily, this paper provides a detailed description of the work-in-progress regarding a new crash test dummy, an ATD (Anthropometric Test Device), intended principally for use in testing PTWs. The question posed was if a new dummy can facilitate evaluations of PTW protective systems. The end goal being to promote more widespread evaluation of protective systems for PTW riders. Importantly, the development of the PTW riding dummy has paired physical and finite element models together, from the start, to support both physical and virtual testing in the future.

The ATD development is based on collision (and injury) statistics of PTWs worldwide, a brief summary of previous research is presented. As with the development of the Motorcyclist Anthropometric Test Device (MATD- ISO 13232-3) an updated modification of the Hybrid III pedestrian is proposed as the principal solution. To this base dummy a small set of modifications are made to allow simple and yet adequate representation of a PTW rider. Demonstration of the dummy in use as a PTW rider is provided by performing full-scale crash tests. Finite element crash simulations are compared with the physical tests, demonstrating the suitability of using the finite element dummy model in virtual PTW tests.

Details of the PTW dummy anthropometry are provided as well as the rationale for design updates in comparison with the MATD.

An overview of testing with the dummy is provided and the results from two full-scale reference tests (without protective system) are given. Injury predictions based on dummy measurements are compared with an injury statistics summary.

Differences between the outputs from the physical and finite element models are discussed in the context of the injury statistics and additional validation of the tools is suggested. The paper also indicates potential areas where the dummy could be improved in the future, depending on injury prediction needs and application, such as to include additional instrumentation in the abdomen region, for example.

Worldwide road traffic statistics suggest that the number of deaths of PTW riders form an equally large group as deaths among drivers and passenger of four-wheeled vehicles. In contrast, the former group has not benefitted from the advancement of protection systems as implemented in the latter. The availability of new tools in the form of a hardware ATD and its finite element model representing the PTW rider, will support development and evaluation of protective systems for PTW riders.

INTRODUCTION

Increasing numbers of people in both developed and low- and middle-income countries are choosing to use Powered Two-Wheelers (PTWs) [1]. Correspondingly, nearly 30% of all crash fatalities reported to WHO (World Health Organization) in 2016 involve PTWs, such as motorcycles, mopeds, scooters, and electrical bikes (e-bikes) [2] and this percentage has been increasing [3].

To combat this trend of increasing casualties, certain road safety interventions specific to PTW safety are accepted as being effective, such as: segregated lanes [4], motorcycle antilock braking systems [5] and the introduction of compulsory training and a skills test to obtain a motorcycle permit or licence [6]. However, without universal implementation and application of these and other known and future preventative solutions, crashes will still occur, and protective countermeasures remain crucial, such as the wearing of a motorcycle helmet [7].

It is more than 40 years since conclusions called for radical design changes to the motorcycle and the clothing of the rider as the only ways of increasing the chances of survival for the rider in high-speed impacts [8]. It is also more than 40 years since energy absorbers on the front of motorcycles, restraining chest pads, airbags and leg protectors have been proposed for motorcycle applications [9]. However, despite the potential benefits shown in research, only an airbag system survived, in a recognisable form, to a modern motorcycle [10].

To facilitate the common evaluation of secondary safety devices on PTWs, ISO 13232 was developed [11]. This standard makes use of the Motorcycle Anthropometric Test Device (MATD) [12]. ISO 13232 is not a safety standard or explicit legal requirement, but provides a methodology by which assertions regarding safety efficacy of proposed devices needs to be evaluated to be accepted by the scientific community [13]. After release of the standard in 1996, the cost of specific motorcycle dummies was already cited as a barrier to testing by 1998 [14]. As a result, Berg et al. and other authors after them choose to use the baseline Hybrid III crash dummy instead of the MATD negating the potential advantages of a bespoke dummy for PTW testing.

To return to, and to accelerate the evaluation of protective systems for PTW riders, a new initiative sought to develop a small set of modifications to the Hybrid III 50th percentile male crash test dummy. These were intended to capture useful features for PTW crash test applications and help proliferate availability of a dummy suitable for use beyond the research domain (i.e., entering system development and potentially even third-party evaluations).

This paper provides details of the resulting PTW riding dummy (PTW dummy). This includes its anthropometry as well as the rationale for design updates in comparison with the MATD. Results from two full-scale reference tests (without protective system) are given. The discussion compares injury predictions based on dummy measurements with expectations from the injury statistics summary. Differences between the outputs from the physical and finite element models are discussed, qualitatively, and additional validation of the tools is suggested.

Collision data direction

In 1981 a benchmark was set for motorcycle accident investigation in Southern California [15]. Data from 900 on-scene, in-depth cases were analysed with regard to injury causes. This evidence later formed a substantial part of the basis for the ISO Standard (13232) and the collision configurations most commonly encountered were encapsulated in the recommended test conditions. There were contemporary, in-depth studies in European countries too, some of which have continued. Five samples, from France, Germany, Netherlands, Spain, and Italy were brought together for the MAIDS research project (In-depth investigations of accidents involving powered two wheelers) [16]. This European PTW collision data of 921 investigations again indicated that the object most frequently struck was a passenger car. However, the frequency with which different configurations occurred varied between the U.S., German (ISO data) and the aggregated European (MAIDS) data [17]. Nevertheless, it was maintained that development and testing of protective devices should use a set of impact conditions including: the PTW impacting the side of the car, head-on impacts, the car impacting the side of the PTW and rear-end impacts.

Across all crash configurations, the three most frequently injured body regions are the same for ISO13232 and MAIDS (Table 1), though the order changes.

Table 1.
Three most frequently injured body regions in PTW crashes [17].

Body region injuries (as a percentage)	ISO 13232	MAIDS
Head	6.6	5.0
Lower legs	5.1	8.0
Upper extremities and shoulders	3.9	9.4

The European Horizon 2020 project PIONEERS subsequently identified key accident scenarios in Europe [18]. In the Pioneers dataset neck, upper extremities, chest, spine, and pelvis all showed a higher injury frequency than those in the ISO 13232.

Country-to-country crash configuration differences were again highlighted with respect to in-depth collision data for Germany, China, and India [19]. In that study the German data indicated a priority with respect to the front of the PTW colliding with the side of the car. Here it can be noted that the impact angle was not always 90 degrees, and the impact position was often in front of the passenger compartment; though an image depicting a 90 degree PTW to passenger compartment of a car is shown in that paper alongside this most frequent configuration (which could be slightly misleading to the variability of angles and positions).

The distribution of injuries by AIS (Abbreviated Injury Scale) [20] body region points towards the extremities and the head being priorities at the AIS2+ (at least moderate) severity and the thorax replacing the upper extremities for AIS3+ (at least serious) injuries [21]. Particularly, for all PTW crashes, the most frequent AIS3+ injuries are femur fracture, rib cage fracture, lung injury, tibia fracture and cerebrum injury.

A difference in injury priorities has been shown depending on the type of PTW [22]. Although, quite similarly to the complete sample, for all PTW crashes where the PTW was a motorcycle (not a scooter), the most frequent AIS3+ injuries are femur fracture, rib cage fracture, tibia fracture, lung injury and fracture to the base of the skull. At the AIS2+ level the equivalent priorities in motorcycle crashes are cerebral concussion, tibia fracture, radius fracture, femur fracture and a vertebral injury.

Throughout all these studies, head and extremity injuries still represent a prime focus for prevention, along with the ribs and lungs for severe cases.

RATIONALE FOR THE PTW RIDER DUMMY

General description

The development of the PTW started with a short-list of requirements and reviewing the MATD features. Candidate dummies that could be used as a platform for the PTW needed to be robust and demonstrate well know performance. Further key features are the availability of spare parts and support, a well-validated CAE (computer-aided engineering) model and known and accepted injury measurements and reference scales. Various candidate dummies were considered (primarily frontal impact dummies for frontal PTW crash applications) such as: the Hybrid III, the THOR, and the Hybrid III pedestrian dummy with standing pelvis. The standard Hybrid III and THOR 50th percentile male dummies were not considered adequate because of their limitations to adapt to PTW sitting postures in the pelvis area, although the Hybrid III was scoring well on all other requirements. The THOR was not further considered because of its complexity and costs, having many features not relevant to PTW loading cases, and was also considered to be less robust.

Anthropometry

The PTW rider anthropometry is based on the RAMSIS Motorbike Posture Models ‘All-rounder’ and ‘Scooter’ [23]. RAMSIS is an ergonomics software tool used for vehicle cabin and workspace design. The motorbike posture models were based on previous experiments involving female and male volunteers sitting on scooters and allrounder motorcycles. Therefore the 50th percentile male rider postures were derived from volunteer data, using a human

anthropometry database and ergonomic posture prediction algorithms implemented in the RAMSIS software. The outputs of the RAMSIS models are both the external surface geometry, as well as the ‘stickman’ coordinates of joint positions in 3D space. The rider posture models were compared with the UMTRI (University of Michigan Transportation Research Institute) Anthropometry of Motor Vehicle Occupants (AMVO) data set [24] [25]. It was found that, after coordinate system transformation, the RAMSIS and AMVO stickmen correlated well for spinal curvature and length between the hip joint up to the occipital condyle joint for the allrounder (Figure 1), although the spine coordinates do not match exactly in between (e.g. from the AMVO point 60 to 57). The scooter posture matched well up until the 4th thoracic vertebra and shoulder height, with more deviations higher up. This study revealed that the spinal curvatures of scooter, allrounder and automotive seated postures are close up to the 4th thoracic vertebra. It seems likely that riders (and drivers) adapt their spinal postures based on the arm length and distance to the handlebars (steering wheel). Likely the spine and neck curvatures above the shoulder joints are adapting to keep the head in the desired angle for good vision and neck curvature adapts for least muscle effort to keep the helmeted head in the desired orientation.

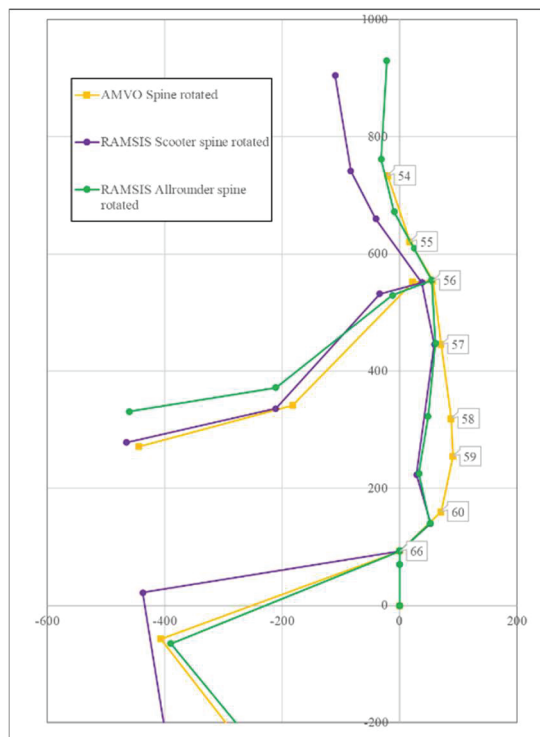


Figure 1. Overlay of AMVO, RAMSIS Scooter and Allrounder stickmen (with AMVO joint numbers: 66 = Hip [h-point]; 60 = L5/S1; 57 = T8/T9; 56 = T4/T5; 54 = Head/Neck [occipital condyle]).

TEST METHOD

Crash-Testing

To evaluate overall dummy behaviour, two crash tests were performed. In agreement with the most common scenario in Germany, these crashes involved the front of the PTW striking the side of a car. The two variations investigated were either a moving PTW to moving car or a moving PTW to stationary car. In both cases the speed of the PTW was nominally 50 km/h [19]. Just a little faster than the 48 km/h used in the ISO standard test requirements. Although, in the stationary car test a speed of only 48.7 km/h was achieved. When moving, the speed of the car was 20 km/h.

The loading to the body of the PTW rider could be different depending on where the PTW contacts the car. For the tests reported here, it was selected to strike the side of the car’s passenger compartment. The intention was that by having an initial point of contact on the B-pillar of the car, then the rider could interact with this stiff structure and, potentially, have head contact with the roof-rail of the car.

For the car, a Honda Accord from 2011 was selected. As a 4-door midsize sedan, it has the body of a typical family car and a closely related finite element model available for use in corresponding simulation efforts [26]. A simplified version of this model was used for initial correlation work to reduce runtimes. Globally, bikes like the Honda CB 125 (and older CG 125) and Yamaha YS or YZ 125 have been market leaders. For this reason, previous research at Autoliv established a finite element model of a Yamaha YS125. Given the relevance of this bike size and type to the global markets, this was selected for the tests. A simulation model of this motorcycle was created at Autoliv prior to this study.

Launch mechanism The motorcycle was not linked directly to the test facility propulsion system, but indirectly accelerated up to speed via a supporting frame. The frame had two supporting tubes in line with the axle through the front wheel. It also provided stability for the rider under the arms and against the sides of the chest (Figure 2). The front wheel supporting tubes rotated and released the bike prior to the crash point so that the bike was clear of the frame and free-running momentarily before hitting the side of the car.



Figure 2. Rider and motorcycle within the frame used to accelerate and launch them to the crash point.

PTW RIDER DUMMY DESCRIPTION

Like the MATD, the PTW dummy is based on the Hybrid III 50th percentile male dummy with the pedestrian standing pelvis design. The pedestrian pelvis assembly is not restricting the legs in an automotive seating position, like the standard Hybrid III sitting pelvis does. It allows for a larger range of motion in the hip joints and enables the dummy to adapt to a range of rider postures seen on various PTW types. The pedestrian pelvis enables the legs to spread around a typical motorcycle tank. Moreover, the larger flexion and extension range of the hip joints allows the dummy to sit in more upright ‘custom bike’ and ‘scooter’ rider postures, as well as with more forward leaning and more flexed legs seen on sports bikes. Modifications to the Hybrid III dummy were implemented in the head & neck, the shoulder, the spinal column, and the pelvis.

PTW dummy features

For development of the dummy postures the RAMSIS models and anthropometry comparison provided good direction. It was concluded that the spine of the dummy could be kept the same for the scooter and allrounder models (Figure 3). The neck needs to be adjustable at its base and the OC-joint (occipital condyle) needs adaptation for head angles. The posture is also adjustable by the rocking of the pelvis which the standing pelvis allows. The shoulder joint position of the PTW rider is somewhat further forward, as compared to an automotive driver posture. A small adaptation in the Hybrid III shoulder components was found to be desirable (Figure 4). The Hybrid III thorax and spine were oriented to match the RAMSIS external surface and stickman, by implementing the pedestrian straight lumbar spine, a new interface bracket between the top of the lumbar and the thoracic spine, and a new adjustable neck bracket. A new sacrum block was also designed which incorporated a standard lumbar load cell.

The WorldSID head was chosen because of its human-like representation of the chin area for improved interaction with a helmet strap. The WorldSID neck was selected, as it is a good compromise demonstrating biofidelic performance in multiple directions: frontal flexion, oblique and lateral [27]. To adapt the head to a PTW rider vision

angle, the neck was modified with a set of bespoke buffers in the upper segment. The buffer set puts the top of the neck into 12 degrees more extension. The adjustable neck bracket is interfacing between the bottom of the WorldSID neck and the Hybrid III spine. The neck bracket provides fine adjustment of the head angle for the various rider postures between forward leaning sports posture (more extension) and relaxed custom rider posture (more flexion). A small modification was needed to fit the thoracic bib between the neck and the new bracket due to the neck moving rearward to match the RAMSIS stickman. The PTW dummy is using rigid knees (without knee sliders) for robustness. An exploded view of the bespoke PTW components is shown in Figure 5. Standard Hybrid III 50th percentile male parts are used to complete the PTW dummy assembly.

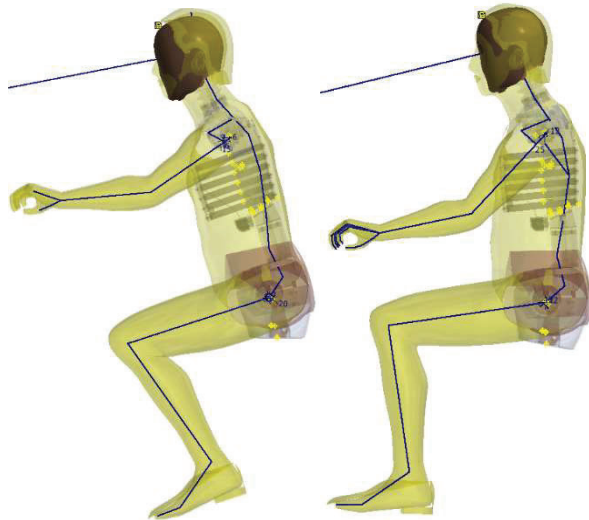


Figure 3. Overlays of the PTW dummy in two rider posture models allrounder (left image) and scooter (right image)

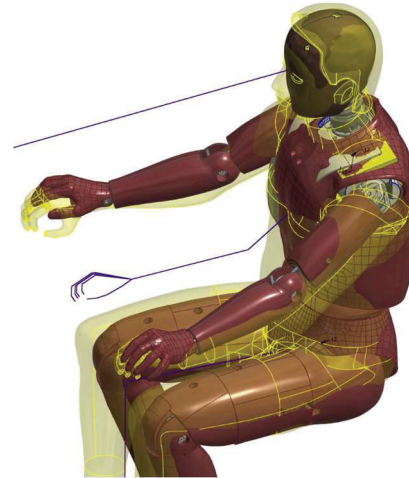


Figure 4. The PTW rider dummy CAD within RAMSIS allrounder external surface (note: only the left shoulder joint is modified to meet the PTW posture in this image to show the effect).

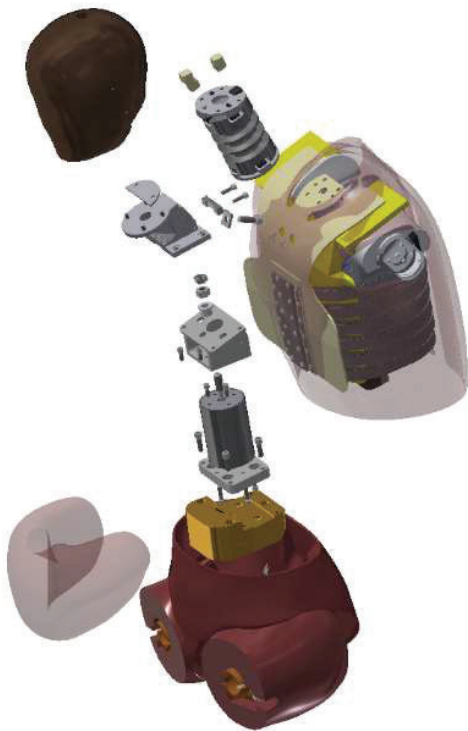


Figure 5. PTW rider dummy bespoke components (Use standard Hybrid III 50 parts to complete the assembly).

Instrumentation The PTW dummy adopted the Hybrid III 50th percentile arms and legs and so features standard options to add load cells in the humerus, the femur, and the tibia. In contrast to the MATD using frangible extremities, the load cells provide time histories of the loading, and data that can be reviewed to established injury criteria and human tolerances with adequate reproducibility. The dummy can be equipped with accelerometers and angular rate sensors in the major body segments, as well as tilt sensors to measure the dummy posture. Further load cells can be implemented in the head -to-neck -, the neck-to-upper spine - and lumbar-to-pelvis interfaces. The dummy is also equipped with the standard Hybrid III chest displacement sensor. Also, there is an option to equip the dummy with an on-board data acquisition system, to avoid cable damage in the, sometimes unpredictable, post-crash landing trajectory. For this testing, the PTW dummy was also equipped with the sensors described in Table 2.

Table 2.
Rider instrumentation

Region	Instruments
Head	3 axis linear accelerometer 3 x angular rate sensors
Helmet	3 axis linear accelerometer 3 x angular rate sensors
Upper neck	Load cell (measuring: 3 x forces and 3 x moments)
Chest	3 axis linear accelerometer Potentiometer (to give chest deflection)
Lumbar spine	Load cell (measuring: 2 x forces and 1 moment)
Pelvis	3 axis linear accelerometer
Femurs	Load cell (measuring axial force, 1 each side)

CAE model of the PTW dummy

Simultaneously with the physical dummy hardware engineering, a finite element dummy model (in LS-Dyna code) was developed (Figure 6) in two stages. Initially the first stage model was based on existing Hybrid III 50th percentile male dummy model finite element components. All the new PTW parts were meshed from CAD (computer-aided design) geometry, and relevant material models were adopted from the existing Hybrid III model material database. In the second stage the PTW dummy model was used in simulated test environments and conditions and validated against experimental data in the same test conditions. Material models and meshes were further fine-tuned and updated, until a satisfactory correlation was achieved between the experiment data and the CAE model response.

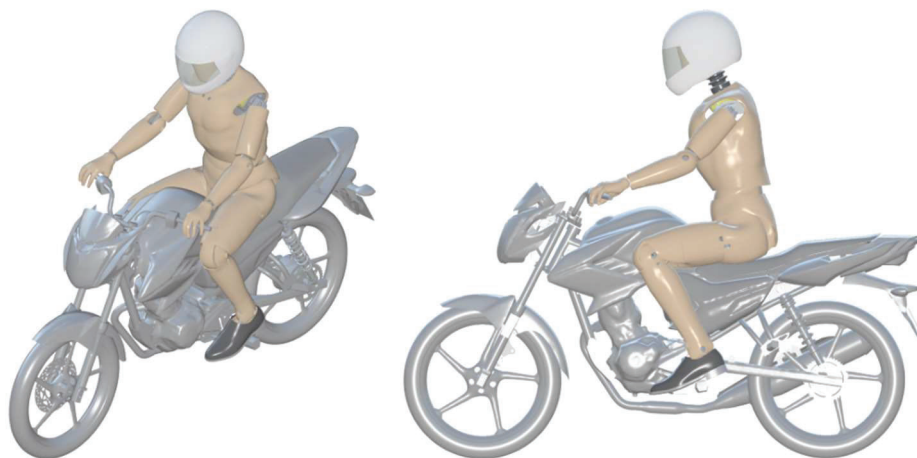


Figure 6. PTW dummy LS-Dyna model on the motorcycle model.

TEST RESULTS

Visual comparison

Visual comparisons of the motion are useful to appreciate the behaviour of the PTW dummy in these tests quickly. Still images from similar video views are provided in Figure 7 for the two physical tests.

For the first 20 milliseconds, there is little difference between the two tests. Distortion of motorcycle components is confined to the front wheel and mudguard. The rider maintains an upright sitting posture with head above the level of the car's roof rail. Then by 40 milliseconds, we see that the test with a stationary car keeps the front wheel of the motorcycle straight, whilst the moving car test begins to turn the front wheel to the right (away from the camera). The front fork is either deforming or turning and deforming. At 60 milliseconds, the rear wheel of the motorcycle lifts a little from the ground. This is more pronounced in the stationary car test and becomes even more obvious as the test progresses. At 80 milliseconds the handlebars of the motorcycle in the moving car test have turned and the change in motorcycle loading has already meant that the head of the rider is slightly closer to the car than in the stationary car test. Although in both tests the trajectory of the head towards the roof rail is now inevitable. At 100 milliseconds we are reaching the point of head contact in both tests. The lower legs of the PTW dummy in the stationary car test have swung forwards under their inertia. At 120 milliseconds it looks as though the body of the dummy is involved with neck loading, and the pelvis is higher in the stationary car test than in the moving car test. At 140 milliseconds the moving car test has produced more rotation of the helmet (and head within it) as it is pulled by the moving roof-rail. This sequence of still images concludes at 160 milliseconds, where the extent of the motorcycle yaw in the moving car test compared with pitch of the motorcycle in the stationary car test is most evident. The rear wheel of the motorcycle in the moving car test is back on the ground by this time.

Equivalent images comparing the physical with simulation stationary car test are available in Figure 9 in the Appendix. Comments on the moving car test are available already [28], although images from the moving car test and updated simulation are included in Figure 10. In both tests the simulations are in general agreement with the kinematics from physical tests. Although, the motorcycle showed more rebound after the initial contact with the car in the simulations compared with the physical tests. This resulted in the motorcycle leaping up off the ground. The deformation of the front wheel appears to be different, particularly in the stationary car setup and the compression and damping of the suspension in the front fork also appears to be different between physical and simulated crashes. The result for the rider is that the impulse coming through the motorcycle body and fuel tank will be different. Indeed, the virtual representation of the dummy lags behind the physical test kinematics. This is observable as the head contact time in the simulations which was, for example, 24 milliseconds later in the stationary car simulation than in the physical test.

Time (s)

Stationary car

Moving car

0.000



0.020



0.040



0.060



0.080





Figure 7. Still images from the video footage of two full-scale motorcycle to car crash tests. The left-hand column of images comes from the stationary car test and the right-hand column of images from the moving car test.

Dummy instrumentation

The instrumentation within the dummy is there to provide an assessment of the severity of loading to the rider. The peak values from some of the sensors are shown in Table 3. For priority metrics (relatable to injury predictions in the head, neck, thorax, and legs), these are matched with the equivalent peak from the virtual dummy in each case. Note that tensile femur forces are presented, rather than compressive as would often be referred to in car occupant protection scenarios, as the values for tension were higher than for compression.

Data were collected from the dummy without issue. Only one channel of data showed a fault, and that was the left femur load cell in the moving car test. Otherwise, the dummy and instrumentation were suitably robust, based on these two tests.

Table 3.
Peak values and selected injury criteria from the PTW dummy, resulting from two full-scale crash tests

Region	Stationary car		Moving car	
	Physical	Simulation	Physical	Simulation
Head – resultant linear acceleration (g)	567	490	209	291
Head – 3 ms exceedance (g)	123	196	161	83
HIC ₁₅	6794	5827	2079	1471
Head – rotational velocity, y-axis (radian/s)	-33	-26	-42	-26
Head – rotational velocity, z-axis (radian/s)	6.5	2.9	39.8	10.9
Helmet – linear acceleration, x-axis (g)	-266		-166	
Helmet – rotational velocity, y-axis (radian/s)	+28.9 -22.6		+18.6 -40.8	
Upper neck - shear (N)	2937	4294	3365	4062
Upper neck – compression (N)	-5515	-9478	-1594	-1769
Upper neck – Moc-y (+flexion, -extension, Nm)	156 -48	124 -69	214 -58	241 -24
Chest - resultant linear acceleration (g)	40	58	66	37
Chest – deflection (mm)	4.6	3.0	6.2	3.6
Lumbar – z-axis (+tension, -compression, N)	+4185 -2005	+6132 -3747	+4292 -2697	+2904 -1973
Lumbar – y-axis moment (Nm)	-180	-166	-179	-136
Pelvis – resultant linear acceleration (g)	57	48	33	24
Femur – force (tensile, N)	3514 (right) 2856 (left)	2122 (right) 1677 (left)	1521 (right) †	978 (right) 600 (left)

† Left femur load cell failure

Alongside the dummy results, the motorcycle was examined after the test leading to certain qualitative observations, such as the deformation of the fuel tank (example in Figure 8). Work continues to create similar deformation patterns in the virtual fuel tank.



Figure 8. Images after the moving car test, showing the deformation of the fuel tank caused by the rider's pelvis.

DISCUSSION

Injury assessment

It is thought to be important to have a PTW contact with a moving collision partner as that relative motion will create yaw in the PTW and a twisting of the handlebars. These features will influence the PTW and rider motions and likely influence the design requirements for protective systems. The rider will not move straight forwards over the centre of the handlebars and engagement of the rider's legs with the handlebars and PTW structures will be biased towards one side. This behaviour was confirmed in these experiments.

In both moving and stationary car cases the dummy experienced a head contact (via the helmet) with the roof rail of the car. The helmet stayed on the head of the rider and the instrumentation within the head was useful to discern the difference between the moving car test and the stationary car test. It was observed that the moving car increased the head rotational metrics (particularly axial rotation) but decreased the linear, including the Head Injury Criterion. A HIC value of 2000 would give a 77% risk of a skull fracture [29] and confidently predict such an injury at 6000. Therefore, these tests provide useful load cases for assessing PTW head injury prevention countermeasures. The rotational velocities would also assess countermeasures intended to prevent concussions; the highest priority injury for PTW riders at the AIS2+ severity level. In that case, the moving car test would be a better representation of the challenges presented by the collision data, as the rotational velocities are higher than in the stationary car test.

The contact to the visor of the helmet is interesting and suggests a need to evaluate head protection in the face region. Full-scale tests are not expected to be ideal for controlled repetitive loading to a particular point on a helmet, but the helmet contact points in these two tests are remarkably similar. Helmet visor deformation was not observed in the simulations pointing towards a need for a more accurate representation of the helmet in future simulations.

The WorldSID neck was able to represent a realistic position of the rider's head with respect to viewing angle ahead of this motorcycle. Upper neck shear, compression, flexion, and extension were all close to levels where injuries to the neck (or base of the skull) could be expected with low but non-zero risk [30]. Neck injuries were not identified in the collision data as being a priority for PTW injury prevention. Therefore, we surmise that, the PTW dummy can position the head in an appropriate place, but it may need further work to understand how the neck loads relate to risk of injury for helmeted PTW riders.

Only limited loading of the chest and shoulders of the PTW dummy against the car was observed in this testing. The chest deflection measurements did not go above 6.2 mm. That corresponds with a negligible risk of serious injury [31]. This conflicts with rib cage fractures being a priority injury type for PTW riders, and with thoracic injuries being increasingly important as the severity of injury increases. Either the crash type is not representing the real-world conditions that create thoracic injuries (i.e., we have missed something in this experimental representation of typical events), or the PTW dummy kinematics created do not represent typical rider interactions, or the dummy chest design is not sensitive to the relevant deformation. It is suggested that, to some extent, all aspects are true though the balance of each is not known from this testing. Furthermore, some thoracic injuries are typically attributed to the ground contact in collision data and there remains the confounding factor that anterior to posterior chest deflection measurements may not be the most appropriate metric for predicting thoracic PTW rider injuries.

As of now, the PTW dummy possesses no possibility to measure abdominal loading. Whilst no clear abdomen penetration was observed in these two tests, the torso of the rider passes over the handlebars and there is potential for the rider's own PTW to cause loading to the abdomen in a slightly different collision or with a different PTW (e.g. a scooter, without prominent fuel tank). It is proposed that some abdomen instrumentation will be necessary in the development of protective countermeasures, and it is proposed that any such a modification to the dummy could also make a continuous frontal surface to the dummy without discontinuities between thorax and abdomen (i.e. to close the gap between the ribs and the abdomen insert – created when the Hybrid III adopts an upright posture).

In setting up equivalent simulation runs, it was evident that the dummy kinematics are influenced by the arm posture, interaction between pelvis and tank and even between foot and footrest. However, these parts in the PTW dummy are carried over directly from the base Hybrid III dummy. They have not been tuned for a PTW rider. Except for the frangible lower extremity bones and gripping hands, the same was true for the MATD, but perhaps those parts could have made a difference. Therefore, there remains an unanswered question as to whether it is important to model leg bone failure in order to represent accurately the behaviour of a PTW rider in a frontal crash. Certainly, the stationary car test generated tensile loading to the femurs; even if not compressive as could be the case

with direct loading to the knee, and at levels likely to be within tolerance limits so that fracture of the femur would not be expected on this input alone. It can be noted that there was little interaction between the PTW dummy and the handlebar in these tests. At the end of the moving car test sequence (Figure 10) the handlebar is over the femur of the rider furthest from the car and this shows how such an interaction could be important in a slightly different configuration with, for instance, earlier rotation of the handlebar or less pelvis restraint from the fuel tank.

The pelvis representation is a crucial factor in relation to three important aspects. The loading to the pelvis is enough to deform the fuel tank in these tests and quite probably create pelvis injury. This loading controls the subsequent kinematics of the rider and is, thus, important in the correct prediction of rider to opponent vehicle contacts. Also, that the force from the pelvis onto the fuel tank influences the motorcycle kinematics so that crash reconstructions looking at vehicle deformations and trajectories could be sensitive to the surrogate pelvis used. A pelvis angular rate sensor would at least help provide information about the interaction with the fuel tank and is recommended for an instrumentation update.

Physical and finite element model outputs

Unlike the physical crash, there was no relative movement in front fork components in these simulations. This absence of spring damper modelling is likely to be one of the reasons for generating a higher pitching angle in simulation than in the physical tests.

The front tyre also seemed to have a high stiffness, since the front wheel rebounded in the simulations once the initial contact with the car happens. Unlike the physical tests, there was no obvious deformation and compression in the base model of the motorcycle, so some alterations were made in generating the results presented here. However, this primary contact defines the main load path between the car and motorcycle, so there is a strong need to check the modified components and the accuracy of their representation in crash conditions.

The timing of helmet impact to the roof rail was delayed by 24 ms in the stationary car simulation compared with the physical test. Also, the timing of the contact between the front plastic components and the door was delayed by 10 ms in the simulation, when compared with the physical test. Both observations are also explainable given the potential lack of fidelity in the primary load path from the car side through the front wheel (and tyre) to the motorcycle frame and engine.

Observations on experimental setup

The experimental setup used for this testing was intended to replicate a typical path conflict, where a car turns across the path of a motorcycle, as seen around road junctions (intersections). It was not intended to recreate any specific rider reaction to the impending threat, though in many cases it seems possible that the rider could notice the conflict and may have time to brake before contact. Therefore, a limitation exists as the setup does not account for the braking response and muscle tensing of the rider. It also does not account, intentionally, for any pre-crash pitching of the motorcycle under emergency braking. However, whilst not planned, the physical representation of the intended setup does create some pre-crash pitching of the motorcycle. As the motorcycle front wheel is carried down the test track it is not rotating, but once released it touches the ground. The rotational inertia of the wheel gives a similar effect to braking and the motorcycle dives (pitches forward) during this free-running period prior to contact with the car. At present, this is a negative aspect of the testing, as it is difficult to recreate accurately in the simulations. In the future, this side effect could be useful if carefully designed to replicate a defined pre-crash braking behaviour. Otherwise, it may have to be removed with a setup modification if a truly non-braking response is desired.

CONCLUSIONS

Details of a PTW riding dummy are provided describing the tools and the rationale for necessary design updates over the base Hybrid III dummy. These include: the WorldSID head and neck, a new adjustable lower neck bracket, a rigid bracket at the top of the lumbar, the straight pedestrian lumbar spine plus the standing pelvis and thigh flesh components. The new PTW dummy exists physically as a prototype and as a finite element simulation model for CAE.

Both the physical and simulation versions of the PTW dummy have been tested in full-scale setups crashing a motorcycle into the side of a stationary or moving car. In both environments the testing concluded satisfactorily with data collected from the in-dummy instrumentation.

The motion of the simulated dummy differs from that observed in the physical test. However, this is not a criticism of the PTW dummy and dummy model as those differences appear to arise from the motorcycle model and from the motorcycle to car interaction. Nevertheless, the physical and simulation versions of the PTW dummy created head loading sufficiently high to generate reasonable risks of a head injury in the crashes. High femur loading was also present corresponding to the highest priority injuries based on the collision data for PTW crashes, albeit femur tension rather than compression.

The chest of the PTW dummy was not loaded severely in these tests, which raises a concern over the ability to investigate thoracic injury risk with this representation of a motorcycle front to car side crash. Both the chest and the pelvis of the dummy could be reviewed for biofidelity and injury prediction capabilities; though it is not yet clear what are the PTW rider-specific targets for these regions.

REFERENCES

- [1] IMMA, “Safer Motorcycling - The Global Motorcycle Industry’s Approach To Road Safety,” International Motorcycle Manufacturers Association (IMMA), Genève, Switzerland, 2019.
- [2] WHO, “Global status report on road safety 2018,” World Health Organization (WHO), Geneva, 2018.
- [3] WHO, “Powered two- and three-wheeler safety: a road safety manual for decision-makers and practitioners, second edition,” World Health Organization (WHO), Geneva, 2022.
- [4] R. U. R. Sohadi and M. a. H. B. Mackay, “Multivariate analysis of motorcycle accidents and the effects of exclusive motorcycle lanes in Malaysia,” *Journal of Crash Prevention and Injury Control*, vol. 2, no. 1, pp. 11-17, 2000.
- [5] E. R. Teoh, “Motorcycle antilock braking systems and fatal crash rates: updated results,” *Traffic Injury Prevention*, vol. 23, no. 4, pp. 203-207, 2022.
- [6] K. Kardamanidis, A. Martiniuk, R. Q. Ivers, M. R. Stevenson and K. Thistlethwaite, “Motorcycle rider training for the prevention of road traffic crashes,” *Cochrane Database of Systematic Reviews*, vol. Art. No.: CD005240, no. 10, 2010.
- [7] B. Liu, R. Ivers, R. Norton, S. Blows and S. K. Lo, “Helmets for preventing injury in motorcycle riders,” *Cochrane database of systematic reviews*, vol. 4, pp. 1-42, 2009.
- [8] J. Whitaker, “A survey of motorcycle accidents,” Transport and Road Research Laboratory, TRRL Laboratory Report 913, Crowthorne, Berkshire, UK, 1980.
- [9] P. M. Watson, “Features of the Experimental Safety Motorcycle ESM1,” in *Seventh International Technical Conference on Experimental Safety Vehicles (ESV)*, Paris, France, 1979.
- [10] T. Kuroe, H. Namiki and S. Iijima, “Exploratory study if an airbag concept for a large touring motorcycle: further research second report,” in *The 19th International Technical Conference on the Enhanced Safety of Vehicles (ESV)*, Washington, DC, USA, 2005.
- [11] H. Van Driessche, “Development of an ISO Standard for Motorcycle Research Impact Test Procedures,” in *The Fourteenth International Technical Conference on Enhanced Safety of Vehicles (ESV)*, Munich, Germany, 1994.
- [12] J. A. Newman, J. W. Zellner and K. D. Wiley, “A Motorcyclist Anthropometric Test Device MATD,” in *IRCOBI Conference*, Berlin, Germany, 1991.
- [13] A. Chawla and S. Mukherjee, “Motorcycle safety device investigation: A case study on airbags,” *Sadhana*, vol. 32, no. 4, pp. 427-443, 2007.

- [14] F. A. Berg, H. Burkle, F. Schmidts and J. Epple, "Analysis of the passive safety of motorcycles using accident investigations and crash tests," in *The sixteenth International Technical Conference on the Enhanced Safety of Vehicles (ESV)*, Windsor, Ontario, Canada, 1998.
- [15] H. H. Hurt, J. V. Ouellet and D. R. Thorn, "Final Report-Motorcycle Accident Cause Factors and Identification of Countermeasures," U.S. Department of Transportation, National Highway Traffic Safety Administration; DOT HS-5-01160, 1981.
- [16] ACEM, "MAIDS Final Report," ACEM (European Motorcycle Manufacturers Association), Brussels, 2009.
- [17] A. Grassi, N. Baldanzini, D. Barbani and M. Pierini, "A comparative analysis of MAIDS and ISO13232 databases for the identification of the most representative impact scenarios for powered 2-wheelers in Europe," *Traffic Injury Prevention*, vol. 19, no. 7, pp. 766-772, 2018.
- [18] G. Mensa, S. Piantini, N. Baldanzini, M. del Mar Rasines, N. Parera, M. Pierini, M. Pieve, P. Zampieri and S. Fodera, "Guidelines for the policy making: Future trends in accident scenarios and ISO 132323 review," PIONEERS Project Deliverable D1.3 [<https://pioneers-project.eu/wp-content/uploads/2020/12/Deliverable-D1.3.pdf>], 2019.
- [19] P. Puthan, N. Lubbe, J. Shaikh, B. Sui and J. Davidsson, "Defining crash configurations for Powered Two-Wheelers: Comparing ISO 13232 to recent in-depth crash data from Germany, India and China," *Accident Analysis and Prevention*, vol. 151, no. 2021, 2021.
- [20] AAAM, The Abbreviated Injury Scale 2015 Revision, Chicago Illinois: AAAM (Association for the Advancement of Automotive Medicine), 2015.
- [21] F. Gidion, J. Carroll and N. Lubbe, "Motorcyclist injuries: Analysis of German in-depth crash data to identify priorities for injury assessment and prevention," *Accident Analysis and Prevention*, vol. 163, no. 2021, 2021.
- [22] J. Carroll, F. Gidion, M. Rizzi and N. Lubbe, "Do motorcyclist injuries depend on motorcycle and crash types? An analysis based on the German In-Depth Accident Study," in *International Motorcycle Conference*, Cologne, Germany, 2022.
- [23] A. Preiss and H. Wirsching, "RAMSIS is facing the 20s. Golden 20s?," in *RAMSIS User Conference*, 2020.
- [24] L. Schneider, D. Robbins, M. Pflug and R. Snyder, "Development of Anthropometrically based Design Specifications for an Advanced Anthropometric Dummy Family," University of Michigan Transportation Research Institute, 1983.
- [25] D. Robbins, "Anthropometric Specifications for a Mid-Sized Male Dummy," University of Michigan Transportation Research Institute, 1983.
- [26] H. Singh, C.-D. Kan, D. Marzougui, R. M. Morgan and S. Quong, "Update to future midsize lightweight vehicle findings in response to manufacturer review and IIHS small-overlap testing. Report No. DOT HS 812 237," National Highway Traffic Safety Administration (NHTSA) , Washington, D.C., 2016.
- [27] B. Been, M. Philippens, R. de Lange and M. van Ratingen, "WorldSID Dummy Head-Neck Biofidelity Response," *Stapp Car Crash Journal*, vol. 48, no. Paper number 2004-22-0019, pp. 431-454, 2004.
- [28] J. Carroll, B. Been, H. Sundmark, M. Burleigh and B. Li, "A Powered Two-Wheeler Crash Test Dummy," in *International Research Council on the Biomechanics of Injury (IRCOBI) Conference Proceedings*, Porto, Portugal, 2022.
- [29] E. Hertz, "A note on the Head Injury Criterion (HIC) as a predictor of the risk of skull fracture," in *37th Annual Proceedings of the Association for the Advancement of Automotive Medicine (AAAM)*, San Antonio, Texas, 1993.
- [30] H. J. Mertz, A. Irwin and P. Prasad, "Biomechanical and Scaling Basis for Frontal and Side Impact Injury Assessment Reference Values," in *Stapp Car Crash Journal*, The Stapp Association, 2016.
- [31] H. J. Mertz, J. D. Horsch, G. Horn and R. W. Lowne, "Hybrid III Sternal Deflection Associated with Thoracic Injury Severities of Occupants Restrained with Force-Limiting Shoulder Belts," *SAE 910812*, 1991.

APPENDIX

Time (s)

Physical test

Simulation

0.000



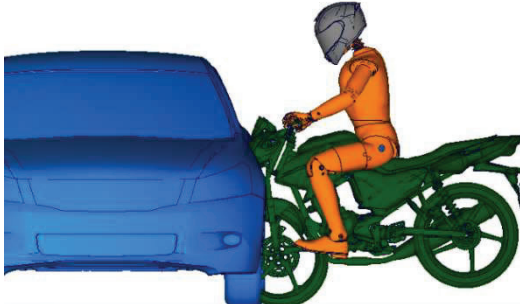
0.020



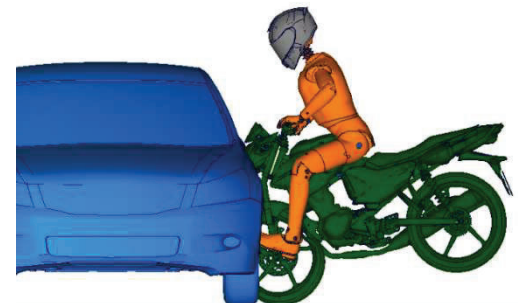
0.040



0.060



0.080



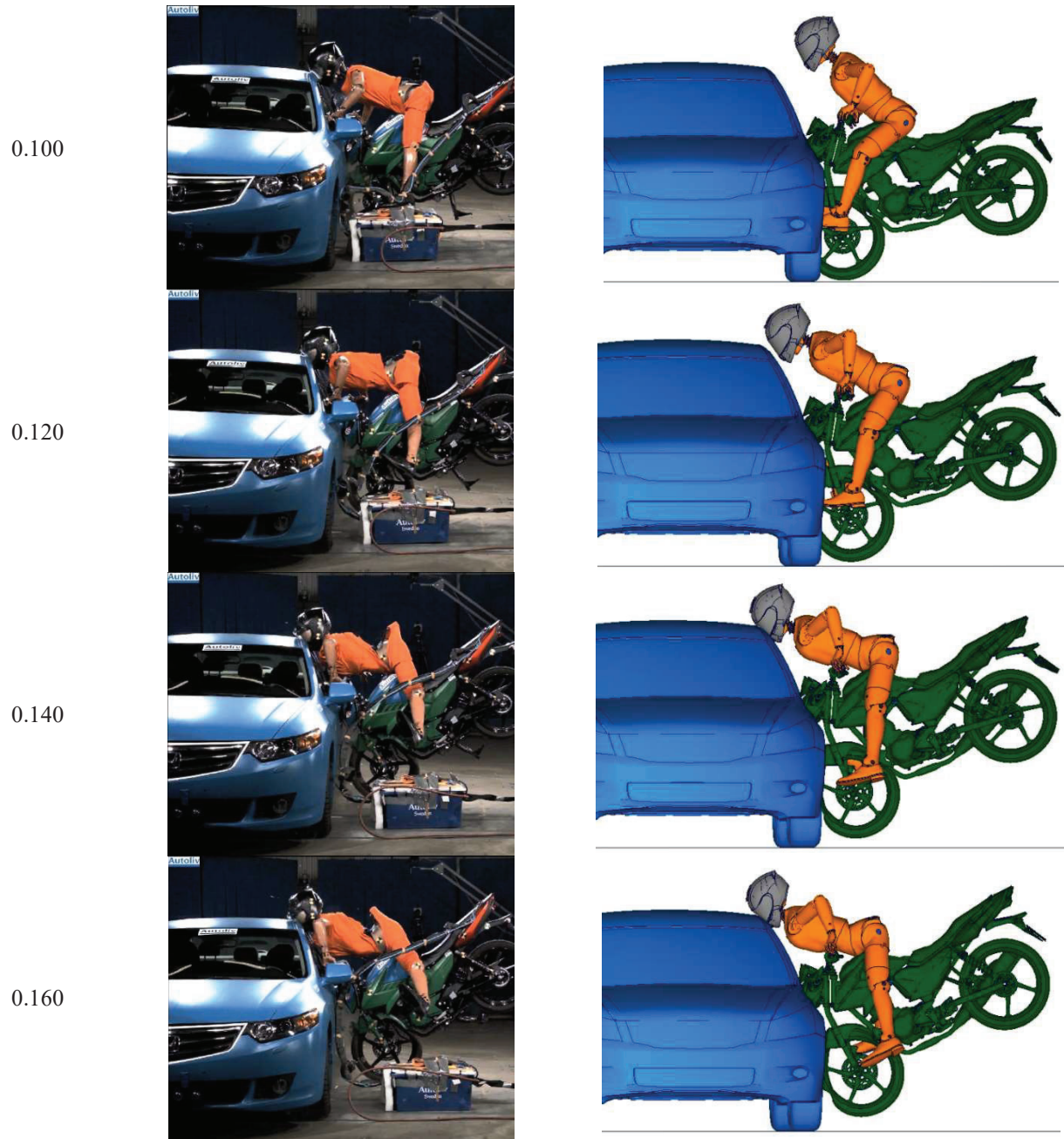


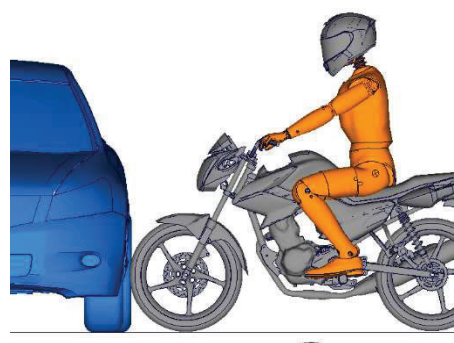
Figure 9. Still images from the videos of a full-scale motorcycle to stationary car crash test. The left-hand column of images comes from the physical test and the right-hand column of images from the finite-element simulation.

Time (s)

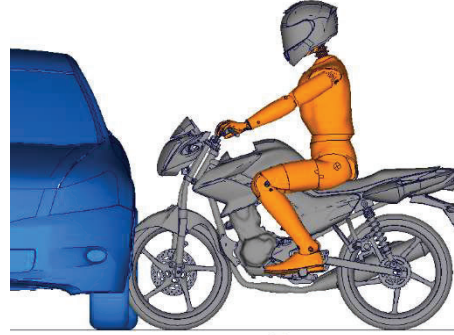
Physical test

Simulation

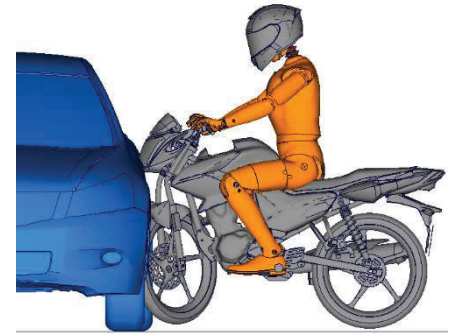
0.000



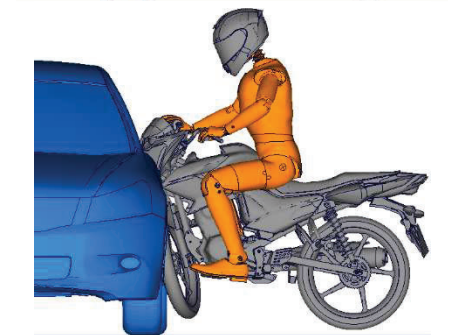
0.020



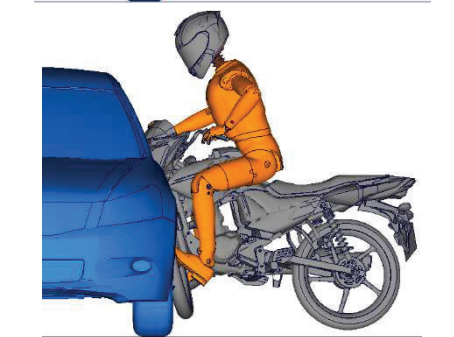
0.040



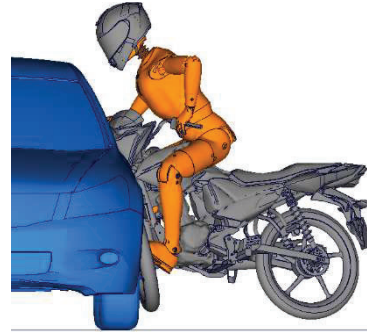
0.060



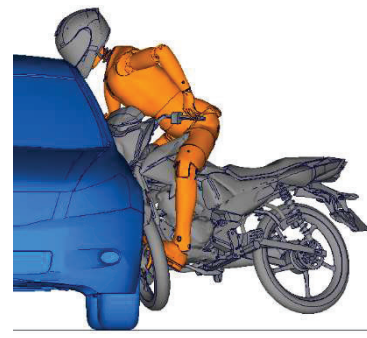
0.080



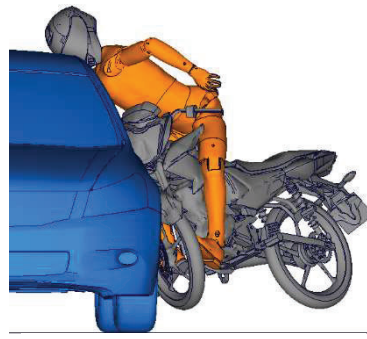
0.100



0.120



0.140



0.160



Figure 10. Still images from the videos of a full-scale motorcycle to moving car crash test. The left-hand column of images comes from the physical test and the right-hand column of images from the finite-element simulation.

PRESSURE-BASED ABDOMINAL INJURY PREDICTION FOR THE THOR-50M

Philippe Beillas, François Bermond

Univ Lyon, Univ Gustave Eiffel, Univ Claude Bernard Lyon 1, LBMC UMR_T9406, Lyon, F69622, France

Philippe Petit, Xavier Trosseille

LAB PSA Peugeot-Citroën Renault
France

Sabine Compigne

Toyota Motor Europe NV/SA
Belgium

Mitsutoshi Masuda

Toyota Motor Corporation
Japan

Pascal Baudrit

CEESAR
France

Mark Burleigh, Jerry Wang

Humanetics Innovative Solutions
UK, US

Jocelyn Perisse

Transpolis SAS
France

Rakshit Ramachandra

Transportation Research Center
US

Jason Stammen

NHTSA
US

Olivier Richard

Forvia
France

Paper Number 23-0171

ABSTRACT

The standard THOR-50M dummy is equipped with sensors to measure the abdomen deflection and assess the risk of abdominal injuries. Since 2016, the “Abdominal Injury and SUBmarining Prediction” (ABISUP) consortium has developed a pressure-measuring abdomen for the THOR-50M to predict abdominal injuries and submarining as a potential alternative to the current THOR-50M abdomen design. A new lower abdomen including Abdominal Pressure Twin Sensor (APTS) was designed and four identical prototypes were built and shipped to consortium member test houses. Numerous abdominal belt loadings replicating tests from the literature were carried-out to check the prototype biofidelity, sensitivity and define a pressure-based AIS3+ injury risk functions (IRFs). Two compression-based IRFs were defined using porcine test results from the literature. Compressions were defined as the ratios between the abdomen deflection and the full abdominal depth, or between the abdomen deflection and the abdominal depth in front of the spine. The abdominal depth in front of the spine was used in an attempt to minimize possible differences between species. It was estimated using simple assumptions and led to compressions exceeding 100% in a few cases. Then transfer functions between THOR abdominal compressions

and pressures were applied to obtain the pressure-based IRFs. Twenty-five sled tests were performed to assess the new abdomen under various restraint conditions and to evaluate the relevance of the IRFs.

The THOR-50M new abdomen showed similar or better biofidelity than the standard abdomen without modifying the dummy kinematics. The abdomen was sensitive to loading height and no damage to the APTS was encountered during tests. Relationships between THOR-50M mean APTS pressure and abdominal compressions were modelled using a 3rd degree polynomial with 0.98 R². The IRF with a log-logistic distribution obtained the lowest Akaike Information Criterion. For the compression based on the full abdomen depth, the AIS3+ injury risks of 25%, 50% and 75% corresponded to APTS pressures of 133, 201 and 304 kPa, respectively. For the compression based on the abdomen in front the spine, the AIS3+ injury risks of 25%, 50% and 75% corresponded to APTS pressures of 108, 197 and 361 kPa, respectively.

The new abdomen discriminated between the restraint conditions: lower pressures (between 90 and 190 kPa) were obtained when the lap belt remained below or on the ASIS and higher pressures (170 to 450 kPa) were obtained when the lap belt loaded the abdomen. Using the IRF, a risk up to 50% could be obtained without submarining, i.e. with the lap belt still engaging the ASIS. This is not consistent with a risk expected to be low for a proper restraint. Possible adjustments are discussed in the paper to decrease APTS sensitivity when the lap belt is positioned below or on the ASIS.

INTRODUCTION

Abdominal injuries represent a significant proportion of the serious injuries sustained by car passengers in frontal crashes and become even more significant as the AIS severity increases [1]. In France, the accident data combining all crash configurations from the Rhône Registry from 2016 to 2020 reveal that 16% of seriously injured car occupants suffered from abdominal injuries [2]. In frontal crash, it is known that the rear seat occupants are generally more at risk to sustain an abdominal injuries ([3], [4]) and that the lap belt is the major source of abdominal injuries [5]. Indeed, the abdominal injuries could be due to a poor routing of the lap belt lying directly on the abdomen before the crash or to the submarining phenomenon resulting from the kinematics of the occupant during the crash which makes the lap belt slip over the pelvis bones into the abdomen. The crash test dummies should also be able to assess these interactions between the occupant and the lap belt.

Today the THOR-50M lower abdomen is instrumented with two IR-TRACCs. A THOR-50M Injury Risk Function has been developed from Kent's porcine tests [7]. It is based on the normalized abdominal deflection calculated by dividing the peak of the left and right abdominal x-axis deflections by the abdominal depth at the location of the IR-TRACCs [8]. The IRF predicts an AIS3+ abdominal injury risk of 25%, 50%, 75% for 80, 98 and 115 mm of abdominal deflection respectively. Moreover, the THOR-50M lower torso design can trap the lap belt between the lower abdomen and the upper abdomen in reclined seat back configuration [9] which does not represent realistic loading conditions. Finally, due to its geometrical characteristics and available space for the IR-TRACC compression, the maximum deflection that can be achieved when subjected to belt compression is unclear. For example, the peak abdomen deflections reported in [8] for frontal rigid barrier and oblique moving deformable barrier tests did not reach 70 mm, or a risk lower than 20%. The Euro NCAP assessment protocol for adult occupant specifies an 88 mm (36% risk) lower limit for the deflection [10].

The ABISUP consortium has developed a new lower abdomen prototype for THOR-50M, named the ABISUP abdomen, which includes Abdominal Pressure Twin Sensor. The APTS has been first introduced in child Q-dummies [11] and more recently NHTSA has also included them in the Large Omni-Directional Child (LODC) dummy [12] and in the THOR-05F [13]. Additionally, the ABISUP consortium has worked on defining a pressure-based Injury Risk Function for the ABISUP abdomen and a submarining predictor [14] to both assess abdominal injury and submarining risk.

METHOD AND DATA SOURCES

The ABISUP abdomen was designed according to the consortium agreed specifications [15], [16] and four identical prototypes were built and shipped to the US, Japan and France. An extensive test campaign was organized among the laboratories of the members. The ABISUP abdomen biofidelity and sensitivity was evaluated through impactor tests and seatbelt loadings. The pressure-based Injury Risk Functions were developed by replicating Kent's porcine belt tests and finally, their response was assessed in sled tests.

ABISUP Abdomen

The ABISUP abdomen can replace the standard THOR-50M lower abdomen without modifying the other dummy parts and its mass is equivalent to the standard lower abdomen assembly. In particular, the upper abdomen was kept in place to avoid changing the thorax response. The ABISUP abdomen was designed for the dummy slouched

position but could also be used for the super slouched position. It is made of a 940g piece of foam going around the lumbar spine and down inside the pelvis bones. The geometry of the ABISUP abdomen was designed to provide a continuous surface with the pelvis flesh in the frontal and lateral aspects of the dummy. The ABISUP abdomen top surface comes into contact with the upper abdomen without interfering with the thoracic lower IR-TRACCS. The front bib between the upper and the lower abdomens used in THOR-50M was kept to prevent the belt being trapped between the two abdomens (Figure 1.c). Abdominal Pressure Twin Sensor of 50 mm diameter and 122.5 mm length was inserted in the abdomen foam into 53 mm diameter holes and fitted into low friction material socks for repeatable contact with the abdomen skin. In the dummy sagittal plane, the APTS was aligned with the dummy spine with their caps pointing downwards inside the pelvis cavity, slightly below the neutral axis of the pelvic ASIS sensors. The upper end of the APTS was aligned with the lower abdomen foam top surface and covered by two Velcro caps to prevent the APTS going out their cavity (Figure 1.a). The back of the lower abdomen was supported on its right and left side by two welded steel brackets (Figure 1.b) attached to the existing IR-TRACC rear attachment plate. The APTS was located with the aim to provide the highest pressure for a loading between the ASIS sensors and the lower thoracic ribs. An exploded view of the prototype is shown in Figure 2.

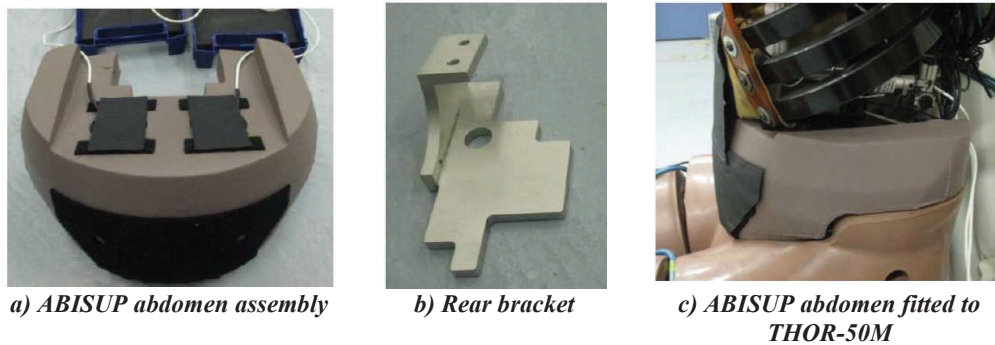


Figure 1. ABISUP abdomen assembly.

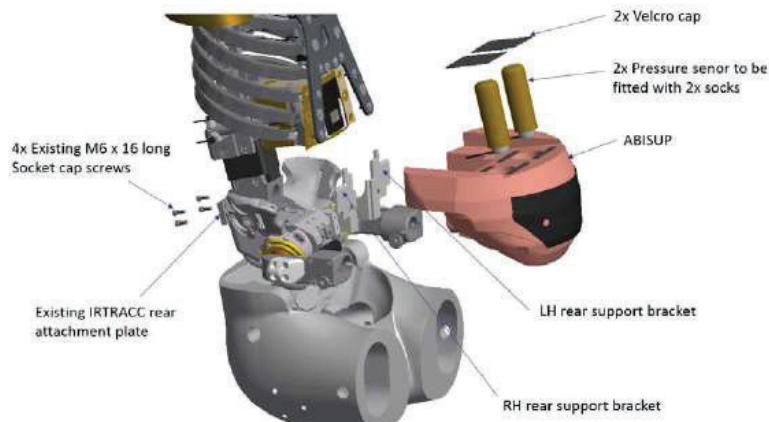


Figure 2. Exploded view of the lower abdomen ABISUP prototype and THOR-50M.

Test Setups

The biofidelity and the repeatability of the ABISUP abdomen was assessed by reproducing Post Mortem Human Surrogates (PMHS) tests of Lamielle [17], Ramachandra [18] and Foster [19]. The sensitivity of the ABISUP abdomen was evaluated by varying the seatbelt belt loading height in Foster [19] and Kent's [7] test setups. The reproducibility of the abdomen was checked under the qualification rigid bar tests of the THOR-50M [20]. The test results from the Kent setup were also used to define the relationship between the ABISUP abdomen pressure and its deflection during the development of the IRF. Sled tests were performed to check the ability of the ABISUP abdomen to discriminate between restraint conditions and evaluate the relevance of the risk predicted by the IRF. It has to be noted that for all the tests performed in Europe (at CEESAR-LAB, Université Gustave Eiffel, Forvia) the ABISUP abdomen was mounted on the same THOR Mod Kit 50th. The ASIS load cell new cover design implemented on the THOR Standard Build Level A and B was not updated but no lap belt being latched into the gap between the ASIS cover and the iliac crest bone were reported during tests. In the US and Japan, the ABISUP abdomen was mounted on a THOR-50M. Considering that the focus of this study is the response of the ABISUP abdomen and its associated IRF, it is assumed that the dummy version had little influence.

Seatbelt pull tests under Lamielle's setup [17] were performed at CEESAR and the setup consisted of a rigid seat and back support against which the dummy was seated upright. A standard seatbelt was initially positioned horizontally on the abdomen above the anterior superior iliac spines of the pelvis and below the ribs (Figure 3.a). The belt was routed backward through pulleys to the loading device. Both belt strands were attached to the loading system. A hydraulic piston was used to pull the belt through rotating rigid arms in order to multiply the belt displacement and speed. Two belt sensors (Figure 3.b), placed at the vicinity of the back plate on the right and left sides, were used to calculate the force applied onto the abdomen. The belt displacement was measured at the mid-point of the abdomen using a custom device with two rotary potentiometers allowing the computation of the x and z belt displacement (Figure 3.c), and at the belt side using an optical sensor or by double integration of the belt accelerations. The force applied on the abdomen was computed by adding the left and right belt forces. The abdomen deflection was calculated as the distance between the processed belt locations at each time step and at time zero. The ABISUP abdomen response was compared with the PMHS corridors defined by Lebarbé et al. [24] from the MHA test series of Lamielle.

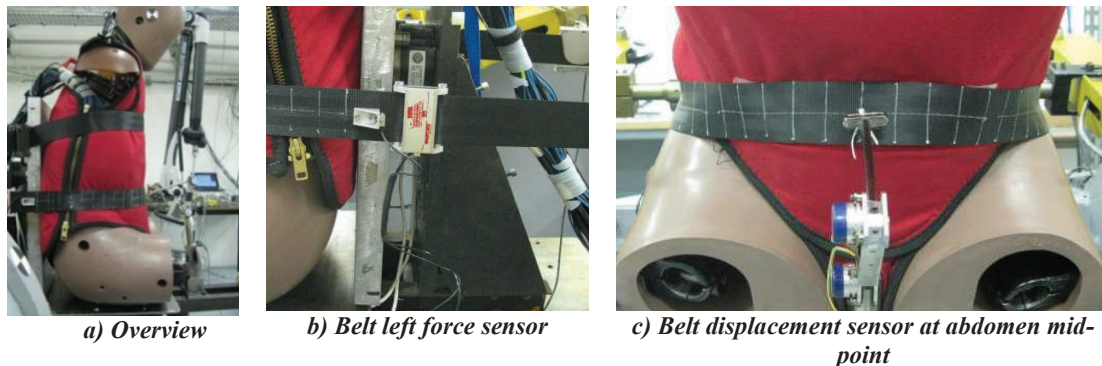


Figure 3. THOR Mod Kit 50th equipped with the ABISUP abdomen under Lamielle's test setup. Dummy on the rigid seat with the lap belt in position

Seatbelt pull tests with free back under Ramachandra's setup [18] were carried out at Transportation Research Center (TRC). The dummy was seated on a table with its back free to move (Figure 4). A seatbelt was wrapped around the dummy abdomen at the mid-abdomen level. The belt sides were tangent to the lateral aspects of the dummy and parallel to each other. The belt was attached on a T-bar connected to a pneumatic piston and was pulled at loading speeds of approximately 4 m/s. Two belt sensors measured the force in each strand and the belt displacement was measured in the mid-sagittal section of the belt using a string potentiometer. A string potentiometer was attached to the T-bar to measure the dummy back motion relative to the ram. The force applied to the abdomen was computed by adding the left and right belt forces. The displacement of the dummy spine was subtracted from the belt displacement. The ABISUP abdomen response was compared with the PMHS responses from Ramachandra et al. [18].

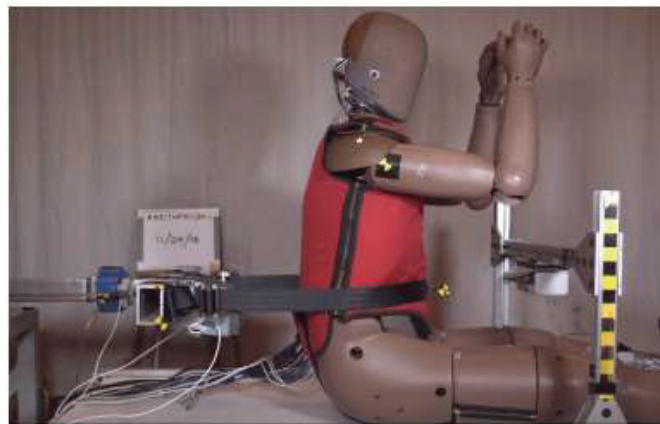


Figure 4. THOR-50M equipped with the ABISUP abdomen under Ramachandra's test setup.

Seatbelt pull tests under Foster's setup [19] were performed at CEESAR. The setup consisted of a rigid seat and back support against which the dummy was seated upright with its legs set horizontally (Figure 5.a). A seatbelt, initially positioned horizontally on the abdomen above the anterior superior iliac spines of the pelvis and below the ribs, was pulled rearwards by one or two pretensioner systems as used by Foster et al. The belt was guided in the lateral direction using two rollers. The position of the rollers was adjusted such that the distance between their most lateral points was equal to the dummy abdomen width. The pretensioners at the end of the belt were fixed onto a rigid support and their mounting axes were aligned horizontally with the centers of the rollers. The belt slack was minimized by adding a 10N pre-load on each belt strand. The dummy sitting height was adjusted to position the belt at three different heights and evaluate the sensitivity of the ABISUP abdomen to belt positioning: (1) the middle height position was where the belt lower border was aligned with the upper edge of the pelvic skin. This corresponded to the belt position in Foster's tests (Figure 5.b), (2) the lower height position was where the belt lower border touched the thigh flesh (Figure 5.c), (3) the upper height position was where the belt center line was aligned with the lower thoracic IR-TRACC attachment points (Figure 5.d). The belt displacement was measured at the mid-point of the abdomen using two rotary potentiometers allowing the computation of the x and z belt displacements. Two belt sensors, placed at the vicinity of the back plate on the right and left sides, were used to calculate the force applied onto the abdomen by summing their measurement. The abdomen deflection was calculated by subtracting the distance of the belt at each time step and the one calculated at time zero. The ABISUP abdomen response was compared with the PMHS responses from Foster et al. [19].

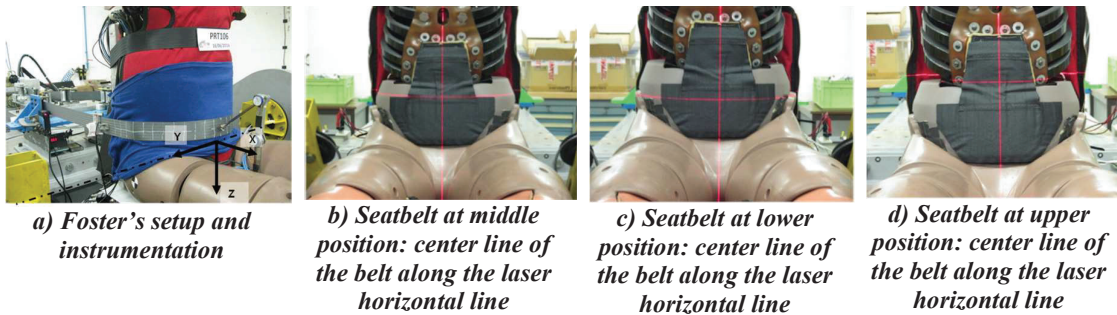


Figure 5. THOR Mod Kit 50th equipped with the ABISUP abdomen under Foster's test setup and seatbelt height variations.

Rigid bar impacts under Qualification setup [20] were performed at CEESAR. The THOR equipped with the ABISUP abdomen was seated on a flat horizontal surface on a thin Teflon sheet, its lower limbs in a horizontal position and its back free to move. The dummy was equipped with a target attached rigidly to the spine at the T12 location. The impactor face was rectangular with dimensions of 178 by 51 mm and rounded edges. The dummy sitting height was adjusted in order to align the IR-TRACC attachment points of the standard abdomen with the center of the impactor face (Figure 6.a, Figure 6). The 32 kg impactor was propelled at a target initial speed of 3.3 m/s. The impact force was calculated by multiplying the impactor mass by the impactor acceleration. The impactor displacement was measured from a target placed on its side. The abdominal deflection was calculated by subtracting the displacement of the target at T12 on the dummy from the target displacement on the impactor (Figure 6.c). The abdomen repeatability and reproducibility were evaluated by calculating the Coefficients of Variation (CV) of the APTS pressure, abdominal deflection and impactor force. CV scores were categorized according to NHTSA [6] as shown in Table 1.

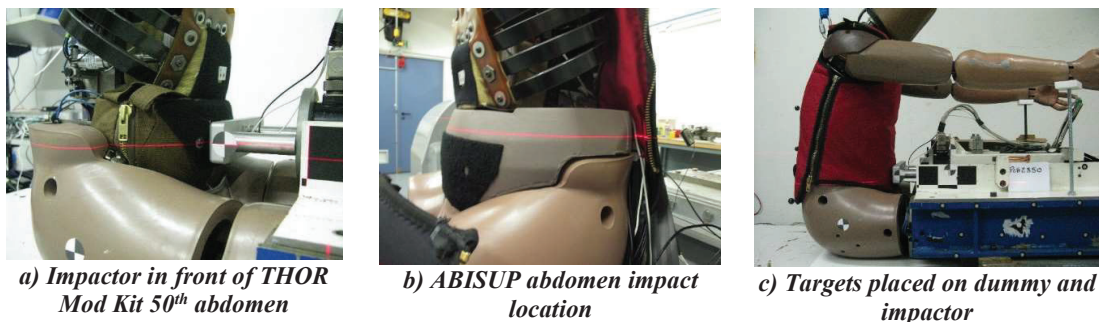


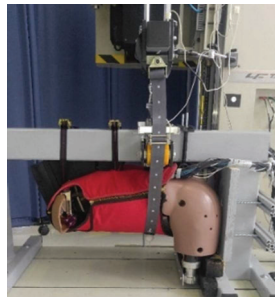
Figure 6. THOR Mod Kit 50th equipped with the ABISUP abdomen under the qualification test setup.

Table 1. Coefficient of Variation (CV) categories

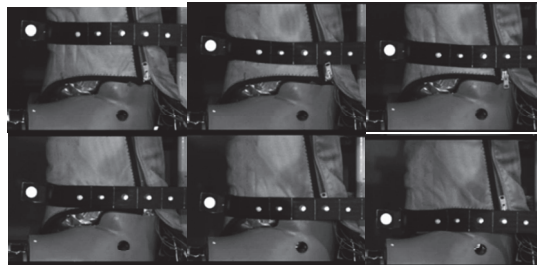
CV (%)	Category
0-5	Excellent
> 5-8	Good
> 8-10	Marginal (Acceptable)
>10	Poor (Unacceptable)

Seatbelt pull tests under Kent's setup [7] were carried out at the University Gustave Eiffel. The trunk of the THOR was fixed on a rigid structure in a seated upright position. It was attached on the rigid structure in several locations using (1) screws and a bracket to hold the pelvis posteriorly, (2) straps around its thoracic spine to pull it against the structure in two locations and (3) screws to hold the femurs in place. The dummy and the test fixture were then tilted with the dummy facing the ground and placed below a hydraulic orientable piston (Figure 7.a). Wedges were positioned behind the thoracic and lumbar spine to remove any gap with the rigid structure and all attachments were tightened. A seatbelt was wrapped around the mid abdomen. For Kent's setup, it was routed against rollers placed on each side on the dummy at the abdomen level as in Kent. Each belt strand end was attached to a transverse bar attached to the piston. The piston displacement was limited depending on the configuration to prevent any dummy damages. The belt strands and piston were parallel and oriented perpendicularly to the rigid structure. Seatbelt sensors measured the force in the belt strands and a target was placed on the seatbelt at the mid sagittal plane of the dummy to measure the belt displacement. The belt was pulled by the piston at various speeds ranging from 1 to 8 m/s.

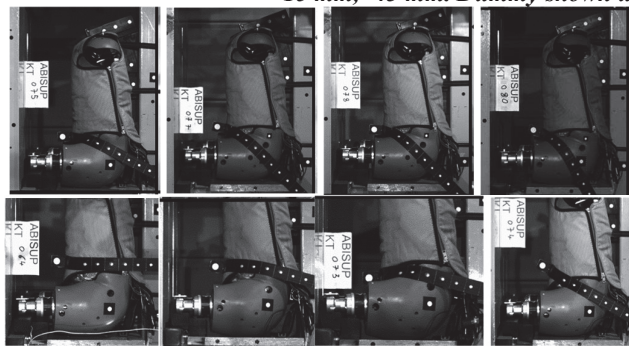
The relationship between the abdomen deflection and the APTS pressures was defined from these tests. Additionally, the sensitivity of the abdomen was studied by varying belt position height (Figure 7.b) and orientation (Figure 7.c) at a belt pull speed of 2 m/s. These tests were performed without the rollers.



a) Dummy positioned below the piston.



b) Seatbelt height variations. From top left to bottom right: +69 mm, +39 mm, +15 mm, Kent's seatbelt height (0 mm), -15 mm, -43 mm. Dummy shown upright for legibility.



c) Seatbelt angle and position variations. Dummy shown upright for legibility.

Figure 7. THOR-50M equipped with the ABISUP abdomen in Kent's (with rollers) and sensitivity (without rollers) setups.

Sled tests under Uriot's setup [21] were performed at Forvia. The front and rear seat configuration tests of Uriot et al. were replicated using the semi-rigid seat and a separated rigid backrest covered by foam pads (Figure 8.a). The THOR was restrained by a separated thoracic and lap belt equipped with Uriot's load limiters at the thoracic belt retractor and both lap belt anchorages. The seat pan orientation and stiffness, and the belt anchorage locations replicated the two configurations used by Uriot. The front seat configuration replicated the geometry and the seat behavior of a front seat (Figure 8.c). The rear seat configuration (Figure 8.d) replicated the geometry of a rear bench and the seat behavior was adjusted to obtain submarining in simulations with a Hybrid III 50th dummy. The dummy feet were positioned on a rigid footrest angled by 55° with respect to the horizontal and maintained in position during the crash. The sled was submitted to Uriot's 14 m/s deceleration pulse (Figure 8.b).

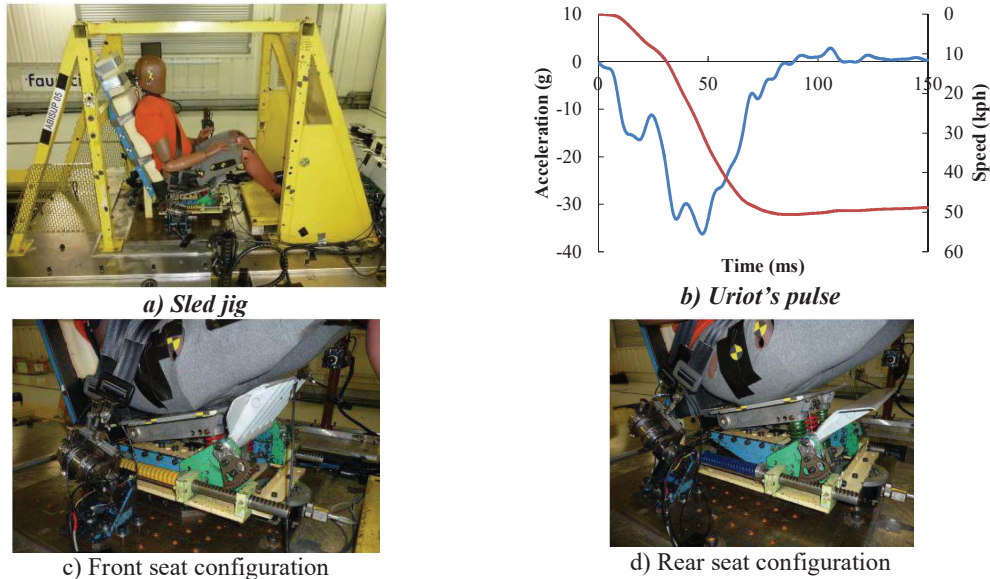


Figure 8. THOR Mod Kit 50th percentile in Uriot's sled test setup.

Sled tests using vehicle seats. Sled tests using vehicle seats were performed at Forvia, Virginia Tech-NHTSA and TMC. Four tests were performed at Forvia using a driver seat and a 3-point belt equipped with a 6 kN load limiter and a pretensioner in the retractor (Figure 9.a). Two tests were performed in a standard configuration for a front passenger seat (Figure 9.c) and two in a slouched configuration (Figure 9.d) where all anchorage points were moved 50 mm rearwards with respect to the seat, the dummy was positioned with its pelvis moved forward by 60 mm and the shoulder pretensioner was not activated. The sled was subjected to a 14 m/s pulse (Figure 9.b). These tests replicated Uriot et al. tests [22].

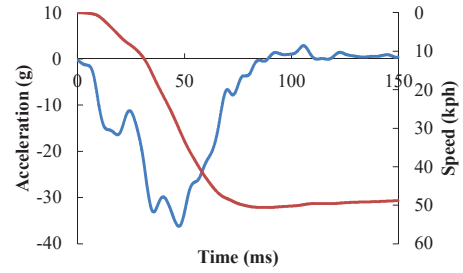
Ten sled tests were performed at Virginia Tech. using a rear seat and a 3-point belt (Figure 10.a). Five tests were performed at 36 km/h and five at 56 km/h. Figure 10.b shows the 56 km/h scaled pulse resulting in a 32 km/h pulse. Finally, a generic 36 km/h pulse (Figure 10.c) was used for the tests [23].

Seven tests were performed at TMC using a production driver seat with a seat-mounted 3-point belt equipped with a 4 kN load limiter and pretensioner in the shoulder retractor (Figure 11.a). A pulse corresponding to a 40 km/h crash between a family car and the Full-width Rigid Barrier (FWRB) was applied to the sled (Figure 11.b). The restraint system was varied by adding to the 3-point belt either a lap belt pretensioner or a knee bolster. Furthermore, the seatback angle was adjusted to obtain either a 21° or a 49° torso angle (Figure 11.c to f).

For this paper, the analysis of the sled tests was limited to the analysis of the ABISUP abdomen pressure and the kinematics including the occurrence of submarining. These results were used to check the applicability of the developed abdominal IRFs.



a) Sled jig



b) Sled pulse



c) Standard configuration

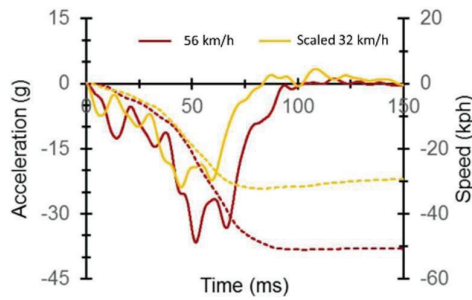


d) Slouched configuration

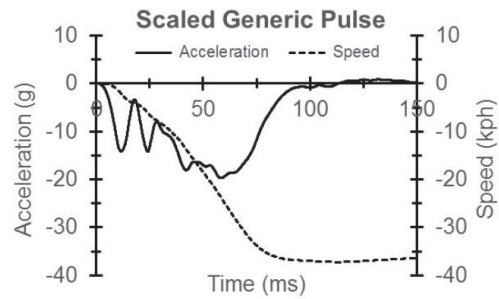
Figure 9. THOR Mod Kit 50th percentile in Forvia sled test setup [22].



a) BIW



b) 56 km/h and 32 km/h scaled pulses

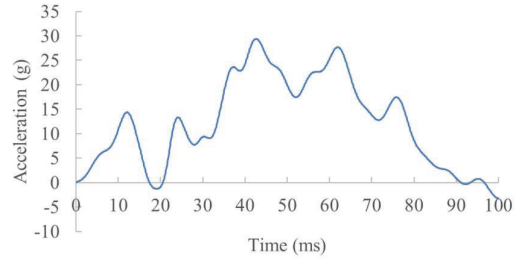


c) 36 km/h generic pulse

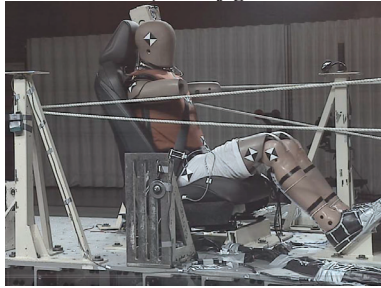
Figure 10. THOR-50M (left) in Virginia Tech and NHTSA Body In White (BIW) sled test setup [23].



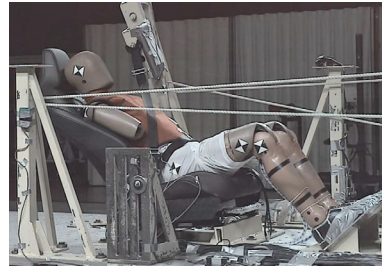
a) Sled jig



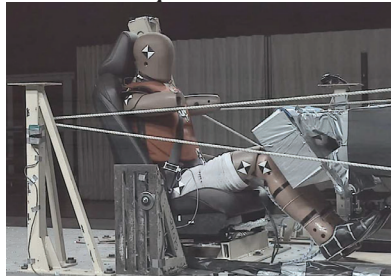
b) Sled pulse



c) 21° torso angle carried out without and with lap belt pretensioner



d) 49° torso angle carried out without and with lap belt pretensioner



e) 21° torso angle and knee bolster configuration



f) 49° torso angle and knee bolster configuration

Figure 11. THOR-50M in TMC sled test setup (the dummy forearms were removed for the tests to prevent them hiding the dummy and seatbelt targets).

Summary: Test matrices

The belt and impactor tests performed on the ABISUP abdomen are summarized in Table 2. Table 3 shows the twenty-five sled tests performed on THOR dummy equipped with the ABISUP abdomen. Some of the tests were also replicated with the standard THOR.

Table 2. Seatbelt pull tests and rigid bar impacts performed on ABISUP abdomen

Reference	Loading type	Number of tests	Comments
Lamielle et al. [17]	4 m/s seatbelt pull test, mid abdomen	2 ¹	Biofidelity
	3.5 m/s seatbelt pull test, mid abdomen	5	Repeatability
Ramachandra et al. [18]	4 m/s free back pull test Mid abdomen	3	Biofidelity and repeatability
Foster et al. [19]	Single pretensioner, Mid abdomen	3	Biofidelity and repeatability
	Dual pretensioner, Mid abdomen	3	Biofidelity and repeatability
	Single pretensioner, Upper abdomen	2	Sensitivity
	Single pretensioner, Lower abdomen	2	Sensitivity
Qualification [20]	32 kg, 3.4 m/s Rigid bar impact	8	Two tests per abdomen
Kent et al. [7]	Seatbelt pull test at various speed	43	Relationship between APTS pressure and belt deflection
	Seatbelt pull test at various heights on the abdomen	6	Sensitivity
	Seatbelt pull test for various belt angles	8	Sensitivity

¹ One test replicated with the standard THOR

Table 3. Sled tests performed on THOR equipped with ABISUP abdomen

Reference	Test conditions	Number of tests
Forvia sled tests (Uriot et al. [21])	50 km/h pulse, Vehicle seat, Standard sitting posture 3-point belt	2
	50 km/h pulse, Vehicle seat, Slouched sitting posture 3-point belt	2
Forvia sled tests (Uriot et al. [22])	50 km/h pulse, Semi-rigid seat, Front seat configuration Separated shoulder and lap belt	2 ¹
	50 km/h pulse, Semi-rigid seat, Rear seat configuration Separated shoulder and lap belt	2 ¹
Virginia Tech, NHTSA sled tests	36 km/h pulse, Rear seat, 3-point belt	5
	56 km/h pulse, Rear seat, 3-point belt	5
TMC sled tests	40 km/h FWRB pulse, Standard sitting posture 3-point belt (repeated), 3-point belt, & lap belt pretensioner, 3-point belt & knee bolster	4 ²
	40 km/h FWRB pulse, 49° torso angle sitting posture 3-point belt (repeated), 3-point belt, & lap belt pretensioner, 3-point belt & knee bolster	3 ²

¹ Two tests replicated with the standard THOR

² Test with the three-point belt only replicated with the standard THOR

Injury Risk Function Definition

The IRFs were developed from Kent et al. [7] porcine tests in which abdominal injuries were observed and various injury metrics including abdominal compression were tested. The tests performed on the ABISUP abdomen under similar conditions were used to define the relationship between the ABISUP compression and the mean of the maximum pressure from the right and left side of the APTS. The mean pressure was used because the setup should have been symmetrical and averaging could therefore partially correct symmetry errors. However, the peak pressure is used when applying the curve as vehicle environments are not symmetrical. Two compressions were calculated. The first one uses the same definition as Kent, i.e. the ratio between the abdominal deflection and abdominal depth. It will be called ABISUP abdomen compression. This definition does not account for possible differences in spine depth between species. The second one was calculated as the ratio between the abdominal deflection and the abdomen compressible depth in front of the dummy lumbar spine. It will be called ABISUP soft abdomen compression. The abdomen depths were measured in the dummy mid sagittal plane of the Finite Element Model (FEM) published by the University of Virginia. The compressible depth was equal to 157 mm whereas the total abdominal depth of the dummy with the ABISUP abdomen was equal to 266 mm. The depths were also checked against the physical dimension of the dummy used in the test. Kent's porcine soft abdominal compression was calculated as well considering the compressible depth in front of the porcine spine. This was done by assuming a constant ratio between the compressible abdomen depth and the total depth across specimen. Details are provided in Appendix 2. Then, assuming an equivalence between the dummy and porcine compressions, the compressions were transformed in pressures using ABISUP abdomen relationships between the compressions and the APTS maximum pressure. IRFs were created for the two compressions following partially an ISO Technical Specification [25]. Survival analysis and different distributions (Weibull, Lognormal, Log-logistic) were used to compute the risk curves with the R software. The distribution with the lowest Akaike Information Criterion (AIC) was kept and it was found to be the Log-logistic distribution. The risk of abdominal injury was given by Equation 1. Then, the risk ratio was computed for different levels of risk and a rating (between good for ratios below 0.5 and unacceptable for ratios above 1.5) was attributed. There was no check for multiple injury mechanisms or overly influential observations.

$$p(AIS \geq 3) = \frac{1}{1 + \exp\{-\ln(\text{Max.pressure}) + \text{Intercept}\} / \exp(\log_scale)} \quad \text{Equation 1}$$

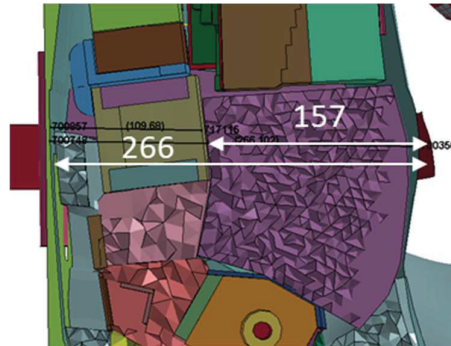


Figure 12. Compressible and total abdominal depths of the ABISUP abdomen shown on the THOR model with the ABISUP abdomen.

RESULTS

ABISUP Abdomen Biofidelity

The biofidelity of the abdomen was assessed by comparing its response to the corridors defined from the PMHS responses of Lamielle et al. [17], Ramachandra et al. [18] and Foster et al. [19]. The belt displacement referred to the displacement of a point placed on one of the belt sides and the abdomen or dummy deflection corresponded to the displacement of a point placed on the belt in the dummy sagittal plane.

Comparison with Lamielle’s PMHS responses. At first, the inputs used for the belt displacement and the belt speed versus time were compared between the PMHS, the standard THOR and the ABISUP abdomen. This showed that the belt displacement for the ABISUP abdomen was on the upper boundary of the PMHS corridors and that the belt speed was slightly higher than the one applied in the PMHS tests (Figure 13.a and b). This difference of input illustrated the difficulty to replicate the exact conditions of such tests as the input was affected by the surrogate characteristics. The comparison of the deflections and forces showed that the ABISUP maximum abdomen deflection was lower than the one of the PMHS and that the ABISUP force did not increase sufficiently at the beginning of the deflection (up to around 50 mm) (Figure 14.a). The ABISUP abdomen deflection and force were increased compared to the standard THOR-M50, however this might be related to the higher belt displacement and speed rather than a difference in the two abdomen behaviors. It has to be noted that the ABISUP abdomen deflection was lower than the belt displacement whereas similar values were observed for the PMHS. This may have to do with differences in the lateral deflection of the ABISUP and PMHS abdomens.

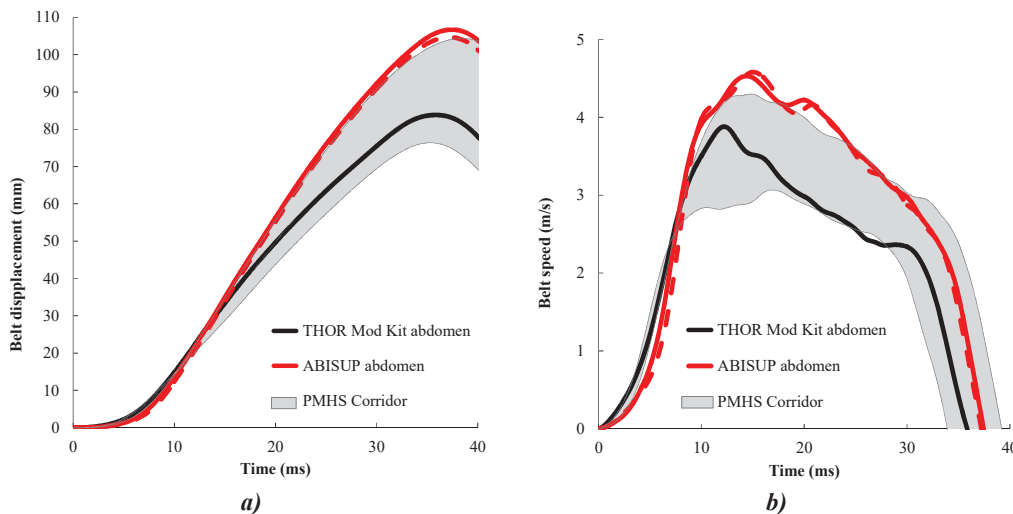


Figure 13. Belt displacement (a) and speed (b) of ABISUP abdomen test versus Lamielle’s PMHS corridors.

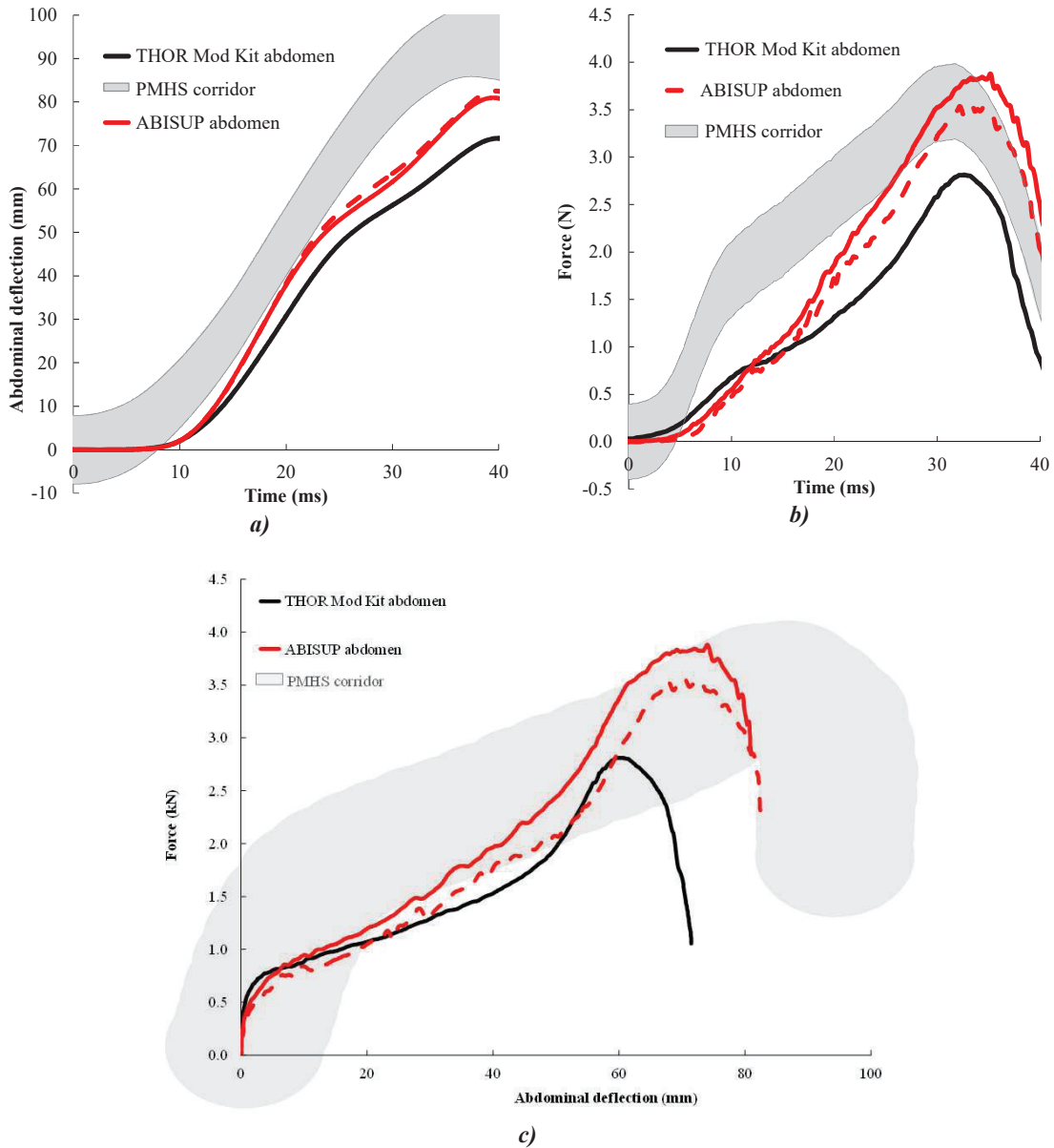


Figure 14. ABISUP abdomen response versus Lamielle's PMHS corridors: Abdomen deflection versus time (a), force versus time (b), force-abdomen deflection (c).

Comparison with Ramachandra's PMHS responses. The responses of the ABISUP abdomen and of the standard dummy were compared with the response corridors defined from the PMHS tests for the free-back test configuration. For both deflection and force, the ABISUP abdomen responded very similarly to PMHS initially, but later in the event, both dummy responses began to deviate from the PMHS, with the result being a much lower dummy peak deflection and higher dummy peak force (Figure 15). This could result from different abdomen behavior and/or differences in whole body translation compared to the PMHS as both dummy and PMHS were free to move. It can be noted that the peak PMHS deflections were close to and sometimes higher than the physical limits of the dummies resulting from their abdomen depths.

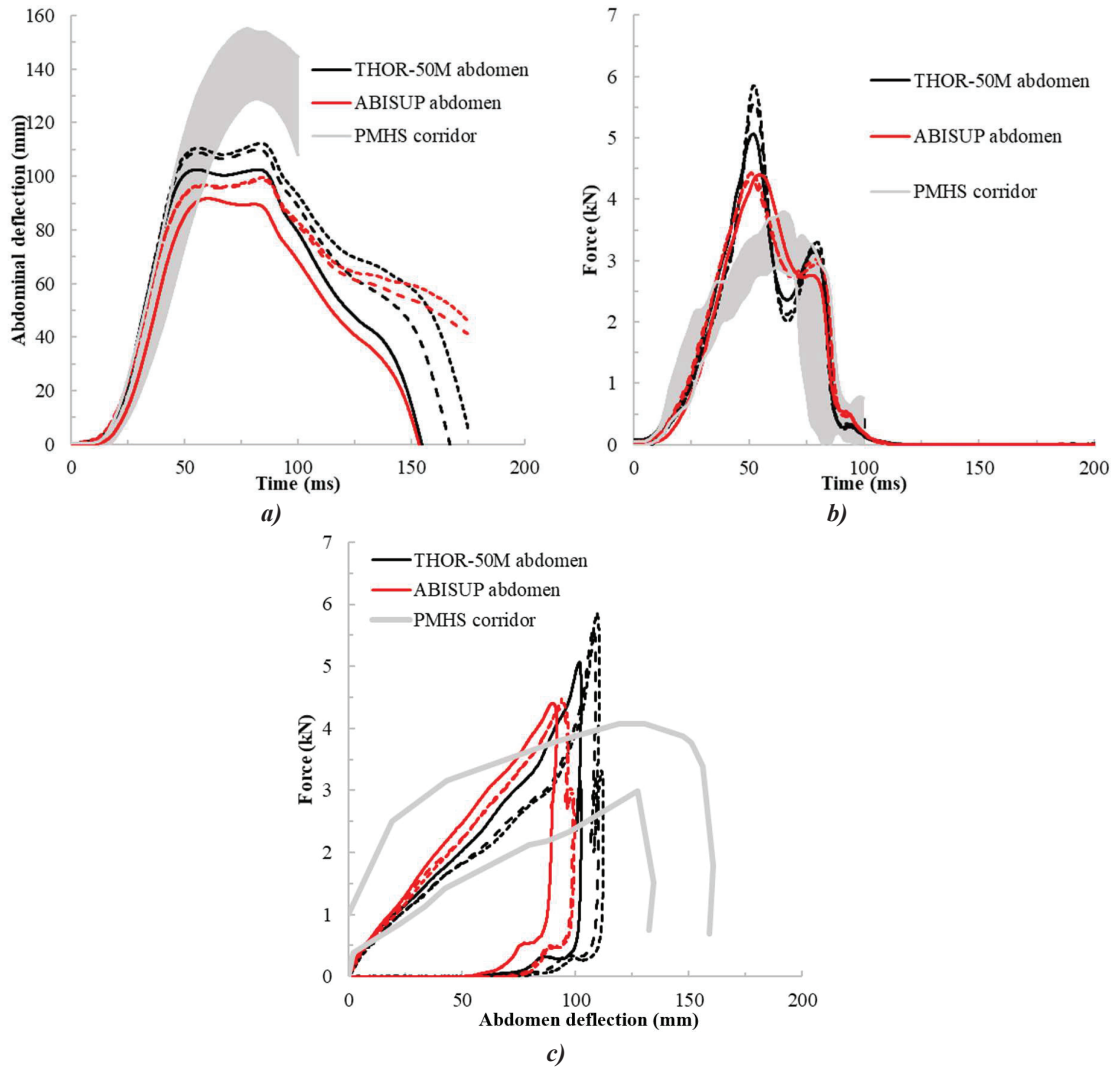


Figure 15. ABISUP abdomen response versus Ramachandra's PMHS corridors in free-back loading: abdomen deflection versus time (a), force versus time (b), force-abdomen deflection (c).

Comparison with Foster's PMHS responses. The ABISUP abdomen response was compared with the corridors defined by Foster at al. [19]. In the single pretensioner test, the ABISUP abdomen force was below the PMHS force-deflection corridor from 0 to 25 mm of deflection, but in the corridor for the remainder of the response (ref Figure 16, bottom left). In the dual pretensioner test, the ABISUP abdomen force was below the PMHS force-deflection corridor from 0 to 40 mm of deflection, but in the corridor for the remainder of the response (Figure 16). The single pretensioner tests created a belt displacement speed of 11 m/s whereas the dual pretensioner tests reached 19 m/s.

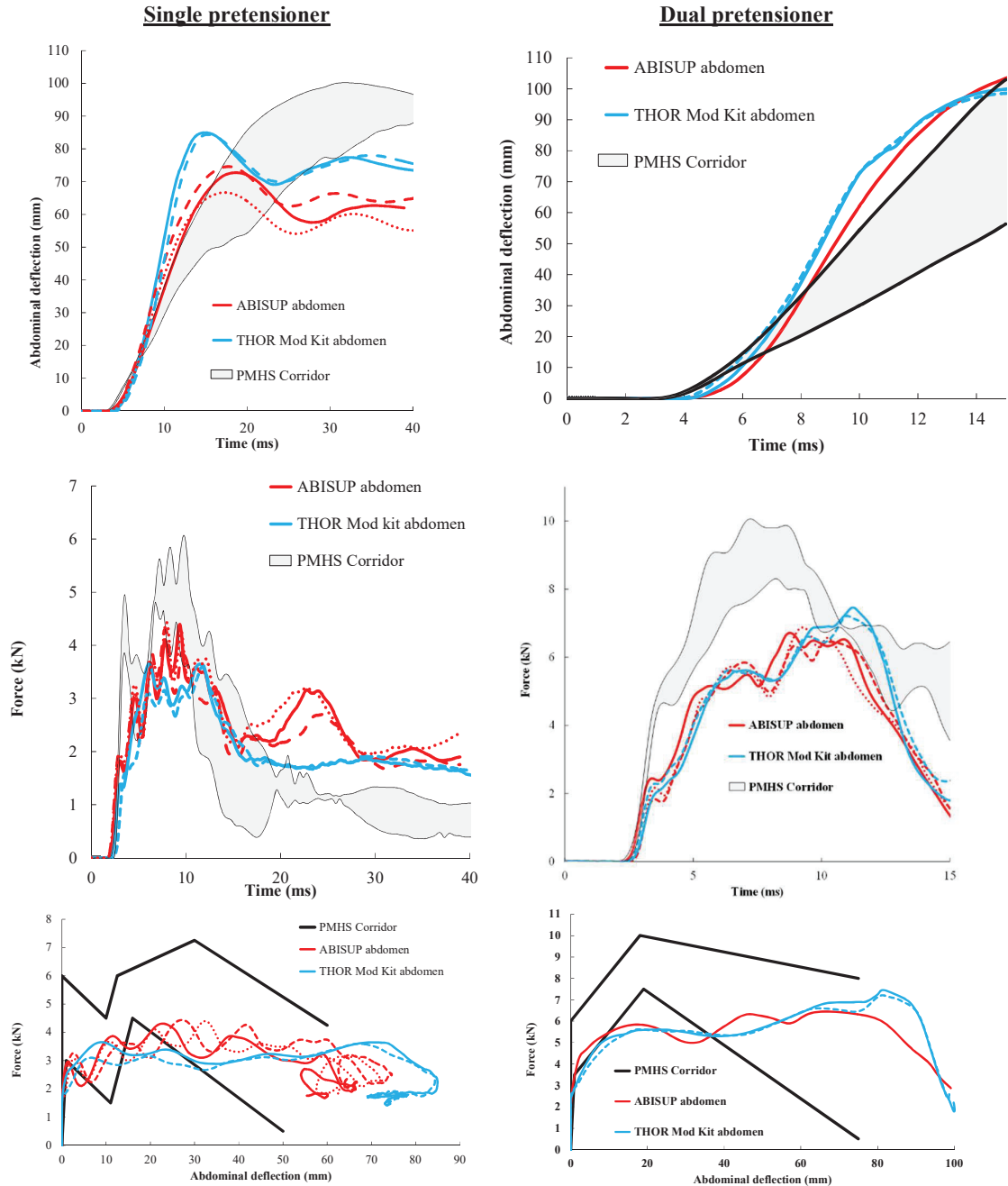


Figure 16. ABISUP abdomen response versus Foster's PMHS corridors in single pretensioner loading (left) and in dual pretensioner loading (right). From top to bottom: abdomen deflection versus time, force versus time and force-abdomen deflection.

ABISUP Abdomen Repeatability

Repeatability in Lamielle's tests Five tests were performed giving the same input to the servo-controlled machine for the piston displacement and speed. However, as it can be observed in Figure 17 and Figure 18, the applied belt displacement and speed were not completely repeatable. Abdominal deflection, belt force and APTS pressures were compared. Maximum values and CVs are displayed in Table 4. Despite the variation of the belt displacement and speed, the abdomen CV values were close to 5%.

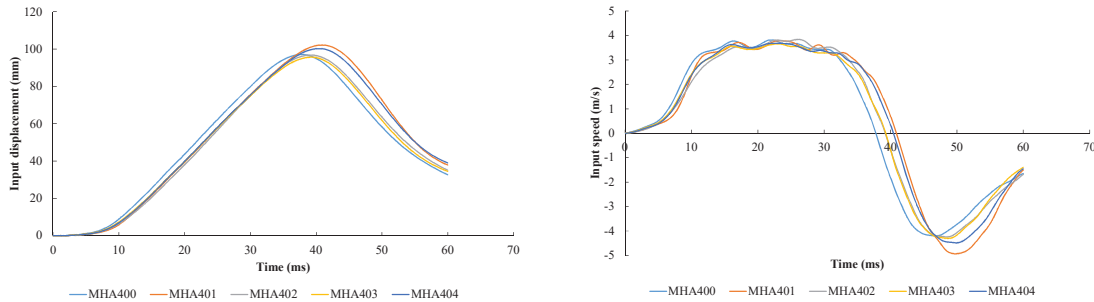


Figure 17. Belt displacement (left) and speed (right) in the five repeated tests.

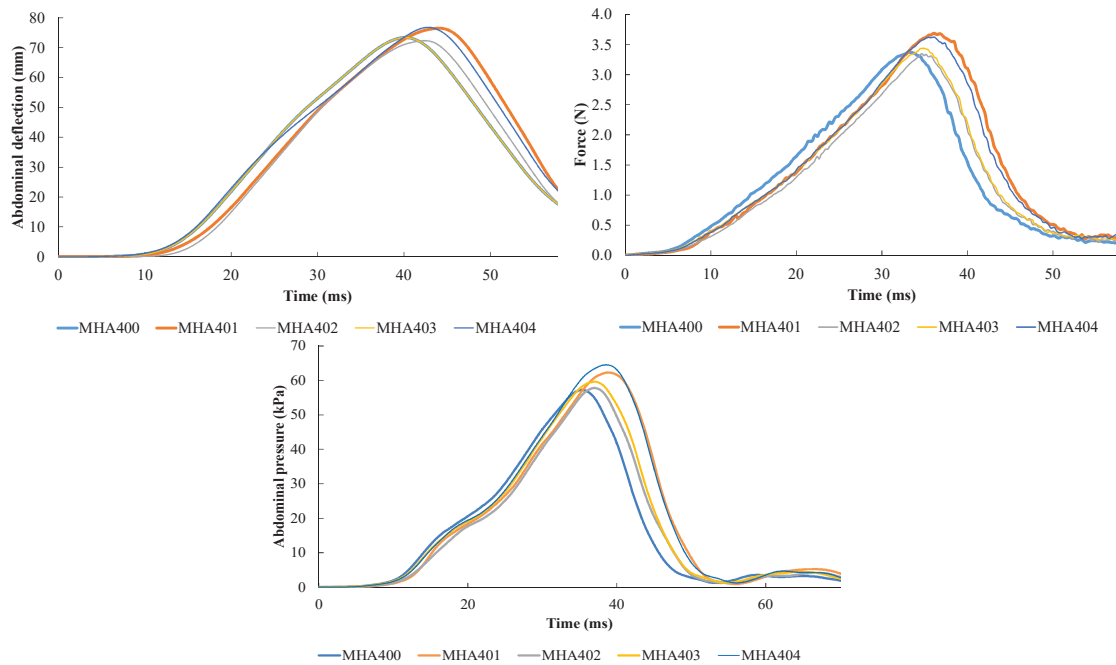


Figure 18. ABISUP abdomen deflection (top left), belt force (top right), right and left APTS average pressure (bottom)

Table 4. Maximum values in repeated Lamielle's tests

Test	Abdomen deflection (mm)	Belt force (kN)	Left APTS maximum pressure (kPa)	Right APTS Maximum pressure (kPa)
MHA400	73	3.0	59	56
MHA401	76	3.4	65	59
MHA402	72	3.0	59	57
MHA403	72	3.1	62	57
MHA404	77	3.3	69	61
Mean	74	3.2	63	58
Standard deviation	2.3	0.19	4.2	1.9
CV	3%	6%	7%	3%

Repeatability in Ramachandra's tests. Three tests were repeated. The abdominal deflection and the belt force CV values were below 5%. The APTS pressure CV values were between 3 and 4% (Table 5). In free back tests, the dummy was free to move and the APTS were therefore less sensitive to possible slightly asymmetrical loading provided by the test set-up as may be encountered in the fixed back tests under Lamielle's conditions (CV values up to 7%). These values correspond to an excellent or good rating according to [6].

Table 5. Maximum values in repeated Ramachandra's tests

Test	Abdomen deflection (mm)	Belt force (kN)	Left APTS maximum pressure (kPa)	Right APTS maximum pressure (kPa)
Fixed back	67	2.5	41	44
Fixed back	70	2.7	47	52
Fixed back	71	2.6	45	47
Fixed back	72	2.5	45	48
Mean	70	2.4	45	48
Standard deviation	1.9	0.09	2.6	3.4
CV	3%	4%	6%	7%
Free back	92	4.4	91	91
Free back	100	4.5	97	95
Free back	99	4.3	98	96
Mean	97	4.4	95	94
Standard deviation	4.3	0.08	3.8	2.9
CV	4%	2%	4%	3%

Repeatability in Foster's tests. Tests were repeated three times for the single and for the dual pretensioner test configurations. The abdomen response was well repeatable with CV values below 5% except in the first single pretensioner test in which a lower abdomen deflection and therefore APTS pressure were recorded (Table 6). The reason was not identified.

Table 6. Maximum values in repeated Foster's tests

Test	Abdomen deflection (mm)	Belt force (kN)	Left APTS Maximum pressure (kPa)	Right APTS Maximum pressure (kPa)
Single pretensioner	67	4.4	101	108
Single pretensioner	75	4.5	137	144
Single pretensioner	73	4.5	132	129
Mean	71	4.5	123	127
Standard deviation	4.1	0.06	19.6	17.9
CV	6%	1%	16%	14%
Dual pretensioner	NA	7.3	207	203
Dual pretensioner	109	6.7	201	199
Dual pretensioner	NA	7.1	202	186
Mean	NA	7.0	203.5	195.8
Standard deviation	NA	0.3	3.3	8.7
CV	NA	4%	2%	4%

ABISUP Abdomen Reproducibility

Four identical prototypes were built (two for the US, one for Japan and one for Europe) and finally all shipped back to CEESAR to be subjected to the qualification test and compared. All prototypes were identical except that one of the US prototypes had a thicker skin implemented after damages were observed on previous prototypes (Table 7, Figure 19).

Figure 20 shows the force-deflection curves of the four prototypes. The damages of two abdomens prior to the qualification tests did not seem to affect their responses compared to the undamaged ones. The reinforced skin also did not seem to influence the mechanical behavior of the abdomen.

The results were normalized using the target impact speed of 3.30 m/s and assuming that all parameters were proportional to the impact speed. The speed varied between 3.24 and 3.54 m/s and the normalization helped to reduce the result variance. The normalized peaks of the qualification tests are summarized in Table 8. The difference between the left and right APTS pressure could not be explained. In average, pressure peaks were almost 10% higher on the right side. The pressure on the right side was also higher than on the left side in seven of the eight tests. This is surprising as the left and right APTS were identical and it was not known at manufacturing on which side they would be installed. This would point towards a difference related to the foam or the test setup.

The four prototypes exhibited a similar response with CV values between 2 and 7% corresponding to an excellent or good rating. The reinforced skin did not modify the response of the abdomen while improving the durability.

Table 7. ABISUP abdomen prototype description

Abdomen (serial number)	APTS.		Number of final certification tests	Region of round robin tests	Comments
	Right side	Left side			
EI 3455	W170DC	W170DA	2	Europe	Damaged*
EI 3466	P182T5	P182T4	2	US	-
EI 3467	P182R9	P182R8	2	Japan	Damaged*
EI 3513	W170DC	W170DA	2	US	Thicker reinforced skin

* Damages to the outer skin and the foam beneath it occurred before the certification due to other tests. The abdomens were repaired with tape.



Figure 19. ABISUP abdomens before the qualification test.

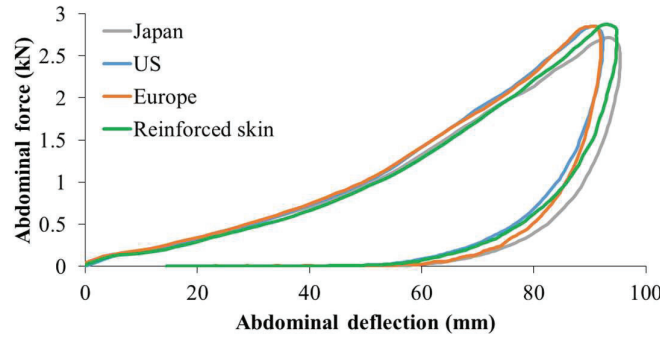


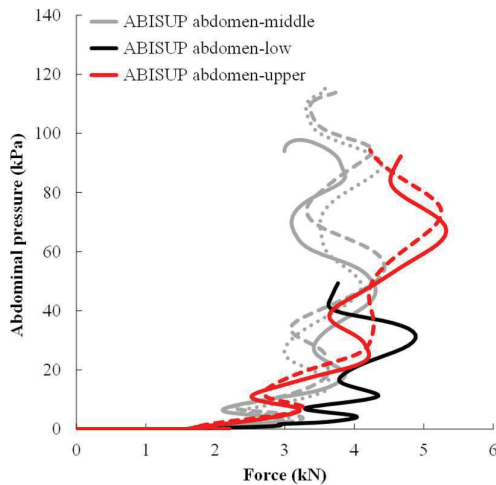
Figure 20. Force-abdomen deflection curves of the four prototypes.

Table 8. Normalized peak values

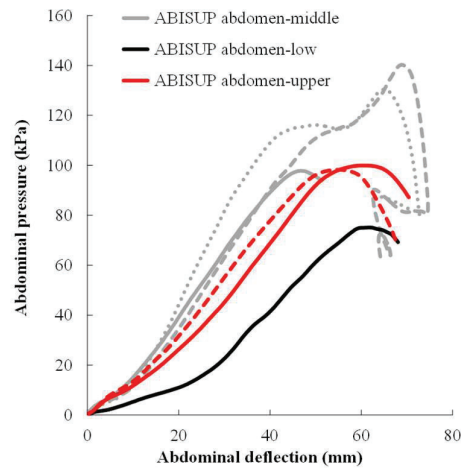
Abdomen prototype	Impact speed (m/s) (not normalized)	Maximum pressure (kPa)		Abdominal deflection (mm)	Impact force (N)
		Left	Right		
EI 3467 (Japan)	3.42	66.8	70.6	99	2714
	3.34	64.5	72.8	95	2717
EI 3455 (US)	3.44	76.8	71.8	94	2810
	3.46	73.4	75.5	92	2853
EI 3455 (Europe)	3.51	69.9	76.3	97	2750
	3.54	69.3	84.9	92	2855
EI 3513 (US, skin reinforced)	3.32	68.1	83.8	97	2854
	3.24	67.9	81.3	97	2878
Mean value	4.41	70	77.1	95.5	2804
Standard deviation	0.10	4	5.6	2.6	67
CV (%)	3	5.6	7.2	2.7	2.4

ABISUP Abdomen Sensitivity

The ABISUP abdomen sensitivity to loading height was evaluated under Foster's test configuration. The average APTS pressure versus belt force and versus abdomen deflection are shown in Figure 21. The highest APTS pressure was recorded for the middle height seatbelt position, when the lap belt laid between the pelvis skin and the lower thoracic ribs. The lowest pressure was measured when the belt was in the low position, in contact with the pelvis (Figure 21.b). From Figure 21.a it can be observed that both pressure and deflection increases were delayed compared to the belt force increase which might be due to an inertial effect (e.g. created by the jacket rib stiffeners), and possibly to some viscous effect of the abdomen under the high initial belt speed delivered by the pretensioner (11 m/s).



a) ABISUP abdomen average APTS pressure versus belt force



b) ABISUP abdomen average APTS pressure versus abdomen deflection

Figure 21. ABISUP abdomen responses versus belt height (middle, lower, upper) under Foster's test setup.

Under Kent's test setup, the rollers guiding the belt were removed, the two strands were made parallel and compression tests were conducted for several seatbelt heights. The pressure versus the abdomen deflection relationships were found to be relatively insensitive to the belt location, with the exception of a drop visible for the +69 mm belt position (on the thorax). The sensitivity to belt force was the highest for the belt position at Kent's test height (Base configuration) and 15 mm caudal from that position (Figure 22 left). At these heights, the belt was mainly in contact with the abdomen with little interaction with the pelvis and no interaction with the thorax. For the other heights, the pelvis or thorax carried some of the loads, which explained the reduced pressure sensitivity as these loads were not applied to the abdomen. The pressure sensitivity to deflection was much less marked with only significant drops visible for the most cranial positions of the belt (+39 and +69 positions, Figure 22 center) and limited differences otherwise even when the pelvis was involved.

The tests were then expanded to use various belt angles. The highest pressure sensitivity versus the belt force was obtained for the belt positioned at the mid abdomen and various angles between 15° and -30° (Figure 23 left). As in the belt height tests, this was consistent with the limited involvement of thoracic and pelvic structures. The highest pressure sensitivity to the abdomen deflection was obtained for the mid abdomen negative belt angles (which may occur during submarining) followed by the base and small positive angles with the belt in the mid abdomen (Figure 23 center). The pressure drop was relatively limited for 30° despite the belt involving the pelvis. This was interpreted as resulting from the sizeable proportion of the abdomen in front of the pelvis.

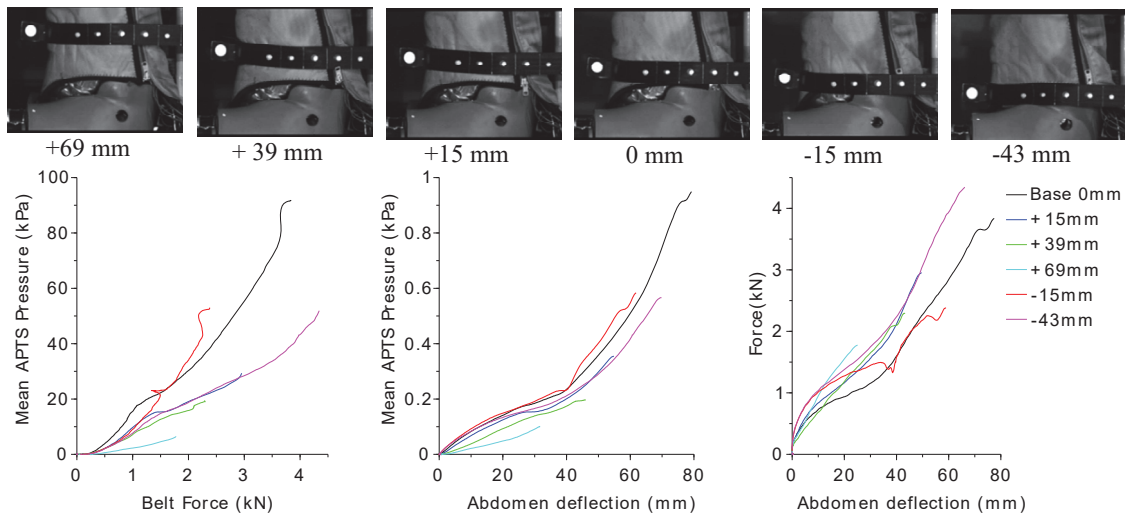


Figure 22. ABISUP abdomen responses versus belt height. The legend indicates the shift from the baseline position (0mm) with positive distances being cranial. The deflection is always measured at the belt in the dummy mid sagittal plane.

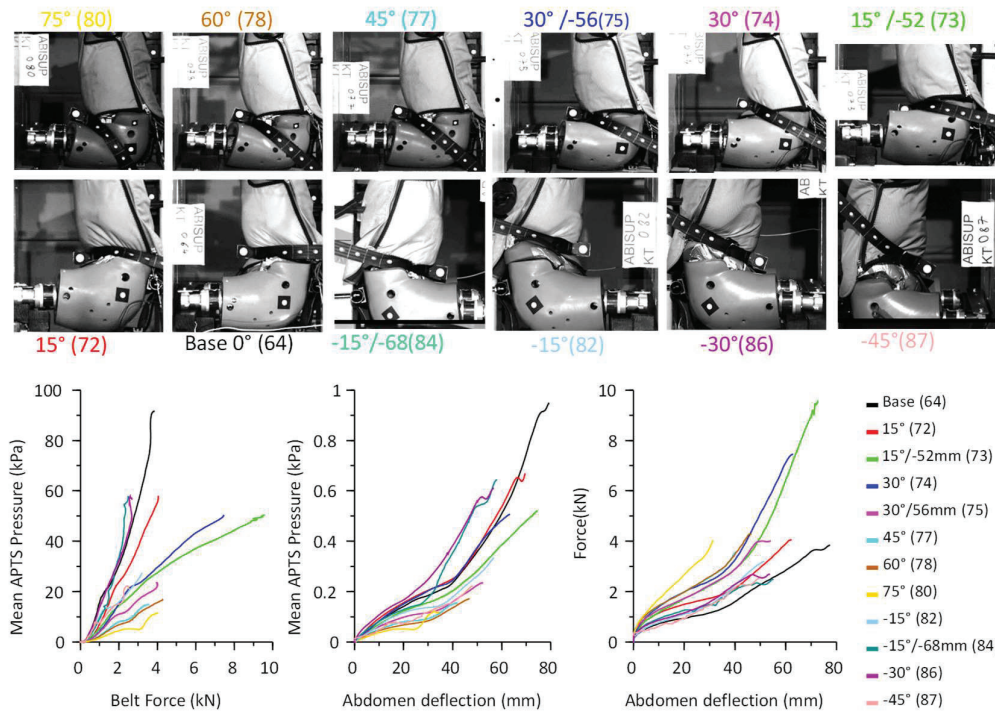


Figure 23. ABISUP abdomen responses versus belt angle. The legend indicates the angle (0° being horizontal, positive values with the belt engaging the pelvis) and, when different from 0mm (baseline) the shift of the mid-sagittal point from the baseline in the cranio-caudal direction with positive distances being cranial. The deflection is always measured at the belt but only the antero-posterior component is kept.

ABISUP Abdomen Injury Risk Function

From the 43 tests performed according to Kent's setup, the relationships between the average pressure of right and left APTS and the abdomen compressions were defined by fitting a second order polynomial curve through the experimental data points (Figure 24, Equations 2 & 3). The data points are provided in Appendix 1. The maximum belt displacement achieved was 118 mm, or about 44% abdomen compression and about 75% soft abdomen compression. It was not attempted to achieve higher compressions as the total belt force was already over 13 kN in that case (measured after the rollers).

Assuming an equivalence of the compressions, Kent's abdomen compressions were then converted to dummy pressure using the equations 2 and 3. Then, Kent's abdomen deflection data was changed to soft abdomen compression considering the compressible depth of other porcine specimen of similar size. It was assumed that the ratio of soft and total abdominal depth would be the same for all specimens. This led to compressions higher than 100% in four cases out of 45 (see details in Appendix 2). The pressure was calculated from the abdomen and soft abdomen compressions using the equations 2 and 3. When the soft abdomen compressions derived from Kent's porcine tests was over 75% (i.e. the maximum reached in the dummy tests), the pressure was calculated by extrapolation.

The AIS3+ IRFs obtained using the survival analysis and a Log-logistic distribution (distribution with the best AIC score) are shown in Figure 25, together with its confidence interval and risk ratio calculated according to ISO [25]. At 50% risk, the risk ratios of the IRFs were 0.61 and 0.85 for the abdomen compression and soft abdomen compression, respectively. Both are rated as "fair" according to ISO [25]. For the abdomen compression, an average of the maximum pressure of the right and left APTS of 133, 201 and 304 kPa corresponded to a 25%, 50% and 75% risk of AIS3+ abdominal injuries, respectively (Table 9). For the soft abdomen compression, an average of the maximum pressure of the right and left APTS of 108, 197 and 361 kPa corresponded to a 25%, 50% and 75% risk of AIS3+ abdominal injuries, respectively (Table 9).

The risks corresponding to the pressures measured in the component tests (seatbelt pull and rigid bar tests) are shown in Figure 26. They were all below 55% risk.

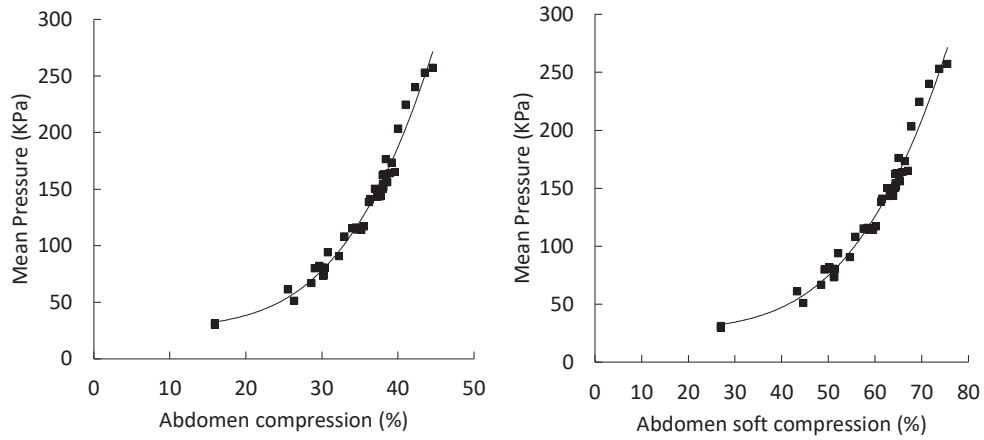


Figure 24. Average pressure of right and left APTS sides versus the abdomen compression: left versus abdomen compression, right versus abdomen soft compression.

For x=Abdominal Compression (C_{max}):

$$\text{Pressure} = 6.9440E-3 x^3 - 2.7868E-01 x^2 + 4.7133 x ; R^2 = 0.978 \quad \text{Equation 2}$$

For x=Soft abdominal Compression ($Soft_C_{max}$):

$$\text{Pressure} = 1.4278E-3 x^3 - 9.7084E-02 x^2 + 2.7819 x ; R^2 = 0.978 \quad \text{Equation 3}$$

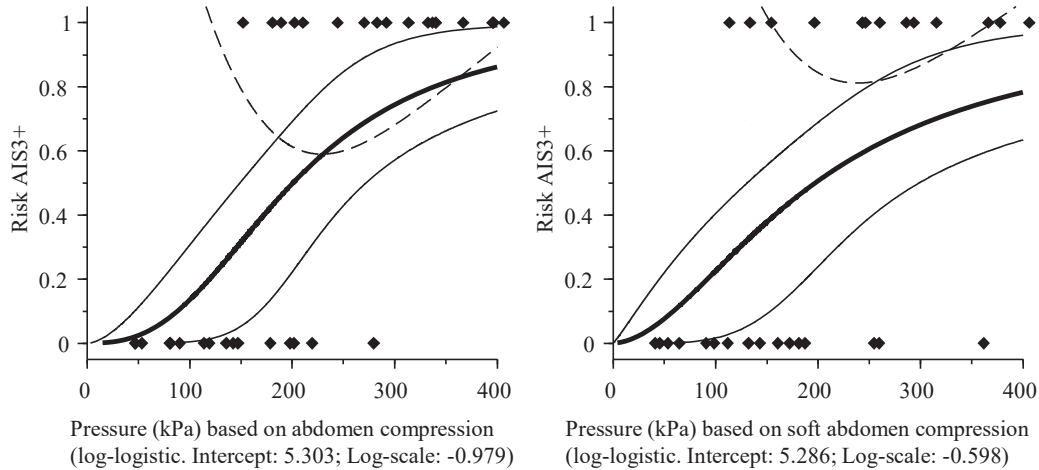


Figure 25. AIS3+ IRF versus APTS pressure (kPa) calculated from abdominal compression (left) or soft abdominal compression (right) (IRF in bold, 95% confidence interval in light, risk ratio in dashed line, injury status as diamonds).

Table 9. Pressure and associated AIS3+ risk calculated from abdominal compression (C_{max}) or soft abdominal compression ($Soft_C_{max}$) equivalence

	25%	50%	75%
Pressure (kPa) calculated from C_{max}	133	201	304
Pressure (kPa) calculated from $Soft_C_{max}$	108	197	361

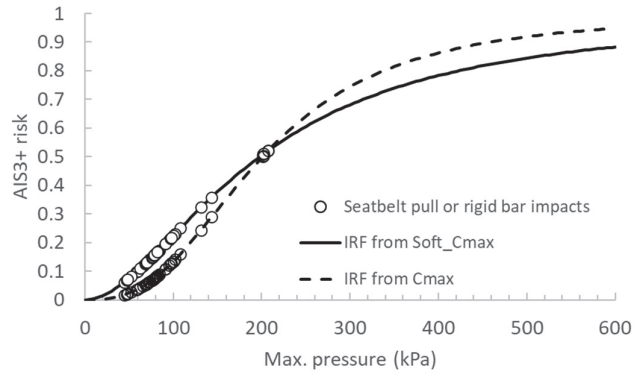


Figure 26. AIS3+ injury risk predicted in component tests.

ABISUP Abdomen Response in Sled Tests

The occurrence of submarining of the THOR equipped with the ABISUP abdomen was checked in the sled tests. The peak values of the APTS pressure, the ASIS forces/moments and lower thoracic IR-TRACC deflections are shown in Appendix 3. Figure 27 shows the maximum APTS pressure versus the submarining occurrence (visually identified from movies) and the risk of abdominal AIS3+ injuries versus the maximum APTS pressure.

Considering the IRF defined from the relationships between the pressure and the soft abdominal compression, in the case of submarining, a risk between 42 to 82% was estimated whereas a risk between 16 and 52% was estimated without submarining. The ABISUP abdomen and the IRF could discriminate restraint system conditions: a 28% risk was estimated for the reclined torso test in which the lap belt was positioned directly on the dummy abdomen and the dummy lower torso was restrained by a knee bolster; a risk between 77 and 79% was estimated for the reclined torso without a knee bolster. Similar risks would be obtained using the IRF defined from the relationships between the pressure and the abdominal compression. Post-test pictures and estimated risks are shown in Table 10.

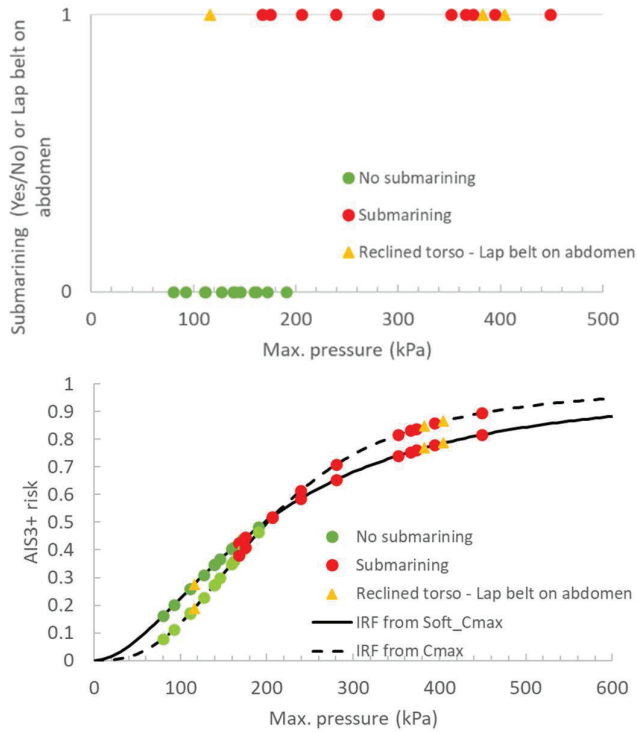

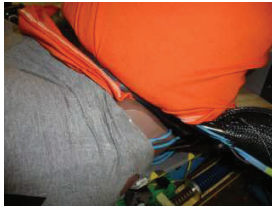




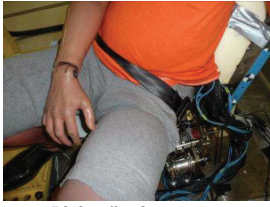


Figure 27. Submarining occurrence and risk of AIS3+ abdominal injury risk versus APTS pressure.

Table 10. Post-test pictures and estimated abdominal injury risk

 <p>50 km/h, slouched sitting posture, Submarining AIS3+ abdominal injury risk= 76 to 78%</p>	 <p>50 km/h, separated belt, rear seat, Submarining AIS3+ abdominal injury risk= 45 to 52%¹</p>	
 <p>40 km/h, reclined torso, knee bolster Lap belt on abdomen AIS3+ abdominal injury risk=28%</p>	 <p>40 km/h, reclined torso Lap belt on abdomen AIS3+ abdominal injury risk= 77 to 79%¹</p>	
 <p>40 km/h, standard position No submarining AIS3+ abdominal injury risk=16 to 44%¹</p>	 <p>50 km/h, standard position No submarining AIS3+ abdominal injury risk=35 to 37%</p>	 <p>50 km/h, front seat, standard position No submarining AIS3+ abdominal injury risk=26%¹</p>

¹ These tests were repeated with the standard THOR equipped with IR-TRACC.

As listed in Table 3, the standard THOR was also used in a few tests. The right IR-TRACC was damaged in the TMC sled test with the 49° torso angle sitting posture. This may be consistent with observations in [23] who noted that it was unknown if the IR-TRACCs “could tolerate submarining events at high speed”. Results and injury risk predicted using NHTSA IRF [8] are shown in Figure 28. Very low risks (below approximately 15%) were predicted whatever the sled conditions and the occurrence or not of submarining. Maximum deflection values were between 46 and 70 mm. These values are much lower than 98 mm which corresponds to a 50% risk and to the 88 mm Euro NCAP limit.

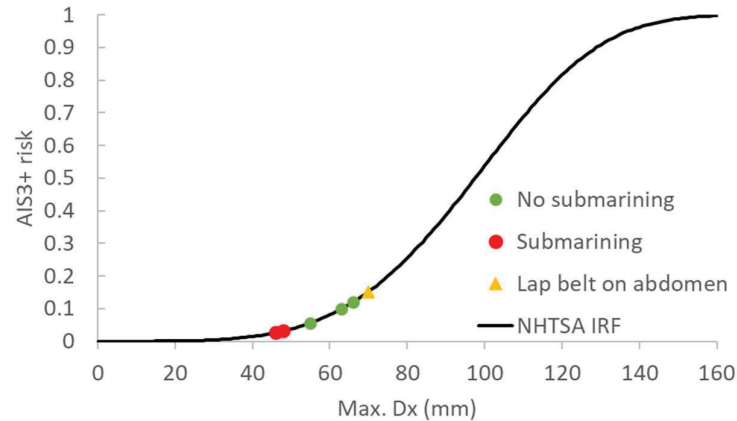


Figure 28. Risk of AIS3+ abdominal injury versus abdominal deflection (x-axis) for the standard THOR-50M: risk function and results from the sled tests.

DISCUSSION AND LIMITATIONS

The ABISUP abdomen geometry was designed to enlarge the existing THOR lower abdomen volume and prevent discontinuities between the lower abdomen and the pelvis or the lower thorax. This would help to prevent belt entrapment between the two body regions. The abdomen internal plate present in the standard dummy was also removed as it did not represent any anatomical structures and limited the compression.

The abdomen biofidelity was assessed under various seatbelt pull test conditions. In three different seatbelt pull conditions, the ABISUP abdomen demonstrated varying degrees of biofidelity in terms of both deflection and force. The peak deflection of the ABISUP abdomen tended to be lower than PMHS with the exception of the dual pretensioner case, but the peak force response consistency with PMHS corridors varied by test condition.

The abdomen durability including the APTS was very good and further improved by the reinforcement of the abdomen skin. The repeatability and the reproducibility of the abdomen was good, however some significant variations between the left and right APTS pressures were observed and could not be explained. Further investigation to understand if this may be caused by the foam, the APTS or the loading would be required. Based on the asymmetry observed in the final certification tests, investigating the foam and the loading setup could be of particular interest.

The sensitivity of the abdomen and its measurement were good as it could discriminate restraint systems with the highest APTS pressures measured when the lap belt was directly on the abdomen compared to when the lap belt was partly or in contact with the pelvis or the lower thoracic ribs.

The IRF could only be defined from the porcine tests of Kent as attempts to create IRF from PMHS tests gave only poor quality IRFs due to inconsistent results between the studies in terms of observed injuries versus abdominal compression. The defined IRFs did not account for the ABISUP abdomen biofidelity since it predicts abdominal injury risk versus the APTS pressure calculated from the compression measured on the porcine specimen and not the compression of the ABISUP abdomen itself. In other words, it was assumed that the same abdominal compression would have been obtained with the ABISUP abdomen than for the porcine specimen under the same loading.

The risks predicted in the case of submarining and non-submarining were overlapping. Some degree of overlap could be possible as the presence of the belt on the abdomen did not necessarily mean that the loading was high. In particular, submarining could occur late in the deceleration with limited belt forces. In many other cases, the predicted risk was high and it could reach up to close to 90% for submarining or lap belt on abdomen conditions. Conversely, it was found that the risk without submarining could be too high (up to 48%, Figure 27) compared to the low occurrence of abdominal injuries for properly restrained occupants. However, one limitation of this study is that the predicted risks were not assessed against injury statistics accounting for actual restraint conditions.

While the exact reason for the mismatch between expected and predicted risk in case of proper restraint is unknown, different reasons could be investigated. The IRFs were defined from seatbelt pull tests in which the injuries were created by the compression of the mid abdomen by the belt with side rollers guiding the belt. In sled tests, the force interaction on the abdomen was more complex as (1) there was no side rollers preventing the lateral compression, (2) there were inertial effects and force of the upper torso on the abdomen, (3) the loading was not necessarily applied to the mid abdomen.

For the first point, the pressure compression curve and the original experimental data from Kent were generated using antero-posterior compression while some of the lateral compression, which could contribute to the pressure, was prevented by the use of rollers. As a result, the ratio between compression and pressure or the relationship between compression and injury could differ from more realistic loading cases. This could be investigated using a simulation-based approach.

For the second point, it was also previously reported that the APTS maximum pressure was coincident with the maximum chest excursion in sled tests [26], however the pressure increase due to the dummy torso flexion was not considered in the IRFs. From [26], it was estimated that the pressure increase due to the torso forward movement was between 28 and 92 kPa depending on the magnitude of torso flexion. Due to the lack of biomechanical data, it is unknown if torso flexion should contribute to the injury risk as some coupling between the thorax and the abdomen is present through the diaphragm. If needed, the APTS location could be adjusted (e.g. moved rearward) to reduce the pressure sensitivity.

For the third point, the sensitivity of the APTS to loading location was found to remain relatively stable on the abdomen including in some cases for which the path of the belt involved some of the pelvis or was below the ASIS. Some of these cases may be considered as acceptable restraints but significant abdomen compression still occurred in the dummy. It must be remembered that in the current THOR-50M design, a large portion of the soft abdomen was located anteriorly to the ASIS (approximately 86 mm at the level of ASIS measured in the mid sagittal plane on the FE model, Figure 29 bottom). As a result, to prevent the APTS from being too close to the spine, they were positioned partially anterior to the ASIS in the current design. Also, approximately a third of the APTS is caudal of the ASIS. To reflect the fact that loading was not expected to be injurious below the ASIS, a reduced pressure sensitivity in that region may be achieved using a different design (e.g. shorter APTS, APTS reinforced at the bottom or with a longer cap) or a different location (e.g. more lateral, cranial and posterior, perhaps with a smaller diameter and length). Preliminary investigations were conducted by simulation.

Some of the abdomen geometric characteristics (largely in front of the ASIS) may also be relevant for some of the responses observed with the IR-TRACC in the standard dummy: the ASIS are only approximately 30 mm in front of the flared overload cones protecting the IR-TRACCs, and the distance between the flared overload cones and the IR-TRACC attachments on the surface of the abdomen is only approximately 105 mm (Figure 29 bottom, measurements made on the FE model). This suggests that (1) in some cases, the first 75 mm of deflection may result from a loading that is in front of the ASIS, and (2) the maximum deflection may be limited to a value around 105 mm (contact with the flared overload cones). Based on the NHTSA IRF [8], a 50% AIS3+ risk would correspond to 98 mm, while 75 mm and 105 mm would correspond to 20% and 61% risks, respectively. In preliminary FE simulations, deflections over 95 mm (46% risk) could not be achieved in part due to the interaction between the belt and the backing plate (illustrated in Figure 30). Higher deflections (up to 98.5mm, or 51% risk) were observed in 32 kg / 6.1 m/s impactor tests [27]. Similar values (99.3 mm, or 53% risk) were reached in this study in Foster dual pretensioner tests. This would suggest that risks of at least up to 53% could be obtained in tests, but that risks below 20 % could result from loading anterior to the ASIS. However, despite this range, risks below 15% were obtained independently of the restraint conditions in the sleds with IR-TRACC performed as part of ABISUP (Figure 28), and the submarining condition was associated with the lowest risk, followed by the non-submarining and belt on abdomen. It is unclear if the high lap belt angles that could occur during the submarining could be recorded by the IR-TRACC.

Overall, despite the limitations listed about the ABISUP abdomen and its associated IRFs, the ABISUP abdomen could better discriminate the restraint systems and predict more realistic abdominal injury risks than the standard THOR.

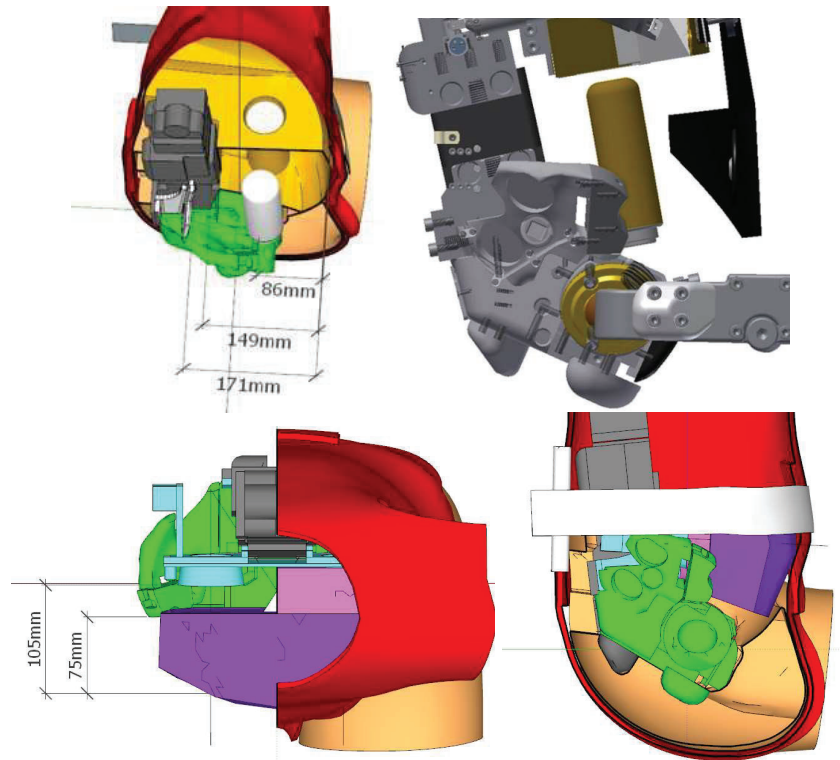


Figure 29. ABISUP abdomen APTS location versus THOR-50M compressible abdominal depth (top) and THOR-50M ASIS (bottom).



Figure 30. Illustration of the possible interaction between the belt (green) and the abdomen internal plate (blue) in a simulation of the standard abdomen with the FE model. The IR-TRACCs are materialized by the line at the center of the backing plate flared overload cones and the abdomen and jacket are not shown. For a belt pull, the belt motion and IR-TRACC compression can be limited by the internal plate (laterally) and the flared overload cones (anteriorly).

CONCLUSIONS

A new abdomen prototype was developed by the ABISUP consortium that could be integrated into the THOR-50M without modification of other dummy parts. The ABISUP abdomen integrated APTS instead of the two IR-TRACCs which could be easily damaged in sled tests and require more complex post-processing. Moreover, the APTS had the advantage of being sensitive to different loading directions. The ABISUP abdomen could discriminate well the different restraint systems used in sled tests and predicted AIS3+ injury risk between 42 to 82% in the case of submarining. In the future, design adjustments might be relevant to decrease the APTS sensitivity to belt loading at the ASIS level.

REFERENCES

- [1] Elhagediab and Rouhana (1998) Patterns of abdominal injury in frontal automotive crashes, 16th International Technical Conference on the Enhanced Safety of Vehicles (ESV), Windsor, Canada.
- [2] Observatoire National Interministériel de la Sécurité Routière (2021) La sécurité routière en France – Bilan de l'accidentalité de l'année 2021, September 2022, p. 15.
- [3] Lamielle S., Cuny S., Foret-Bruno JY. et al. (2006) Abdominal injury patterns in real frontal crashes: influence of crash conditions, occupant seat and restraint systems, 50th Association for the Advancement of Automotive Medicine: 103-118, October 16-18, 2006.
- [4] Martin JL., Lardy A., Compigne S. (2010) Specificities of rear occupant protection: Analysis of French accident data. Proceedings of the 2010 IRCOBI Conference, September 15-16, 2010, Hanover, Germany.
- [5] Kuppa S., Saunders J., Fessahaie O. (2005) Rear seat occupant protection in frontal crashes, 19th International Technical Conference on the Enhanced Safety of Vehicles (ESV), June 6-9, 2005, Washington D.C., US.
- [6] McFadden J., Moorhouse K., Hagedorn A. (2015) THOR-M 50th Male ATD repeatability and reproducibility in qualification tests, THOR Public Meeting, January 20, 2015, Washington, D.C.
- [7] Kent R., Stacey S., Kindig M. et al. (2008) Biomechanical response of the pediatric abdomen, Part 2: Injuries and their correlation with engineering parameters, Stapp Car Crash Journal 52: 135-166, November 2008, doi: 10.4271/2008-22-0006.
- [8] Craig M., Parent D., Lee H. et al. (2020) Injury criteria for the THOR 50th male ATD, NHTSA September 2020 Report. Available at <https://www.regulations.gov/docket/NHTSA-2019-0106>.
- [9] Compigne S., Mitsutoshi M. (2017) Evaluation of THOR prototype lower abdomen in sled tests – Capability of the prototype lower abdomen to discriminate loading conditions, International Journal Of Automotive Engineering, Vol. 8, No. 2: pp. 95-104.
- [10] Euro NCAP (2022) Assessment Protocol – Adult Occupant Protection. Implementation 2023. Version 9.2.1. 14th November 2022. <https://cdn.euroncap.com/media/75471/euro-ncap-assessment-protocol-aop-v921.pdf>
- [11] Beillas P., Alonzo F., Chevalier M-C. et al. (2012) Abdominal Twin Pressure Sensors for the assessment of abdominal injuries in Q dummies: in-dummy evaluation and performance in accident reconstructions, Stapp Car Crash Journal 56: 387-410, October 2012, doi: 10.4271/2012-22-0010.
- [12] Suntay B., Stammen J., Carlson M. (2021) Abdominal and thoracic injury risk functions for the Large-Omni-Directional Child (LODC) ATD, Proceedings of the 2021 IRCOBI Conference, On-line, September 8-10, 2021.
- [13] Wang Z., Lee E., McInnis J. et al. (2017) THOR 5F percentile female ATD design. 25th International Technical Conference on the Enhanced Safety of Vehicles (ESV), June 5-8, 2017, Detroit Michigan USA.
- [14] Trosseille X., Petit P., Bermond F. et al. (2022) THOR-50M and THOR-5F submarining probability, 27th International Technical Conference on the Enhanced Safety of Vehicles (ESV), April 3-6, 2022, Yokohama, Japan.
- [15] Compigne S. (2016) Abdomen design specifications, ABISUP Deliverable D1.1, May 2016.
- [16] Burleigh M. (2018) THOR-50M ABISUP specification and design history, July 2018.
- [17] Lamielle S., Vezin P., Verriest JP. et al. (2008) 3D deformation and dynamics of the human cadaver abdomen under seatbelt loading, Stapp Car Crash Journal 52: 267-294.
- [18] Ramachandra R., Kang Y-S, Bolte IV J.H. et al. (2016) Biomechanical responses of PMHS subjected to abdominal seatbelt loading, Stapp Car Crash Journal 60: 59-87.
- [19] Foster C.D., Hardy W.N., Yang K.H. et al. (2006) High-speed seatbelt pretensioner loading of the abdomen. Stapp Car Crash Journal 50: 27-51.
- [20] National Highway Traffic Safety Administration. (2018) THOR 50th percentile male (THOR-50M) qualification procedures manual, Docket NHTSA-2019-0106-0001, September 2018.
- [21] Uriot J., Potier P., Baudrit P. et al. (2015) Reference PMHS sled tests to assess submarining, Stapp Car Crash Journal 59: 203-223, November 2015.
- [22] Uriot J., Potier P., Baudrit P. et al. (2015) Comparison of HII, HIII and THOR dummy responses with respect to PMHS tests, Proceedings of the 2015 IRCOBI Conference, Lyon, France, September 9-11, 2015.
- [23] Hardy W.N., Kemper A.R., Untaroiu C. D. et al. (2022) Rear-Seat Frontal Crash Protection Research With Application to Vehicles With Automated Driving Systems, Volume 1, DOT HS 813 269, <https://rosap.ntl.bts.gov/view/dot/63425>, September 2022.
- [24] Lebarbé M, Donnelly B R, Petit P et al. (2015) A Frontal Response Specification for Assessing the Biofidelity of an Anthropometric Test Dummy: Part 1 - Lower Body, Proceedings of the IRCOBI Conference, 2015, Lyon, France.
- [25] ISO/TS 18506:2014 (en) Procedure to construct injury risk curves for the evaluation of road user protection in crash tests.

- [26] Compigne S., Masuda M. (2017) Evaluation of THOR Prototype Lower Abdomen in Sled Tests, International Journal of Automotive Engineering, Vol. 8, No. 2, pp.95-104.
- [27] Abdomen Impact Testing of the THOR-50M Anthropomorphic Test Device. DOT/FRA/ORD-21/08 Final Report | February 2021 Available at <https://railroads.dot.gov/sites/fra.dot.gov/files/2021-02/Abdomen%20Impact%20Testing-A.pdf>

Appendix 1: ABISUP abdomen maximum values in Kent's setup (with rollers)

Test ID	Speed (m/s)	Deflection (mm)	Compression (%)	Soft Compression (%)	Mean Pressure (kPa)
ABISUP_KT_001	3.9	42.3	15.9	26.9	30.1
ABISUP_KT_002	4.1	42.3	15.9	26.9	31.3
ABISUP_KT_003	4.7	67.9	25.5	43.3	61.3
ABISUP_KT_004	4.9	77.3	29.0	49.2	80.1
ABISUP_KT_005	5.2	80.1	30.1	51.0	80.8
ABISUP_KT_006	5.2	80.8	30.4	51.5	80.6
ABISUP_KT_007	2.2	70.0	26.3	44.6	51.4
ABISUP_KT_008	2.9	76.1	28.6	48.5	66.9
ABISUP_KT_009	2.6	92.2	34.7	58.7	114.4
ABISUP_KT_010	2.5	93.6	35.2	59.6	114.1
ABISUP_KT_011	2.6	85.7	32.2	54.6	90.7
ABISUP_KT_012	2.5	80.5	30.3	51.3	74.1
ABISUP_KT_013	2.6	80.4	30.2	51.2	73.5
ABISUP_KT_014	7.5	87.6	32.9	55.8	108.2
ABISUP_KT_015	7.4	81.8	30.8	52.1	94.1
ABISUP_KT_016	6.6	78.9	29.7	50.3	82.2
ABISUP_KT_017	5.1	90.4	34.0	57.6	115.4
ABISUP_KT_018	5.0	91.7	34.5	58.4	116.1
ABISUP_KT_019	6.7	96.2	36.2	61.3	138.7
ABISUP_KT_020	6.5	98.4	37.0	62.6	150.4
ABISUP_KT_021	6.4	101.0	38.0	64.3	162.4
ABISUP_KT_022	6.7	101.4	38.1	64.6	162.6
ABISUP_KT_023	6.8	101.6	38.2	64.7	163.0
ABISUP_KT_024	5.0	94.5	35.5	60.2	117.2
ABISUP_KT_025	5.0	100.4	37.7	63.9	143.7
ABISUP_KT_026	5.0	99.2	37.3	63.2	143.5
ABISUP_KT_027	5.1	101.1	38.0	64.4	154.4
ABISUP_KT_028	5.2	101.3	38.1	64.5	151.7
ABISUP_KT_029	5.0	101.1	38.0	64.4	151.9
ABISUP_KT_030	5.1	101.0	38.0	64.3	150.5
ABISUP_KT_031	5.0	102.6	38.6	65.3	156.2
ABISUP_KT_032	5.0	102.3	38.5	65.2	157.4
ABISUP_KT_033	2.6	104.2	39.2	66.4	173.5
ABISUP_KT_034	2.5	103.4	38.9	65.9	164.0
ABISUP_KT_035	1.4	105.3	39.6	67.1	165.1
ABISUP_KT_036	7.9	91.4	34.4	58.2	115.4
ABISUP_KT_037	8.0	96.6	36.3	61.5	141.1
ABISUP_KT_038	7.9	102.1	38.4	65.0	176.4
ABISUP_KT_039	5.1	106.5	40.0	67.8	203.5
ABISUP_KT_040	5.0	109.1	41.0	69.5	224.7
ABISUP_KT_041	5.0	112.4	42.2	71.6	240.1
ABISUP_KT_042	5.1	115.8	43.5	73.8	253.1
ABISUP_KT_043	5.0	118.6	44.6	75.5	257.4

Appendix 2: Kent's data summary and transformation

Specimen	Location	AIS soft tissues	Defl (mm)	Abdo depth (mm) ¹	Compr (%)	Estimated soft depth (mm) ²	Soft Compr (%) ³
PAC1.1	lower	2	67	149	45.0	82	82.0
PAC1.2	lower	4	72	135	53.3	74	97.2
PAC1.3	lower	3	58	122	47.5	67	86.7
PAC1.4	lower	3	68	140	48.6	77	88.5
PAC1.5	upper	4	74	148	50.0	96	77.2
PAC1.6	upper	4	96	149	64.4	96	99.5
PAC1.7	lower	3	53	132	40.2	72	73.2
PAC1.8	upper	4	56	149	37.6	96	58.1
PAC1.9	lower	0	48	129	37.2	71	67.8
PAC1.10	lower	2	89	146	61.0	80	111.1
PAC1.11	lower	0	47	137	34.3	75	62.5
PAC1.12	lower	2	41	113	36.3	62	66.1
PAC1.13	upper	2	47	135	34.8	87	53.8
PAC1.15	lower	2	54	132	40.9	72	74.6
PAC1.16	lower	3	59	127	46.5	70	84.7
PAC1.17	lower	0	41	174	23.6	95	43.0
PAC1.18	upper	0	37	146	25.3	95	39.1
PAC1.20	lower	3	61	134	45.5	74	83.0
PAC1.21	lower	3	61	141	43.3	77	78.9
PAC1.22	lower	3	52	127	40.9	70	74.6
PAC1.23	lower	2	59	145	40.7	80	74.2
PAC1.24	upper	2	75	190	39.5	123	61.0
PAC1.25	lower	4	64	129	49.6	71	90.4
PAC1.26	upper	3	61	137	44.5	89	68.8
PAC1.27	lower	1	41	135	30.4	74	55.4
PAC1.28	upper	2	65	155	41.9	100	64.8
PAC1.29	lower	3	73	140	52.1	77	95.0
PAC1.30	upper	0	37	158	23.4	102	36.2
PAC1.31	upper	3	58	140	41.4	91	64.0
PAC1.32	lower	0	56	152	36.8	83	67.2
PAC1.33	upper	3	61	154	39.6	100	61.2
PAC1.34	upper	3	68	143	47.6	93	73.4
PAC1.35	lower	3	60	133	45.1	73	82.2
PAC1.36	upper	0	46	151	30.5	98	47.1
PAC1.37	lower	0	45	142	31.7	78	57.8
PAC1.38	upper	3	64	135	47.4	87	73.2
PAC1.39	upper	3	71	143	49.7	93	76.7
PAC1.40	lower	3	56	108	51.9	59	94.5
PAC1.41	lower	3	60	127	47.2	70	86.1
PAC1.42	lower	3	65	131	49.6	72	90.4
PAC1.43	lower	2	79	154	51.3	84	93.5
PAC1.44	lower	3	92	152	60.5	83	110.3
PAC1.45	upper	4	103	151	68.2	98	105.4
PAC1.46	upper	3	89	138	64.5	89	99.6
PAC1.47	lower	3	70	124	56.5	68	102.9

¹ Calculated by dividing the deflection by the abdominal depth.

² Estimation of the soft abdomen depth in front of the spine. The ratio (soft depth)/(abdomen depth) was assumed to be the same as in supine CT-scans of two porcine specimens of similar size as in Kent's study. The scans were collected for an unrelated study and used retrospectively at Univ. Eiffel. The mean ratio was 79/144 and 101/156 at the lower and upper locations, respectively.

³ Calculated by dividing the deflection by the estimated soft depth.

Appendix 3: Sled test results

Reference	Test conditions	Submarining No/Yes @time (ms)	Left APTS (kPa)	Right APTS (kPa)	Left ASIS Fx (kN)	Right ASIS Fx (kN)	Left ASIS My Min/Max (Nm)	Right ASIS My Min/Max (Nm)	Left lower thoracic IR- TRACC (mm)	Right lower thoracic IR- TRACC (mm)
Forvia sled tests (Uriot et al. [21])	50 km/h pulse, Vehicle seat Standard sitting posture 3-point belt	No	129.4	146.1	6.1	4.8	-73.2/1.7	-64.3/0.4	8.6	39.3
		Yes @57 ms	111.3	138.9	4.6	4.7	-54.3/2.3	-70.3/0.1	13	43.5
Forvia sled tests (Uriot et al. [22])	50 km/h pulse, Vehicle seat Slouched sitting posture 3-point belt	Yes @56 ms	339.7	373.2	6.4	5.4	-1.4/36.7	-5.2/24	20.4	35.4
		No	103.7	111.3	3	2.7	-33.7/0.1	-32/0.4	16.5	52.1
Virginia Tech, NHTSA sled tests	50 km/h pulse, Semi-rigid seat Front seat configuration Separated shoulder and lap belt 50 km/h pulse, Semi-rigid seat Rear seat configuration Separated shoulder and lap belt	No	98.1	111.0	3.2	2.8	-33.1/0.4	-29.6/0.5	18.4	50.5
		Yes @72 ms	126.0	175.2	4.2	3.4	-12.2/15.6	-10.3/21.6	21.8	48.8
		Yes @75 ms	105.6	206.0	4	3.6	-17.8/15	-4/16.4	22.6	43.1
		No	117.7	190.6	2.3	2.2	-1.9/16.7	-2.4/12.9	18.2	33.7
		Yes @74 ms	239.0	189.4	2.8	3.5	-0.9/24.6	-0.8/38.8	28.7	33.9
		No	80.4	92.5	2.8	2.6	-1.8/10	-3.4/28.8	18.8	28.4
TMC sled tests	56 km/h pulse Rear seat, 3-point belt	Yes @74.9 ms	89.8	280.3	3.3	2.5	-9.3/12.6	-1.1/27.4	29.0	37.6
		Yes @76.4 ms	99.8	167.2	3.1	3.3	-1.0/16.7	-2.2/28.6	30.3	29.5
		No	113.8	161.5	2.5	2.7	-1.8/12.4	-3.7/19.7	18.3	32.9
		Yes @61.1 ms	351.9	294.1	4.3	3.95	-1.3/43.1	-2.1/46.5	27.6	37.5
		No	127.1	126.0	3.9	4.2	-3.9/27.9	-1.1/27.7	19.3	54.5
		Yes @65.8 ms	366.1	326.1	4.5	2.2	-1.3/52.7	-1.7/26.0	38.3	46.3
TMC sled tests	40 km/h FWRB pulse 3-point belt Standard sitting posture	Yes @73.8 ms	427.6	448.7	4.6	3.5	-0.9/56.5	-1.6/30.6	31.7	38.6
		No	149.2	159.2	4.7	3.8	-3.2/10.9	-10.1/4.03	14.2	24.6
		No	149.3	171.9	4.6	3.7	-6.2/10.4	-13.9/2.9	15.1	27.6
		No	129.8	139.8	4.0	3.4	-3.3/31.9	-3.5/17.4	14.8	23.3
		No	79.9	76.2	0.3	0.49	-2.6/1.5	-4.3/2.1	10.3	22.7
		Lap belt on abdomen	382.6	339.2	1.1	0.46	-19.4/0.78	-5.6/0.82	15.8	29.5
TMC sled tests	40 km/h FWRB pulse 3-point belt 49° torso angle sitting posture	No	404.5	357.9	1.5	0.76	-21.3/1.6	-8.5/1.1	14.4	33.1
		No	116.3	81.8	0.5	1.0	-3.6/4.1	-6.82/0.3	17.2	17.1

Construction of a Prediction Model for the Time Series of Brain Strain of a Novel Head Surrogate Using Deep Learning

Shuntaro Tamai

Yusuke Miyazaki

Hiroki Yamamoto

Tokyo Institute of Technology

Japan

Katsushi Yoshii

Ichiro Amamori

Joyson Safety Systems Japan

Japan

Paper Number 23-0239

ABSTRACT

An effective brain injury risk assessment is required to minimize the risk of brain injury from traffic accidents. Thus, anthropomorphic test devices (ATD) have been used for overall vehicle safety evaluation. We developed a novel ATD head that incorporates detailed intracranial structures with the brain and can measure the relative displacement between the brain and the skull. However, the strain inside the deep brain of the head surrogate cannot be measured or estimated. Although we can simulate the brain strain waveform using the finite element model, the computational cost is high, and the real-time evaluation of brain strain during crash tests is difficult. To compute the brain strain response in real-time, deep learning (DL) methods can be used to predict brain strain behavior. Therefore, this study aims to propose a method to predict the waveforms of maximum principal strain in the brain using a DL method called long short-term memory (LSTM). Reconstructed simulations for impact tests using a finite element head model were conducted to obtain the principal strain waveforms of the brain and construct a dataset for machine learning. The impact tests included 125 occipital head impact tests, 7 frontal sled tests, 35 vehicle frontal crash tests, and 53 American football impact tests, constituting a total of 220 head impact tests. Furthermore, the LSTM model was trained on triaxial angular velocity and acceleration waveforms, and the models were constructed to predict the principal strain waveforms in the cerebellum, brainstem, and right and left cerebrums. Subsequently, to validate the predictive model of brain strain, CORA was calculated as an index of the prediction error. The average CORA score between the brain strain waveforms predicted by LSTM and those of the dataset was 0.963 for occipital head impact tests, 0.928 for frontal sled tests, 0.898 for vehicle frontal crash tests, and 0.875 for American football tests. The occipital head impact tests, vehicle frontal crash tests, and frontal sled test cases were predicted with high accuracy. However, the football impact test cases were inferior to the other three test cases. The football impact cases included more multidirectional impact patterns and failed to learn similar collisions. However, an error in the waveform was observed in the rebound phase of the head impact in the latter half of the brain strain waveform. Therefore, the impact test dataset should be expanded, including cases with rebound behavior of the head, and the set of features that can reflect the rebound behavior of the head should also be examined further. In conclusion, the maximum principal strain waveforms of the brain can be rapidly and accurately predicted from the angular acceleration and angular velocity of the ATD head in occipital head impact, frontal sled, and vehicle crash test cases using LSTM. This method enables real-time evaluation of brain strain waveforms during impact tests.

INTRODUCTION

The number of fatalities from traffic accidents in Japan has been decreasing, but it remains high, accounting for over 40% of all injuries [1]. A more effective assessment of the brain injury risk is required to minimize the risk of brain injury due to accidents. Although we cannot directly measure the principal strain in the brain, which is a factor in the occurrence of brain

damage, we can simulate the deformation behavior of the human brain using finite element analysis (FEA). Therefore, integrating the calculation of brain deformation behavior using a human finite-element model with crash dummies can provide an injury evaluation function based on brain strain indices in crash tests. However, the FEA has computational costs, and real-time evaluation during crash tests is difficult. Therefore, developing a method that can minimize the computational cost while maintaining computational accuracy is necessary to obtain brain deformation behavior in real time. Wu et al. [2] applied a convolutional neural network (CNN) to estimate the 95% maximum principal strain (95%MPS) in the brain from entire-brain images. However, the output data are static and not time-series data. This study aims to propose a fast and simple method for predicting the time-series waveform of the principal strain in the brain using long short-term memory (LSTM) and bidirectional LSTM with triaxial angular velocity and acceleration waveforms as an alternative to FEA. First, the 95%MPS in the brain induced by a head impact was calculated using FEA, and then, a model was constructed to predict the 95%MPS in the brain using LSTM by learning with triaxial angular velocity and angular acceleration waveforms. For training, we used head impact data obtained from occipital head impact tests [3], frontal sled tests [4], vehicle crash tests [5], and reconstruction tests of American football accidents [6][7]. The results show that LSTM and bidirectional LSTM quickly predict time-series waveforms.

METHODS

A flowchart of the study is shown in Figure 1. First, using the angular velocities of the three axes of the head obtained from various head impact tests as inputs, we conducted simulations using a finite element model of the head to obtain 95%MPS waveforms and constructed a dataset for deep learning. The deep learning model was then trained on the training dataset after appropriate pre-processing, and its performance was evaluated.

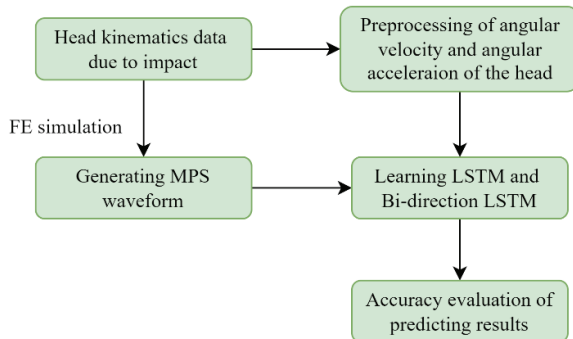


Figure 1. Flowchart

Data Description

The dataset used for training consisted of head impact data obtained from four tests: occipital head impact tests, frontal sled tests, vehicle crash tests, and reconstruction tests of American football collisions. An overview of these tests is provided below:

Occipital Head Impact Tests

The dataset of reconstruction tests of Depretiere's cadaver test was used [3]. Hybrid III AM50 with a novel anthropomorphic dummy head was used. An impactor (15.6 kg) was placed on the back of the dummy's head. The results of 125 occipital head impact tests obtained by varying the mass and velocity of the impactor were used.

Frontal Sled Tests

The dataset from frontal sled tests was used; a total of seven tests were used, varying the TTF of the delta-V and restraint system, using a full-body dummy with the head of the Hybrid III AM50 dummy replaced by a novel anthropomorphic dummy head [4]. Seven simulations were conducted.

Vehicle Crash Tests

Head motion data obtained from vehicle crash tests in the United States New Car Assessment Program were used. The three crash modes used in the simulations were the full-lap rigid barrier (FRB), left oblique impact (LOI), and right oblique impact (ROI). The simulations were performed on 35 cases: 6 FRB cases, 19 LOI cases, and 10 ROI cases.

Reconstruction tests head collision in American football

Head motion data were obtained from the head impact reconstruction test in American football conducted by Sanchez et al. [7]. In this experiment, the head impact position, angle, and velocity were estimated from the head impact video of American football games, and a Hybrid III dummy head wearing a helmet was used to reproduce the head impact situation. In total, 53 simulations were performed.

Finite Element Analysis

The head finite element model used in the simulation was constructed based on medical images of an adult male, as shown in Figure 2 [4]. The head finite-element model consists of the skin, skull, brain, meninges, venous sinus, cerebrospinal fluid, and ventricles. The skull has a cortical membrane and a trabecular body. The brain is modeled as a viscoelastic body using Maxwell–Kelvin viscoelastic material and consists of the right brain, left brain, cerebellum, and brain stem. The meninges were modeled as elastic bodies with the dura mater, soft membrane, cerebellar tent, and cerebral sickle. Cerebrospinal fluid, ventricles, and venous sinuses were modeled as fluids. The skull and skin of the model were made rigid, and simulations were conducted using the 6-axis motion data of the head in the various head impacts described above as inputs. The simulation output was the time-history waveforms of the 95th percentile maximum principal strain in the left and right cerebrum, brainstem, and cerebellum. LS-DYNA R11.1 was used as the solver.

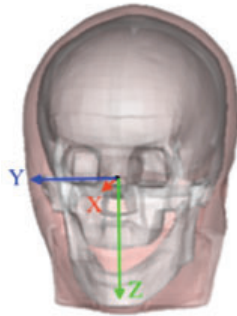


Figure 2. Entire structure of the FE head model and the head coordinate system

Feature Engineering and Data Preprocessing

A total of 31 features of the following four types obtained from the triaxial angular velocity waveforms were used as model inputs (Figure 3).

- (1) Triaxial angular velocity (ω_x , ω_y , ω_z)
- (2) Angular acceleration in each of the three axes (α_x , α_y , α_z)
- (3) Absolute angular velocity ($|\omega|$)
- (4) Angular velocity change ($\Delta\omega_x$, $\Delta\omega_y$, $\Delta\omega_z$, $\Delta|\omega|$).

The angular velocity change is the magnitude of the change in angular velocity over T ms, calculated in Eq. 1 from the angular velocity and absolute value of angular velocity in the three axes. Six types of T were used (5, 10, 20, 30, 40, and 50), resulting in 24 features.

$$\begin{aligned} \Delta\omega(t) &= \omega(t) - \omega(T) & (T \leq t) \\ \Delta\omega(t) &= \omega(t) & (T > t) \end{aligned} \quad \text{Equation (1)}$$

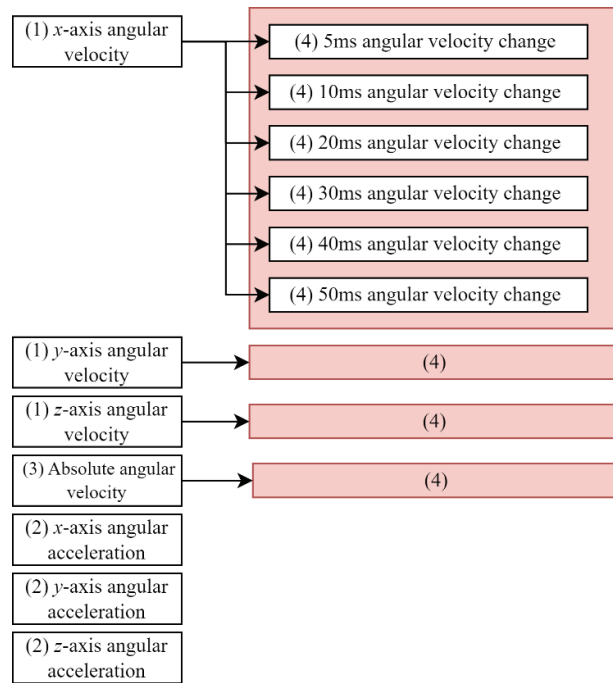


Figure 3. Overview of the input features

After feature engineering, the data were converted into a 31-column matrix for standardization and data augmentation. For data augmentation, the following two methods were applied to the training dataset.

- (1) Inverted motions were created for each of the x- and z-axes to quadruple the dataset.
- (2) The dataset was doubled by creating randomly scaled data at $0.9 \leq rate \leq 1.1$ for all features as input and all brain strain as output.

Finally, the total number of impact datasets is 1760 ($220 \times 4 \times 2$).

Deep Learning Model and Assessment

The head impact dataset was split into 80% training and 20% test data. The training data were inputted into a deep-learning model for training. The prediction error between the predicted and simulated principal brain strain waveforms was calculated for validation data. Accuracy was verified using the five-fold cross-validation method shown in Figure 4. In this study, LSTM and bidirectional LSTM were used as deep learning models.

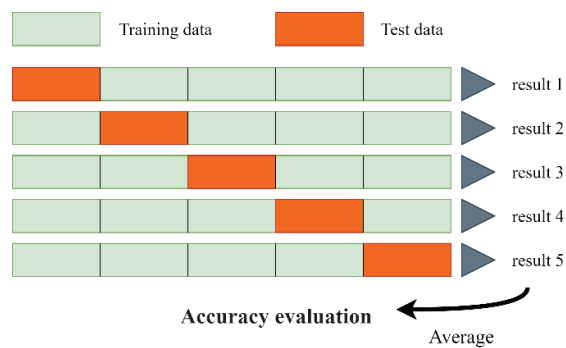


Figure 4. Fivefold cross-validation

LSTM Structure

LSTM is a network with a long-term dependency structure within the recurrent neural network (RNN). LSTM was proposed to address the long-term dependence [8][9]. In LSTM (Figure 5), the memory layer $C^{(t)}$, which plays the role of long-term memory, is added from the RNN. After selecting the input information at the forgetting gate (f), the information is stored in the memory layer, and the next time step inherits the information from the memory layer. The information stored in the memory layer was transformed by an activation function and used to compute the output. The addition of this addresses the gradient loss problem.

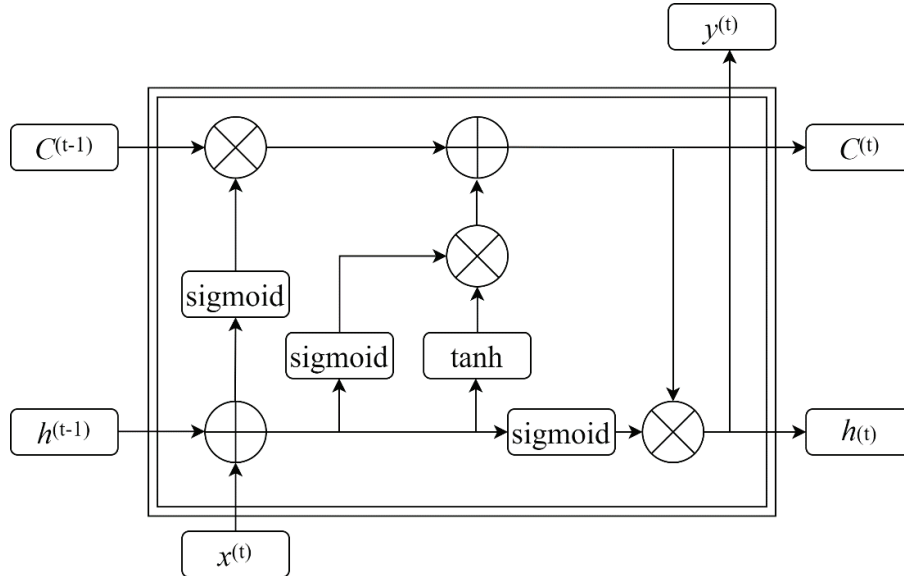


Figure 5. LSTM cell structure

The LSTM structure used in this study consists of five layers. (1) Input layer (31 units), (2) masking layer, (3) hidden layer (200 units, dropout: 0.2), (4) time-distributed layer with linear activation function, and (5) output layer (1 unit). Using the mean squared error as the loss function and adaptive moment estimation optimizer as the optimization function, the batch size was increased to 200-time steps to improve learning efficiency. The initial learning rate was set to 0.0004 and halved every two epochs for a total of six epochs.

Bi-directional LSTM Structure

Bi-directional LSTM [10] combines LSTM in the forward direction and LSTM in the reverse direction in a time series, as shown in Figure 6. The data used to construct the prediction model for the time-series waveform of brain strain can also be used to predict the data after the desired prediction. Therefore, we could make predictions in the reverse direction of a time series. Using both past and future information to predict a certain point in time is effective in improving accuracy.

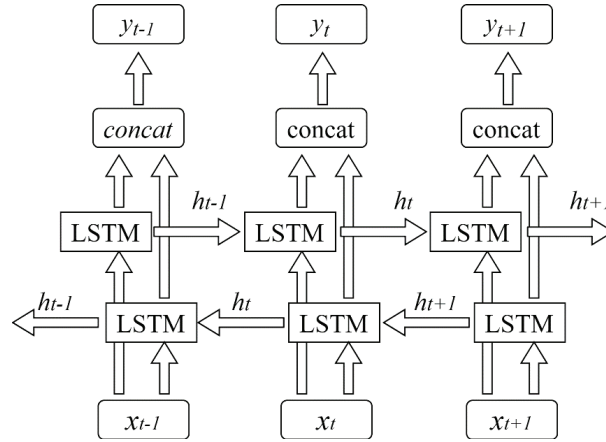


Figure 6. Bi-directional LSTM structure

The structure of bi-directional LSTM used in this study consisted of six layers: (1) the input layer (31 units), (2) the masking layer, (3) the hidden layer (200 units, dropout: 0.2), (4) the hidden layer (200 units, dropout: 0.2), (5) time-distributed layer with linear activation function, and (6) output layer (1 unit). Using the mean squared error as the loss function and adaptive moment estimation optimizer as the optimization function, the batch size was increased to 200-time steps to improve learning efficiency. The initial learning rate was set to 0.0004 and halved every two epochs for a total of six epochs.

Using these trained models, we make predictions on the test data and verify their accuracy. The actual and predicted time historical data were quantitatively compared using CORA [11].

RESULTS

Tables 1 and 2 show the CORA evaluation of the prediction results from LSTM and bidirectional LSTM. The horizontal axis of the table indicates the predicted brain region, and the vertical axis indicates the type of test. The prediction accuracy was excellent ($\text{CORA} > 0.94$) for the left and right cerebrum and good ($0.8 < \text{CORA} \leq 0.94$) for the cerebellum and brainstem. Comparing the accuracy of the LSTM and bidirectional LSTM, the latter was found to be more accurate.

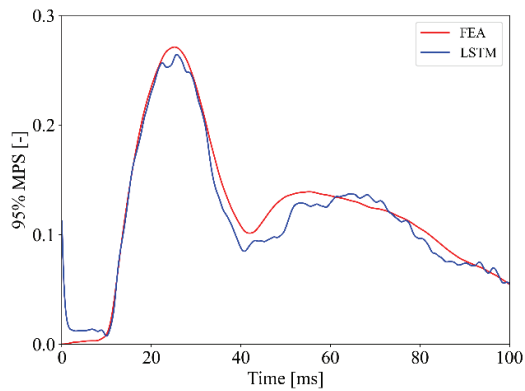
Figures 7–10 show examples of the results of the FEA and the LSTM predictions for the left cerebrum principal strain waveforms in each test configuration. For the example of the occipital impact test shown in Figure 7, the waveform predicted by LSTM accurately captured the first peak and accurately predicted the subsequent decay. For the frontal sled test example shown in Figure 8, three small peaks appeared, the first and second peaks were accurately predicted, and the third peak was highly predicted. The vehicle crash test example in Figure 9 shows large peaks at 100 m and 120 m and a small peak at 230 m. The first and second peaks were accurately predicted, while the third small peak was highly predicted.

Table 1
Averaged CORA value of prediction result by LSTM

	Cerebellum	Stem	Cerebrum R	Cerebrum L
Occipital head impact test ($n=125$)	0.952 ± 0.065	0.958 ± 0.053	0.973 ± 0.030	0.970 ± 0.033
Frontal sled test ($n=7$)	0.911 ± 0.091	0.920 ± 0.063	0.935 ± 0.025	0.946 ± 0.018
Vehicle crash test ($n=35$)	0.872 ± 0.072	0.876 ± 0.048	0.923 ± 0.046	0.921 ± 0.040
Football impact test ($n=53$)	0.831 ± 0.109	0.885 ± 0.066	0.894 ± 0.061	0.891 ± 0.075
Full data ($n=220$)	0.908 ± 0.096	0.926 ± 0.068	0.944 ± 0.054	0.942 ± 0.058

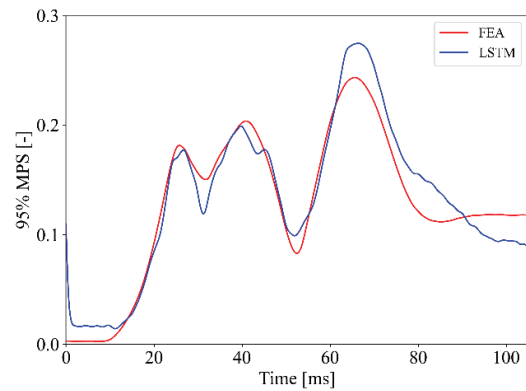
Table 2
Averaged CORA value of prediction result by bi-directional LSTM

	Cerebellum	Stem	Cerebrum R	Cerebrum L
Occipital head impact test ($n=125$)	0.956 ± 0.061	0.963 ± 0.058	0.974 ± 0.033	0.972 ± 0.038
Frontal sled test ($n=7$)	0.901 ± 0.124	0.912 ± 0.055	0.939 ± 0.030	0.956 ± 0.027
Vehicle crash test ($n=35$)	0.873 ± 0.080	0.880 ± 0.055	0.934 ± 0.043	0.936 ± 0.042
Football impact test ($n=53$)	0.826 ± 0.136	0.888 ± 0.071	0.892 ± 0.080	0.898 ± 0.068
Full data ($n=220$)	0.909 ± 0.106	0.930 ± 0.072	0.946 ± 0.060	0.948 ± 0.056



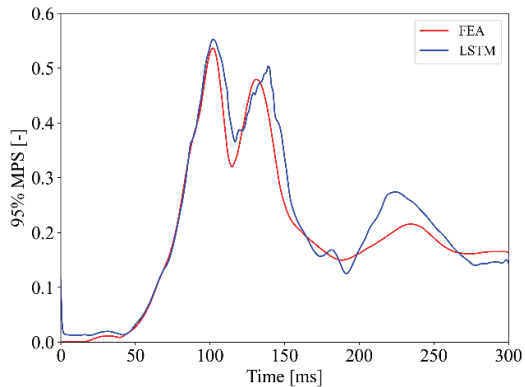
CORA: 0.971

Figure 7. Comparison of waveforms of maximum principal strain between true value (finite element analysis) and predicted value by LSTM in an occipital head impact test case



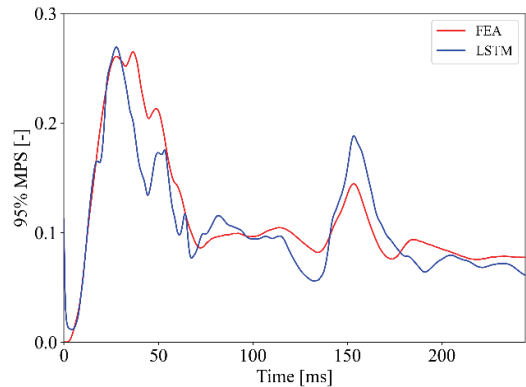
CORA: 0.951

Figure 8. Comparison of waveforms of maximum principal strain between true value (finite element analysis) and predicted value by LSTM in a frontal sled test case



CORA: 0.919

Figure 9. Comparison of waveforms of maximum principal strain between true value (finite element analysis) and predicted value by LSTM in a vehicle crash test case



CORA: 0.890

Figure 10. Comparison of waveforms of maximum principal strain between true value (finite element analysis) and predicted value by LSTM in a reconstruction test case of American football

DISCUSSION

Prediction Accuracy of LSTM and Bi-directional LSTM

In Table 2, the bidirectional LSTM yielded a slightly higher prediction accuracy than LSTM. Bi-directional LSTM is mainly used in fields such as natural language processing because it can use the information after a certain point in time when predicting series data. Because the series data used in this study are physical phenomena, future inputs and states did not effectively predict the current outputs and thus did not significantly improve the accuracy.

Prediction Accuracy by Parts of the Brain

As shown in Table 2, the CORA of the right and left cerebrum were larger than those of the cerebellum and brainstem. This was mainly because of the difference in the magnitude of the 95% MPS for each region. The average maximum values of the principal brain strain in the study data are listed in Table 3. The brain strains in the cerebellum and brainstem were small; therefore, the difference in peak values from the brain strain after the impact was small. Therefore, the learning of the brain strain waveform performed poorly.

Table 3
The maximum value of 95 percentile MPS

	cerebellum	stem	cerebrum R	cerebrum L
Averaged max value of MPS	0.107	0.170	0.277	0.271

Prediction Accuracy for Each Head Impact Type

According to the evaluation of each test by CORA shown in Table 2, the prediction accuracy of the waveforms was higher for the occipital impact test, vehicle crash test, frontal sled test, and reconstruction of the football accident. Figures 11 and 12 show the mean and standard deviation of the angular velocity for the occipital head impact tests and reconstruction tests of American football. The head impact tests are characterized by a significant change in angular velocity around the y -axis and a small change in angular velocity around the x -axis immediately after impact. However, the angular velocity waveforms in the reconstruction tests of American football are widely distributed along the x , y , and z axes. This is because the reconstruction tests of American football cases include head-impact conditions from various directions. Therefore, the prediction accuracy was low because there were few learning opportunities for input waveforms with similar characteristics in the American football cases dataset. The frontal sled test performed poorly because, for the football head impact tests, the number of datasets for the frontal sled test was small, and there were few learning opportunities for impacts with similar characteristics. However, the prediction accuracy did not deteriorate significantly because the dataset of the FRB vehicle crash test and occipital impact tests, which include similar head behavior, were also trained.

Afterward, the prediction errors of the waveforms are discussed for specific examples of the predicted waveforms for each head impact condition, as shown in Figures 7–10. First, the triaxial angular velocity waveforms used as inputs in the prediction are shown in Figures 13 and 14. When predicting the multimodal brain strain waveforms for any collision type, the prediction accuracies of the second and subsequent peaks were slightly less accurate than those of the first peak: the peaks were at 65 ms in the frontal sled test (Figure 8), at 130 and 230 ms in the vehicle crash test (Figure 9), and 150 ms in the reconstruction test case of American football (Figure 10). The multimodal brain strain waveform is caused by head rebound behavior, in which the head rotates in the opposite direction of the initial impact owing to a collision with an airbag. It was difficult to predict changes in brain strain because of this behavior from angular velocity alone because the angular velocity at 70 ms in the frontal sled test (Figure 13) and 130 ms in the vehicle crash test (Figure 14) was small. However, using the features of angular velocity change created by feature engineering, we could incorporate longer-term brain strain changes into the prediction, and the prediction accuracy was improved. Because over half of the current dataset consists of data from occipital impact tests without rebound behavior, further improvement would be expected by expanding the dataset to include rebound behavior or by considering features that can better reflect head rebound behavior.

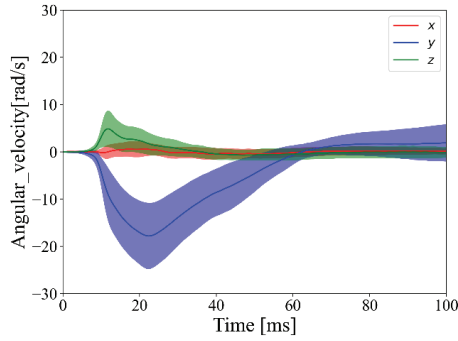


Figure 11. Angular velocity of occipital head impact tests

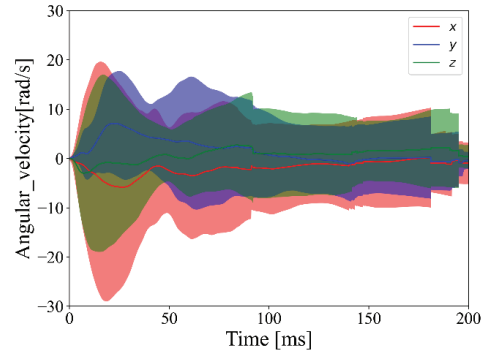


Figure 12. Angular velocity of reconstruction tests of American football

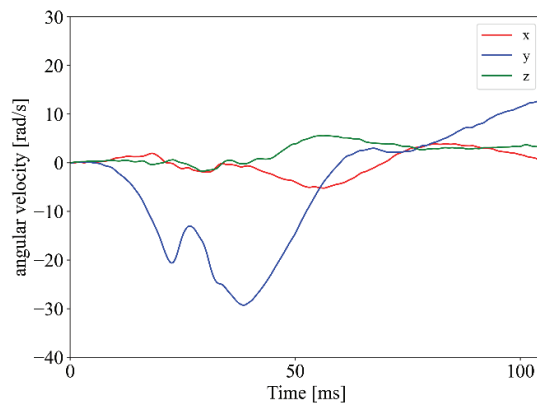


Figure 13. Angular velocity input of frontal sled test

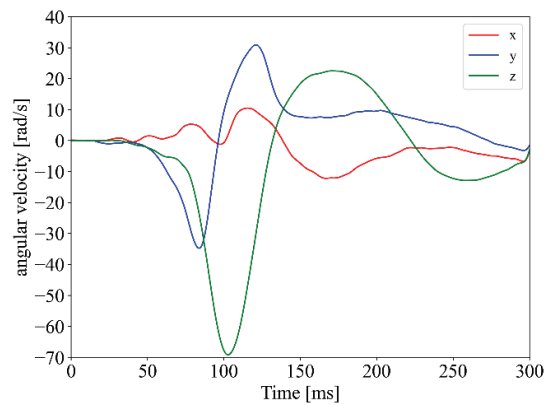


Figure 14. Angular velocity input of vehicle crash test

CONCLUSION

This study proposed a fast and simple method for predicting brain strain waveforms as an alternative to FEA, using LSTM and bidirectional LSTM, which are deep learning methods that can predict time-series waveforms. FEAs were performed on four types of head impact: occipital head impact tests, frontal sled tests, vehicle crash tests, and a reconstruction test of American football. Prediction models of brain strain waveforms using LSTM or bidirectional LSTM were constructed and evaluated. The results indicated that the LSTM model accurately predicted the brain strain waveforms.

REFERENCES

- [1] National Police agency, Traffic accident information, (2021). (in Japanese)
- [2] S. Wu, W. Zhao, K. Ghazi, and S. Ji, Convolutional Neural Network for Efficient Estimation of Regional Brain Strains. Scientific Reports, 9(17326):1-11. (2019).
- [3] H. Yamamoto, Y. Miyazaki, S. Awamori, A. Kokeyuchi, I. Amamori, K. Yoshii, Development of a Method to Measure Intracranial Brain Motion of a Novel Anthropometric Test Dummy Head using 6DOF Sensors, Student Research Symposium of AAAM2020 (2020)
- [4] Y. Miyazaki, A. Railkar, S. Awamori, A. Kokeyuchi, I. Amamori, M. Katagiri, K. Yoshii, Intracranial Brain Motion Measurement in Frontal Sled Tests by Using a New Anthropometric Test Dummy Head Capable of Direct Brain motion Evaluation and Visualization, Proceedings of IRCOBI conference, IRC-17-45 (2017)

- [5] NHTSA, NHTSA Vehicle Crash Test Database, <https://www-nrd.nhtsa.dot.gov/database/veh/veh.htm>
- [6] E. J. Pellman, D. C. Viano, A. M. Tucker, I.R. Casson, & J. F. Waeckerle, Concussion in Professional Football: Reconstruction of Game Impacts and Injuries. *Neurosurgery* 53, 799-814(2003).
- [7] E. J. Sanchez, et al. A reanalysis of football impact reconstructions for head kinematics and finite element modeling. *Clin. Biomech.* (2018).
- [8] F. Gers, J. Schmidhuber, and F. Cummins, Learning to Forget: Continual Prediction with LSTM, *Neural Computation* 12,2451-2471, (2000).
- [9] S. Hochreiter and J. Schmidhuber, Long Short-Term Memory, *Neural Computation*, 9(8): 1735-1780, (1997).
- [10] Graves, A., Schmidhuber, J.: Framewise Phoneme Classification with Bi-directional LSTM and Other Neural Network Architectures. *Neural Networks* 18(5), 602–610(2005).
- [11] Gehre, C., Gades, H. & Wernicke, P. Objective Rating of Signals Using Test and Simulation Responses. In *Enhanced Safety of Vehicles* (2009)

A SIMULATION STUDY ON THE KNEE-THIGH-HIP LOADING OF THE THOR COMPARED TO HUMAN BODY MODELS

Peres, Jeremie

Praxl, Norbert

Partnership for Dummy Technology and Biomechanics
Germany

Paper number 23-0271

ABSTRACT

The THOR-50M dummy is instrumented with acetabulum force sensors which is a novelty when compared to previous dummies like the Hybrid III. It has been proposed to use the acetabulum resultant force to predict hip injuries. Injury Risk Curves (IRCs) for cadavers have previously been developed, however it is not clearly established if the cadaver IRCs can directly be applied to the THOR measurements or if a transfer function is needed. As femur and acetabulum forces are located on the same load path, it is also questionable if it is necessary to use two different injury criteria to predict knee-thigh-hip injuries.

To investigate these questions, a simulation study was performed using a THOR model and two human body models (HBMs). Load cases included impactor tests derived from published cadaver testing as well as sled simulations in belted and unbelted configurations with a validated environment. The knee, femur and acetabulum forces measured in the different models were compared and the ratios between these forces were also analyzed. Additionally, based on the measurements from the THOR and HBMs simulations and published Injury Risk Curves for cadavers and the THOR, the risks of hip and knee/femur injuries were calculated for each load case.

Results show that the relationship between the forces measured in the THOR model and in the HBMs could depend on the loading conditions. The forces measured in the unbelted sled simulations are similar between the three models, however the acetabulum forces measured for the HBMs in the belted sled configuration are significantly lower than that of the THOR. For impactor configurations, the risk calculated at the hip for the THOR overestimates the likelihood of cadaveric injuries. For sled configurations, no cadaver test result was available, findings are based on simulations only and comparison with field data. For all simulations, the risk of hip injury predicted for the THOR was significantly higher than the risk predicted for both HBMs. The risk of hip injuries for the THOR was also, for all simulated load cases, higher than the risk of knee/femur injuries which is contrary to the injury frequencies observed in the field for belted occupants.

Overall, the risks calculated for the THOR from the acetabulum forces seem overestimated which is likely caused by the transfer coefficient used to calculate the THOR risks based on the human IRCs. An adjustment of the transfer coefficient is necessary and might require a different value for belted and unbelted cases.

This study has limitations. Firstly, the ability of the human body models to measure accurately the acetabulum force in sled configurations is not established due to the lack of relevant cadaver data. Secondly, parameter studies and real car simulations would be needed to generalize the results.

To conclude, it is necessary to define a transfer function for the acetabulum force to predict hip injury risks properly. This transfer function might be load case dependent.

INTRODUCTION

Several studies have emphasized that lower limb injuries are the most common AIS2+ injuries sustained in frontal crashes [1] [2]. In a more recent study, [3] observed that newer car models show a significant decrease in Knee-Thigh-Hip (KTH) injuries which could be explained by the progressive introduction of knee airbags [4]. These types of injuries could be more prevalent for small overlap and oblique frontal crashes for the driver and front passenger [5]. NHTSA reviewed NASS-CDS data from 2000 to 2015 for belted and airbag restrained drivers in frontal crashes [6]. Most of the KTH injuries were to the knee or femur, however two-third of hip/pelvis injuries occurred in the absence of knee/femur injuries. The vast majority of these injuries occur in compression.

It is known that the hip joint is the weakest part of the KTH complex, meaning that under the same force level, the hip joint would sustain injuries before the thigh and the knee [7] [8] [9]. However, during a frontal impact only a certain percentage of the force is transferred from the contact surface at the knees to the hip joint. The percentage of force transmitted is related to several factors such as mass recruitment, contact surface stiffness, adduction/abduction, and flexion angle at the hip. Generally, the more mass is recruited behind the hip and the softer the impact surface, the more the percentage of force transmitted from the knee to the hip is, leading to increased risk of hip injuries.

In FMVSS No. 208 and frontal NCAP tests, only the peak femur compressive force is used to predict the KTH injury risk. However, contrarily to the Hybrid III dummy, the THOR is instrumented with acetabulum force sensors in addition to the femur force sensors. NHTSA recommended to use the axial compressive femur force to predict knee/femur injuries and the resultant acetabulum force to predict hip/pelvis injuries. NHTSA also proposed corresponding Injury Risk Curves (IRCs) [6]. A transfer coefficient for the acetabulum was defined to account for differences in KTH force transmission between THOR and humans.

The current study investigates, with the help of dummy and human body models (HBMs) simulations, the force transmission between the knee, the thigh and the hip and evaluates the NHTSA proposed injury assessment of the THOR KTH injuries.

METHOD

All simulations were performed using LS-Dyna MPP single precision version 9.3.1 r140922. Three occupant models were used:

- The THOR-50M model from ATD-MODELS version D0.15
- The THUMS M50 version 5.03
- The GHBM M50 version 6.0

The use of the THUMS version 5 rather than the THUMS version 4 was justified because the hip modeling in version 4 is deficient, particularly the acetabulum surface seems unrealistically flat, and the cartilage is not represented leading to a lack of geometrical congruence with the head of the femur. For both HBMs, bone failure was deactivated so as not to affect the force transmission, allowing a proper comparison with the dummy. HBMs were instrumented in a similar way as the THOR, particularly, femur and acetabulum force sensors were defined in the corresponding bony structures at a similar position. For the femur force, only the axial compressive component was measured whereas for the acetabulum, the resultant force was calculated. Forces measured at the acetabulum while the femur was under tension were not considered. The knee force was defined as the resultant contact force between the impactor, or in the sled simulation the knee pad, and the knee of the occupant. Force signals were all filtered in accordance with CFC600.

Load cases

Three different load cases were selected, an impactor test with a fixed pelvis, an impactor test with a free pelvis and a sled test.

- Fixed pelvis impactor test

[7] performed 35 PMHS impactor tests at 1.2 m/s. Pelvis, sacrum, and lower extremities were removed before testing. The iliac wing was fixed to the test apparatus after removal of the iliac wing flesh. A stiff molded interface was positioned at the knee interface before impact. A 250 kg platform was accelerated to 1.2 m/s before impacting a ram attached to the molded knee interface. Between the ram and the platform, energy absorption materials consisting of a combination of Hexcel (9.5 mm cell diameter) and 13 mm thick flotation foam were used to limit the knee loading rate under 300 N/ms. The pelvis was positioned so that the angle between the horizontal and a line from the pubic symphysis to the anterior superior iliac spine (ASIS) measured in the xz plane was 120°. This angle was varied around this reference position. The femur was for all tests aligned to the global x-axis. Hybrid III tests were performed in a similar configuration, the only difference being that the pelvis was not included, and the femur head positioned in metallic acetabular cup. A finite element model of this setup was developed and validated based on the comparison of the Hybrid III test and the corresponding simulation results (see appendix 1).

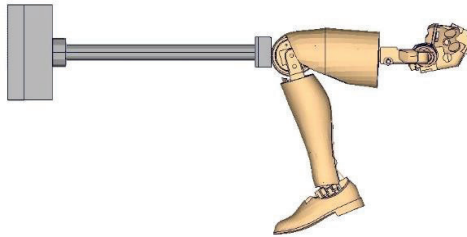


Figure 1. Fixed pelvis impactor load case.

- Free pelvis impactor test

[10] performed a series of sub-injurious tests on 15 (3*5) PMHS at velocities of 1.2, 3.5 and 4.9 m/s. The cadavers were seated on a bench and a symmetric horizontal load was applied to both knees using a 255 kg weighted platform accelerated pneumatically. The left and right knee impact surfaces were padded. In the tests with 1.2 m/s, the padding consisted of a single 38 mm thick, 50-durometer Sorbethane (Sorbothane Inc., Kent, Ohio) block. In the 3.5 and 4.9 m/s tests, the padding consisted of a 25 mm thick, 50-durometer block placed over a 70-durometer, 25 mm thick one. The knee force was measured via a loadcell placed behind the impacting surface. The femur force was measured directly using a loadcell implanted in the bone, whereas the force at the hip was calculated from the femur force using inertial compensation. The test setup was modeled, and Hybrid III test results reported in the same paper were used for validation (see appendix 2).

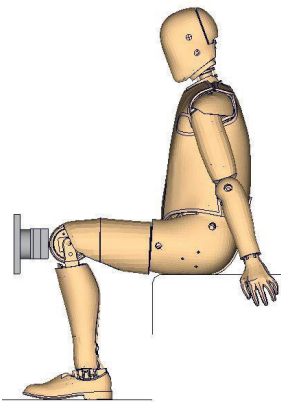


Figure 2. Free pelvis impactor load case.

- Sled load case
PDB used a simplified vehicle-like sled environment for frontal testing. It consists of a rigid seat, a rigid dashboard, a deformable knee bolster, a 3-point belt system with pre-tensioner and a 4 kN load limiter, and a deployed and pressurized airbag. The pulse was derived from a 0° full-width rigid wall test. This environment has been used to test various dummies and a corresponding simulation model has been validated with the corresponding dummy models. Comparison of simulation and experimental tests for the THOR-50M dummy can be found in appendix 3. Sled simulations in this study were performed both belted and unbelted. All three occupant models were positioned similarly with a particular focus on the pelvis and leg position. The x-position and the angle of the pelvis, measured between the horizontal and a line connecting the pubic symphysis and the ASIS, for the HBMs were matched to those of the THOR model which was positioned according to the experimental tests. Feet positions and distance between the knees for the HBMs were also matched to the THOR simulation model.

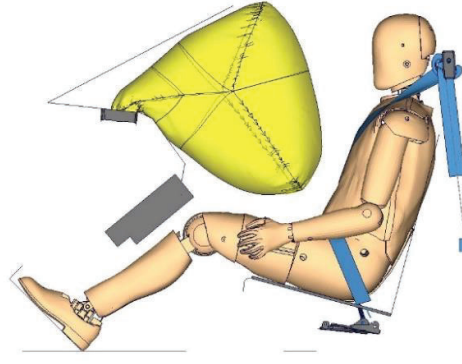


Figure 3. sled impactor load case.

Analysis

To analyze the load transmission through the KTH complex, several force ratios were calculated for each simulation:

$$R_{fk} = \frac{F_f}{F_k},$$

$$R_{af} = \frac{F_a}{F_f},$$

$$R_{ak} = \frac{F_a}{F_k},$$

With F_k , the knee force; F_f , the femur force and F_a , the acetabulum force.

Additionally, risks of knee/femur AIS 2+ and hip AIS 3+ injuries were calculated using the IRCs proposed by Craig et al. (2020) for the THOR-50M:

$$\text{Knee/Femur injury risk: } p(\text{AIS } 2+) = \Phi \left[\frac{\ln(1.299 * F_f) - 2.62}{0.3014} \right] \quad (1a)$$

$$\text{Hip fracture injury risk: } p(\text{AIS } 3+) = \Phi \left[\frac{\ln(T_{hip} * F_a) - 1.5751}{0.2339} \right] \quad (1b)$$

Where:

Φ is the cumulative normal distribution function.

T_{hip} , the ratio of estimated PMHS hip force to THOR measured peak acetabulum resultant force. NHTSA proposed a value of 1.429 for T_{hip} .

F_f and F_a the previously described femur and acetabulum forces.

RESULTS

First the peak forces obtained with the three models in the free pelvis impact simulations were compared to box plots derived from corresponding PMHS results published by [10] as illustrated in Figure 4 and Figure 5. Generally, for all models, the knee forces and the acetabulum forces are within or very close to the range of the PMHS. From these results, it is considered that both HBMs are validated for KTH loading and that the THOR shows comparable biofidelity for this loading.

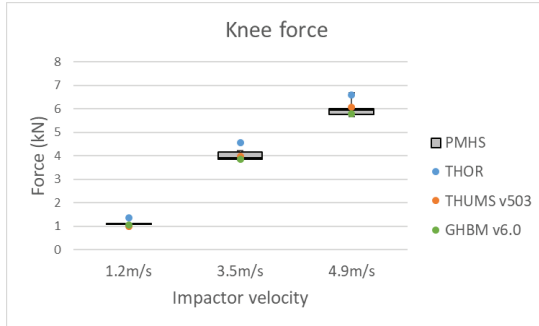


Figure 4: Knee force in Rupp et al. 2008 simulations compared to PMHS results.

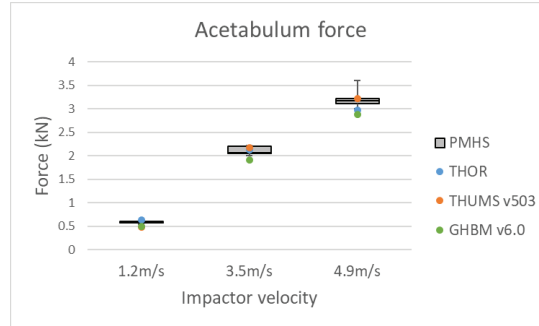


Figure 5: Acetabulum force in Rupp et al. 2008 simulations compared to PMHS results.

Free and fixed pelvis impactor tests resulted in fundamentally different behavior in terms of force transmission from the knee to the hip. When the pelvis is fixed, mass recruitment is not relevant anymore and 100% of the force is transmitted from the knee through the femur and to the acetabulum (see Figure 6). On the contrary, when the pelvis is not fixed, only a portion of the knee force is transmitted to the femur and an even lower portion to the acetabulum (see Figure 7).

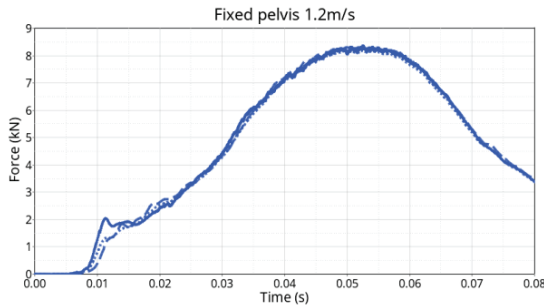


Figure 6: Knee (solid), femur (dashed) and acetabulum (dotted) forces in the 1.2 m/s fixed pelvis impactor simulation with THOR.

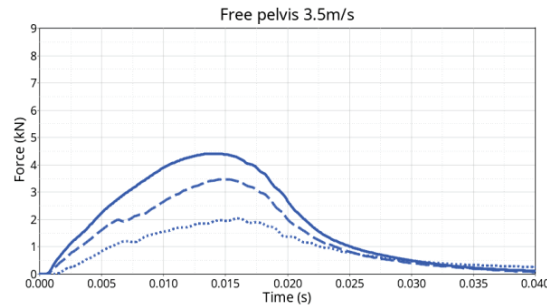


Figure 7: Knee (solid), femur (dashed) and acetabulum (dotted) forces in the 1.2 m/s free pelvis impactor simulation with THOR.

For the fixed pelvis impact tests, the forces are directly related to the overall stiffness of the KTH complex and differ between the three tested models (see Figure 8, Figure 9 and Figure 10). In the free pelvis tests, the three models show similar knee, femur, and acetabulum forces for the three impact velocities. The peak forces increase with velocity and decrease when moving from the knee to the acetabulum ($F_k < F_f < F_a$).

The same trend between knee, femur and acetabulum forces is observed for the sled simulations whether belted or unbelted. The force levels are similar for the three models in the unbelted configuration; however, the forces are significantly lower in both HBMs compared to the THOR model in the belted configuration. Note, for reason of simplification, the left and right forces have been averaged for the sled simulations.

The general kinematic is similar in the sled simulations between all three models, however, in the belted simulation, some differences are observed at the pelvis level. Indeed, the HBMs showed a backward rotation, whereas the THOR showed very little pelvis rotation. Also, the HBMs had less peak pelvis forward excursion (THUMS v503: -6.5 mm, GHBM v6.0: -10 mm). The timing of the knee impact was similar between all models at around 40 ms.

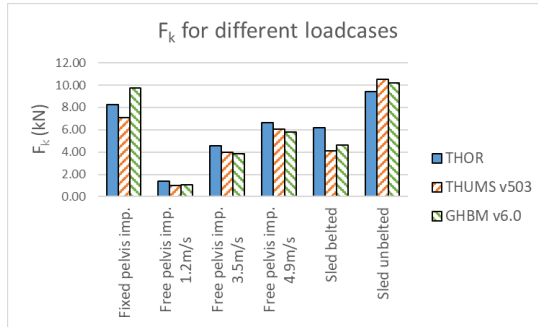


Figure 8: Knee force in simulated load cases.

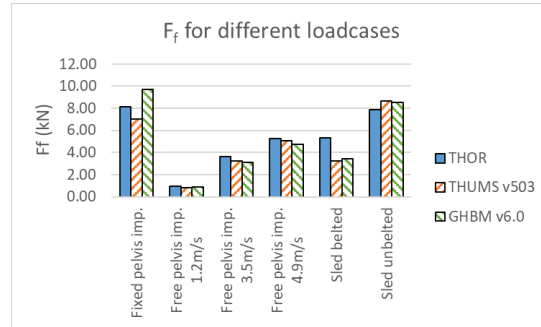


Figure 9: Femur force in simulated load cases.

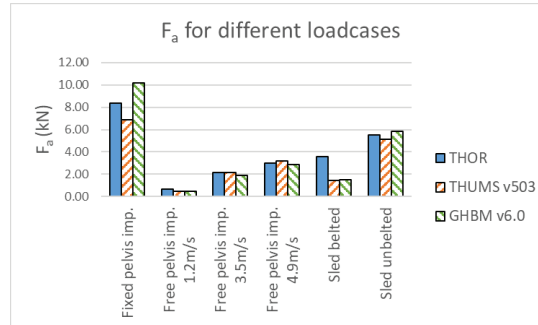


Figure 10: Acetabulum force in simulated load cases.

Table 1 shows the calculated risks based on the Injury Risk Curves from [6] for the femur and acetabulum forces. For the HBMs, the factor T_{hip} has been set to 1, meaning that the HBMs are treated as if they were PMHS. Some notable differences are observed, particularly, the risk of hip injuries is consistently higher for the THOR when compared to both HBMs. The GHBM model predicts higher risks of knee/femur injuries for the fixed pelvis than THUMS and THOR. Both HBMs predict no risks for all impactor tests with a free pelvis and the belted sled case whereas the THOR predicts significant risks of hip injury for the 4.9 m/s impactor and both sled simulations.

Table 1.
Injury risk for every simulated load case.

		THOR		THUMS v503		GHBM v6.0	
		AIS2+ Risk knee/femur	AIS3+ Risk hip	AIS2+ Risk knee/femur	AIS3+ Risk hip	AIS2+ Risk knee/femur	AIS3+ Risk hip
Fixed pelvis	1.2 m/s	0.19	1.00	0.09	0.94	0.38	1.00
Free pelvis	1.2 m/s	0.00	0.00	0.00	0.00	0.00	0.00
	3.5 m/s	0.00	0.02	0.00	0.00	0.00	0.00
	4.9 m/s	0.01	0.29	0.01	0.04	0.00	0.01
Sled belted	Left	0.01	0.34	0.00	0.00	0.00	0.00
	Right	0.02	0.78	0.00	0.00	0.00	0.00
Sled unbelted	Left	0.17	0.98	0.26	0.58	0.24	0.78
	Right	0.17	0.98	0.26	0.62	0.24	0.79

DISCUSSION

As presented in the results for the belted sled simulations, the THOR showed generally much higher forces at the knee thigh and hip compared to the HBMs. An analysis of the kinematic and the belt forces, shows that the interaction between the seatbelt and the pelvis is very different. The HBMs show an earlier engagement of the seatbelt with the iliac wings which is confirmed by a much higher lap belt force than for the THOR. The main cause for this is the geometry of the thigh and abdomen. The THUMS model has thinner thighs compared to both other models, which leads to a lower position of the lap belt compared to the pelvis, the upper edge of the lap belt being around the same height as the ASIS. The GHBM and the THOR differ in the abdomen geometry, the THOR abdomen is flat at the junction with the thigh, whereas the GHBM has an inward curvature in the same region. Due to this curvature, the belt lies closer to the iliac wing in the GHBM simulation. Thigh size and abdomen

shapes can vary significantly between individuals even for a given percentile and are influenced by the posture and the types of clothes worn [11] [12], so it is not possible to make a definitive statement as to which model is more human-like.

All tested PMHS (n=26) were injured in the fixed pelvis cases and most of the injuries were to the hip or pelvis which is consistent with the injury prediction for all models in this load case. The free pelvis tests were designed to be sub-injurious and none of the PMHS were injured (n=5 per velocity). The THOR predicts very little risk for the 1.2 and 3.5 m/s velocities. However, an injury risk of 29% for the hip is calculated for the 4.9 m/s case, which seems overestimated. On the contrary, both HBMs show low injury risk for all three velocities. HBMs also predict no injury risk for the belted sled test; whereas the THOR predicts relatively high (Left: 0.34, Right: 0.78) hip injury risks but no knee/femur injury risk. Field data show on the contrary that for belted occupants the occurrence of knee/femur injuries is significantly higher than that of hip injuries [6]. This risk prediction seems particularly inconsistent with field data when considering that the hip injury risk is calculated for AIS3+ injuries while the risk of knee/femur is calculated for AIS2+.

The incidence of KTH injuries in frontal crashes for unbelted occupants is about three times higher than that for belted occupants [13] and the proportion of knee/femur and hip injuries seem to be consistent between the belted and unbelted cases. All three models predict higher risks of hip injuries than knee/femur with the THOR showing the highest hip injury risk (98%) and the lowest knee/femur risk (17%).

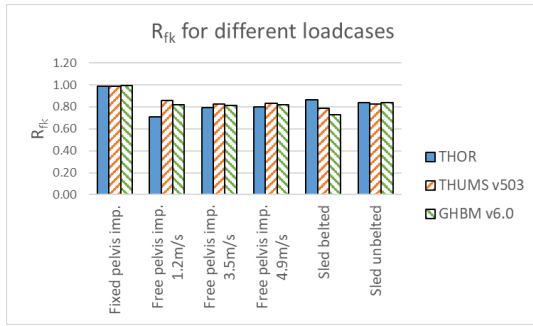


Figure 11: Ratio of femur to knee force in all simulated load cases.

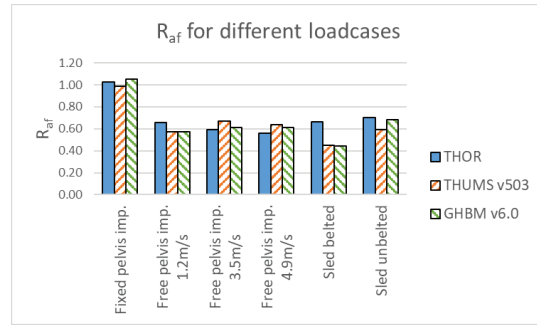


Figure 12: Ratio of acetabulum to femur force in all simulated load cases.

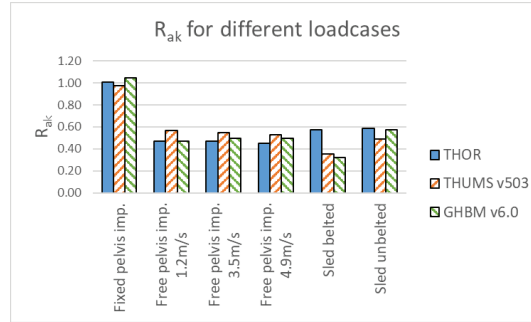


Figure 13: Ratio of acetabulum to knee force in all simulated load cases.

Given that the THOR seems to overestimate the risk of hip injuries for the free pelvis impactor tests and for the sled simulations, it is worth questioning the validity of the T_{hip} value. This value was calculated using the equation below [6]:

$$T_{hip} = \frac{r_{PMHS}}{r_{THOR}} = \frac{r_{PMHS}}{r_{fk} * r_{fa}} = \frac{0.55}{0.77 * 0.5} = 1.429 \quad (2)$$

Where:

$$r_{PMHS} = r_{ak}(PMHS)$$

$$r_{THOR} = r_{ak}(THOR)$$

The value of 0.55 for r_{PMHS} is based on the PMHS results from [10]. This value is relatively close to the values observed in the HBM simulations for the free pelvis simulations and the unbelted sled as can be seen in Figure 13. However, 0.55 is an approximate value, recalculating the mean based on the values reported in paper leads to a value of 0.54. For r_{fk} [6] assumed that the THOR behaves similarly to the Hybrid III and therefore defined the same value for both dummies. Generally, the values found in this study are slightly higher for this ratio except for the free pelvis at 1.2 m/s which might be due to the low impact velocity in this case. Excluding this load case and the fixed pelvis one, which is not representative of a frontal crash loading, the mean r_{fk} value in this study is 0.83. The 0.5 value for r_{fa} is based on an analysis by [14] of THOR-NT test results. A review of internal dummy experimental tests in the same belted sled condition described in this paper lead to a value of 0.61 ± 0.05 over 29 tests involving 7 THOR dummies. This value seems consistent with the results from the simulation study. Recalculating T_{hip} with $r_{PMHS} = 0.54$, $r_{fk} = 0.83$, and $r_{fa} = 0.61$, leads to a value of 1.07. Figure 14 shows the ratio of the acetabulum force for the HBMs to the THOR for the simulated cases. The ratio is close to 1 for the 3.5, 4.9 m/s and unbelted sled tests. The ratio is much lower, around 0.4 for the belted case, meaning that in this case, the HBMs predict only 40% of the acetabulum force predicted by the THOR.

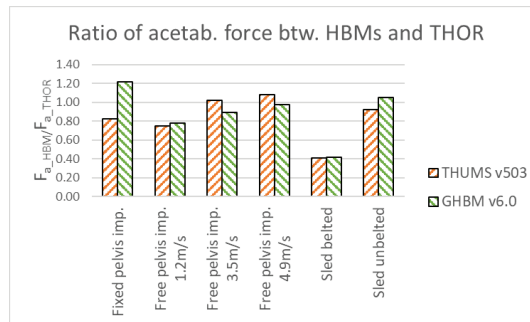


Figure 14: Ratio of acetabulum force between HBMs and THOR.

Based on the observations described above, a value of T_{hip} of 1 was considered and all risks for the THOR model were recalculated (Table 2). The risks for the impactor tests are consistent with the PMHS injuries, particularly the hip injury risk for the free pelvis case at 4.9 m/s is reduced from 29% to 2%. Hip injury risks calculated for the belted sled tests are reduced from 34% and 78% to 3% and 23% for the left and right side respectively. For the unbelted case, the risks are reduced from 98% on both sides to 73% on the left and 72% on the right side. However, in both sled simulations, the hip injury risks are still higher than the knee/femur injury risk which is not consistent with expectations based on field data. It could be that T_{hip} is lower than 1.0 in the belted configuration as is suggested by the difference between THOR and the HBMs in this study, but this needs to be confirmed by experimental results.

Table 2. Injury risk for every simulated load case with $T_{hip}=1.429$ and $T_{hip}=1.0$.

		THOR		
		AIS2+ Risk knee/femur	AIS3+ Risk hip for $T_{hip} = 1.429$	AIS3+ Risk hip for $T_{hip} = 1.0$
Fixed pelvis	1.2 m/s	0.19	1.00	0.99
Free pelvis	1.2 m/s	0.00	0.00	0.00
	3.5 m/s	0.00	0.02	0.00
	4.9 m/s	0.01	0.29	0.02
Sled belted	Left	0.01	0.34	0.03
	Right	0.02	0.78	0.23
Sled unbelted	Left	0.17	0.98	0.73
	Right	0.17	0.98	0.72

In the experimental sled tests mentioned above, the R-square value between the femur and acetabulum force data from the experiments is 0.89 which suggests a good correlation between these two values. This could be due to the high repeatability and reproducibility of the sled tests when compared to real situations including various car models and/or various loading conditions (e.g., direction, speed). However, in the simulations, R_{af} for the THOR remains also relatively close to 0.6, except the fixed pelvis test, despite the different nature of the impactor tests

compared to the sled tests. More data are necessary to conclude on the variability of the R_{af} ratio, however, based on currently available data, there is no indication that it is varying significantly. If this is confirmed, it is likely that independently of the IRCs, one sensor will consistently predict higher risks than the other. Therefore, the use of both the knee/femur and the hip injury risks for the THOR would be redundant and unnecessary and it would seem more suitable to use only one of the two sensors. More research is needed to determine which of these two sensors should be used and if only one is used how the corresponding IRC would be defined, particularly if both types of injuries (knee/femur and hip) should be considered.

This study has limitations. Firstly, the ability of the human body models to measure accurately the acetabulum force in sled configurations is not established due to the lack of relevant cadaver data. Another point is that the results in the belted sled configuration seem to be very sensitive to the belt position which mostly depends on the thigh and hip geometry. It could be that the difference observed between the HBMs, and the THOR are very specific to the particular parameters of this load case such as belt system or knee pad stiffness. To generalize the results, it would be necessary to run parameter studies as well as to verify the findings in real car environments.

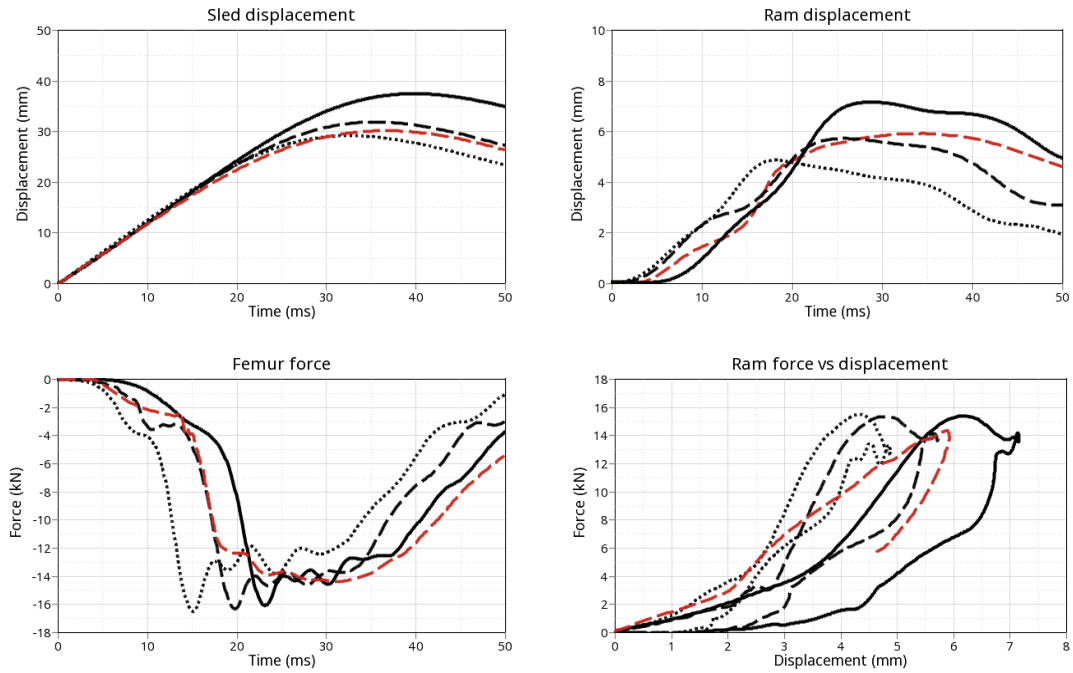
CONCLUSION

A simulation study was performed using a THOR-50M model and two HBMs to investigate Knee-Thigh-Hip injuries. It has been previously proposed to use the THOR acetabulum force sensor to predict hip/pelvis injuries and the femur force sensor to predict knee/femur injuries. The current studies show that over different loading conditions, the femur and acetabulum force measurements have a very good correlation, and it might therefore not be necessary to use both measurements. The Injury Risk Curve for hip/pelvis proposed by NHTSA overpredicts the injury likelihood. Based on the results of this study, the overprediction is most likely due to the transfer coefficient defined between the THOR and humans. The proposed value of 1.429 for this coefficient is generally too high and could be load case dependent. Based on the presented results, a transfer coefficient of 1 seems reasonable for the unbelted cases; and for belted cases, a coefficient of less than 1 is necessary. Further investigation is needed possibly using parameter studies and real car interior models.

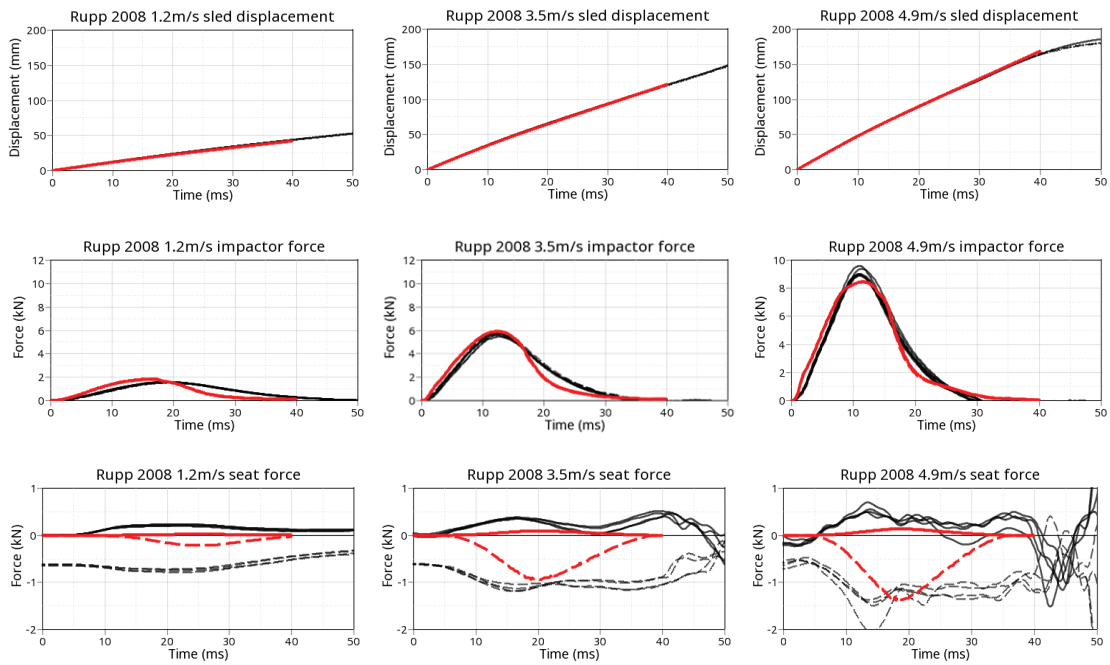
REFERENCES

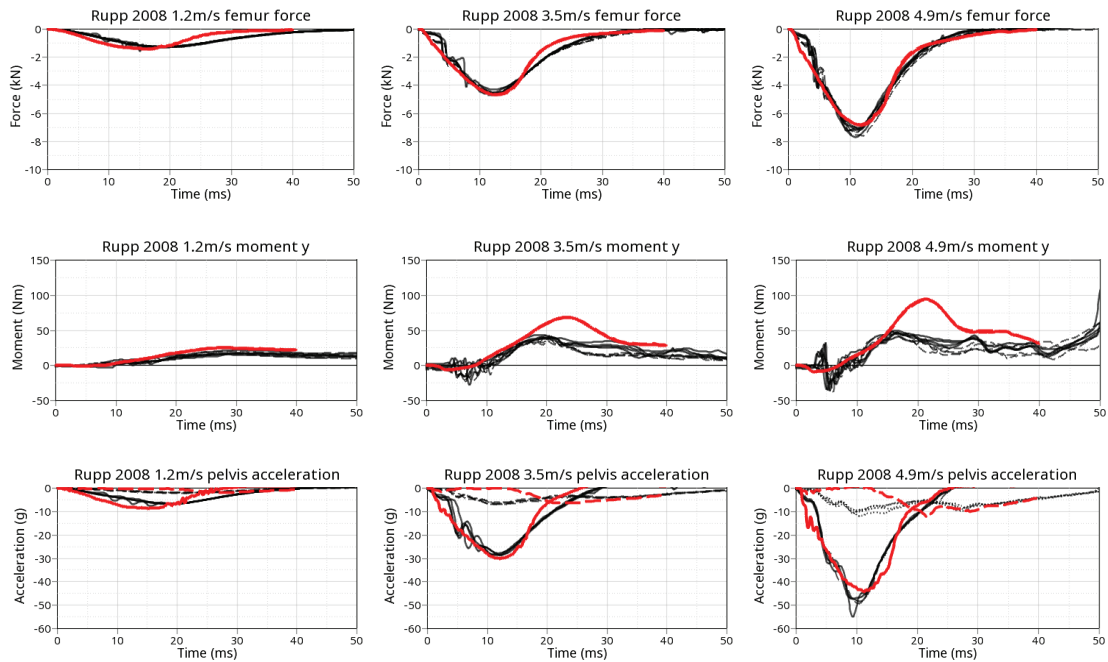
- [1] Page, Y., Cuny, S., Hermitte, T., Labrousse, M. 2012. A comprehensive overview of the frequency and the severity of injuries sustained by car occupants and subsequent implications in terms of injury prevention. *Annals of Advances in Automobile Medicine*. 2012, 56:165-74.
- [2] Ye, X., Poplin, G., Bose, D., Forbes, A., Hurwitz, S., Shaw, G., Crandall, J. 2015. Analysis of crash parameters and driver characteristics associated with lower limb injury. *Accident Analysis & Prevention*. 2015, 83:37-46.
- [3] Forman, J., Poplin, G., Shaw, G., McMurry, T., Schmidt, K., Sunnevang, J. & C. 2019. Automobile injury trends in the contemporary fleet: Belted occupants in frontal collisions. *Traffic Injury Prevention*. 2019, 20:6, 607-612.
- [4] McMurry, T., Forman, J., Shaw, G., Cradall, J. 2020. Evaluating the influence of knee airbags on lower limb and whole-body injury. *Traffic Injury Prevention*. 2020, 21(1):72-77.
- [5] Rudd, R. 2009. Updated analysis of lower extremity injury risk in frontal crashes in the United States. *21st ESV Conference proceedings*. 2009, No. 09-0556.
- [6] Craig, M., Parent, D., Lee, E., Rudd, R., Takhounts, E., Hasija, V. 2020. *Injury Criteria for the THOR 50th Male ATD*. s.l. : National Highway Traffic Safety Administration, 2020.
- [7] Rupp, J., Reed, M., Van Ee, C., Kuppa, S., Wang, S., Goulet J., Schneider, L. 2002. The tolerance of the human hip to dynamic knee loading. 2002. *Stapp Car Crash Journal*, pp. 46:211-28. Vol. 46, 2002-P-383.
- [8] Rupp, J., Reed, M., Madura, N., Kuppa, S., Schneider, L. 2003. Comparison of knee/femur force-deflection response of the THOR, HYBRID 3, and human cadaver to dynamic frontal-impact knee loading. *18th ESV Conference Proceedings*. 2003, 03-160.
- [9] Rupp, J. 2006. *Biomechanics of hip fractures in frontal motor-vehicle crashes*. Ph. D. Dissertation. s.l. : The University of Michigan, Ann Arbor, MI, 2006.
- [10] Rupp, J., Miller, C.S., Madura, N., Reed, M. 2008. Characterization of Knee-Thigh-Hip Response in Frontal Impacts Using Biomechanical Testing and Computational Simulation. 2008. *Stapp Car Crash Journal*. Volume 52:pp.421-74.
- [11] Park, B-K., Jones, M., Ebert, S., Reed, M. 2021. A parametric modeling of adult body shape supported seated posture including effects of age. *Ergonomics*. 2021, 1-9.
- [12] Tanaka, Y., Nakashima, A., Feng, H., Mizuno, K., Yamada, M., Yamada, Y., Yokoyama, Y., Jinzaki, M. 2021. Analysis of lap belt fit to human using CT images. *Stapp Car Crash Journal*. 2021, Volume 65: pp. 49-90.
- [13] Kirk, K., Kuppa, S. 2009. Application and evaluation of a novel KTH injury criterion for the hybrid III dummy in frontal crash test environments. *21st ESV Conference Proceedings*. 2009, 09-0196.
- [14] Martin, P., Scarboro, M. 2011. THOR-NT: Hip injury potential in narrow offset and oblique frontal crash. *22nd ESV Conference Proceedings*. 2011, 11-0234.

Appendix 1: Validation of fixed pelvis simulation environment based on Hybrid III-50 simulations

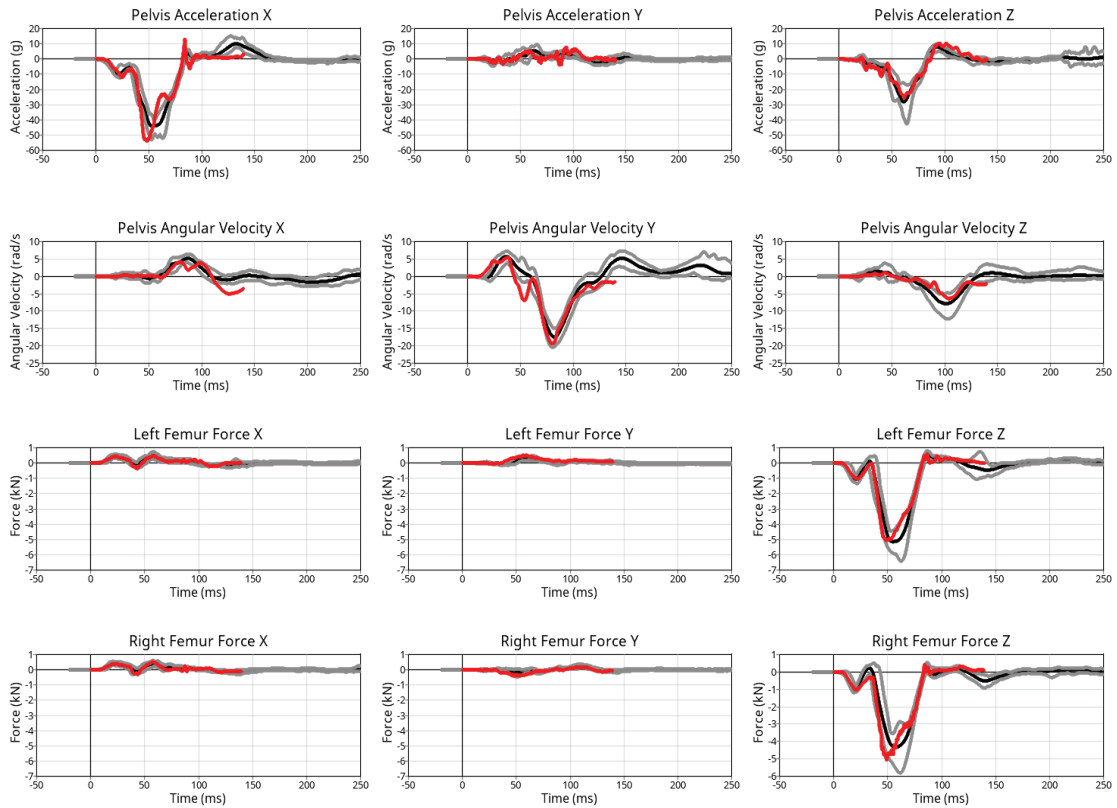


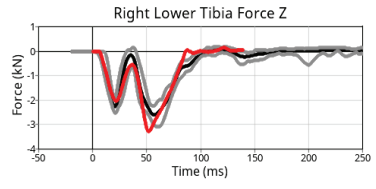
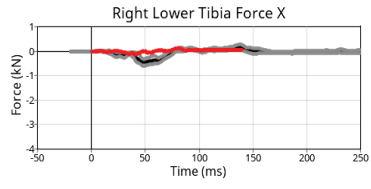
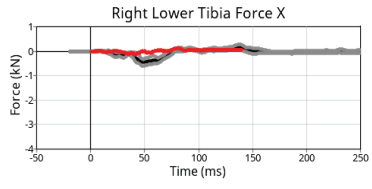
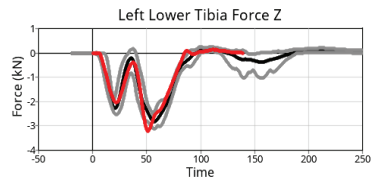
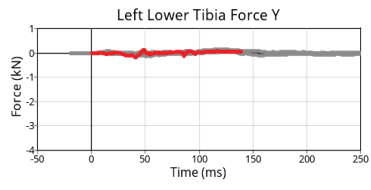
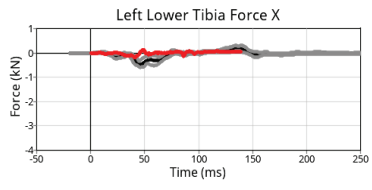
Appendix 2: Validation of free pelvis simulation environment based on Hybrid III-50 simulations





Appendix 3: Validation of belted sled simulation environment based on THOR-50M simulations





DEVELOPMENT OF A MULTI-POINT CHEST DEFLECTION MEASUREMENT SYSTEM FOR THE LARGE OMNIDIRECTIONAL CHILD (LODC) ANTHROPOMORPHIC TEST DEVICE (ATD)

Mike Carlson

Brian Suntay

Transportation Research Center Inc.
USA

Jason Stammen

National Highway Traffic Safety Administration
USA

Paper Number 23-0275

ABSTRACT

OBJECTIVE The objective of this study is to evaluate the feasibility and accuracy of a multi-point chest deflection sensing system installed in the LODC using static, quasi-static, and two dynamic test conditions.

METHOD The multi-point LED chest deflection system was evaluated at four levels: (1) calibration verification, (2) quasi-static, (3) dynamic probe impact, and (4) dynamic drop tower in order to demonstrate that the sensor gave a reasonable and accurate measurement of chest deflection.

RESULTS Individual sensors were found to be quite accurate in static verification tests, and sensors installed in the LODC ribcage were also observed to match well with CMM measurements. In dynamic testing with the full array of sensors installed in the ribcage, LED deflection matched probe-measured deflection closely. In both frontal and oblique drop tower tests, individual sensor deflection time histories showed how the full array could capture full ribcage deformation.

CONCLUSIONS A novel non-contact sensor array to measure LODC chest deformation has been developed. This system has gone through a battery of both static and dynamic tests thus far to evaluate the system's performance. Initial results indicate that the system is promising for monitoring overall chest deformation in the LODC. Future work will include more dynamic testing to further understand how the system can describe three-dimensional ribcage deformation.

Keywords: LODC; chest deflection; multi-point; LED; testing

INTRODUCTION

Thoracic injuries sustained by rear seated child occupants involved in vehicle crashes have been attributed to complex loading mechanisms including the belt and seatback [1]. Because children make up a large percentage of rear seated occupants [2], protection of the pediatric chest is critical. Historically, chest deflection has been the primary correlated measure to thorax injury risk when using anthropomorphic test devices (ATDs). It has also been hypothesized that thoracic injury in children is dependent on the rate of loading, more so than in adults [3]. Increased thorax flexibility in younger occupants permits deformation to the underlying viscoelastic tissue, where a high loading rate results in lung injuries such as pulmonary contusion, without rib fracture. There have been pediatric biomechanical studies [4-6] aimed at characterizing the pediatric thoracic response in varying loading conditions including both distributed and belt loading that reported thorax compression magnitudes, thorax loads, and thorax compression rates along with injuries. This work has provided baseline information on pediatric thorax response and injury mechanisms to help guide child ATD development.

The National Highway Traffic Safety Administration (NHTSA) used this information, in part, to develop the Large Omni-directional Child (LODC) ATD. This ATD has been demonstrated to possess biofidelic thoracic response characteristics [7]. Using information from pediatric biomechanical studies, LODC thorax test data, and field injury

data, an injury risk function based on deflection rate has been proposed for the LODC [8] so that the ATD can be used to design optimized restraint strategies that mitigate thoracic trauma to children. To measure complex thoracic deformation, the LODC requires instrumentation that accurately tracks the distance between the compliant ribcage and flexible spine. Because of the ribcage and spinal compliance required to meet biofidelity criteria from pediatric studies, it would be ideal if the operation of deflection-measuring sensors is not affected by potentially extreme levels of deformation at the sensor connection points on the spine or ribcage. In early testing of the LODC with an IR-TRACC installed to measure chest deflection, because of the small LODC size, the IR-TRACC took up a large percentage of thoracic space and was prone to interference with the spine especially when the ribcage was loaded obliquely. This interference resulted in IR-TRACC damage or erroneous signals. Because of this, NHTSA initiated the development of an optical sensor system to measure deflection in the LODC ribcage [9]. This single laser sensor mounted to the thoracic spine was found to measure sternum deflections consistent with an IR-TRACC in controlled test setups.

Because initial bench testing of the single optical sensor in both static and dynamic modes was encouraging, full dummy testing was subsequently conducted to further evaluate the single sensor's performance. The LODC is intended to be tested in a variety of commonly used child restraint systems (CRS) as well as seating postures that do not use a CRS. The different test conditions will cause variations in the seat belt routing and will dramatically change the crash kinematics. The variation of the shoulder belt routing over the thorax means that a single sensor centered over the sternum may not detect maximum ribcage deflection if the belt doesn't cross in front of the sensor. A dramatic difference can be seen in the position of the shoulder belt relative to the ATD thorax when comparing the backless belt positioning booster (BPB) and the No CRS slouch test conditions (Figure 1). Figure 2 shows the internal chest deflection measured in these two seating conditions. When the shoulder belt crosses in front of the sensor measurement location on the ribcage with the booster, we see a higher deflection. When the shoulder belt crosses closer to the neck in the no booster case, the single deflection sensor located at the sternum understandably does not measure a similar result. However, from real-world cases, severe pneumothorax injuries can occur when the shoulder belt is not properly positioned on the chest [10]. This finding indicates that maximum ribcage deformation doesn't always occur mid-sternum in crashes and demonstrates the need to measure deflection at multiple locations on the ribcage.



Figure 1. LODC seated on FMVSS No. 213 bench¹ with BPB (top) and slouch position without BPB (bottom).

¹ FMVSS No. 213 bench shown is the proposed bench specified in the Notice of Proposed Rulemaking (NPRM). See <https://www.regulations.gov/search?filter=NHTSA-2020-0093-0004> for details of the bench.

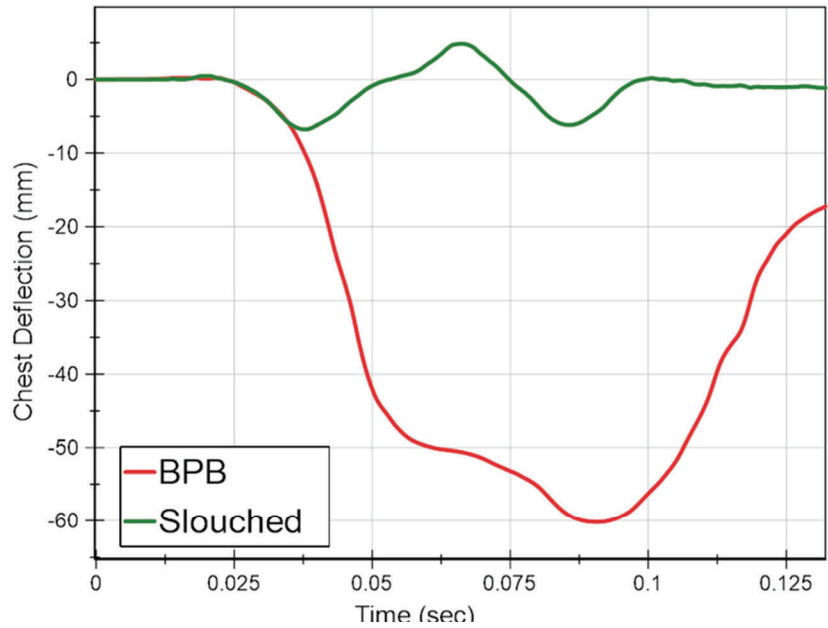


Figure 2. Chest deflection as measured at the sternum of the LODC.

DESCRIPTION OF MULTI-POINT LED SYSTEM

To facilitate measurement of deflection at multiple locations within the ribcage, a non-contacting optical sensor with a smaller footprint was required to fit into the LODC. The sensor chosen for this application is an off-the shelf optical triangulation distance sensor (Sensopart Model FT 25-RA-170-PNSUL_M4M) that is commonly used in industrial applications (Figure 3). This particular sensor emits a beam of light that produces a spot on the inside of the ribcage. A lens focuses the spot image onto a photodiode that allows the calculation of the distance from the sensor to the spot (Figure 4). The optical triangulation sensor is limited by a standoff distance and a measurement range. The standoff distance is the closest distance in front of the sensor that will produce a measurement. The measurement range is the range of distance past the standoff distance that the sensor can measure. The chosen sensor specifications are expected to be able to measure the entire range of expected LODC ribcage deflection and motion.



Figure 3. Sensopart distance sensor.

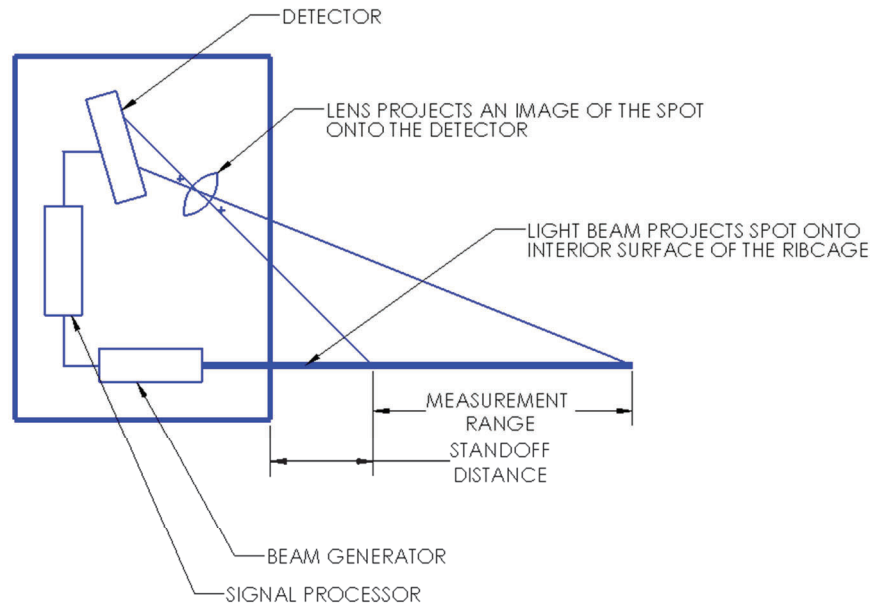


Figure 4. Diagram of the optical triangulation distance sensor measurement.

In the LODC, all seven sensors are attached to the center vertebrae element using brackets (Figure 5 and Figure 6). Five of the sensors face forward and two face obliquely. One sensor is located centered on the sternum between ribs 2 and 3. There are two forward facing sensors between ribs 1 and 2 and spaced laterally left and right of the midsagittal. There are two forward facing sensors between ribs 3 and 4 also spaced laterally left and right of the midsagittal. Finally, there are two sensors facing obliquely left and right between ribs 2 and 3 and rotated 70 degrees from the frontal direction. Figure 7 shows the system installed with LED spots visible on the inside surface of the ribcage.

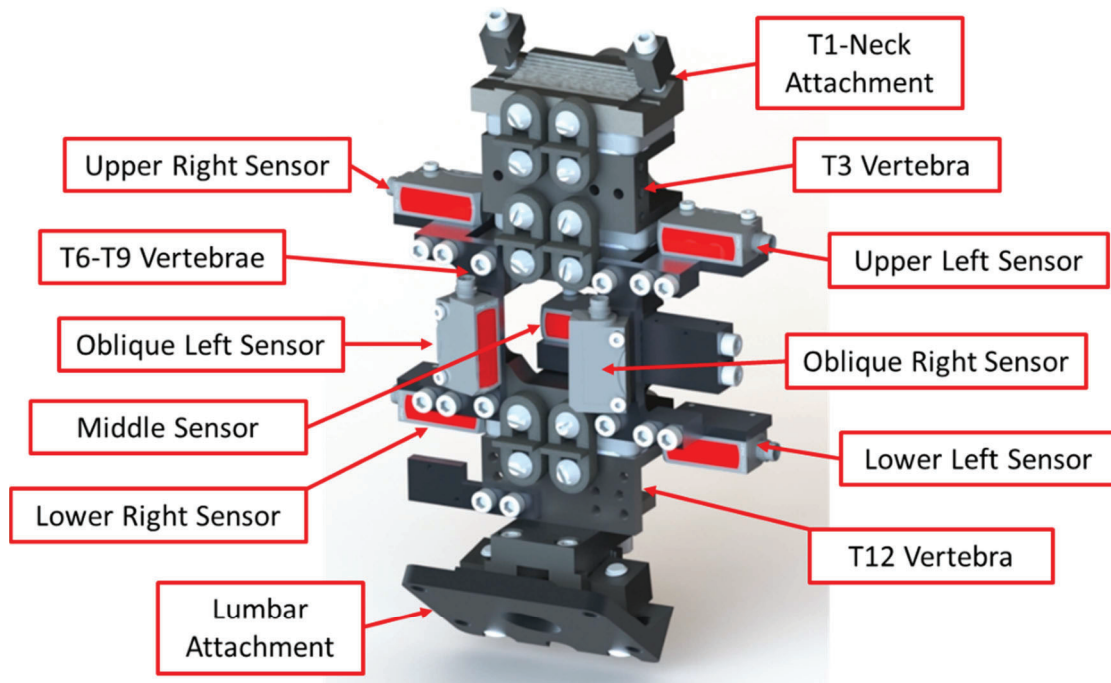


Figure 5. LODC thoracic spine with the 7 optical sensors installed.

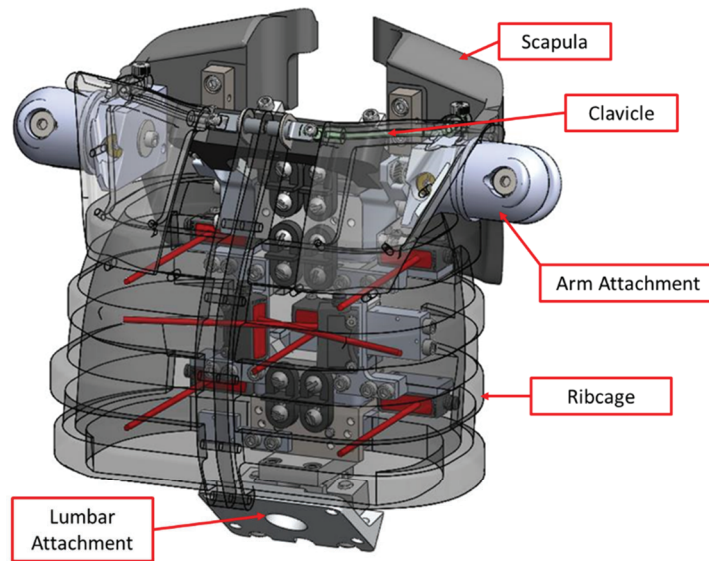


Figure 6. Measurement locations of the optical sensors inside the LODC ribcage.

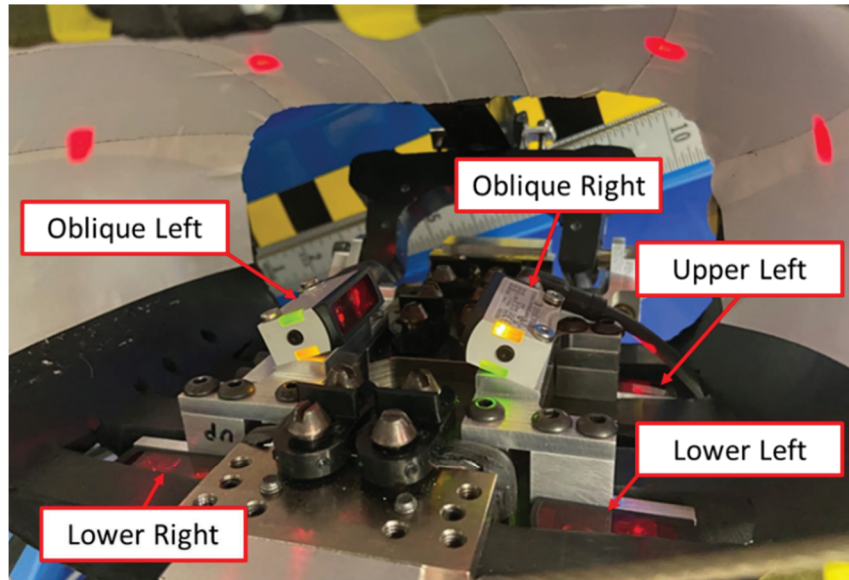


Figure 7. Interior view (looking upwards) of ribcage showing sensors (upper right & midsternum not shown).

Because of the difficulties associated with the IR-TRACC in the LODC, a triangulation sensor measurement system has been developed. The original optical system consisted of a single sensor located at the midsternum. After verifying proper operation of that system and recognizing the benefit of collecting chest deflection data at multiple locations in the ribcage, a multi-sensor configuration has been implemented into the LODC. The objective of this study is to evaluate the feasibility of a multi point sensing system in static, quasi-static and dynamic conditions.

EVALUATION OF MULTI-POINT LED SYSTEM

The multi-point chest deflection measurement system was evaluated in static, quasi-static, and dynamic conditions. Each sensor was first evaluated in a static calibration fixture prior to installation in the ribcage. The sensors were then evaluated quasi-statically through compression of the ribcage in a universal test machine (UTM). Thorax probe impacts and drop tower tests were performed to dynamically evaluate the multi-point system.

Static Evaluation

The calibration fixture consists of a linear slide connected to a linear scale with a digital readout. The sensor is clamped to the fixture as shown in Figure 8 and the slide is moved in 5 mm increments while the sensor reading is recorded.

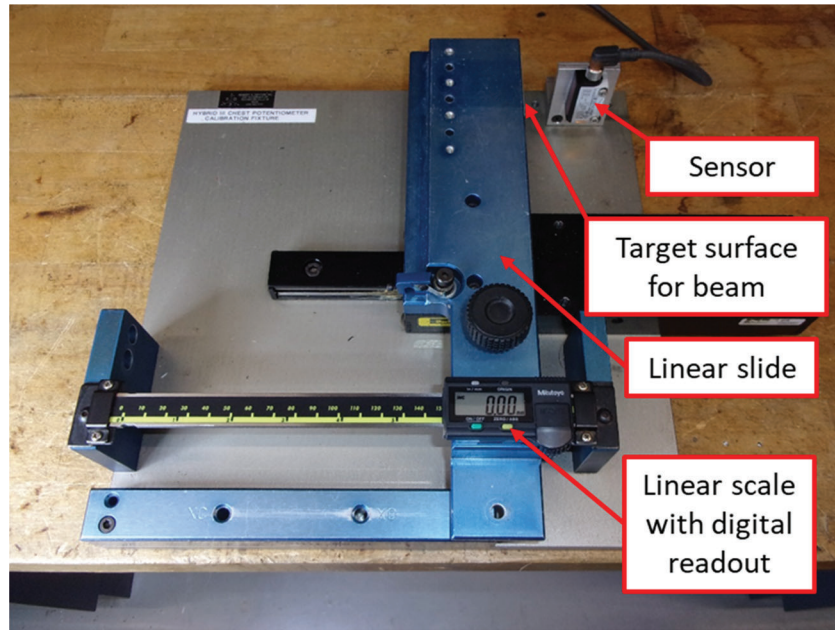


Figure 8. Calibration fixture for static evaluation.

A comparison of the linear scale readouts and sensor deflection readings are summarized in Table 1 for seven different sensors at each of the 5 mm increments. A plot of average sensor deflection versus linear scale deflection is shown in Figure 9.

Table 1.
Comparison of the linear scale readout and sensor deflection readings

Linear Scale Readout	Deflection (mm)							Average
	#1	#2	#3	#4	#5	#6	#7	
0	0.0	0.0	0.0	0.0	0.0	0.0	0.0	0.0
5	5.1	5.1	5.3	5.5	5.2	5.5	5.2	5.3
10	10.1	10.1	10.4	10.3	10.2	10.7	10.2	10.3
15	15.1	15.1	15.3	15.4	15.2	15.6	15.3	15.3
20	20.0	20.2	20.4	20.5	20.1	20.6	20.3	20.3
25	25.1	25.2	25.5	25.5	25.4	25.6	25.4	25.4
30	30.1	30.2	30.3	30.4	30.2	30.6	30.3	30.3
35	35.1	35.1	35.3	35.5	35.2	35.5	35.3	35.3
40	40.0	40.2	40.3	40.3	40.2	40.6	40.2	40.3
45	44.9	45.2	45.3	45.4	45.3	45.5	45.2	45.3
50	50.0	50.2	50.3	50.5	50.3	50.6	50.3	50.3
55	55.0	55.2	55.2	55.3	55.2	55.5	55.2	55.2
60	60.0	60.1	60.3	60.4	60.2	60.5	60.1	60.2
65	65.0	65.0	65.1	65.5	65.2	65.7	65.3	65.3
70	70.0	70.0	70.2	70.4	70.2	70.5	70.2	70.2
75	75.1	75.1	75.2	75.4	75.1	75.4	75.2	75.2
80	80.1	80.1	80.4	80.2	80.1	80.5	80.2	80.2
85	85.1	85.0	85.5	85.3	85.3	85.4	85.1	85.2
90	90.0	90.1	90.7	90.4	90.1	90.5	90.2	90.3
95	95.1	95.2	94.9	95.3	95.2	95.4	95.3	95.2

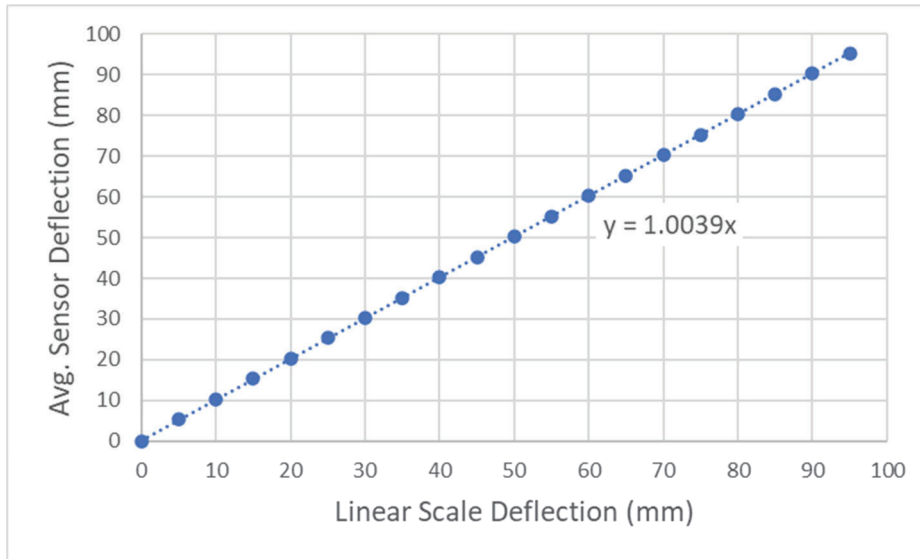


Figure 9. Static evaluation – average sensor deflection versus linear scale deflection.

The deflections as recorded by the sensors agree with the linear scale readings with an average difference of 0.268 mm over the 95 mm measurement range. Figure 9 indicates that over the full range, the sensor is on average 0.39% greater than the linear scale measurement.

Quasi-static Evaluation

The quasi-static tests were performed using a United Testing Systems universal test machine (United UTM) to evaluate the accuracy of the sensors when integrated into the ribcage. The ribcage was assembled onto the thoracic spine and the spine was rigidly mounted in the United UTM so that the spine curvature was in the design position (as it would be in the assembled LODC). The mounting fixture was also designed to position the thorax such that the loading axis of the United UTM can be aligned with the primary axis of a particular sensor (Figure 10).

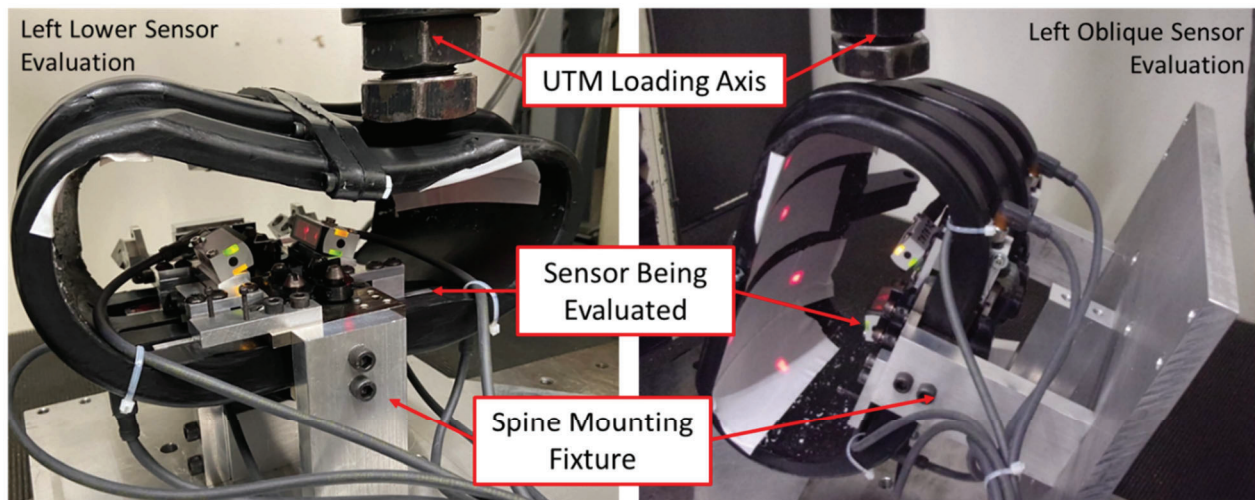


Figure 10. Quasi-static testing of lower left sensor (left image) and left oblique sensor (right image).

Each sensor was evaluated individually. The primary axis of the sensor being evaluated was aligned with the United UTM loading axis and the ribcage was then compressed to 10 mm, 20 mm and 30 mm. At each compression level, the sensor reading was recorded and a measurement of the sensor LED location on the inside surface of the ribcage was manually taken using a coordinate measuring machine (CMM) for comparison (Figure 11).

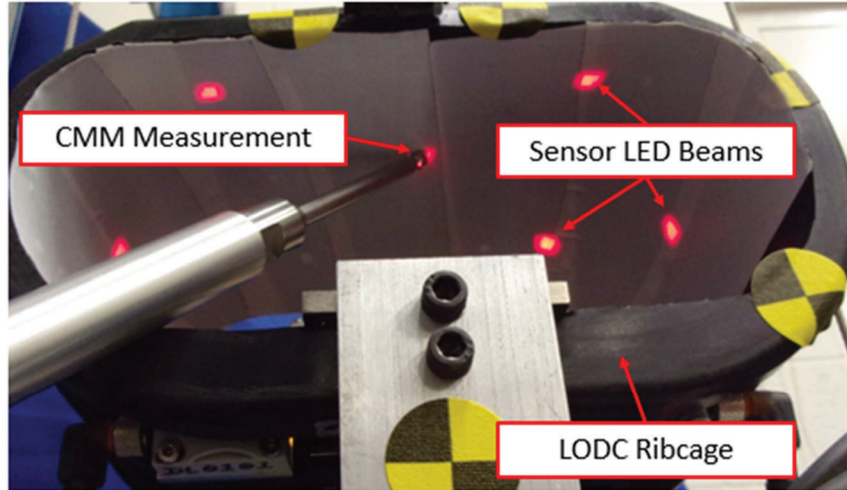


Figure 11. Sensor spot measurement using coordinate measuring probe.

Ribcage deflections at each of the United UTM compression levels were calculated from the sensor recordings and from the CMM measurements. Deflection results are summarized in Table 2.

Table 2.
Ribcage deflections from sensor recordings and CMM measurements at each compression level

Sensor Location	United UTM Deflection (mm)	Average Deflection (mm)		Sensor-CMM Difference	
		Sensor	CMM	(mm)	%
Center	10	9.7	10.0	0.33	3%
	20	19.5	19.9	0.43	2%
	30	29.5	29.9	0.41	1%
Left Upper	10	8.9	9.0	0.10	1%
	20	17.9	18.4	0.55	3%
	30	27.0	27.7	0.65	2%
Left Lower	10	9.7	10.1	0.40	4%
	20	19.9	20.3	0.40	2%
	30	30.5	31.1	0.66	2%
Left Oblique	10	8.7	8.8	0.12	1%
	20	17.1	17.3	0.20	1%
	30	25.8	26.0	0.26	1%

The results show good agreement between the deflections as measured by the sensors and by the CMM with percent differences less than 5% at each of the sensor locations. In a controlled, quasi-static environment, the multi-point deflection sensors can accurately track the interior ribcage deflections.

Dynamic Evaluation

Probe Impacts The LODC ribcage with the multi-point sensors installed was tested dynamically using a modified thorax qualification test setup. For this test the LODC was seated on a table with its flesh jacket, wetsuit, shoulders and arms removed. A fixed seatback was installed to prevent the LODC from sliding during the impact. Video captures from a test are shown in Figure 12. A probe impact to the LODC ribcage was performed at 4 m/s using the standard 6.99 kg LODC thorax qualification probe, which is equipped with an internally mounted accelerometer behind the front impact face. In addition to the multi-point deflection sensors, the LODC was also equipped with a T6 x-axis accelerometer to record motion of the spine during the test.

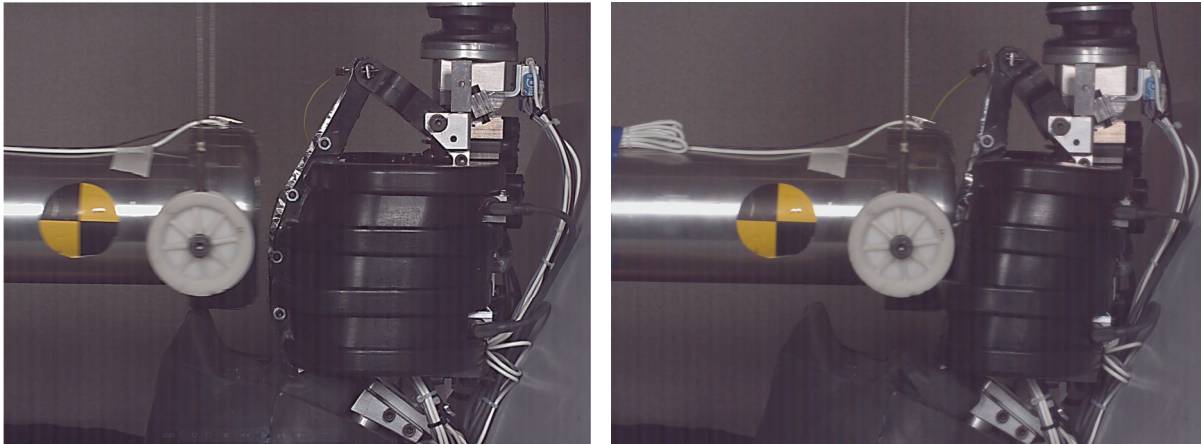


Figure 12. Thorax probe impact. Right picture shows time of maximum ribcage compression.

Internal ribcage deflections were calculated from each of the sensors during the impact event. Additionally, external ribcage deflection was calculated by subtracting the spine motion recorded by the T6-mounted accelerometer from the probe-mounted accelerometer and then double integrating that signal. Time histories of internal ribcage deflection as recorded by each of the sensors along with the calculated external deflection are shown in Figure 13. Unfortunately in this test, the right oblique sensor was not recorded as this sensor was out for calibration at the time of testing.

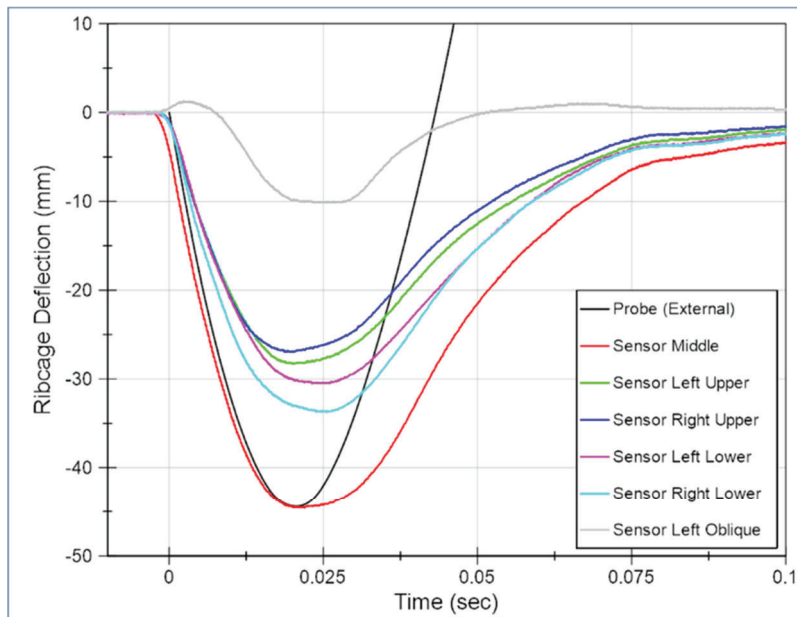


Figure 13. Ribcage deflection-time histories during a dynamic probe impact. Internal ribcage deflections are measured by the multi-point sensors. External ribcage deflection is calculated from the impact probe.

Although the LODC is not normally tested with a bare ribcage, dynamically impacting the LODC in this manner removes the effects of the flesh jacket and wetsuit to better evaluate the sensors. A direct impact to the ribcage can allow for the comparison of the internal deflection sensors with the external deflection as calculated by the impact probe. From the deflection-time histories in Figure 13, the midsternum or middle sensor deflection (red curve) shows good agreement with the calculated external deflection (black curve). The difference in duration between the probe-calculated deflection and the middle sensor is attributed to the test setup and calculation error in using the probe and T6 accelerations. Although a fixed seatback was used, soon after the ribcage reached maximum deflection, the thorax was observed to tilt backwards causing the probe and T6 mounted accelerometers to no longer

be in the same plane. This misalignment is why the calculated external deflection appears to rebound earlier than the ribcage sensors. The accelerometer from the probe can no longer track the actual ribcage position once the thorax begins to tilt, whereas the ribcage sensors can accurately track this position. This suggests that the sensors can accurately measure the internal deflection or motion of the ribcage throughout the loading phase of the event.

Additionally, the other internal deflection sensors were recorded (the right oblique sensor was not present) and show how the entire ribcage moves throughout the event. The midsternum or middle sensor (red curve) shows the largest deflection, which is understandable as this sensor is at the most forward part of the ribcage. The other four front-facing sensors (left and right lower, left and right upper) are grouped together with the lower sensors (magenta and cyan curves) showing slightly more deflection than the upper sensors (green and blue curves). The lower portion of the ribcage is unsupported unlike the upper portion of the ribcage, which is supported by a sternum bracket. The lack of support on the lower portion of the ribcage could explain the higher deflections of the lower sensors than the upper sensors. The left oblique sensor (grey curve) actually shows slight ribcage expansion (deflection in the positive direction) before compression. Although the right oblique sensor data was not available for this test (out for calibration), it can be expected to follow a similar pattern as the left oblique sensor since this impact was targeted at the center of the LODC.

An attempt was made to evaluate the LODC ribcage with the multi-point sensors in a similar test setup but in an oblique direction. However, it was difficult to prevent the motion of the thorax in this setup, so the ribcage with multi-point sensors was dynamically tested in the oblique direction using a drop tower instead.

Drop Tower The LODC ribcage with multi-point sensors was tested dynamically using a drop tower setup. The primary goal of this test condition was to examine how a full set of sensors would respond in an oblique loading scenario. The ribcage was mounted and positioned under a drop tower using the same mounting fixture used in the United UTM quasi-static test as shown in Figure 14.

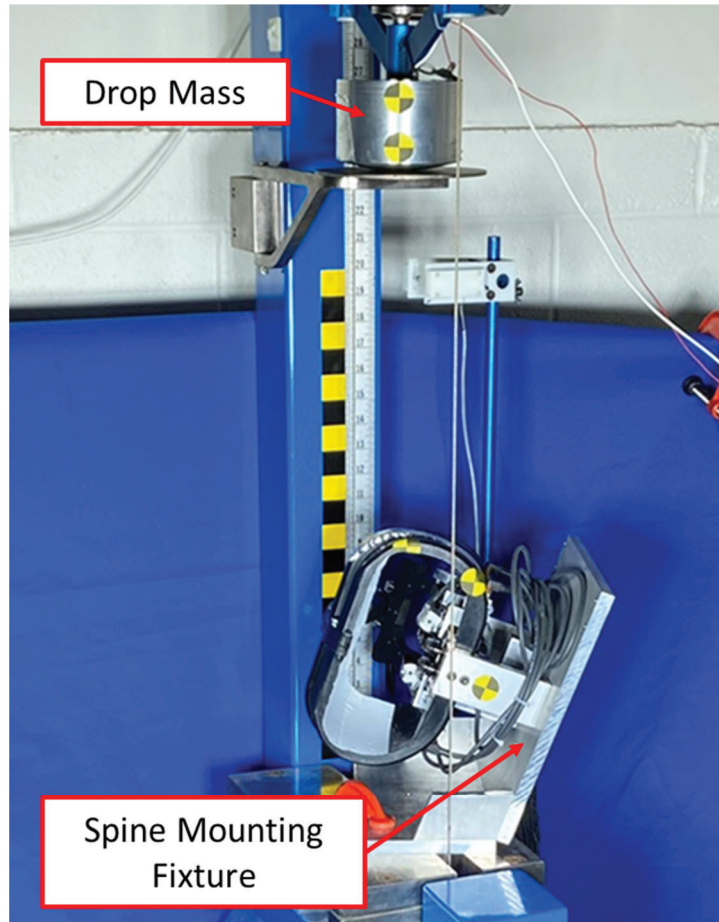


Figure 14. Drop tower test setup for evaluating the left oblique sensor.

Two tests were run using the drop tower as shown in Figure 15. For one test, a 1.86 kg mass was centered over the left oblique sensor and dropped at a velocity of 4 m/s. For the second test, the same mass was centered over the midsternum sensor and also dropped at a velocity of 4 m/s.

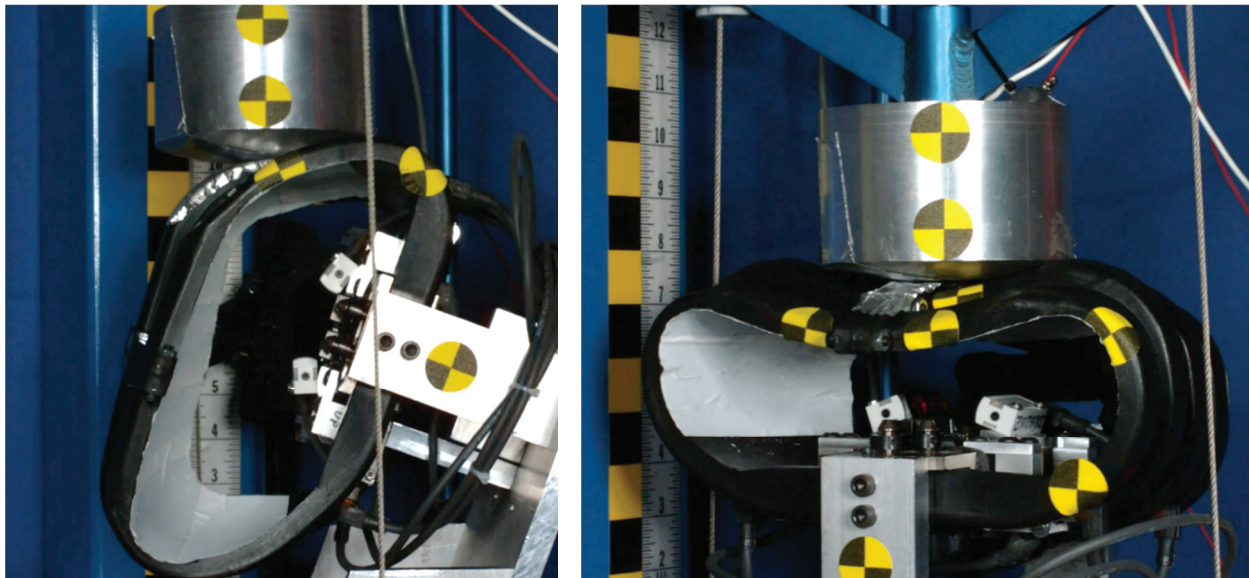


Figure 15. Drop tower testing of the left oblique sensor (left image) and midsternum sensor (right image).

Deflection-time histories for all sensors in the dynamic drop tower test aligned with the left oblique sensor are shown in Figure 16. As demonstrated earlier by the dynamic probe impact, this oblique drop tower test similarly shows how the entire ribcage moves and deflects throughout an oblique impact scenario. From the time history, there appear to be three groups of data traces. The left side of the ribcage was impacted in this test and the three left sensors (green, magenta and grey curves) show the greatest amount of deflection. The right front-facing (blue and cyan curves) and midsternum (red curve) sensors show the least amount of deflection and their data traces show slight ribcage expansion early in the event followed by ribcage compression. The right oblique sensor (orange curve), which was opposite of the impact side shows a large amount of ribcage expansion, which can also be observed in Figure 15 (left image).

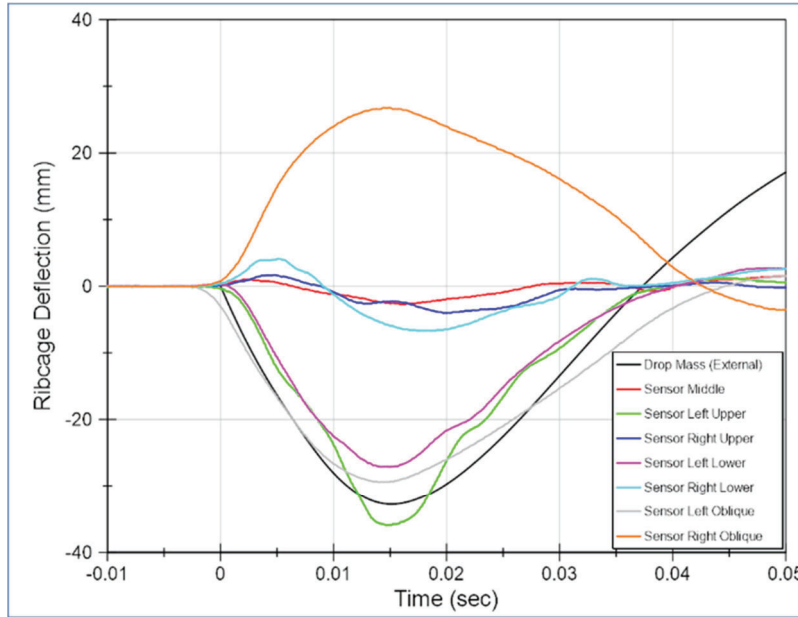


Figure 16. Deflection-time histories for all sensors in the drop tower test aligned with left oblique sensor.

Deflection-time histories for all sensors in the dynamic drop tower test aligned with the mid-sternum sensor are shown in Figure 17. The shape of the curves in this test are similar to those in the dynamic probe impact. The midsternum sensor (red curve) showed the greatest amount of deflection. The left lower (magenta curve) and right lower (cyan curve) sensors showed a greater amount of deflection than the left upper sensor (green curve), which is likely due to the lack of support at the bottom of the ribcage. The right upper sensor was out for calibration for this test, but it can be expected to follow a similar trend as the left upper sensor, as illustrated by the dynamic probe impact (Figure 13). The left oblique sensor (grey curve) and right oblique sensor (orange curve) similarly show the least amount of deflection and are characterized by ribcage expansion followed by compression, again similar to the dynamic probe impact.

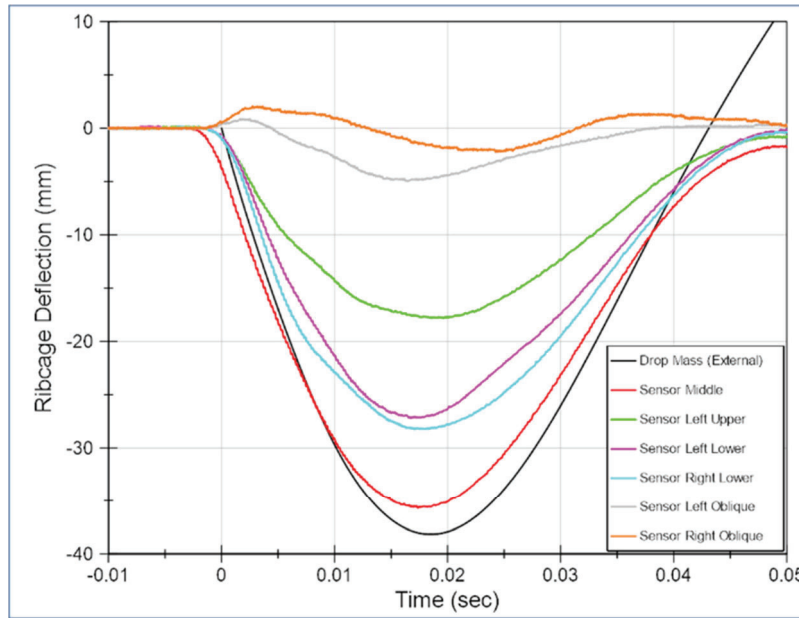


Figure 17. Deflection-time histories for all sensors in the drop tower test aligned with midsternum sensor.

The external drop mass deflections (black curves) show approximately 3-4 mm greater deflection than the sensors aligned with the impact: the left oblique sensor (grey curve in Figure 16) and the midsternum sensor (red curve in Figure 17). This is due to the rounded impact face of the drop mass used in this test. The rounded impact face allowed the drop mass to slide outward along the curvature of the ribcage and beyond peak ribcage deflection. This can be observed in Figure 15 (left image) where the centerline of the drop mass is no longer in line with the oblique sensor when the ribcage is at maximum deflection. As with the dynamic probe impact, the sensors were able to accurately measure the internal deflection and motion of the ribcage throughout the event.

Overall, the sensors performed well in dynamic impact scenarios as they agreed with externally measured deflections as well as provided a picture of how the ribcage deforms throughout a dynamic impact event.

CONCLUSIONS

A novel non-contact sensor array to measure LODC chest deformation has been developed. This system has gone through a battery of both static and dynamic tests thus far to evaluate the system's performance. Individual sensors were found to be quite accurate in static verification tests, and sensors installed in the LODC ribcage were also observed to match well with CMM measurements. In dynamic testing with the full array of sensors installed in the ribcage, LED deflection matched probe-measured deflection closely. In both frontal and oblique drop tower tests, individual sensor deflection time histories showed how the full array could capture full ribcage deformation. This feature will be beneficial when the LODC is used in sled or crash testing. Future work will include more dynamic testing to further understand how the system can describe three-dimensional ribcage deformation.

REFERENCES

- [1] Beck B, Bilston L, Kazzi M, Brown J. "Injury mechanisms in rear seated children aged 9-17 years and the implications for assessing rear seat protection in crash tests," *23rd Enhanced Safety of Vehicles Conference*, 2013, Paper No. 13-0392. Seoul, Korea.
- [2] Durbin D, et al. "Effects of seating position and appropriate restraint use on the risk of injury to children in motor vehicle crashes," *J Pediatrics*, 2005, 15:3.
- [3] Arbogast K, Locey C, Zonfrillo M. "Differences in thoracic injury causation patterns between seat belt restrained children and adults," *Annals of Advances in Automotive Medicine*, 2012, 56:213-221. Seattle, WA, USA.

- [4] Kent R, Lopez-Valdes F et al. "Characterization of the pediatric chest and abdomen using three post-mortem human subjects," 22nd *Enhanced Safety of Vehicles Conference*, 2011, Paper No. 11-0394. Washington, DC, USA.
- [5] Ouyang J, Zhao W, Xu Y, Chen W, Zhong S. "Thoracic impact testing of pediatric cadaveric subjects," *The Journal of Trauma*, 2006, 61(6):1492-1500.
- [6] Maltese M, Castner T et al. "Methods for determining pediatric thoracic force-deflection characteristics from cardiopulmonary resuscitation," *Stapp Car Crash Journal*, 2008, 52:83-105. San Antonio, TX, USA.
- [7] Stammen J, Suntay B, Moorhouse K, Carlson M, Kang YS. "The large omnidirectional child (LODC) ATD: Biofidelity comparison with the Hybrid III 10 year old," *Stapp Car Crash Journal*, 2016, 60:581-623. Washington, DC, USA.
- [8] Suntay B., Stammen J., Carlson M. "Abdominal and thoracic injury risk functions for the Large-Omnidirectional Child (LODC) ATD," Proceedings of the 2021 IRCOBI Conference, On-line, September 8-10, 2021.
- [9] Carlson M, Suntay B, Stammen J. "Development & evaluation of a new chest deflection measurement sensor for the Large Omnidirectional Child (LODC) ATD," *2020 SAE Government/Industry Meeting*.
- [10] García-España, J. and D. Durbin. "Injuries to belted older children in motor vehicle crashes," *Accident Analysis and Prevention*, 2008. 40(6): p. 2024-2028.

THE INFLUENCE OF THE REPRODUCIBILITY OF ANTHROPOMORPHIC TEST DEVICES ON INJURY RISK FUNCTIONS

Norbert Praxl

Christian Gehre

Partnership for Dummy Technology and Biomechanics

Germany

Paper Number 23-0278

ABSTRACT

The design of advanced ATD is moving towards being more human-like and therefore is more complex. More complexity generally leads to more degrees of freedom, the uncertainty of an ATD as a measurement tool rises. The uncertainty of a measurement tool is described by the repeatability and the reproducibility.

An ATD alone can only provide measurements. These measurements do not directly reveal the safety level of a vehicle in a crash test. By using a mathematical function, a so-called injury risk function, the ATD measurements can be related to injury risks. The injury risk is a measure to show how well a vehicle protects the occupant or vulnerable road user. The influence of a poor repeatability or reproducibility on the calculation of the injury risk is obvious. For a given measurement variability it is simple to check the associated risk variability by putting the values in the relevant injury risk function. Much less obvious is the effect of poor repeatability and reproducibility on the injury risk function itself. The injury risk function for an ATD is typically a combination of PMHS test results and matched ATD test results. This simple fact reveals that the repeatability as well as the reproducibility of an ATD can already influence the development of the injury risk function and not only the calculation of the injury risk.

This study aims to get a basic understanding how the measurement variability of ATD can influence the resulting injury risk function. The study uses data from real repeatability and reproducibility tests with the THOR-50M. For reasons of simplicity the study focuses on the influence of the reproducibility, that is, a perfect repeatability is assumed. Two theoretical PMHS data sets are used to study the reproducibility influence: one with current status data (left and right censored data) and one with exact data. In addition, two different methods for the mapping of ATD measurements onto PMHS results in the risk function development are deployed. This study shows that injury risk curves depend on ATD reproducibility. Current injury risk function development is only reliable with a good ATD reproducibility. Data of THOR-50M used in this study reveals that the current injury risk function development procedure should consider the reproducibility of the ATD.

The study used only one data set for the reproducibility of the ATD which limits the generality of the results. In addition only a theoretical and simple injury risk function was applied. More complex injury risk functions with additional co-variants or complex criteria may lead to diverging results. The general effect that the reproducibility is influencing the injury risk function is unaffected.

As reproducibility cannot be easily improved because of technical and practical reasons, a methodology needs to be developed that includes the effects of reproducibility in the calculation of injury risk curves.

INTRODUCTION

Modern Anthropomorphic Test Devices (ATDs) are getting increasingly more complex with more and more mechanical degrees of freedom. A mechanical system with more degrees of freedom typically gets less predictable. For the same reason ATDs with a higher complexity have the tendency to show more measurement uncertainty.

The assessment of vehicle safety is usually done by using an ATD in a prescribed crash test and a specific measurement or indicator, the so-called injury criterion (e.g., R_{max} , a injury criterion regarding thorax injuries). For each injury criterion value determined with an ATD there is an associated injury risk which is typically calculated with a specific function - the injury risk function (IRF). The smaller the calculated injury risk the better the safety rating of the vehicle. It is obvious that with a higher uncertainty of the injury criterion value the vehicle safety rating becomes less precise. Therefore, attention needs to be paid to a high precision of the injury criterion measurement of an ATD.

Regarding the measurement precision two components need to be distinguished: repeatability and reproducibility. With respect to ATDs the repeatability is the precision of measurements with one ATD whereas the reproducibility describes the measurement variance between two or more ATDs of the same type. More precisely the reproducibility is the difference between the mean injury criterion responses of two ATDs in repeated tests.

If two ATDs of the same make measure different criterion values in equal vehicle tests, the calculated risks will be different too - assumed the same injury risk function was used. Consequently, those two ATDs will lead to two different ratings of the vehicle safety. However, this obvious adverse result of a poor reproducibility isn't the only negative effect. The injury risk function itself depends on ATD measurements and thus might be influenced by the ATD reproducibility.

FUNDAMENTALS

Some basic knowledge about the principles of developing ATD injury risk functions are needed to be able to understand the implication of a poor reproducibility on the injury risk assessment with an ATD. An ATD can only provide measurements which are used to determine injury criterion values. These injury criterion values do not reveal the injury risk by itself. Only by relating the ATD injury criterion values to injury risks, an ATD can show the risk of injury. In the present paper relating the ATD injury criterion values to injury risks is called mapping. To apply the mapping each test must be performed at least with one PMHS (Post Mortem Human Subject) and one ATD in the exact same way. These kind of tests are often called matched pair tests. Mapping combines PMHS test results and matched ATD test results to build a ATD injury risk function. That is, an injury risk function that can be used with measurements from the same type of ATD that was used in the matched pair tests. To obtain a reliable injury risk function, the biomechanical tests are typically performed with many PMHS because the test responses of different PMHS of a population normally differ substantially. The matched ATD tests are mostly performed only with one or a very few different ATDs of the same type.

Mapping

The mapping of ATD injury criterion values to PMHS injury risks can be done in different ways. Basically, there are two fundamentally different mapping methods:

- mapping of ATD injury criterion values onto PMHS injury responses - further on called injury mapping.
- mapping of ATD injury criterion values onto PMHS injury criterion values - further on called criterion mapping.

The typical ATD injury risk function development process using injury mapping is (figure 1):

1. Perform biomechanical tests on a sample of PMHS.
2. Record the (binary) PMHS injury responses (e.g., injury severity \geq AIS3: yes or no).
3. Repeat the PMHS tests with an ATD.
4. Measure the ATD injury criterion values.
5. Calculate an ATD injury risk function using the ATD injury criterion values and the PMHS injury responses.

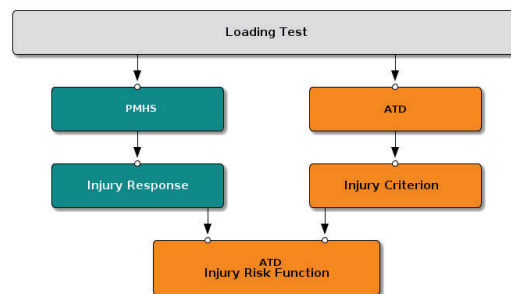


Figure 1: Typical ATD injury risk function development process using injury mapping. ATD injury criterion values are used together with the PMHS injury response to calculate an injury risk function for the ATD.

Criterion mapping is realised by using a so-called transfer function. The typical ATD injury risk function development process using criterion mapping is (figure 2):

1. Perform biomechanical tests on a sample of PMHS.
2. Record the (binary) PMHS injury responses (e.g., injury severity \geq AIS3: yes or no).
3. Measure the PMHS injury criterion values.
4. Calculate a PMHS injury risk function using the PMHS injury responses and PMHS injury criterion values.
5. Repeat the PMHS tests with an ATD.
6. Measure the ATD injury criterion values.
7. Calculate a transfer function to transform the ATD injury criterion values to PMHS injury criterion values (e.g., using a linear regression between PMHS and ATD injury criterion values).
8. Build the ATD injury risk function by using the transfer function inside of the PMHS injury risk function (i.e., substituting the PMHS criterion value by the transferred ATD criterion values).

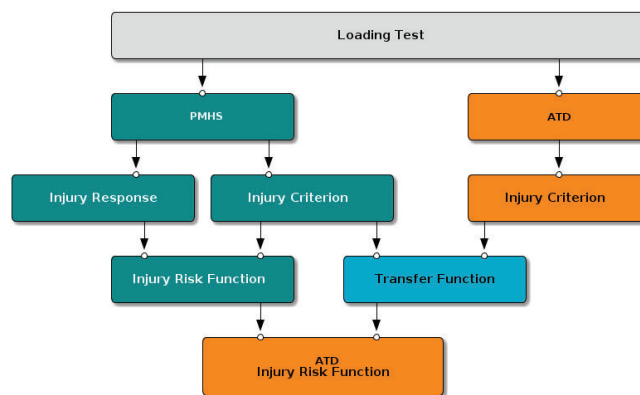


Figure 2: Typical ATD injury risk function development process using criterion mapping. ATD injury criterion values are converted to PMHS criterion values with a so-called transfer function to build the injury risk function for the ATD.

It's important to note that different mapping methods lead to different injury risk functions on principle. By using injury mapping, the injury risk function shows the injury risk of a random person with respect to an ATD injury criterion value. By using criterion mapping, the injury risk function shows the injury risk of a person with a mean injury criterion response with respect to an ATD criterion value. The following example illustrates the above statement about criterion mapping. An ATD measures a chest deflection of 10 mm in a sled test. According to the injury risk function - which was built by criterion mapping - this 10 mm chest deflection is associated with an injury risk of 20%. This does not imply that a random person in this sled test has an injury risk of 20%. It rather indicates that there is an injury risk of 20% for a person which has an average chest deflection response. Only a subgroup of all the people will have a 20% injury risk, those with an average chest deflection response. The reason for this is because the criterion mapping using a conventional transfer function maps the ATD injury criterion values to the average PMHS criterion values. With this approach an ATD injury criterion value is associated with an average PMHS injury criterion response and thus the ATD injury risk function shows the injury risk of a PMHS with an average injury criterion response.

It should be noted that there are more possibilities to transfer ATD injury criterion values to injury risks. The methods described above are the most frequently used ones.

Data Censoring

To relate ATD injury criterion values to injury risks, either by injury mapping or by criterion mapping, data from PMHS tests are indispensable. Without PMHS data it isn't possible to predict the risk of injury by ATD measurements. Especially the information about the injury response of a PMHS is indispensable. More precisely the onset of the injury in terms of an injury criterion needs to be known. This onset of the injury is the so-called biomechanical tolerance limit of a person and the distribution of biomechanical tolerance limits of a PMHS sample describes the injury risk function.

Unfortunately, the biomechanical tolerance limit often can't be measured directly in a biomechanical test because the injury criterion and the injury outcome are recorded independently at different times and can't be related exactly with a measured injury criterion value. This specific form of uncertainty about the actual biomechanical tolerance limit is called censoring. Biomechanical test data often is censored.

For the correct calculation of an injury risk function, it is important to know whether the injury criterion value was measured exactly at the onset of injury. If an injury was observed in a biomechanical loading test, the injury criterion value measured in this loading test exceeded the biomechanical tolerance limit of the test subject. However, often it's unknown how much the measured injury criterion value exceeded the biomechanical tolerance limit. Such data is called left censored data. If no injury was observed on the subject, the injury criterion value didn't exceed the biomechanical tolerance limit of this subject. If it's unknown how much lower the measured injury criterion value was compared to the biomechanical tolerance limit the data is called right censored data. If all data in a data set is either left or right censored, the data is called current status data. That is, the (binary) injury status of a PMHS at a measured injury criterion value is known. It is known if the subject has an injury of a prescribed severity or not but the injury criterion value at the onset of the injury - at the biomechanical tolerance limit - is unknown. If one individual was tested twice, one test without injury and a second test with injury. The interval in which the biomechanical tolerance limit is located is known. Such data is called interval censored data. In case the injury criterion value marks the onset of the injury the data is called exact data, data without any censoring. Figure 3 schematically shows all possible data censoring types.



Figure 3: Different types of data censoring.

OBJECTIVES

Injury risk functions which are used with ATDs are typically built by using ATD test results, more precisely by using injury criterion values determined from ATD measurements. Thus, the measurement uncertainty of an ATD is in principle able to influence the ATD injury risk function. This raises the question if this fact needs to be taken into account in the development process of injury risk functions for ATDs. As described above, the measurement uncertainty - the repeatability and reproducibility - of an ATD is interconnected with the injury risk function for the ATD. Thus, the repeatability and reproducibility of an ATD might affect its injury risk function such that the safety ratings based on tests with this ATD are unreliable.

This study is focused on the effect of the reproducibility on the injury risk function to get a better basic understanding of its influence on the injury risk function and aims to:

1. illustrate how the reproducibility of ATDs influence the resulting injury risk function,
2. elucidate the role of the injury risk function development method and data censoring, and
3. discuss the consequences of the results.

METHODS

This study is a theoretical study. All data are theoretical data except the reproducibility data of the ATD. The reason to use theoretical data was to be able to systematically manipulate characteristics of the data and observe the effect. The theoretical but realistic biomechanical test data were generated by simulating the PMHS sampling and all subsequent steps like they are performed in a real injury risk function development process. A data set resulting from this data generation process can be found in the appendix of the paper (table 3). Based on the simulated biomechanical test results an injury risk function can be calculated (all calculations have been performed with the statistical software R [1]). The resulting injury risk curve depends on the random PMHS sample - like in reality. On the left side of figure 4 this randomness of the injury risk curve is illustrated by presenting the injury risk curves from five different theoretical PMHS samples of the same sample size. On the right side of figure 4 the injury risk curve based on one PMHS sample and its underlying theoretical biomechanical test results are shown. Not only the randomness due to sampling of test subjects are replicated by the data generation process but also the variability of the injury criterion values with respect to different test subjects. PMHS test results are shown for each defined load case in figure 5. Eight load cases and ten PMHS per load case were utilised in the analyses. Four different variabilities of PMHS injury criterion responses were used to study its effect and called "No", "Low", "Mid", and "High" variability.

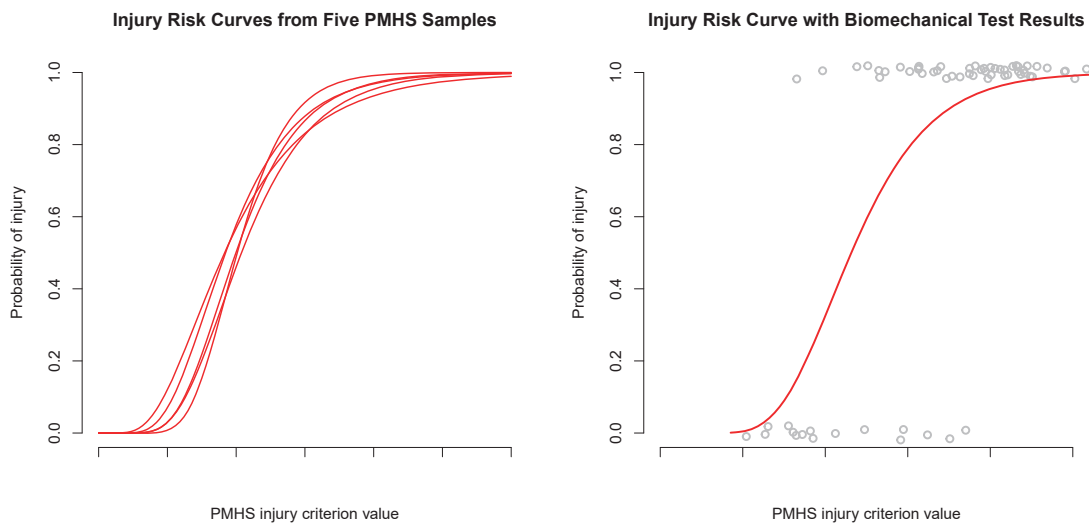


Figure 4: Left: Injury risk curves based on different theoretical PMHS samples (same sample size); right: Biomechanical test results and injury risk curve from one theoretical PMHS sample (points shown on top of the graph are injury cases, points at the bottom are non-injury cases).

Like the PMHS test data, the ATD injury criterion values are theoretical data. They are defined to represent the mean injury criterion response of the underlying PMHS population for each load case. The injury mapping was performed by using the eight ATD injury criterion values defined by the eight load cases with the censoring status of the eighty PMHS test results in a survival analysis. The criterion mapping was done by using a transfer function defined as the linear regression between ATD injury criterion values and PMHS injury criterion values. Figure 5 shows the linear regressions for the four different PMHS injury criterion variabilities.

With the procedures described above it is possible to generate realistic biomechanical test data, perform the mapping of ATD injury criterion values onto PMHS results, and calculate the ATD injury risk function. The theoretical

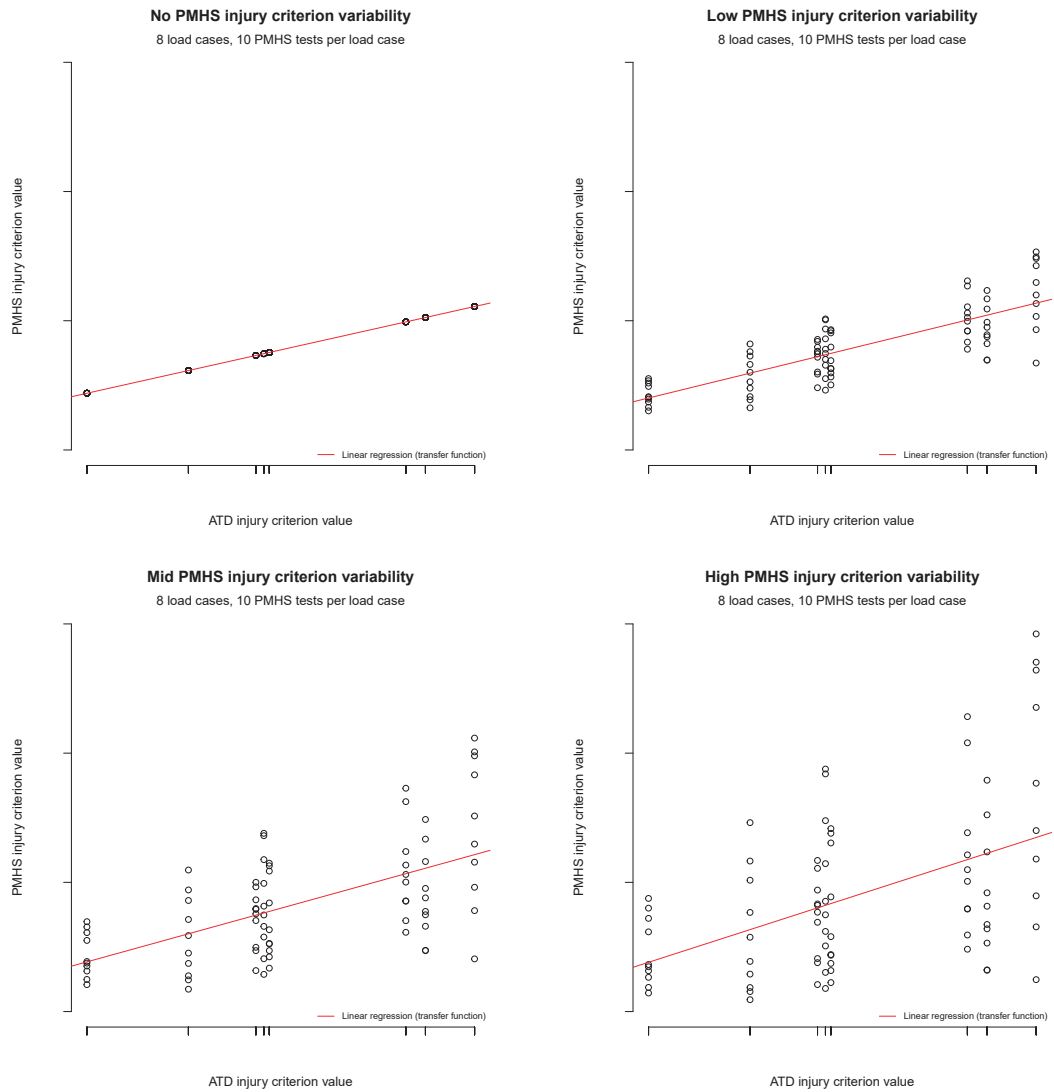


Figure 5: Four theoretical data sets with different PMHS injury criterion variabilities and the associated transfer functions.

PMHS and ATD test data is subsequently used to study the effect of the reproducibility of ATD measurements on the resulting ATD injury risk curve. Since this study focuses on the reproducibility of ATDs and for reasons of simplification a perfect repeatability is assumed. Simulated test data from one single ATD are used for the mapping between ATD and PMHS results.

To show the effect of ATD reproducibility on the resulting injury risk function two hypothetical ATDs were defined and used for the calculation of ATD injury risk functions. Although this is a theoretical study, realistic data regarding the ATD reproducibility are used for the definition of the two ATDs. The Partnership for Dummy Technology and Biomechanics performed so-called repeatability and reproducibility tests (R&R tests) with seven different 50th percentile male THOR dummies (THOR-50M) [2][3]. The same test was performed multiple times with each THOR-50M. Table 1 shows the number of repeated tests for each THOR-50M.

Table 1: Number of tests performed with each THOR-50M

ATD	Number of performed tests
THOR-50M A	3
THOR-50M B	3
THOR-50M C	6
THOR-50M D	3
THOR-50M E	3
THOR-50M F	5
THOR-50M G	6

The THOR-50M was a THOR-50M Standard Built Level B (SBL-B) with THOR-LX legs. The dummies were from two different manufacturers. The simplified vehicle-like test environment included a rigid seat, a rigid dashboard with deformable knee bolster, a deployed and pressurized airbag, and a 3-point belt with pre-tensioner and single-stage force limiter. The boundary conditions of the test were derived from a 0° degree full-width rigid wall test. The crash pulse was downscaled because of the rigid parts of the test environment. The positioning of the THOR-50M was done with high precision to avoid any influence of different dummy positions on the test outcome. Therefore, the variance in real vehicle crash tests might be higher. The repeatability and reproducibility data included a total of 29 test observations. For each test the injury criterion R_{\max} have been determined. From these data set the mean and standard deviation of the mean R_{\max} values of the seven ATDs are used to define a Normal distribution. Based on this Normal distribution a hypothetical ATD with a two standard deviations higher than the mean injury criterion measurement was defined and called ATD-HIGH. A second hypothetical ATD called ATD-LOW was defined by a two standard deviations lower than the mean injury criterion measurement. According to the so-called empirical rule (equation (1)) these two hypothetical ATDs contain ninety five percent of all ATDs with respect to the R_{\max} measurement. Therefore, the comparison of ATD-HIGH and ATD-LOW represents a reasonable spread in regards of the reproducibility but at the same time is not the worst case. The left graph in figure 6 schematically depicts the definition of the two theoretical ATDs with respect to the distribution of the average injury criterion measurements of different ATDs.

$$P(\mu - 2\sigma \leq X \leq \mu + 2\sigma) \approx 95\% \quad (1)$$

The approach to get theoretical but realistic injury risk functions as described above is only valid for current status data. Exact data is measured at the onset of the injury and represents the biomechanical tolerance limit of the PMHS. Thus, every test response is an injury case (with an injury of a certain severity). Dynamic ATD tests in which the ATD injury criterion value is determined independent of the injury onset of the PMHS can't be used for injury mapping with exact biomechanical test data. For each load case there is one ATD injury criterion value which must be mapped to some matched PMHS responses and those are all injury cases. Thus, the distribution of the ATD injury criterion values determines the injury risk function. However, the ATD injury criterion values are independent of the biomechanical tolerance limits of the PMHS. So there is no meaningful relationship between the ATD injury risk function and the PMHS injury risk. For this reason injury mapping with exact data isn't possible. To perform criterion mapping with exact data, ATD injury criterion values are needed that are linked to PMHS injury criterion values. With these data a transfer function can be calculated and used to transfer the PMHS injury risk function into a ATD injury risk function. The only difference to criterion mapping with current status data is that the PMHS injury risk function is built with exact data. The ATD to PMHS mapping is equal for current status data and exact data. For that reason it is not

necessary to study the effect of ATD reproducibility with exact data separately.

It has to be emphasised that the results of the simulation study are used to illustrate the effect of ATD reproducibility on the ATD injury risk function by way of example. The used method leads to realistic but not real data and is based on some unproven assumptions, for example the variability of PMHS injury criterion values with respect to a load case. Thus, the results and conclusions can't be generalised and might not fit to other data. Different and especially more complex injury criteria, the consideration of the ATD repeatability, and the use of covariates in the injury risk function might lead to other conclusions. To prevent an over-interpretation of the results all diagrams are without values.

RESULTS

The evaluation of the mean R_{max} values of the seven THOR-50M revealed that in this specific test data sample a ATD-LOW would measure 15% lower R_{max} values than a ATD-HIGH if they are defined as described in the methods section (right graph of figure 6). Based on this result from real THOR-50M R&R tests the injury criterion values of ATD-LOW were defined to be 15% lower than the injury criterion values of ATD-HIGH. In this example the 15% difference in injury criterion values corresponds to a difference between the mean plus two standard deviations and the mean minus two standard deviations (left and right graph of figure 6). For other injury criteria or other data samples a difference of ± 2 standard deviations from the mean might be higher or lower than 15%.

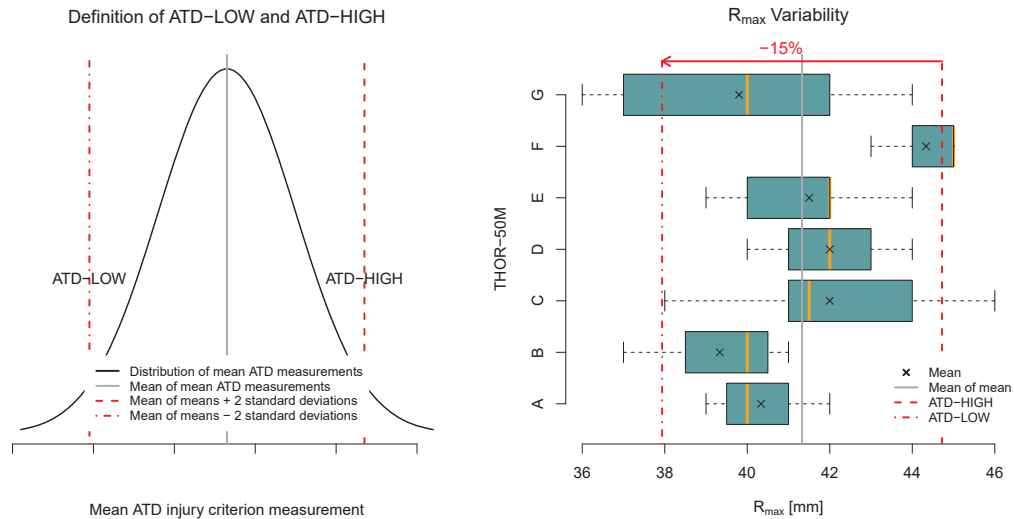


Figure 6: Left: Generic definition of ATD-LOW and ATD-HIGH; right: Distribution of R_{max} criterion values of seven THOR-50M dummies and the calculated mean R_{max} values of ATD-LOW and ATD-HIGH.

Before presenting the results regarding the main objectives of the study, more general results from the simulated injury risk function development are shown in figure 7 and 8. Figure 7 demonstrates that an ATD injury risk curve in principle depends on the method used to map ATD measurements to PMHS results. This result is in line with the theoretical considerations presented earlier in this paper. The actual difference between injury risk curves built with different mapping methods depends on the PMHS injury criterion variability as demonstrated in figure 7. Only if the injury criterion values of different PMHS do not vary in the same load case both mapping methods result in the same injury risk function (upper left plot of figure 7). However, it seems unrealistic that PMHS injury criterion values do not vary between different subjects. The difference between ATD injury risk curves built with different mapping methods do not only depend on the PMHS injury criterion variability but also on the actual PMHS sample as the results shown in figure 8 reveal.

With these general findings about factors of influence regarding the ATD injury risk curves the main objective of the current study, namely the influence of ATD reproducibility on the ATD injury risk function, can be addressed. As described in the methods section, two ATDs have been defined with different mean injury criterion responses. Using the same biomechanical test data with the results from these two ATDs leads to two different ATD injury risk

functions. Figure 9 shows the ATD injury risk functions built with the injury criterion values of ATD-HIGH and ATD-LOW. The risks are higher with the injury risk curve based on ATD-LOW compared to the risks for ATD-HIGH. No matter if the PMHS injury criterion values of the PMHS sample possess "no", "low", "mid", or "high" variability the injury risk curve built with the ATD-LOW is located left of the injury risk function based on ATD-HIGH (figure 9). Furthermore, the injury risk curves of ATD-LOW and ATD-HIGH are equally affected by the mapping method. The difference between the injury risk curves of ATD-LOW and ATD-HIGH is independent of the actual PMHS sample used in the development of the ATD injury risk curve (figure 10) and is as big as the difference between ATD-LOW and ATD-HIGH injury criterion measurements (figure 11).

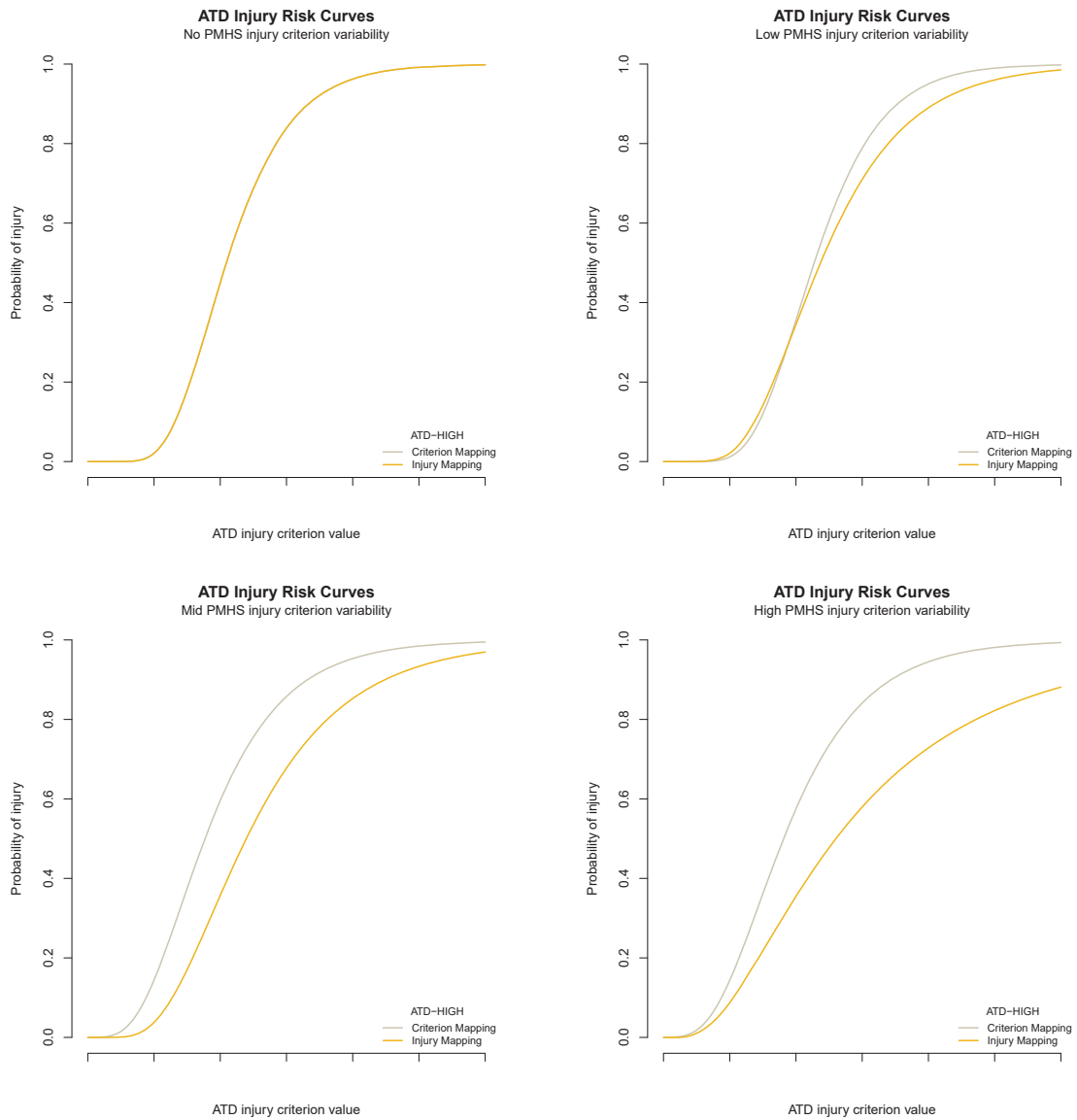


Figure 7: Influence of different mapping methods and different PMHS criterion variabilities on the ATD injury risk curve. All curves are based on one PMHS sample.

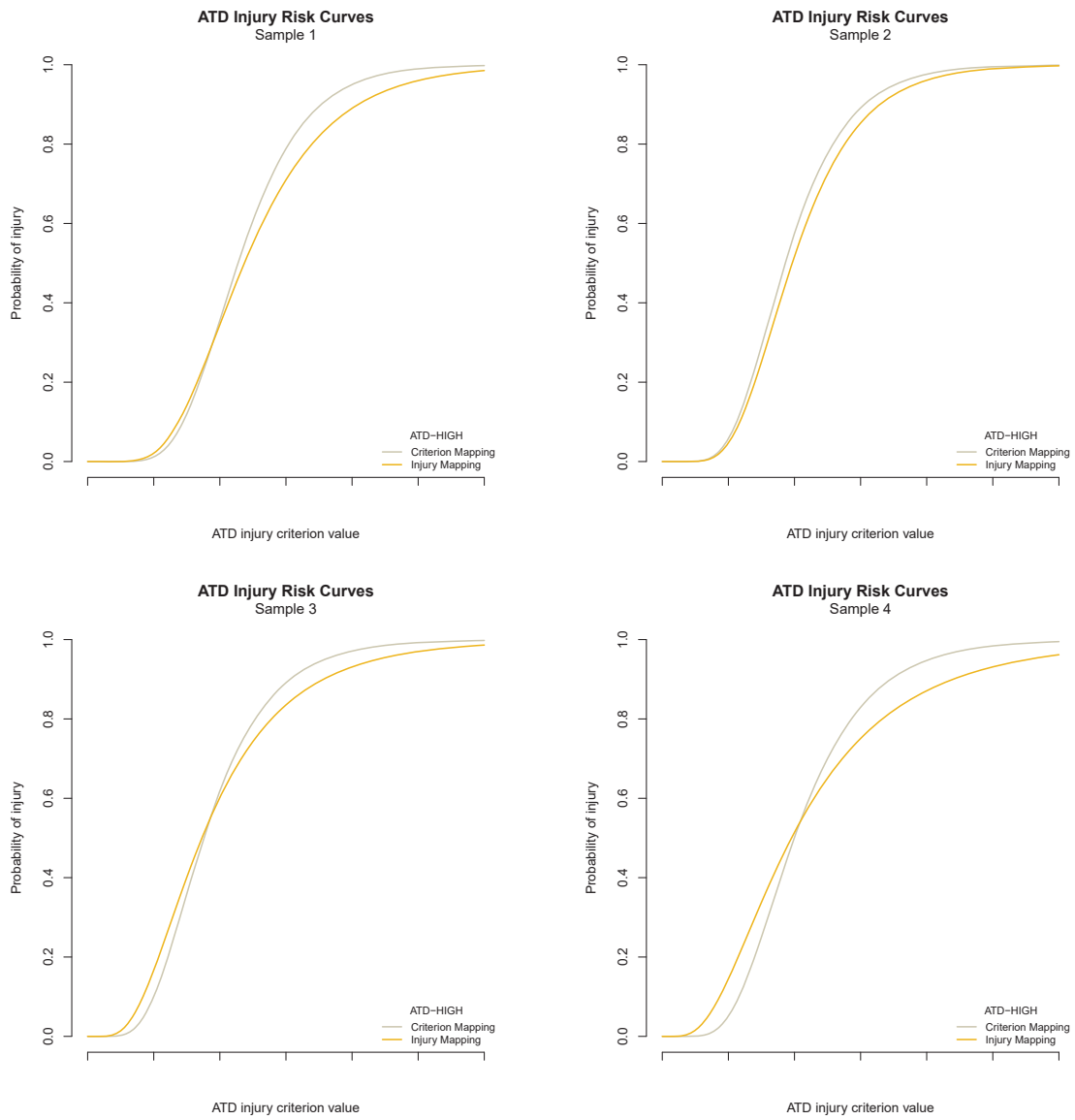


Figure 8: Effect of different PMHS samples on the ATD injury risk curves built with different mapping methods. All curves are based on mid PMHS injury criterion variability.

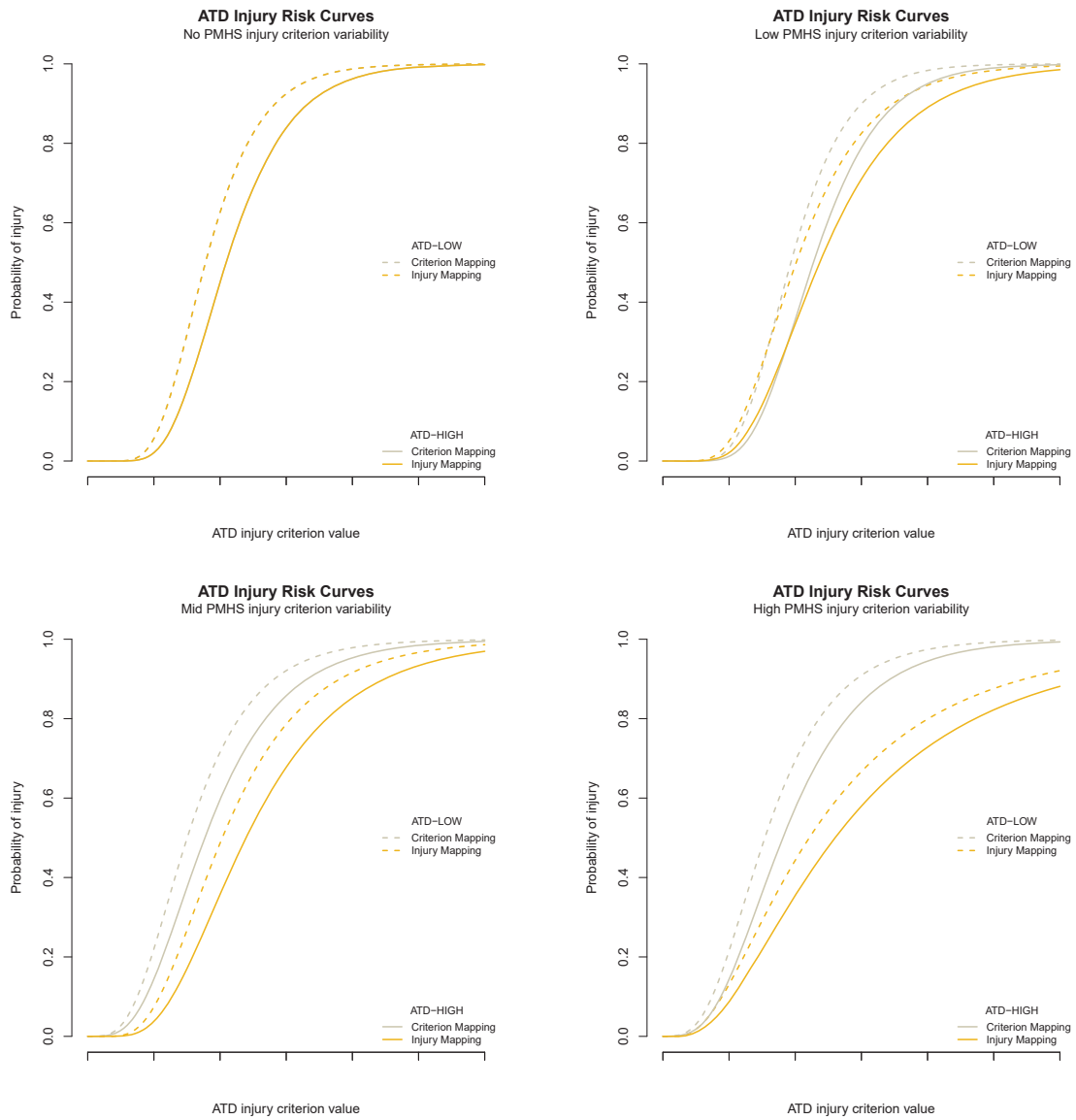


Figure 9: Comparison of injury risk curves based on ATD-LOW and ATD-HIGH injury criterion measurements. The injury risk curves are shown for different mapping methods and different variability of injury criterion values. All curves are based on one PMHS sample.

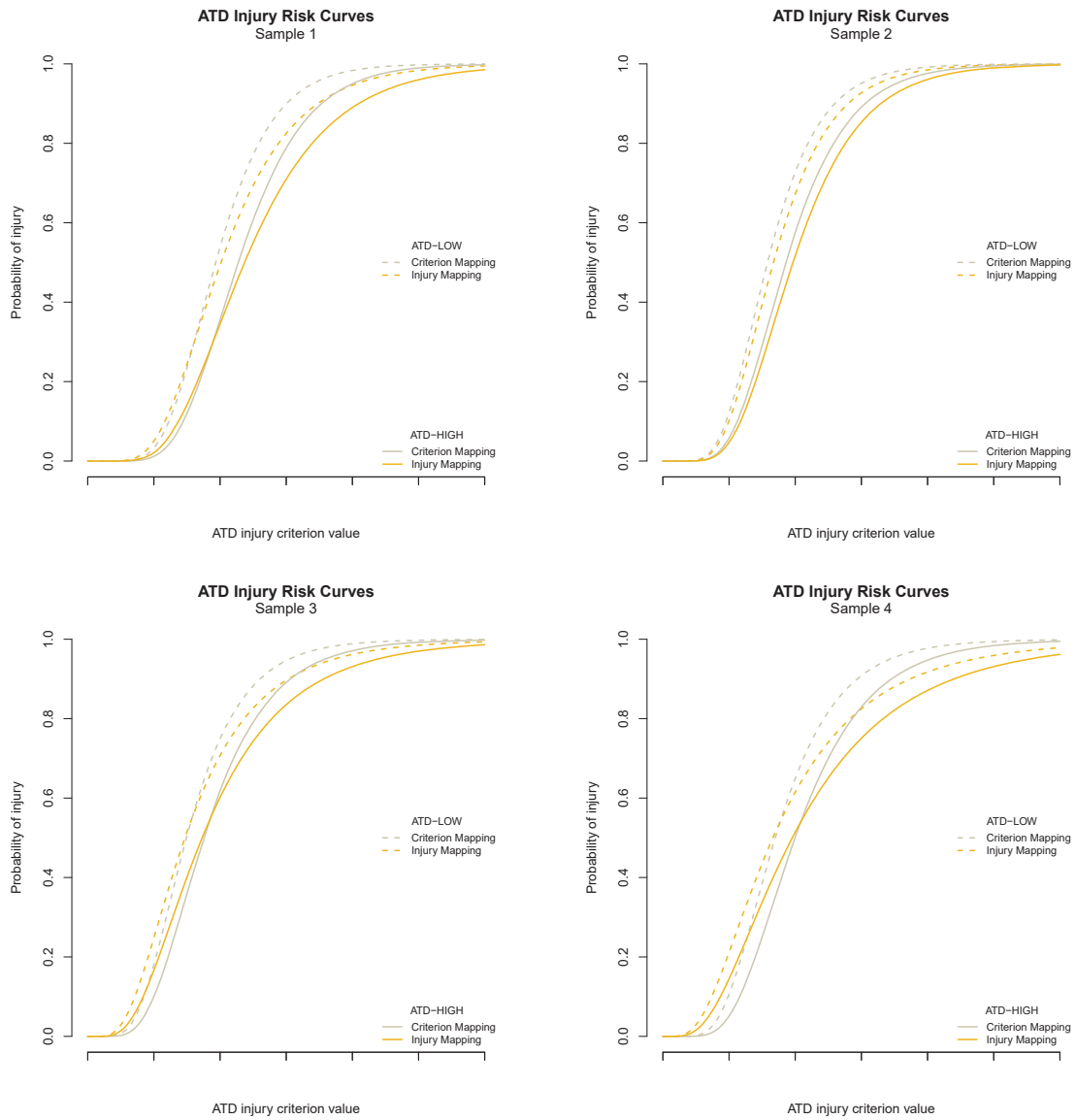


Figure 10: Comparison of injury risk curves based on ATD-LOW and ATD-HIGH injury criterion measurements. The injury risk curves are shown for different mapping methods and different PMHS samples. All curves are based on mid PMHS injury criterion variability.

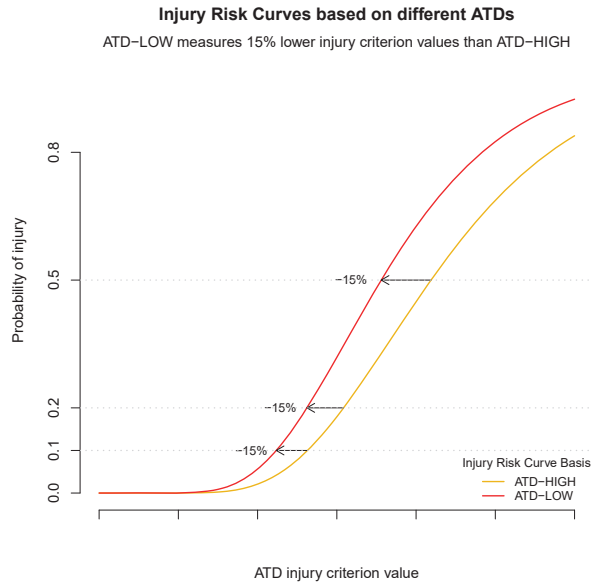


Figure 11: Shift of the ATD injury risk curve when built on basis of an ATD which measures 15% lower injury criterion values.

CONCLUSIONS

From the results of this study it can be concluded that a poor reproducibility of a specific ATD type will affect the resulting ATD injury risk curve which is in line with previous findings [4]. More precisely, an ATD injury risk function directly depends on the actual ATD which was used for the mapping of the ATD injury criterion values onto the PMHS test results. Different ATDs of specific type with poor reproducibility will lead to different injury risk functions. Characteristics of the PMHS sample, like the distribution of the biomechanical tolerance limit and the injury criterion variability in relation to a given load, do not change the effect of the poor reproducibility on the resulting injury risk curve. The same applies to the mapping method, it doesn't influence the effect of a poor reproducibility. Thus, a poor reproducibility can't be compensated by changing the biomechanical test data or the method of injury risk function development. The influence of a poor reproducibility on the ATD injury risk function can only be solved on the ATD side, not on the PMHS test side.

The main problem of a poor reproducibility of ATD injury criterion values is depicted in figure 12. If the injury risk curve was built with ATD-LOW but ATD-HIGH is used in a vehicle crash test then the calculated injury risks are higher than the biomechanical test data would actually indicate. Thus, the injury risk assessment is distorted and can lead to misleading conclusions about the safety rating of a vehicle. The extent of the distortion due to a poor reproducibility isn't known in reality. Solely because of the theoretical approach used in this study the distortion could be determined. In real vehicle crash tests, it is not known whether the ATD used corresponds to an ATD-LOW or an ATD-HIGH. Furthermore, it is not known how the ATD used in the crash test relates to the ATD used in the development of the injury risk function. The reason for this is not only that it is not known whether an ATD-LOW or an ATD-HIGH was used in the crash test, but also that it is not known which ATD was used in the development of the injury risk function. The certification of an ATD doesn't comprise such kind of information. Currently the implication of a poor ATD reproducibility on the safety rating of a vehicle is neither known nor addressed. To date no comprehensive knowledge about this potential problem is available and in-depth analyses of the implications of the ATD reproducibility are essential to understand the extent of the issue.

Due to the missing knowledge about the impact of the ATD reproducibility on injury risk functions only very general recommendations can be given to minimise a potential negative influence of a poor reproducibility on vehicle safety ratings. Selecting an injury criterion for a vehicle safety assessment not only its biomechanical performance needs to be considered but also its reproducibility with the utilised ATD. To reduce the probability of a significant distortion in the vehicle safety assessment as many ATDs as feasible should be used to determine the ATD injury risk

function. Another general approach to limit the extent of the problem is to use a ATD with mean injury criterion measurements within the whole population of ATDs of the same type. However, this approach requires a thorough assessment of the repeatability and reproducibility of the ATD type in question.

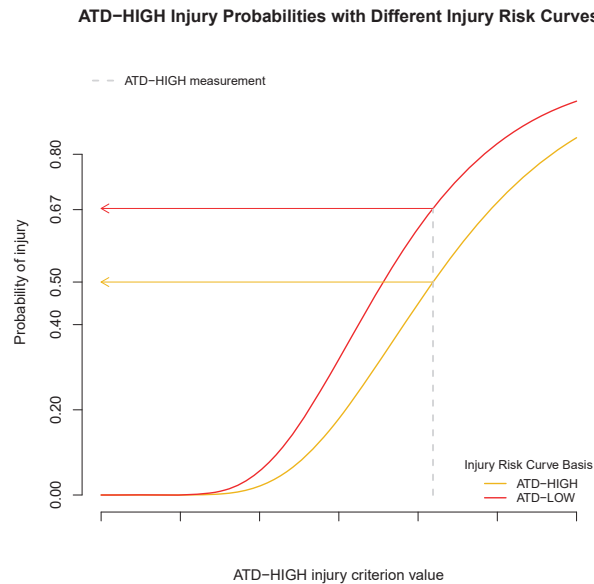


Figure 12: ATD-HIGH injury probabilities calculated with injury risk curves based on ATD-HIGH and ATD-LOW.

Limitations

This study has some limitations that need to be acknowledged. Firstly, no analytical universal prove is presented for the conclusions. All conclusions are based on theoretical simulation results based on artificial, albeit realistic, data. These data are dependent on specific assumptions which are non-verifiable. Secondly, only a theoretical and simple injury risk function was applied in the analyses and more complex injury risk functions with additional covariate may lead to diverging results. More complex injury criteria may also show diverging results. Thirdly, the repeatability of the ATDs wasn't considered. And last but not least only a low number of repeated ATD tests have been performed in the R&R study.

REFERENCES

1. R Core Team (2013). *R: A language and environment for statistical computing*. R Foundation for Statistical Computing, Vienna, Austria. ISBN 3-900051-07-0.
2. Gehre C. (26.-27. Sept. 2019). *THOR 50M – R&R compared to current consumer rating schemes* [Conference presentation]. Humanetics Europe Crash Meeting 2019, Wiesloch, Germany.
3. Gehre C. (2019). *THOR 50M – R&R compared to current consumer rating schemes*. ISO TC 22 SC36 WG5 N1210.
4. Praxl N. (2019). *Influence of THOR Measurement Variability on Injury Risk Assessment*. ISO TC 22 SC36 WG6 N1211.

APPENDIX

Table 2: PDB R&R data

dummy	test	rmax
dummyA	1	39
dummyA	2	40
dummyA	3	42
dummyB	1	40
dummyB	2	37
dummyB	3	41
dummyC	1	44
dummyC	2	46
dummyC	3	41
dummyC	4	41
dummyC	5	38
dummyC	6	42
dummyD	1	44
dummyD	2	42
dummyD	3	40
dummyE	1	42
dummyE	2	42
dummyE	3	44
dummyE	4	42
dummyE	5	39
dummyE	6	40
dummyF	1	45
dummyF	2	45
dummyF	4	43
dummyG	1	44
dummyG	2	37
dummyG	3	36
dummyG	6	40
dummyG	7	42

Table 3: Generated artificial current status biomechanical test data [load: load expressed as injury criterion values (= ATD measurement), btl: biomechanical tolerance limit, crit.pmhs: injury criterion value measured on the PMHS, cens: censoring status (0: right censored, 2: left censored)]

load	btl	crit.pmhs	cens
3773	2785	3538	2
3773	9194	4438	0
3773	2176	4276	2
3773	2421	4390	2
3773	4780	4695	0
3773	2786	4018	2
3773	1994	3559	2
3773	5402	3717	0

Continued on next page

Continued from previous page

load	btl	crit.pmhs	cens
3773	4997	3761	0
3773	2965	3865	2
2194	2958	2439	0
2194	3836	2535	0
2194	3660	2458	0
2194	3703	1752	0
2194	7779	1774	0
2194	1213	1576	2
2194	4308	1538	0
2194	5810	2342	0
2194	5658	1607	0
2194	1488	2289	2
3657	8581	3325	0
3657	2219	4438	2
3657	1973	5360	2
3657	1392	4268	2
3657	4630	2415	0
3657	4553	6870	2
3657	5438	4792	0
3657	3864	4002	2
3657	5442	3669	0
3657	3085	3215	2
3726	2384	2864	2
3726	5033	4681	0
3726	1880	3274	2
3726	7189	4768	0
3726	6472	3611	0
3726	4539	4972	2
3726	1861	3553	2
3726	7675	3446	0
3726	4574	4424	0
3726	2554	3804	2
5550	5520	6713	2
5550	2649	6407	2
5550	2306	6086	2
5550	2861	4341	2
5550	3813	5726	2
5550	2543	4498	2
5550	4461	4780	2
5550	4076	4940	2
5550	4131	5627	2
5550	4571	6105	2
3073	3296	2076	0
3073	9246	2156	0
3073	6468	4139	0
3073	4951	2533	0
3073	3570	2903	0
3073	4564	4840	2
3073	3300	4162	2
3073	3762	3170	0

Continued on next page

Continued from previous page

load	btl	crit.pmhs	cens
3073	3996	3643	0
3073	3853	3122	0
5125	6081	4988	0
5125	2307	6254	2
5125	8046	5383	0
5125	2785	5783	2
5125	6388	4784	0
5125	2409	5242	2
5125	4329	3434	0
5125	2236	6196	2
5125	3464	3924	2
5125	3339	6536	2
4955	3711	6752	2
4955	2646	6784	2
4955	6037	6091	2
4955	2465	4718	2
4955	4594	7429	2
4955	2904	3612	2
4955	8881	5543	0
4955	3534	7002	2
4955	3207	2851	0
4955	5852	3306	0

INVESTIGATION OF THE BIOFIDELITY OF HUMAN BODY MODELS AND ATD MODELS IN SLED TEST CONDITIONS

Autonomous Vehicle Occupant Safety Consortium

AVOS

Paper Number 23-0288

ABSTRACT

Unique cabin configurations associated with Automated Driving System (ADS) equipped vehicles offer seating options, such as recline, not previously available in conventional vehicles. Occupants seated in a reclined posture may be at an increased risk of submarining. There is relatively little known about the effectiveness of current restraint systems to protect reclined occupants as these systems are traditionally optimized for only upright seated postures. Anthropomorphic Testing Devices (ATDs) with the ability to differentiate between submarining and non-submarining events are vital for the development of restraint systems capable of protecting reclined occupants. This study evaluates the biofidelity of the GHBM, THUMS, THOR, and THOR-AV finite element (FE) occupant models against two post-mortem human subject (PMHS) test series in respect of submarining behavior. The first test series evaluated upright occupant kinematics in two seat configurations defined in Uriot et al. 2015: a front-seat configuration expected to prevent submarining and a rear-seat configuration expected to allow for submarining. The second test series evaluated upright and reclined occupant kinematics in a seat configuration as defined in UMTRI test conditions: both configurations expected to prevent submarining. Special consideration was given to pelvis kinematics and submarining response. The four FE occupant models properly differentiated between non-submarining and submarining responses in each of the evaluated test conditions. The NHTSA Biofidelity Ranking System (BRS) was used to objectively evaluate the biofidelity of the models with respect to overall occupant kinematics, as well as interaction with the restraint system (seat, anti-sub ramp, and belts). The BioRank score classifies biofidelity as *excellent*, *good*, *marginal*, or *poor*. In the first test series, the BRS scores for the interaction between all FE occupants and the restraint system corresponded to *good* biofidelity, except for THOR in the rear-seat submarining configuration (*marginal* biofidelity). In the second test series, the BRS scores for the interaction between the FE occupants and the restraint system corresponded to *marginal* biofidelity. With respect to kinematics, the BRS scores for the FE occupants ranged from *good* to *excellent* biofidelity in both test series. For each FE occupant, an average BRS score was calculated from the four test conditions. In terms of the interaction between the occupant and the restraint system, the average BRS scores for the GHBM, THUMS, and THOR-AV corresponded to *good* biofidelity, while the average BRS score for the THOR corresponded to *marginal* biofidelity. With respect to kinematics, the GHBM, THUMS, THOR, and THOR-AV FE models demonstrated good biofidelity.

INTRODUCTION

ADS-equipped vehicles offer seating options for occupants not previously available in conventional vehicles, including traditional upright or recline, forward or rearward facing, or a combination of these seated postures. Occupants seated in a reclined posture may be at an increased risk of submarining as the restraint system may not have been designed with this posture considered. There is relatively little known about the effectiveness of current restraint systems to protect the reclined occupants as these systems are traditionally optimized for only upright seated postures. ATDs with the ability to differentiate between submarining and non-submarining events are vital for the development of restraint systems capable of protecting reclined occupants.

Occupant submarining has been studied over the past few decades [1]-[8]. Submarining can be defined as lap belt disengagement with the human pelvis due to slipping of the lap belt over the anterior superior iliac spine (ASIS). Submarining increases the risk of abdominal injuries due to direct loading of the lap belt to the abdomen and increases the risk of lower extremity injuries due to increased forward pelvic excursion resulting in impact of the knee with the bolster or frontal panel. Leung et al. [1] compared the Hybrid II dummy pelvis geometry with anthropometry data from pelvis bone X-rays of 28 volunteers. It was found that the Hybrid II dummy has a greater tendency to submarine than a human subject (80% for the dummy vs. 40% for the cadaver in similar tests). Leung et al. noted that the direction

and the length of sartorius were critical parameters that influenced the submarining responses of the dummy. The “sartorius” refers to the line between the ASIS and the notch between the ASIS and anterior inferior iliac spine (AIIS). The authors suggested a revision to the Hybrid II dummy pelvic bone to represent the sartorius to improve its submarining response.

Uriot et al. [2] conducted sled tests to compare the interaction between the pelvis and the lap belt for both dummies and post-mortem human subjects (PMHSs). The test setup was designed to mimic the conditions in a frontal car crash environment. The study found that the belt angle relative to the pelvis was greater for the pelvis of dummies evaluated than for those of PMHS. In 2015, Uriot et al. [3] investigated the pelvis behavior and submarining with a semi-rigid seat in sled test conditions. The semi-rigid seat had springs built in the seat pan and the anti-submarining plate. The spring stiffness for both the seat pan and anti-submarining plate can be adjusted to mimic the front- and rear-seat stiffness of a small size passenger vehicle. The PMHS did not submarine in the front-seat configuration and did not experience pelvis fractures, while the PMHS did submarine in the rear-seat configuration and did experience pelvic fractures.

Richardson et al. [4][5] studied the kinematics of the 50th percentile male PMHS in a reclined seat configuration with a nominal recline angle of 50°. The restraint system included double lap belt pre-tensioners, a shoulder belt pretensioner, a 3.5 kN shoulder belt load limiter, and a crash locking tongue. The study focused on kinematics of the pelvis, spine, and head. Four of the five PMHSs did not submarine, while one of the PMHSs experienced submarining on the inboard side. In two of the tests, the PMHSs experienced iliac wing fractures near the ASIS area where the PMHS interacted with the lap belt.

In 2019, Gepner et al. [6] compared the responses of the Global Human Body Model Consortium simplified model (GHBMC-S v1.8.4) and detailed models (GHBMC-D v4.5), and the Total Human Model for Safety (THUMS v5) in a reclined setup which served as the basis for the Richardson et al. PMHS tests [4][5]. All of these HBMs showed good pelvis engagement with the lap belt, however the GHBMC-D still submarined. In addition, large differences were observed in the pelvis and lumbar spine responses between the GHBMC and THUMS models. At the time, no PMHS test data were available to make any comparison or judge which model represents the human occupant better.

Mroz et al. [7] evaluated the effects of seat and seat belt characteristics on lumbar spine and pelvis loading with the SAFER Human Body Model (HBM) in reclined postures. The SAFER HBM responses were compared with PMHS responses using the same test condition. The HBM head, T1, T8, T11, L1, L3, and pelvis excursion, pelvis rotation, and belt forces correlated well with the PMHS results. Östth et al. [8] investigated the feasibility of restoring the occupant from reclined posture to upright during the pre-crash event with SAFER HBM. The transition could be achieved by the inertia of the occupant during pre-braking, as well as by moving the seatback. However, the occupant submarined as the pelvis did not fully return to the upright posture due to the flexibility of the lumbar spine.

Wang et al. evaluated THOR-AV in front-seat and rear-seat configurations as defined in Uriot et al. [3][10] and the upright and reclined seat configurations as defined by the University of Michigan Transportation Research Institute (UMTRI) Automated Vehicle Occupant Kinematics (AVOK) project against the corresponding PMHS test results [11]. The THOR-AV dummy kinematics demonstrated *good to excellent* biofidelity according to National Highway Traffic Safety Administration’s (NHTSA) biofidelity ranking method (BioRank).

OBJECTIVE

The objective of this study is to investigate the biofidelity of existing finite element (FE) occupant models in both upright and recline seated postures, considering the pelvis kinematics and submarining responses.

METHODS

In this study, the GHBMC detailed model (v5.1), THUMS (v6.1), THOR FE model (v1.8.1), and THOR-AV FE model (v0.6) were evaluated against two PMHS tests series, in a total of four configurations. The first test series, based on Uriot et al. [2], consisted of an upright configuration representative of a front-seat in which submarining was not likely to occur, and an upright configuration representative of a rear-seat in which submarining was likely to occur. The

second test series, based on UMTRI report [9], consisted of an upright and reclined configuration which used the same front-seat setup from Uriot et al. [2]. The matrix of the simulations with additional details is shown in Table 1.

For the readers' convenience, the THOR-AV physical test data and BioRank scores from Wang et al. [10][11] were included in the tables and plots for comparison. The THOR-AV physical tests conducted in Case #1 and #2 configurations used a prototype pelvis flesh, which placed its hip joints approximately 20 mm higher than an average male. The THOR-AV physical tests conducted in Case #3 and #4 used a revised pelvis flesh with hip joint height matching that of an average male.

Table 1
Simulation matrix and associated test configurations

Case #	Description	Test Configurations	Reference
1	Front-seat (22° seatback)	50 km/h, inboard and outboard lap belt load limit 5 kN, shoulder belt load limit 7 kN	Uriot et al. [2]
2	Rear-seat (22° seatback)	50 km/h, inboard and outboard lap belt load limit 5 kN, shoulder belt load limit 7 kN	Uriot et al. [2]
3	UMTRI (25° seatback)	32 km/h, shoulder pretensioner only, shoulder belt load limit 3.5 kN, dynamic locking tongue	Wang et al. [11]
4	UMTRI (45° seatback)	32 km/h, shoulder pretensioner only, shoulder belt load limit 3.5 kN, dynamic locking tongue	Wang et al. [11]

FE models

The FE models of the semi-rigid seat and the restraint system were provided by LAB France for Case #1 and #2. The FE models of the semi-rigid seat and restraint system were provided by UMTRI for Case #3 and #4. The GHBMC M50-O (v5.1) and THUMS M50 (v6.1) were obtained through the respective license agreement with the model suppliers by the members of the AVOS consortium. The THOR (v1.8.1) and THOR-AV (v0.6) FE models were provided by Humanetics Innovative Solutions (Humanetics). A revised THOR-AV pelvis flesh design that allows proper buttock flesh compression to match a human was incorporated in the THOR-AV FE model v0.6 used the current study. THUMS, THOR, and THOR-AV simulations were all run on LS-Dyna vR9.3.0., and the GHBMC was run on LS-Dyna v9.3.1. The friction coefficient between occupant models and the seat and between the occupant models and the belts was 0.3 for all simulations.

Initial Position

For Case #1 and #2, the HBMs were pre-positioned to best match the average PMHS landmarks reported from Uriot et al. [2]. For Case #3 and #4, the HBMs were pre-positioned to best match the PMHS landmarks reported by UMTRI [9]. The landmarks for Case #3 were taken from PMHS b13109 (25°, mass 80.3 kg, stature 170.1 cm) and the landmarks from Case #4 were taken from PMHS b12795 (45°, mass 76.1 kg, stature 174.9 cm). These two specimens best matched the average-sized male. The HBMs were initially positioned with their hip joints coincident with those of the PMHS, which produced initial penetration of the buttocks with the seat pan. The seat pan was then translated downward until the initial penetration was removed. A pre-simulation was then run with the HBM skeleton held rigid while the seat pan was translated back into its original location using a boundary prescribed motion, compressing the buttocks flesh.

For THOR-AV, measurements from the dummy positioning targets were used to guide the FE model positioning. The tilt sensor readings of the pelvis, T1, and head were used to set the pelvis, torso, and head orientation. Pre-simulation was carried out to position the dummy to the prescribed positions that matched the THOR-AV physical dummy measurements. For the THOR, a similar process was used; however gravity simulation was used instead since there was no dummy positioning data available to reference.

Oasys Primer (ARUP) was used to pre-position the HBMs and ATDs. No pre-stress was carried over from the pre-positioning simulations into the main simulations. The initial positions of the FE models in the test configurations are shown in Figure 1 through Figure 3. In the UMTRI sled tests, a foam-padded knee bolster was included in the sled

fixture as a safety measure. The knee bolster was located far enough away from the lower extremities to avoid impact in a non-submerging event, yet close enough to prevent catastrophic forward excursion of the PMHS if submerging occurred. No footrest was used in the UMTRI sled tests.

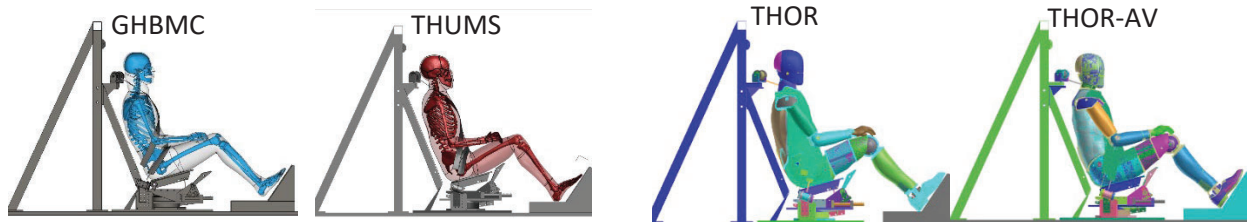


Figure 1 Initial position for the Uriot front- and rear-seat configurations.

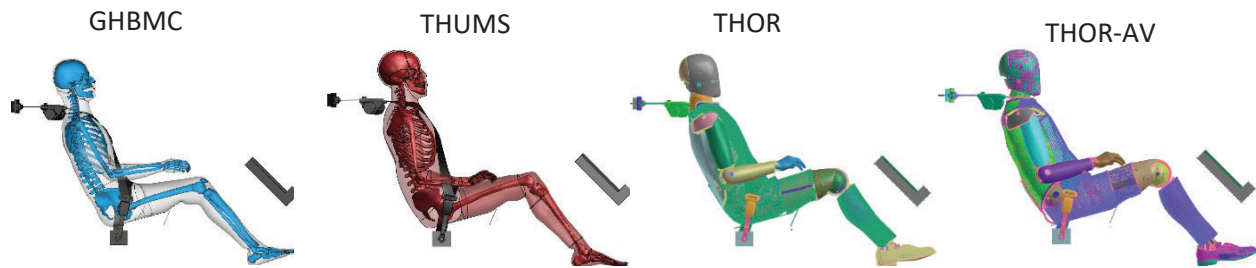


Figure 2. Initial position for the UMTRI 25° seatback configuration.

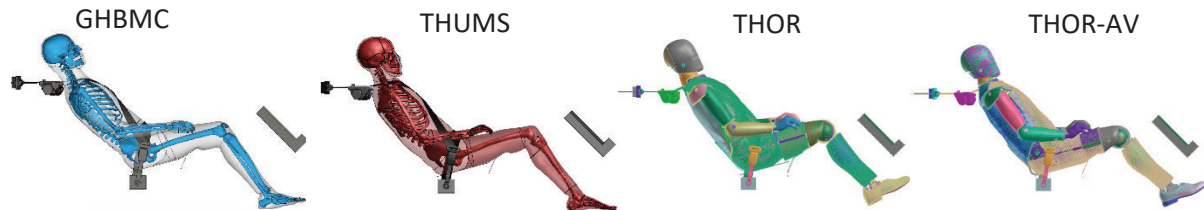


Figure 3. Initial position for the UMTRI 45° seatback configuration.

Data Processing

All data were filtered per SAE J211 filter class recommendations before BioRank calculation. To reduce the noise, CFC180 was applied to the accelerations of the head and the iliac bone in x-, y- and z-directions in UTMRI's PMHS data analysis (Case #3 and #4) instead of CFC1000 as recommended by SAE J211. For consistency, all four FE models used CFC180 for these data channels as well.

BioRank Method

The National Highway Traffic Safety Administration (NHTSA) has been developing a biofidelity ranking (BioRank) method to objectively rank the crash test dummies for its biofidelity for many years [12]-[15]. The most recent updates were documented in Kang et al. [16]. The BioRank method described in Kang et al. [16] was followed in this study. The most recent NHTSA BioRank calculation method was outlined by Rhule et al. [15]. The calculation of the BRS score is the root mean square of the Shape and Magnitude (SM) and the Phase (P) values. In 2020, NHTSA updated the method to only use the SM score [16]. The method recommends alignment of the data curves between a dummy and the PMHS corridor mean by shifting the dummy test curve until the area between the dummy data curve and the PMHS corridor mean curve is minimized. The SM score is calculated after this alignment. The shift of the dummy data curve is referred to as the Dummy Phase Shift (DPS). The DPS is monitored for each data channel. The BioRank score and the biofidelity relationship are summarized in Table 2. The typical goal for the dummy development is to achieve a BRS score equal to or less than 2.0 for each body segment and the whole dummy, which corresponds to *good* biofidelity.

Table 2
Relationship between BRS scores and dummy biofidelity

BRS	BRS ≤ 1.0	1.0 < BRS ≤ 2.0	2.0 < BRS ≤ 3.0	BRS > 3.0
Biofidelity	<i>Excellent</i>	<i>Good</i>	<i>Marginal</i>	<i>Poor</i>

RESULTS

The BioRank scores were calculated for each test configuration. The interaction of the FE occupant with the restraint system was evaluated separately from the occupant kinematics. The BRS scores are reported in this section and the data plots with biofidelity corridors are presented in the Appendix.

Uriot Front Seat (Case #1)

The BRS scores for the restraint system are summarized in Table 3. In general, most of the BRS scores for the restraint system are less than 2.0, corresponding to either *excellent* or *good* biofidelity. However, the BRS scores of the seat-pan force in the z-direction and the seat-pan y-rotation were rated as *marginal* or *poor* for all four FE occupant models with a BRS scores greater than 2.0, except the force in the z-direction for THUMS which was rated as good. The average of the restraint system BRS scores are 1.48, 1.56, 1.51, and 1.54 for the GHBMCM, THUMS, THOR FE, and THOR-AV FE models, respectively; all corresponding to *good* biofidelity.

In the front-seat, upright configuration defined in Uriot et al.[2], neither the HBM nor the ATD FE occupants submarined, consistent with the PMHS response. The kinematics BRS scores for the occupant models are summarized in Table 4. There are limited parameters from the PMHS tests for biofidelity evaluation in this test configuration. Out of these parameters evaluated, the majority of them have BRS scores less than 1.0, corresponding to *excellent* biofidelity. The average BRS scores for the GHBMCM, THUMS, THOR FE, and THOR-AV FE, are 0.84, 0.72, 0.61 and 0.70 respectively, all corresponding to *excellent* biofidelity.

Table 3
BRS scores of the restraint system for the GHBMCM, THUMS, THOR, and THOR-AV FE models in the front-seat test configuration

Restraint System	GHBMCM		THUMS		THOR FE		THOR-AV FE	
	BRS	DPS(ms)	BRS	DPS(ms)	BRS	DPS(ms)	BRS	DPS(ms)
Seat (average)	1.92	3	1.90	-1	1.98	-1	2.01	-1
Seat Pan Force X	1.68	2	1.36	-1	1.04	1	1.30	3
Seat Pan Force Z	2.06	8	1.88	-1	3.16	-7	2.67	-7
Seat Pan Rotation Y	3.17	-4	3.18	-4	2.97	-2	3.19	0
Anti-Sub Plate Rotation Y	0.79	5	1.18	0	0.75	5	0.89	0
Belt (average)	1.03	-1	1.23	-2	1.03	-2	1.06	-1
Upper Shoulder Belt Force	1.01	-1	0.58	-3	0.84	2	0.86	1
Lower Shoulder Belt Force	1.35	1	1.39	1	1.06	2	1.23	0
Inner Lap Belt Force	1.48	1	1.05	-2	0.84	-4	0.82	-4
Outer Lap Belt Force	0.89	-1	0.61	-1	0.77	-5	0.72	-4
Inner Lap Belt Rotation Y	0.90	-8	1.01	-6	1.68	-9	2.31	3
Outer Lap Belt Rotation Y	1.14	0	3.01	0	1.40	0	1.07	0
Pelvis to Lab Belt Rotation Y	0.46	-2	0.92	-3	0.67	0	0.45	-1
Overall Restraint Average	1.48	1	1.56	-2	1.51	-2	1.54	-1

Table 4

The BRS scores of the GHBMC, THUMS, THOR, and THOR-AV models in the front-seat test configuration

Body Region	GHBMC		THUMS		THOR		THOR-AV	
	BRS	DPS(ms)	BRS	DPS(ms)	BRS	DPS(ms)	BRS	DPS (ms)
Thorax	0.85	1	0.73	0	0.63	4	0.81	0
Chest Acceleration	0.85	1	0.73	0	0.63	4	0.81	0
Pelvis (average)	0.82	1	0.70	3	0.60	0	0.60	0
Pelvis Resultant Acceleration	1.43	0	1.08	0	0.74	-7	1.14	-6
Pelvis Rotation Y	0.76	2	0.90	9	0.48	5	0.45	3
Pelvis Displacement X	0.28	0	0.12	1	0.57	2	0.22	2
Overall Average	0.84	1	0.72	1	0.61	2	0.70	0

The pelvis x-displacement and y-rotation for all four FE models were well within the PMHS corridors, as shown in Figure 4. As mentioned earlier, the THOR-AV tests in Cases #1 and #2 were from a prototype pelvis flesh that placed the dummy hip joint higher by approximately 20 mm than an average male. A revised THOR-AV pelvis flesh design that allows proper buttock flesh compression to match a human was incorporated in the THOR-AV FE model v0.6 in this study.

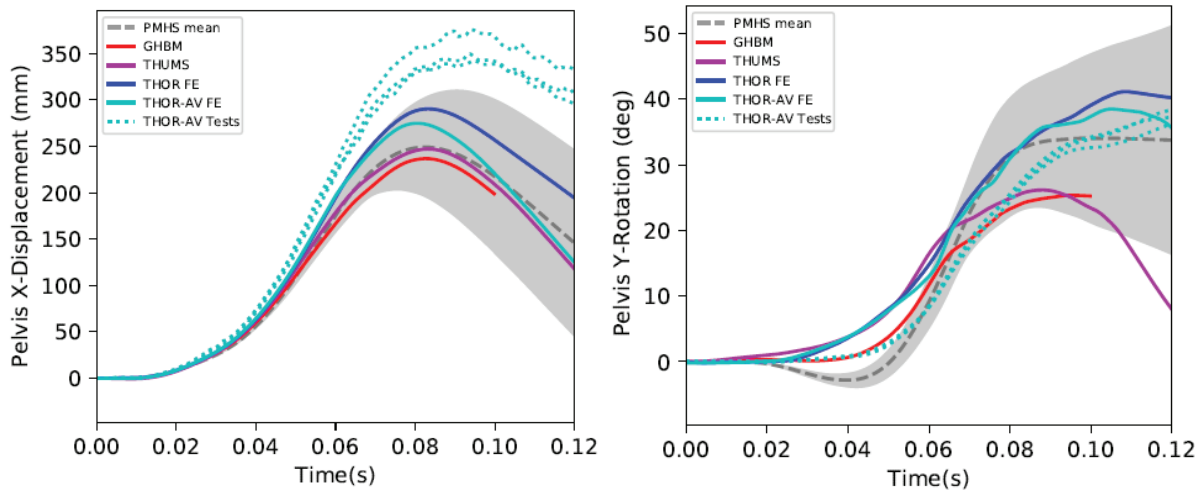


Figure 4. Pelvis x-displacement (left) and pelvis y-rotation (right) in the front-seat test configuration.

Uriot Rear Seat (Case #2)

The BRS scores for the restraint system are summarized Table 5. Overall, the interaction between the restraint system and the dummy is reasonable with a majority of the BRS scores less than 2.0. The BRS scores for seat-pan force in the z-direction for the GHBMC and THUMS HBMs are 2.32 and 2.28, respectively; both corresponding to *marginal* biofidelity. The BRS scores of the seat pan force in the z-direction for the THOR and THOR-AV ATDs are 4.85 and 3.12, respectively; both corresponding to *poor* biofidelity. The BRS score of the seat-pan rotation for the THOR is 4.35, corresponding to *poor* biofidelity. In addition, *marginal* or *poor* biofidelity of the lap belt rotation and the lap belt relative-to-pelvis rotation was observed for the GHBMC model. *Marginal* biofidelity of the outer lap belt force and lap belt rotation for the THOR-AV model was observed as well. Overall, the GHBMC, THUMS, THOR FE, and THOR-AV FE models have BRS scores of 1.34, 1.18, 2.03, and 1.80 for the restraint system; corresponding to *good*, *good*, *marginal*, and *good* biofidelity, respectively.

In the rear-seat, upright test configuration defined in Uriot et al. [2], all HBM and ATD models submarined, consistent with the PMHS responses. The kinematics BRS scores for the occupant models are summarized in Table 6. The average BRS scores of the four models are 0.93, 0.83, 0.71 and 0.84; all corresponding to *excellent* biofidelity.

Table 5

The BRS scores of the restraint system for the GHBMC, THUMS, THOR, and THOR-AV models in the rear-seat test configuration

Restraint System	GHBMC		THUMS		THOR FE		THOR-AV FE	
	BRS	DPS (ms)	BRS	DPS (ms)	BRS	DPS (ms)	BRS	DPS (ms)
Seat (average)	1.20	-4	1.33	-6	3.01	-4	1.88	-2
Seat Pan Force X	0.88	-4	0.83	-5	1.44	0	1.46	0
Seat Pan Force Z	2.32	-2	2.28	-5	4.85	0	3.12	0
Seat Pan Rotation Y	1.24	-3	1.49	-6	4.35	-10	1.74	-7
Anti-Sub Plate Rotation Y	0.36	-8	0.72	-9	1.38	-6	1.18	0
Belt (average)	1.48	2	1.02	0	1.06	1	1.72	1
Upper Shoulder Belt Force	0.71	2	0.80	1	0.84	6	0.82	3
Lower Shoulder Belt Force	0.56	1	1.25	0	0.80	4	0.80	1
Inner Lap Belt Force	0.54	7	0.61	6	0.80	0	1.85	10
Outer Lap Belt Force	0.62	7	0.44	5	0.76	1	2.07	8
Inner Lap Belt Rotation Y	3.58	0	2.21	-2	1.66	-8	2.42	-6
Outer Lap Belt Rotation Y	2.13	0	0.83	-9	1.71	0	2.60	0
Pelvis to Lab Belt Rotation Y	2.24	-3	1.03	-2	0.84	0	1.47	-7
Overall Average	1.34	-1	1.18	-3	2.03	-2	1.80	0

Table 6

The BRS scores for the GHBMC, THUMS, THOR, and THOR-AV models in the rear-seat test configuration

Body Region	GHBMC		THUMS		THOR FE		THOR-AV FE	
	BRS	DPS (ms)	BRS	DPS (ms)	BRS	DPS (ms)	BRS	DPS (ms)
Thorax	0.80	5	0.72	-2	0.77	-1	0.96	0
Chest Acceleration	0.80	5	0.72	-2	0.77	-1	0.96	0.4
Pelvis (average)	1.06	0	0.94	2	0.64	0	0.71	0
Pelvis Resultant Acceleration	1.20	2	1.05	7	0.64	-4	0.98	-3
Pelvis Rotation Y	0.95	4	0.92	2	0.61	6	0.70	3
Pelvis Displacement X	1.04	-5	0.86	-2	0.68	-1	0.45	-1
Overall Average	0.93	3	0.83	0	0.71	0	0.84	0

The pelvis x-displacement and y-rotation for the four FE models were well within the PMHS corridors, as shown in Figure 5.

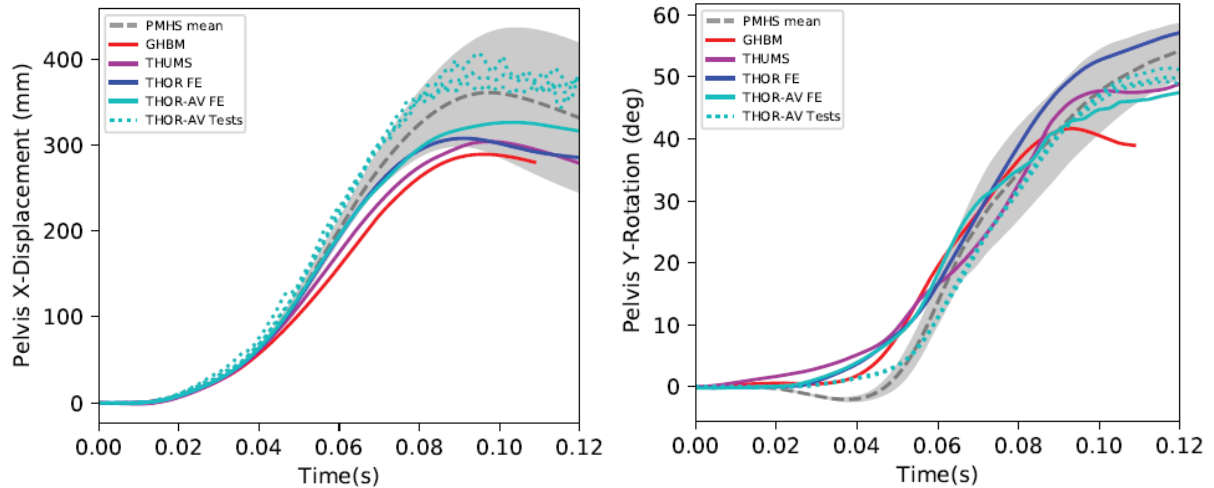


Figure 5. Pelvis x-displacement and y-rotation in the rear-seat test configuration

UMTRI 25° (Case #3)

The BRS scores for the restraint system are summarized in Table 7. The BRS scores of the seat force in the z-direction for the THUMS, THOR, and THOR-AV models are 2.12, 2.59 and 2.62, respectively; all corresponding to *marginal* biofidelity. The seat-pan rotation and anti-submarine plate rotation of all four models showed either *marginal* or *poor* biofidelity. The BRS scores of the lap belt forces at the outer side and the buckle locations are greater than 2.0 for THUMS, corresponding to *marginal* biofidelity. The overall restraint system response showed *marginal* biofidelity for the GHBM, THUMS, THOR, and THOR-AV models.

In this front-seat, upright test configuration, neither the HBM nor the ATD models submarined, consistent with the PMHS responses reported by UMTRI. The kinematics BRS scores for the occupant models are summarized in Table 8. The BRS scores of all parameters evaluated are less than 2.0 with many of them less than 1.0, corresponding to either *good* or *excellent* biofidelity. The average kinematic BRS scores for the GHBM, THUMS, THOR, and THOR-AV models are 0.94 (*excellent* biofidelity), 1.06 (*good* biofidelity), 1.26 (*good* biofidelity), and 0.87(*excellent* biofidelity), respectively.

Table 7

The BRS scores of the restraint system for the GHBM, THUMS, THOR, and THOR-AV models in the UMTRI 25° test configuration

Restraint System	GHBM		THUMS		THOR		THOR-AV	
	BRS	DPS (ms)	BRS	DPS (ms)	BRS	DPS (ms)	BRS	DPS (ms)
Seat (average)	2.77	3	2.61	0	2.84	1	2.88	2
Seat Force X	1.69	6	1.49	1	1.19	0	1.19	6
Seat Force Z	1.82	6	2.12	-1	2.59	5	2.62	4
Seat Pan Rotation Y	2.85	2	2.54	-1	3.70	0	2.56	0
Anti-Sub Plate Rotation Y	4.71	0	4.29	0	3.90	0	5.17	0
Belt (average)	1.49	-3	1.94	-4	1.73	0	1.28	-3
Outer Lap Belt Force	1.69	0	2.39	-2	1.29	-4	1.16	-4
Lap Belt Buckle Force	1.58	-2	2.16	-5	2.01	-1	1.40	-2
Upper Shoulder Belt Force	1.20	-5	1.29	-6	1.90	6	1.29	-2
Restraint Overall Average	2.13	0	2.28	-2	2.29	1	2.08	0

Table 8

The BRS scores for the GHBMC, THUMS, THOR, and THOR-AV models in the UMTRI 25° test configuration

Body Region	GHBMC		THUMS		THOR		THOR-AV	
	BRS	DPS (ms)	BRS	DPS (ms)	BRS	DPS (ms)	BRS	DPS (ms)
Head (average)	1.07	-1	1.28	1	1.03	-1	0.63	2
Head Acceleration X	0.93	-7	1.52	0	1.36	-6	0.81	-5
Head Acceleration Z	1.40	0	1.41	0	1.34	0	0.73	0
Head Angular Velocity Y	1.00	0	0.93	0	1.27	0	0.97	6
Head Displacement X	1.55	2	1.63	3	0.28	1	0.32	1
Head Displacement Z	0.47	0	0.92	0	0.89	0	0.33	9
Spine (average)	0.90	-1	1.17	0	1.46	0	0.92	-1
T1 Acceleration X	1.17	0	1.37	-5	1.19	0	1.05	-1
T1 Acceleration Z	1.09	0	1.12	0	1.68	0	1.35	0
T1 Displacement X	0.90	-1	1.81	4	1.47	-1	0.88	1
T1 Displacement Z	0.65	0	1.40	0	1.79	0	0.32	0
T8 Displacement X	0.72	1	1.41	3	NA	NA	NA	NA
T8 Displacement Z	0.75	0	0.59	0	NA	NA	NA	NA
T12 Acceleration X	1.66	-5	1.40	-3	1.52	1	1.23	-3
T12 Acceleration Z	0.96	0	0.85	-4	1.05	-4	0.94	-4
T12 Displacement X	0.57	0	1.13	2	1.26	2	1.17	2
T12 Displacement Z	0.54	0	0.29	0	1.75	2	0.43	0
L4 Acceleration X	1.17	1	1.81	-1	NA	NA	NA	NA
L4 Acceleration Z	0.64	-5	0.82	1	NA	NA	NA	NA
Pelvis (average)	0.85	0	0.74	1	1.28	-1	1.06	0
Pelvis Acceleration X	1.41	-4	1.39	0	1.81	0	1.32	0
Pelvis Acceleration Z	1.59	-2	0.74	-1	1.25	-5	1.07	-5
Pelvis Angular Velocity Y	0.96	0	0.81	4	0.99	2	0.87	0
Pelvis Rotation Y	0.48	6	0.82	0	0.73	0	0.36	0
Pelvis Displacement X	0.16	0	0.27	1	1.24	0	0.90	2
Pelvis Displacement Z	0.47	0	0.40	0	1.67	0	1.84	0
HBM/ATD Overall Average	0.94	-1	1.06	0	1.26	-1	0.87	0

Note: NA – no data available, the dummies were not instrumented for these channels

The head center of gravity, T1, T8, T12, and hip joint mid-sagittal trajectory overlays are illustrated in Figure 6. Due to anthropometric differences between the FE occupants and physical surrogates, the starting location of these trajectories are different. For illustrative purposes, each trajectory was transformed so that the starting location of the trajectory for a particular body region was aligned with the corresponding starting location of the THUMS FE model.

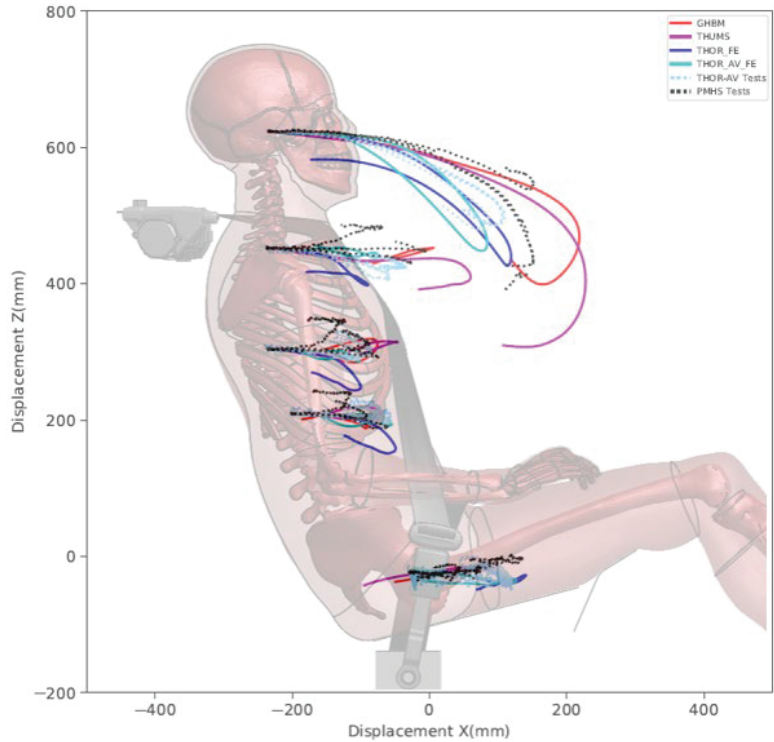


Figure 6. Trajectory overlays for the GHBMC, THUMS, THOR, THOR-AV models and the PMHS data for Case #3

UMTRI 45° (Case #4)

The BRS scores for the restraint system are summarized in Table 9. Many of the parameters evaluated have a BRS score less than 2.0, corresponding to *good* biofidelity. However, the anti-submarining plate rotation for all models is greater than 4.29, corresponding to *poor* biofidelity, which affected the overall biofidelity results. The seat force in the x-direction for the GHBMC model has a BRS score of 2.30, corresponding to *marginal* biofidelity, and the lap belt buckle force and the shoulder belt force for the THOR model have BRS scores of 2.69 and 2.80, respectively, both corresponding to *marginal* biofidelity. The overall biofidelity for all models is *marginal*.

Table 9

The BRS scores of restraint system for the GHBMC, THUMS, THOR, and THOR-AV models in the UMTRI 45° test configuration

Restraint System	GHBMC		THUMS		THOR		THOR-AV	
	BRS	DPS (ms)	BRS	DPS (ms)	BRS	DPS (ms)	BRS	DPS (ms)
Seat	3.28	1	2.42	-2	2.63	1	3.22	2
Seat Force X	2.30	-1	1.74	-6	1.59	1	1.93	4
Seat Force Z	1.47	4	1.75	-5	1.17	4	1.40	4
Seat Pan Rotation Y	1.84	0	1.89	3	2.00	0	1.17	0
Anti-Sub Plate Rotation Y	7.52	0	4.29	0	5.78	0	8.38	0
Belt	1.85	0	1.62	-3	2.46	-1	1.41	1
Outer Lap Belt Force	1.69	0	1.80	-3	1.88	-2	1.16	4
Lap Belt Buckle Force	1.87	2	1.67	-2	2.69	-1	1.20	0
Upper Shoulder Belt Force	1.99	-1	1.39	-3	2.80	-2	1.88	0
Restraint Overall Average	2.56	1	2.02	-2	2.55	0	2.32	2

In this front-seat, reclined test configuration, neither the HBM nor the ATD models submarined, consistent with the PMHS responses reported by UMTRI. The kinematics BRS scores for the occupant models are summarized in Table 10. Most of the parameters evaluated have a BRS score less than 2.0, with many of them less than 1.0 for all four models; corresponding to either a *good* or *excellent* biofidelity. The average kinematic BRS scores for the GHBM, THUMS, THOR, and THOR-AV models are 1.28, 1.45, 1.36, 1.12, respectively; all corresponding to *good* biofidelity.

Table 10

The BRS scores for the GHBM, THUMS, THOR, and THOR-AV models in the UMTRI 45° test condition

Body Regions	GHBM		THUMS		THOR		THOR-AV	
	BRS	DPS(ms)	BRS	DPS(ms)	BRS	DPS(ms)	BRS	DPS(ms)
Head	1.51	1	2.19	0	1.29	0	0.86	-1
Head Acceleration X	1.66	0	1.67	0	1.08	-7	0.66	-4
Head Acceleration Z	1.27	0	1.98	0	2.28	0	0.87	5
Head Angular Velocity Y	2.16	0	2.81	0	2.01	3	1.32	5
Head Displacement X	1.19	-2	1.10	-2	0.65	-3	0.84	-3
Head Displacement Z	1.25	8	3.39	0	0.42	6	0.59	-7
Spine	0.96	-1	1.22	-2	1.61	-2	1.14	-1
T1 Acceleration X	0.66	0	0.63	0	0.63	-6	0.62	0
T1 Acceleration Z	0.77	0	0.71	0	1.16	0	0.90	0
T1 Displacement X	0.76	-4	2.42	1	1.43	-4	3.14	-4
T1 Displacement Z	0.91	0	1.67	0	2.23	0	0.66	-3
T8 Displacement X	0.76	-4	0.16	-1	NA	NA	NA	NA
T8 Displacement Z	0.91	0	2.29	0	NA	NA	NA	NA
T12 Acceleration X	1.47	0	1.11	-2	1.44	0	0.86	-1
T12 Acceleration Z	0.69	-3	0.70	-6	0.88	-9	0.64	1
T12 Displacement X	1.06	-2	0.20	-1	1.25	1	0.47	-1
T12 Displacement Z	2.10	0	2.83	0	3.83	0	1.79	0
L4 Acceleration X	0.77	-2	1.31	-7	NA	NA	NA	NA
L4 Acceleration Z	0.70	5	0.67	-5	NA	NA	NA	NA
Pelvis	1.37	1	0.92	-2	1.18	1	1.36	1
Pelvis Acceleration X	2.13	0	1.42	-9	2.21	0	1.68	0
Pelvis Acceleration Z	1.35	-2	1.03	-4	1.18	2	0.94	5
Pelvis Angular Velocity Y	1.25	0	1.34	-5	0.60	1	1.41	0
Pelvis Rotation Y	1.13	7	0.95	0	0.10	1	1.61	0
Pelvis Displacement X	0.44	0	0.33	0	0.89	1	0.61	-1
Pelvis Displacement Z	1.94	0	0.47	7	2.11	0	1.90	0
HBM/ATD Overall Average	1.28	0	1.45	-1	1.36	-1	1.12	0

The trajectory overlays are illustrated in Figure 7.

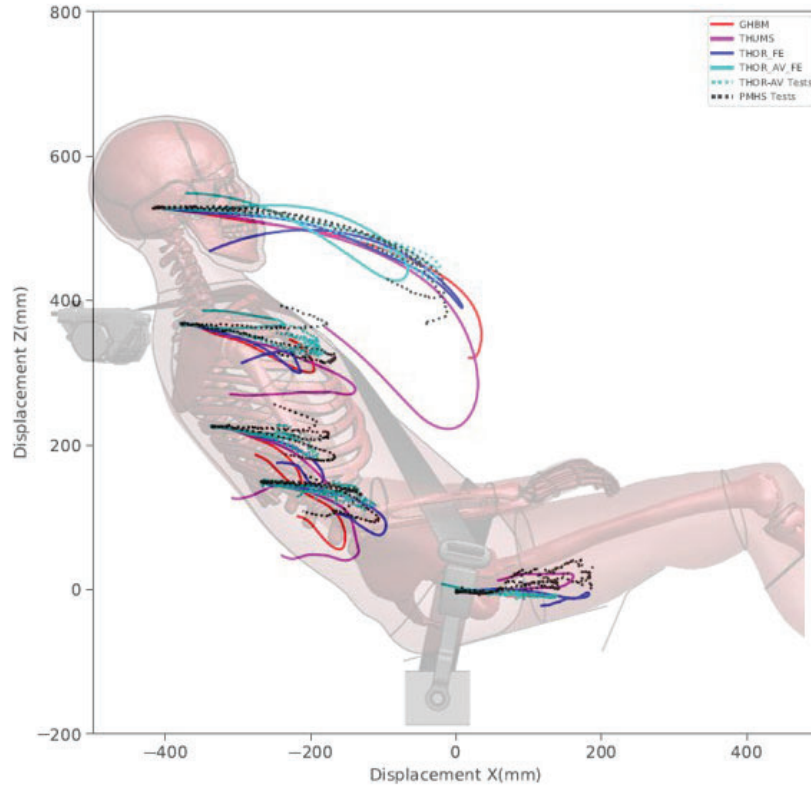


Figure 7. Trajectory overlays for the GHBM, THUMS, THOR and THOR-AV models and the PMHS data for Case #4.

Overall Averages (Cases #1-4)

The overall averages of the restraint system for these four test configurations are summarized in Table 11, and the overall kinematics average of the responses of the FE occupant models for the four test configurations are summarized in Table 12. The biofidelity of the THOR-AV was evaluated by Wang et al. [10][11]. For the reader's convenience, the THOR-AV dummy's BRS scores are included for references. Except for the THOR FE model, the restraint system BRS scores are within 2.0, corresponding to *good* biofidelity. The kinematic BRS scores for the GHBM, THUMS, THOR, and THOR-AV models are close to 1.0, corresponding to *good* or *excellent* biofidelity.

Table 11

The average restraint system BRS scores for the GHBM, THUMS, THOR, THOR-AV models and the THOR-AV test

Restrainer	GHBM		THUMS		THOR FE		THOR-AV FE		THOR-AV Test	
	BRS	DPS(ms)	BRS	DPS(ms)	BRS	DPS (ms)	BRS	DPS (ms)	BRS	DPS(ms)
Case #1	1.48	1	1.56	-2	1.51	-2	1.54	-1	1.54	-5
Case #2	1.34	-1	1.18	-3	2.03	-2	1.80	0	1.64	-4
Case #3	2.13	0	2.28	-2	2.29	1	2.08	0	1.29	-4
Case #4	2.56	1	2.02	-2	2.55	0	2.32	2	1.32	-3
Average	1.88	0	1.76	-2	2.09	-1	1.93	0	1.45	-4

Table 12

The average kinematics BRS scores of the GHBMC, THUMS, THOR, and THOR-AV models, and the THOR-AV test

HBM/ATD	GHBMC		THUMS		THOR FE		THOR-AV FE		THOR-AV Test	
	BRS	DPS(ms)	BRS	DPS(ms)	BRS	DPS(ms)	BRS	DPS(ms)	BRS	DPS(ms)
Case #1	0.84	1	0.72	1	0.61	2	0.70	0	0.84	3
Case #2	0.93	3	0.83	0	0.71	0	0.84	0	0.77	-3
Case #3	0.94	-1	1.06	0	1.26	-1	0.87	0	0.73	0
Case #4	1.28	0	1.45	-1	1.36	-1	1.12	0	0.89	-1
Average	1.00	1	1.01	0	0.98	0	0.88	0	0.81	0

DISCUSSION

In general, the kinematics of all four FE models matched their PMHS counterpart reasonably well; evidenced by their BRS scores. However, the occupant-to-restraint interaction requires improvement.

The restraint system used for test series 2 (Case #3 and #4) simulations did not include a dynamic locking tongue. The authors were made aware that a 2 kN dynamic locking tongue was used in the corresponding PMHS tests when writing this manuscript. The authors reviewed the shoulder belt and lap belt loads time history and found that the belt loads of the simulations matched the outputs of the PMHS tests reasonably well. The shoulder belt payout of the FE simulations also matched the PMHS results reasonably well. Based on this analysis, the authors do not believe the simulation outputs were compromised due to the lack of a dynamic locking tongue.

The seat force in the z-direction was higher than the PMHS results in Case #1 (Figure A6) and #3 (Figure A17) for all four occupant models. The PMHS mass (average of 68.1 kg with a range of 53.0 to 80.3 kg) used to derive the PMHS corridors was much lower than the mass of an average male (76.8 kg). This mass-mismatch may have contributed to the lower seat force in the z-direction for PMHS corridors. Normalization of the PMHS test data could reduce this force discrepancy and improve the BRS scores for the FE occupants.

It was noticed that the anti-submarining plate rotations were significantly higher for the FE models in Case #3 and #4 (Figure A19). In physical dummy tests, it was observed that the rotations of the seat pan and the anti-submarining plate did not correlate well with the PMHS responses [10][11]. The causes were not very clear and is worthy of further investigation.

The lap belt force of the four FE models matched that of the PMHSs reasonably well in Case #1 and #2 (Figure A1 through Figure A4). However, the lap belt force of the GHBMC and THUMS models in Case #3 and #4 were higher than the PMHS results (Figure A20 and Figure A21), while the shoulder belt force for all four FE models matched the PMHS results reasonably well. The results did not give a clear direction for future optimization of the FE models. To understand the issue better, the pelvis flesh stiffness was investigated to understand the lap belt engagement with the pelvis using the UMTRI simulations (Case #3 and #4). The investigation focused on the belt forces and pelvis hip displacement relationship, which was expected to be a reasonable indicator of the stiffness of the flesh in front of the ASIS. Since the buckle side load cell measured the sum of the shoulder belt and lap belt forces, the force for the lap belt alone on the buckle side cannot be segregated. Therefore, the outboard lap belt force was doubled for this analysis. As shown in Figure 8, the stiffnesses of the pelvis flesh (slope of lap belt force vs. hip displacement) for the GHBMC, THUMS, THOR, and THOR-AV models are comparable to the stiffnesses of pelvis flesh for the PMHS.

The body mass and stature of the PMHS specimens varied from 53 kg to 80.3 kg and 166.3 cm to 175.7 cm respectively, for the UMTRI tests. The specimens that best matched the average male weight and height were the PMHS 2104 (body mass 80.3 kg, stature 170.1 cm) in the 25° seatback test condition, and the PMHS 2002 (body mass 76.1 kg, stature 174.9 cm) in the 45° seatback test condition. For the belt force vs hip displacement responses, both the THOR and THOR-AV models showed comparable results to these PMHS tests respectively in each test configuration. The GHBMC and THUMS models matched the stiffer responses of the PMHSs, shown in Figure 8.

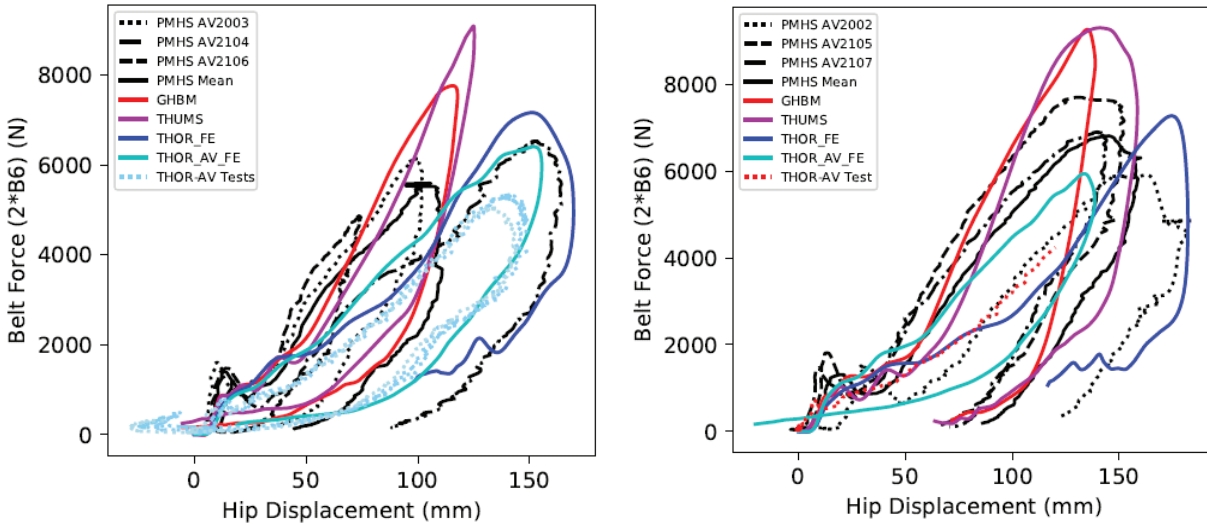


Figure 8. Belt force vs hip displacement in the 25° (left) and 45° (right) UMTRI test configurations

The GHBMC, THUMS, THOR, and THOR-AV restraint system biofidelity was notably worse than the kinematics biofidelity (Table 11 and Table 12), and should be investigated in the future.

In the front- and rear-seat test configurations (Case #1 and #2), the pelvis rotations matched the PMHS response well (Figure A11). For the UMTRI 25° test condition (Case #3), the pelvis y-rotation fell within the PMHS corridor for all models; the THOR model near the upper bound and THOR-AV and THUMS models near the lower bound (Figure A41). For the 45° recline condition (Case #4), the pelvis rotation for the GHBMC and THOR-AV models fell out of (i.e. below) the lower bound, while the THUMS model was near the upper bound and the THOR model was in the middle. It was noted the pelvis rotation in y-direction was opposite to PMHS pelvis rotation observed in Richardson et al. study [18], most probably explained by the difference in restraint system and impact pulse. Also, the UMTRI test used a 32 km/h delta velocity and no lap belt pretensioner, versus a 50 km/h and dual lap belt pretensioner in Richardson et al.

LIMITATIONS

No effort was made to improve the biofidelity of the four FE models in the current study. As presented in this paper, the THOR-AV physical dummy test results had slightly better biofidelity than the THOR-AV FE model (v0.6). This will be addressed by Humanetics in the next release. As mentioned in the discussion, a dynamic locking tongue was not simulated in Case #3 and 4, even though one was used in the physical tests. Since the shoulder belt payout and shoulder belt loads were comparable between the simulations and the PMHS tests, the authors do not believe there was a negative effect on the results.

CONCLUSIONS

The biofidelity of the GHBMC, THUMS, THOR, and THOR-AV models was evaluated in four test configurations. Using the NHTSA BioRank method, the four FE occupant models demonstrated *good* to *excellent* kinematic biofidelity as compared to PMHSs. The restraint system BioRank scores were not as good as the models' kinematic responses; however, except for the THOR model, they were ranked as *good*. The interaction between all four occupant models and the restraint system needs improvement. The THOR-AV FE model was modified to match the human hip joint height, improving its seated height, and potentially the submarining responses of the dummy. The stiffness in front of the ASIS appeared to be reasonable when comparing with the PMHS results under lap belt loading condition. It was also observed that the HBM responses were comparable to the ATD responses for all test configurations.

ACKNOWLEDGEMENT

The AVOS Consortium would like to express its gratitude for the support of the consortium member companies. The views expressed in this manuscript are those of the consortium's individual participants and may not represent the views of their respective organizations.

For any questions related to this paper, please contact the lead author, Z. Jerry Wang, Ph.D., Tel +1 248 778 2133, Email jwang@humaneticsatd.com, Humanetics Innovative Solutions, Inc., 23300 Haggerty Road, Farmington Hills, Michigan 48335, USA. Humanetics Innovative Solutions is the host company of the AVOS Consortium.

REFERENCES

- [1] Leung Y.C., Terriere C., Fayon, A., Mairesse P., Delmas A., Banzet P., A comparison between part 572 dummy and human subject in the problem of submarining, 23rd Stapp Car Crash Conference, October 1979.
- [2] Uriot J., Baudrit P., Portier P., Trosseille X., Petit P., Guillemot H., Guerin L., Vallancien G. Investigation on the belt-to-pelvis interaction in case of submarining. Stapp Car Crash Journal, Vol. 50 (Nov 2006), pp.53-73.
- [3] Uriot, J, Potier, P, Baudrit, P, Trosseille, X, Richard, O. and Douard, R, Comparison of HII, HIII and THOR dummy responses with respect to PMHS sled tests, IRCOBI Conference Proceedings, Lyon France, Sept 9-11, 2015.
- [4] Richardson R., Donlon J.P., Jayathirtha M., Forman J.L., Shaw G., Gepner B., Kerrigan J.R., Östling M., Mroz K., Pipkorn B., Kinematics and injury response of reclined PMHS in frontal impacts, Stapp Car Crash Journal, Vol. 64, November 2020.
- [5] Richardson R., Jayathirtha M., Donlon J.P., Forman J.L., Gepner B., Östling M., Mroz K., Pipkorn B., Kerrigan J.R., Pelvis kinematics and injuries of reclined occupants in frontal impacts, IRCOBI, 2020.
- [6] Gepner B.D., Draper D., Mroz K., Richardson R., Östling M., Pipkorn B., Forman J. L., Kerrigan J. R. 2019. Comparison of human body models in frontal crashes with reclined seatback. 2019. IRCOBI Conference Proceedings, September 11-13, 2019, Florence, Italy.
- [7] Mroz K., Östling M., Richardson R, Kerrigan K, Forman J, Gepner B, Lubbe N, Pipkorn B, 2020. Effect of seat belt characteristics on the lumbar spine and pelvis loading of the SAFER Human Body Model in reclined postures, IRCOBI, 2020 (virtual).
- [8] Östling J., Bohman K., Jakobsson L., Evaluation of kinematics and restraint interaction with repositioning a driver from a reclined to an upright position prior to frontal impact using active human body model simulations, IRCOBI conference, 2020.
- [9] NHTSA test report, NHTSA Biomechanics Database, September 20, 2020, test # b12795, <https://nrd-static.nhtsa.dot.gov/reports/biodb/b10000/b12700/b12795R005.pdf> and January 25th, 2021, test # b13109 <https://nrd-static.nhtsa.dot.gov/reports/biodb/b10000/b13100/b13109R001.pdf>.
- [10] Wang Z.J., Richard O., Lebarbé M. Uriot J., Kabadayi E., Kleessen C., Biomechanical responses of THOR-AV in a semi-rigid seat that mimicked the front and rear seat, IRCOBI conference, Porto, Portugal, September 14-16, 2022.
- [11] Wang Z.J., Zaseck L.W., Reed M.P., THOR-AV 50th percentile male biofidelity evaluation in 25 and 45 seatback angle test conditions with a semi-rigid seat, IRCOBI conference, Porto, Portugal, September 14-16, 2022.
- [12] Rhule H.R., Maltese M.P., Donnelly B.R., Eppinger R.H., Brunner J.K. and Bolte IV J.H., Development of a new biofidelity ranking system for anthropomorphic test devices, Stapp Car Crash Journal, 46th Stapp Car Crash Conference, November 2002.

- [13] Rhule H., Moorhouse K., Donnelly B., Stricklin J., Comparison of WorldSID and ES-2RE biofidelity using an updated biofidelity ranking system, 21st International Technical Conference on Enhanced Safety of Vehicles (ESV), Stuttgart, Germany, June 2009.
- [14] Rhule H., Donnelly B., Moorhouse K., Kang Y-S., A methodology for generating objective target for quantitatively assessing the biofidelity of crash test dummies, 23rd International Technical Conference on Enhanced Safety of Vehicles (ESV), Seoul, Korea, May 27-30, 2013.
- [15] Rhule H., Stricklin J., Moorhouse K., Donnelly B., Improvements to NHTSA’s biofidelity ranking system and application to the evaluation of the THOR 5th female dummy, IRCOBI Conference Proceedings, 2018, paper # IRC-18-12.
- [16] Kang Y-S., Stammen J., Ramachandra R., Agnew R.M. Hagedorn, A., Thomas C., Kwon H.J., Moorhouse K., Bolte IV J.H., Biomechanical responses and injury assessment of post-mortem human subjects in various rear-facing seating configurations. Stapp Car Crash Journal, vol. 64 (November 2020), pp. 155-212.
- [17] Schneider, L.W., Robbins, D.H., Pflug, M.A., Snyder, R.G., 1983. Anthropometric specifications for mid-sized male dummy, Vol. 2, UMTRI-83-53-2.
- [18] Richardson R., Donlon J.P., Jayathirtha M., Forman J.L., Shaw G., Gepner B., Kerrigan J.R., Östling M., Mroz K., Pipkorn B., Kinematics and injury response of reclined PMHS in frontal impacts, Stapp Car Crash Journal, Vol. 64 (November 2020).

APPENDIX

The overlay of the channels from GHBM, THUMS, THOR, and THOR-AV FE models are shown in this appendix for all four cases.

Plots for the front- and rear-seat test configurations (Case #1 and #2)

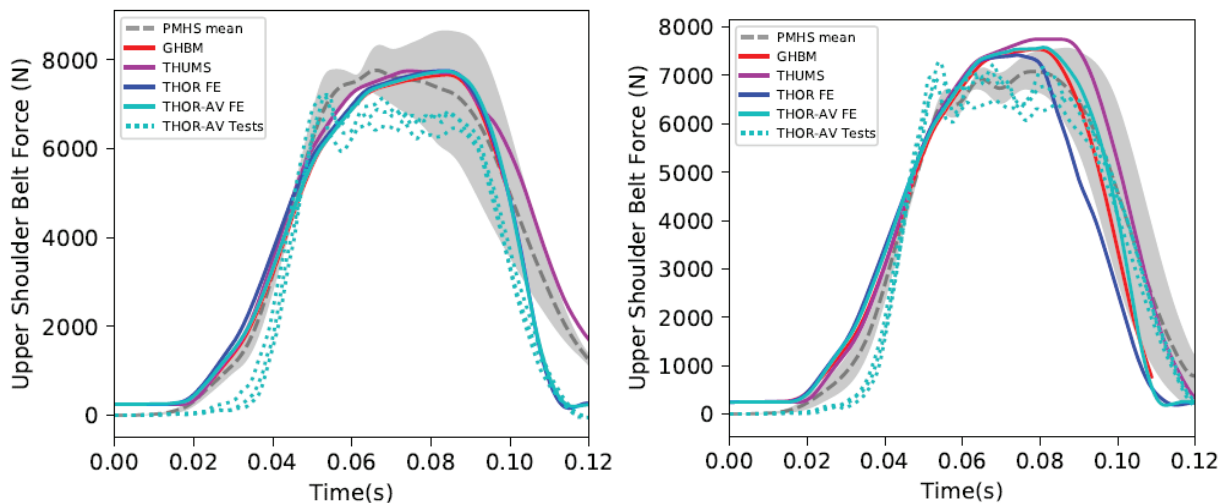


Figure A1. Upper shoulder belt force in the front-seat (Case #1, left) and the rear-seat (Case #2, right) test configurations.

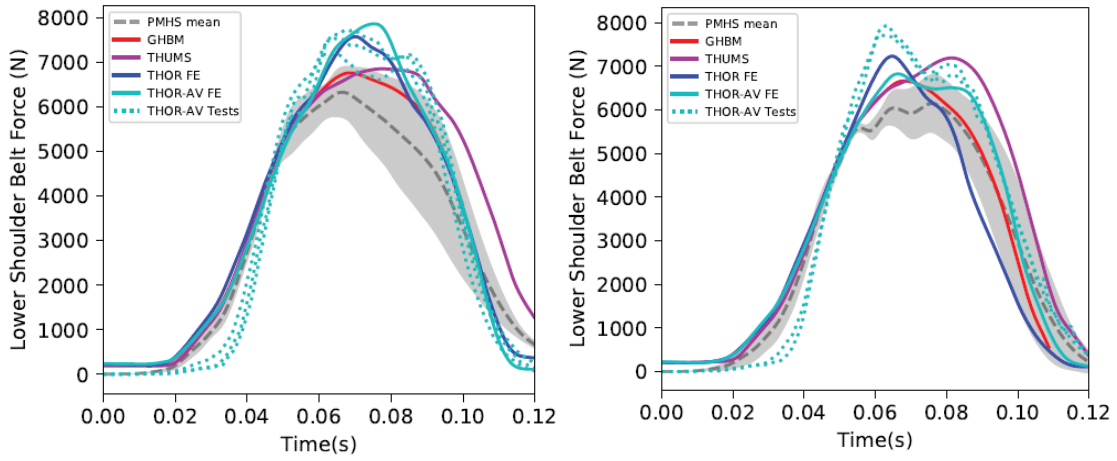


Figure A2. Lower shoulder belt force in the front-seat (Case #1, left) and the rear-seat (Case #2, right) test configurations.

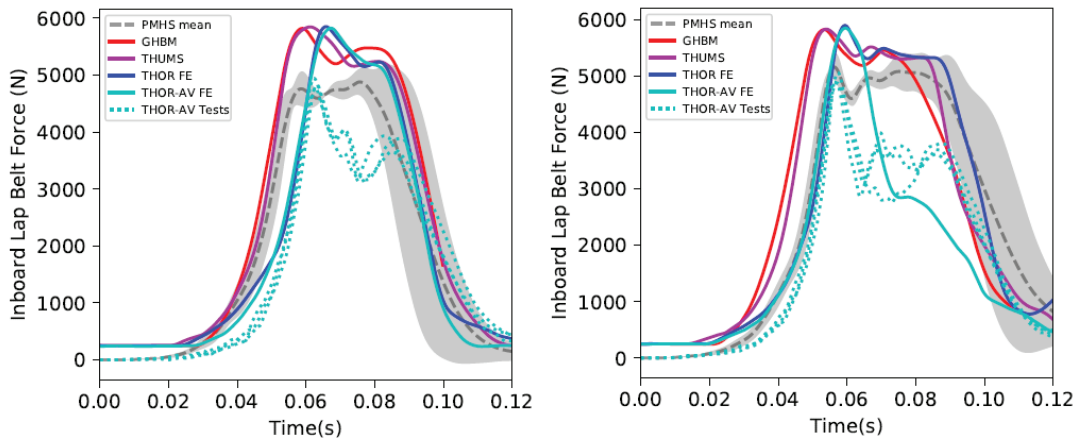


Figure A3. Inboard lap belt force in the front-seat (Case #1, left) and the rear-seat (Case #2, right) test configurations.

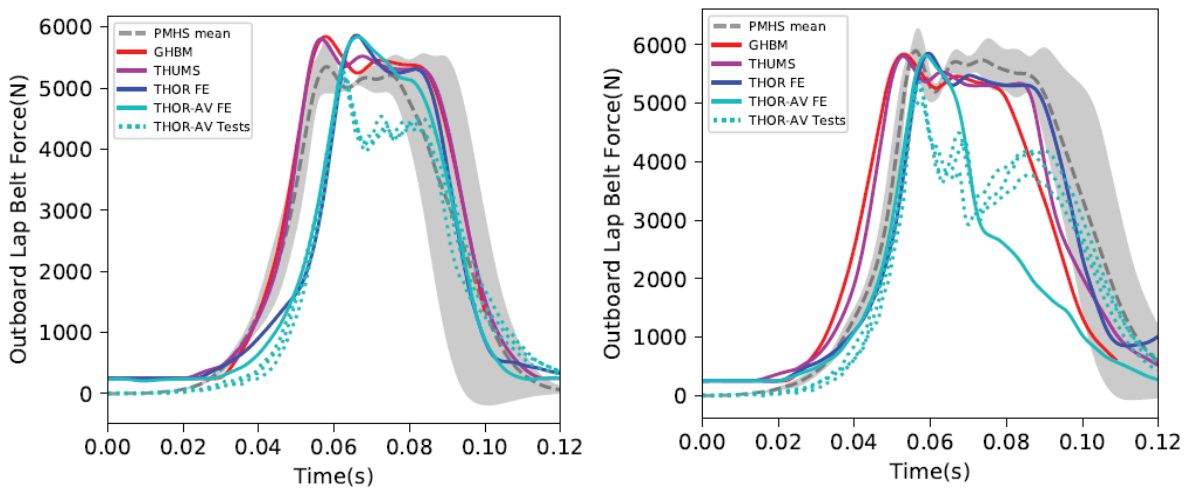


Figure A4. Outboard lap belt force in the front-seat (Case #1, left) and the rear-seat (Case #2, right) test configurations.

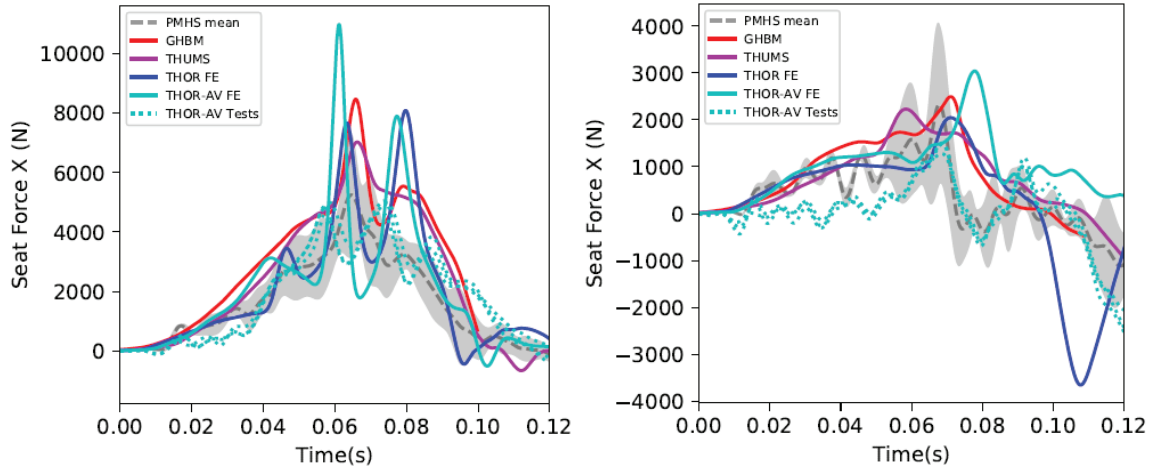


Figure A5. Seat force X in the front-seat (Case #1, left) and the rear-seat (Case #2, right) test configurations.

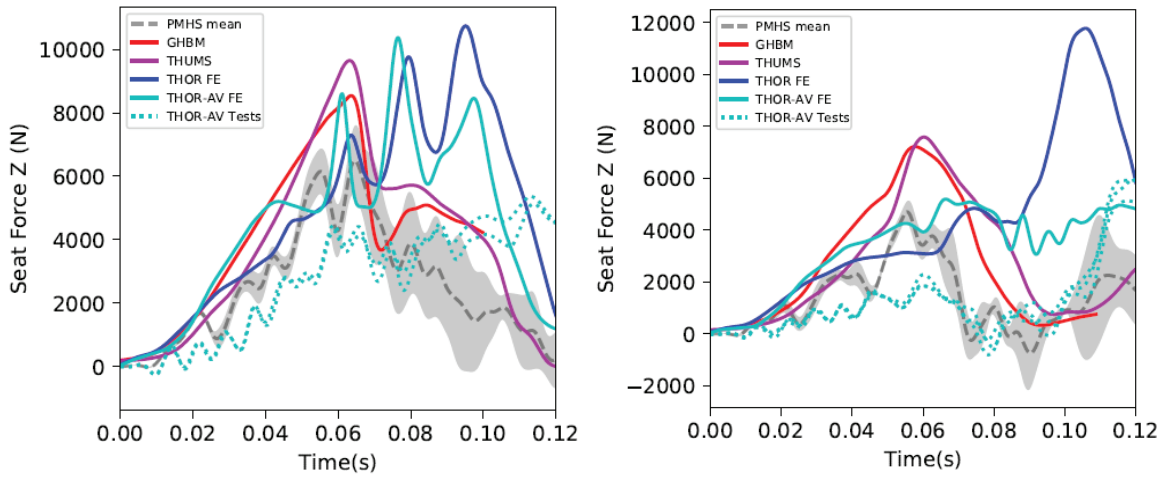


Figure A6. Seat force Z in the front-seat (Case #1, left) and the rear-seat (Case #2, right) test configurations

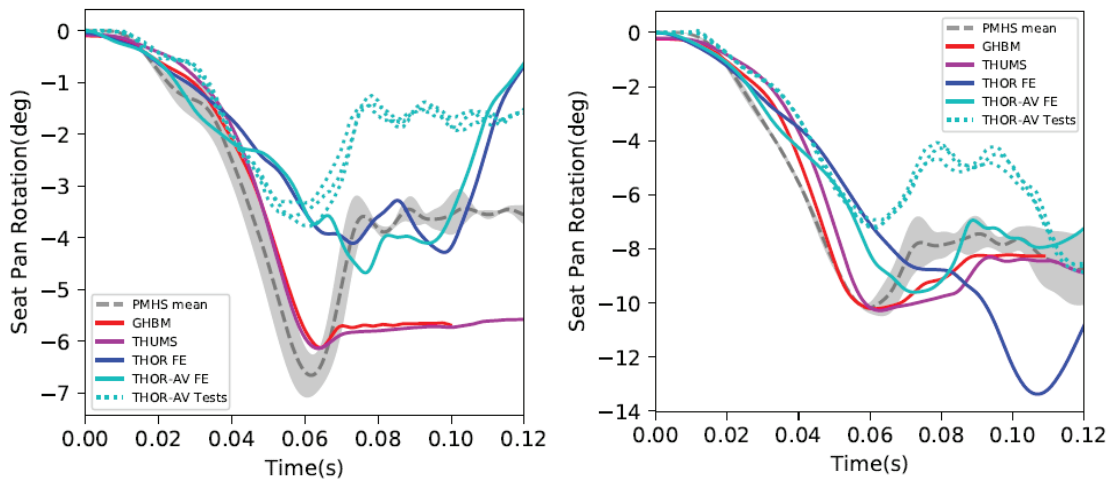


Figure A7. Seat pan rotation in the front-seat (Case #1, left) and the rear-seat (Case #2, right) test configurations.

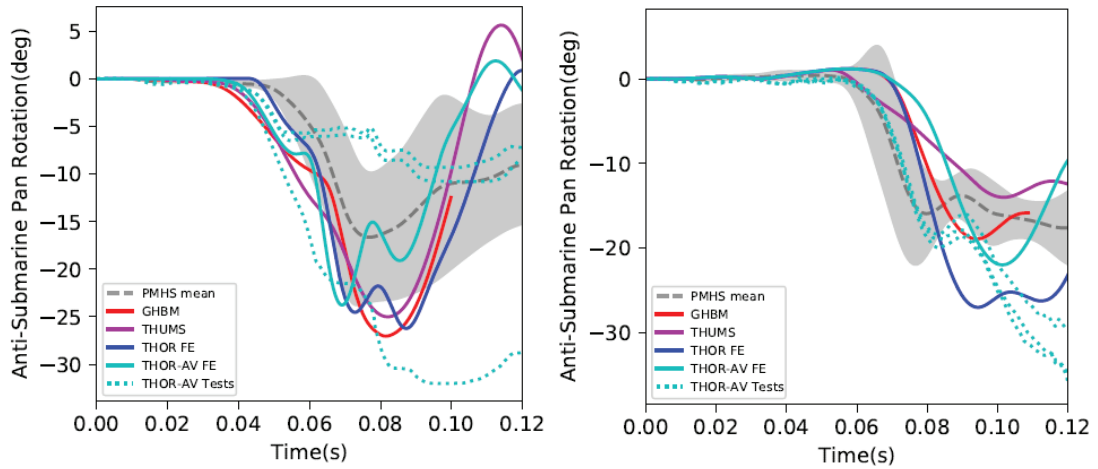


Figure A8. Anti-submarine plate rotation in the front-seat (left) and the rear-seat (right) test configurations.

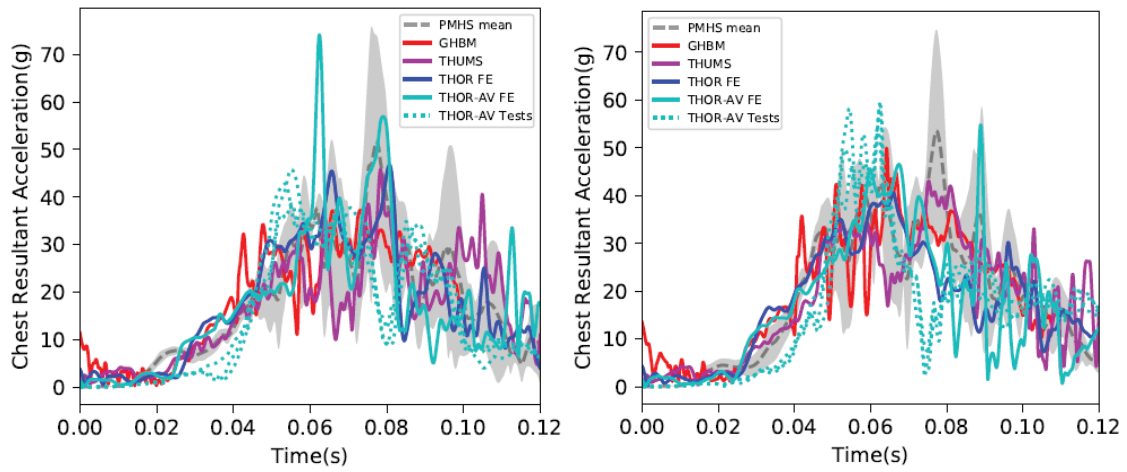


Figure A9. Chest resultant acceleration in the front-seat (Case #1, left) and rear-seat (Case #2, right) test configurations.

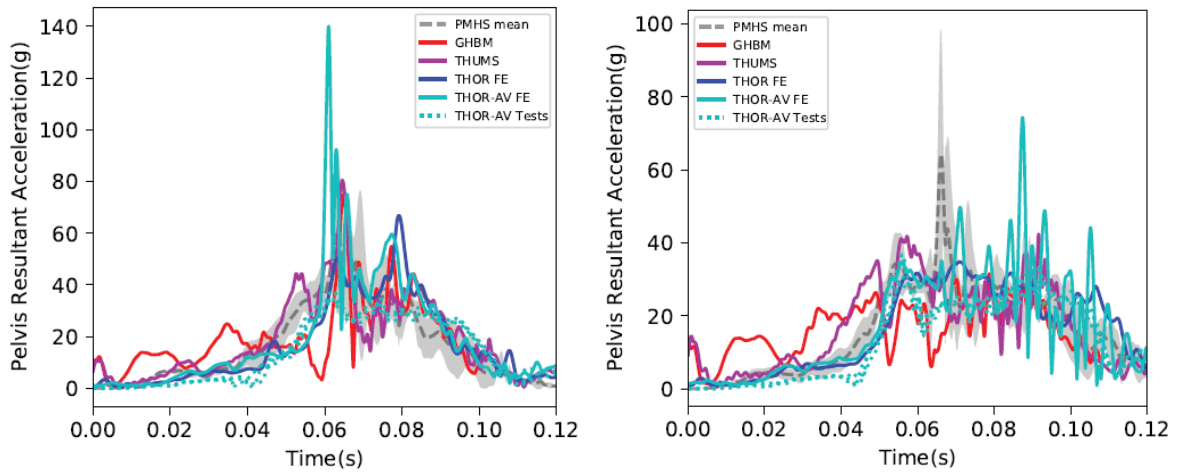


Figure A10. Pelvis resultant acceleration in the front-seat (Case #1, left) and the rear-seat (Case #2, right) test configurations.

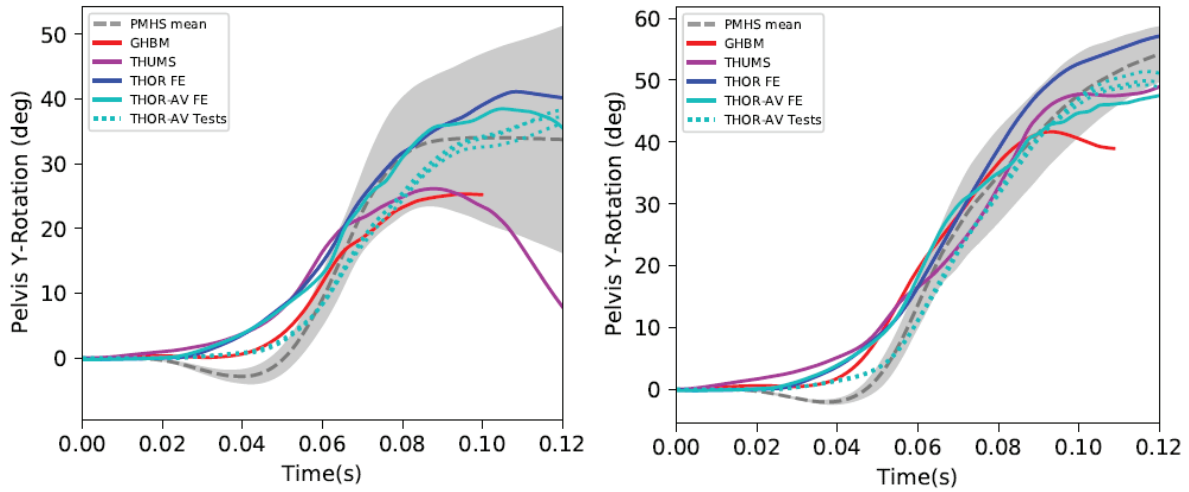


Figure A11. Pelvis y-rotation in the front-seat (Case #1, left) and the rear-seat (Case #2, right) test configurations.

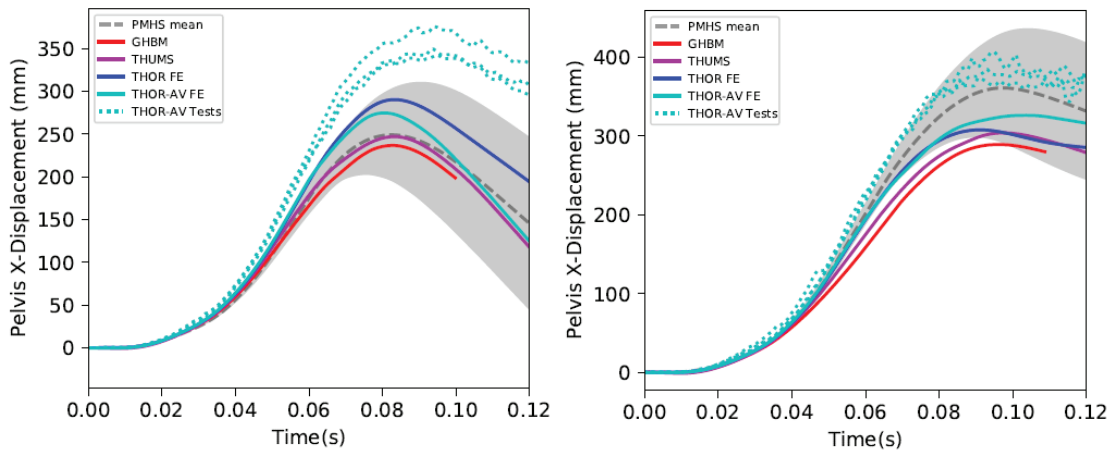


Figure A12. Pelvis x-displacement in the front-seat (Case #1, left) and rear-seat (Case #2, right) test configurations.

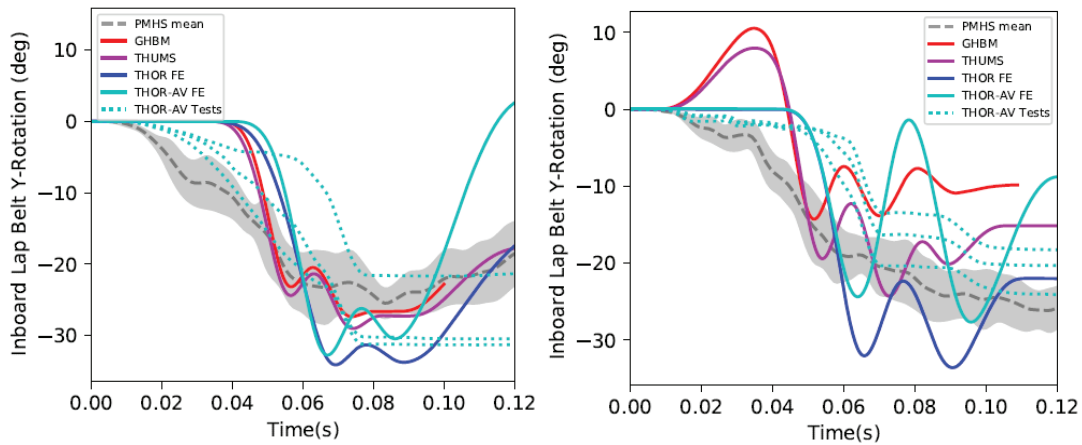


Figure A13. Inboard lap belt y-rotation in the front-seat (Case #1, left) and the rear-seat (Case #2, right) test configurations.

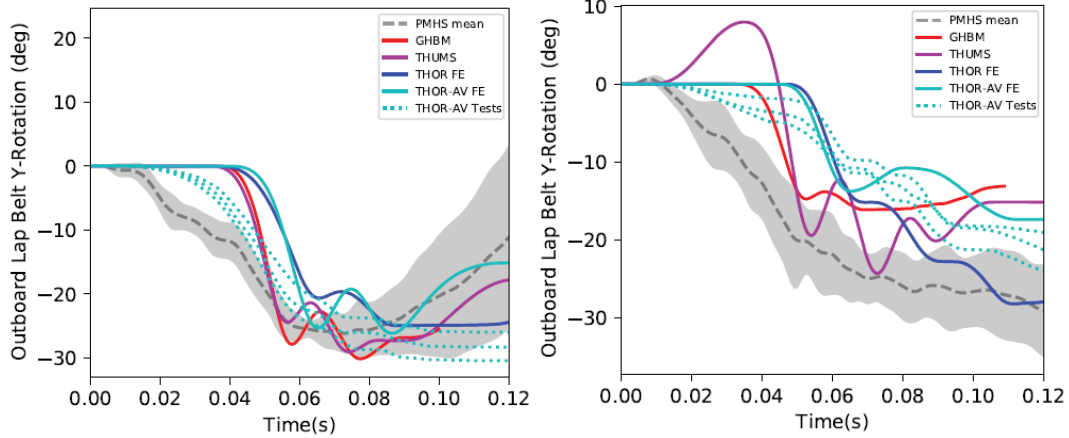


Figure A14. Outboard lap belt y-rotation in the front-seat (Case #1, left) and the rear-seat (Case #2, right) test configurations.

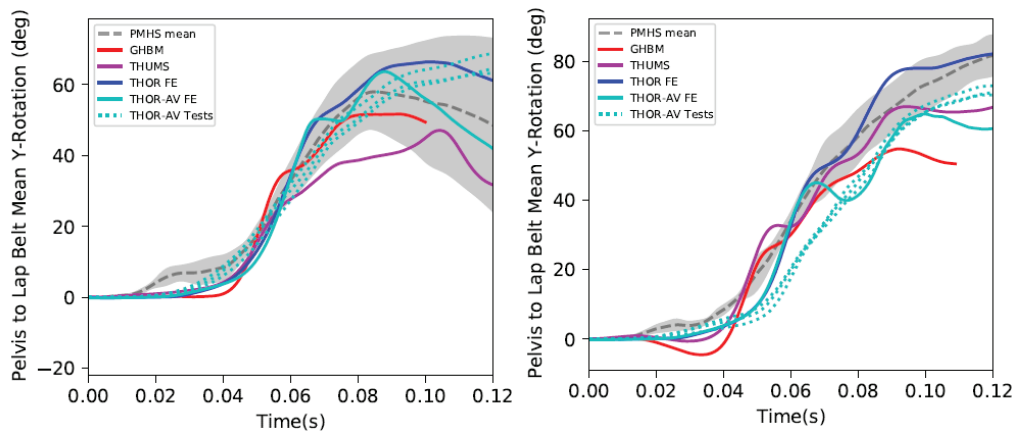


Figure A15. Pelvis to lap belt mean relative y-rotation in the front-seat (Case #1, left) and rear-seat (Case #2, right) test configurations.

Plots for the UMTRI 25° and 45° test configurations (Case #3 and #4)

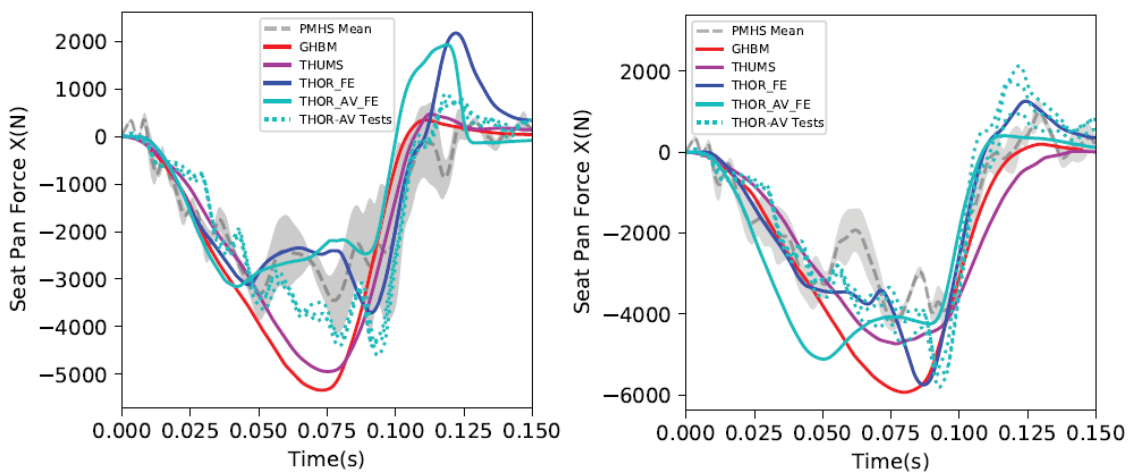


Figure A16. Seat pan force X in 25° (Case #3, left) and 45° (Case #4, right) seatback UMTRI test configurations.

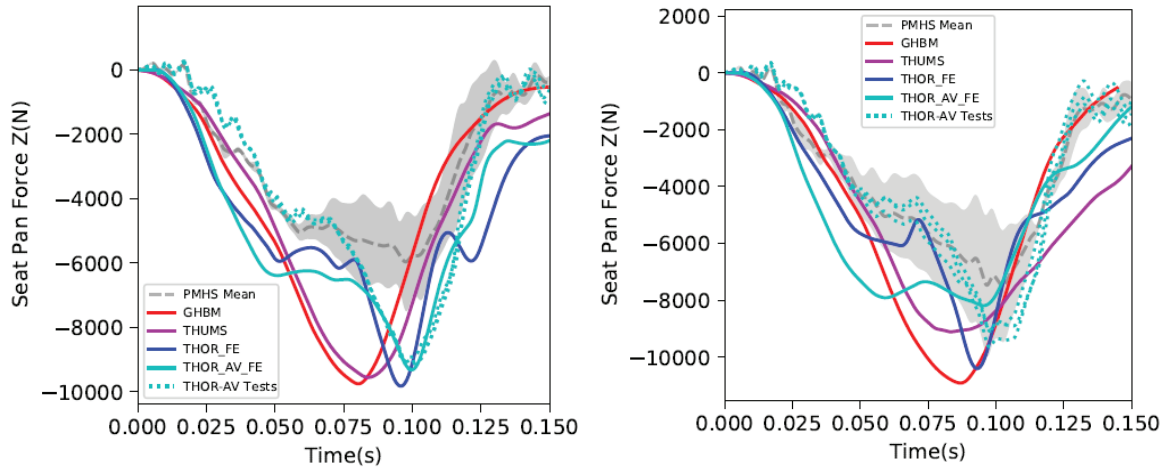


Figure A17. Seat pan force Z in 25° (Case #3, left) and 45° (Case #4, right) seatback UMTRI test configurations.

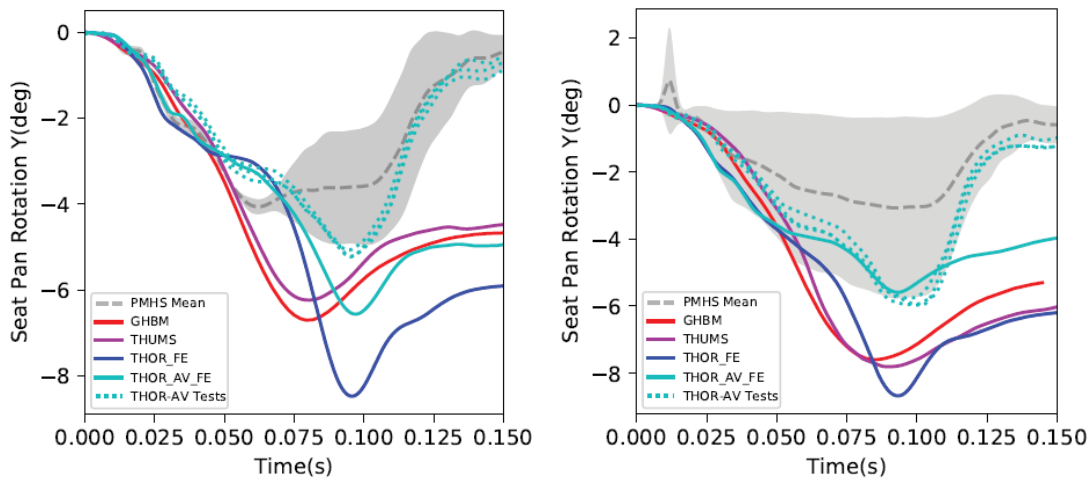


Figure A18. Seat pan rotation Y in 25° (Case #3, left) and 45° (Case #4, right) seatback UMTRI test configurations.

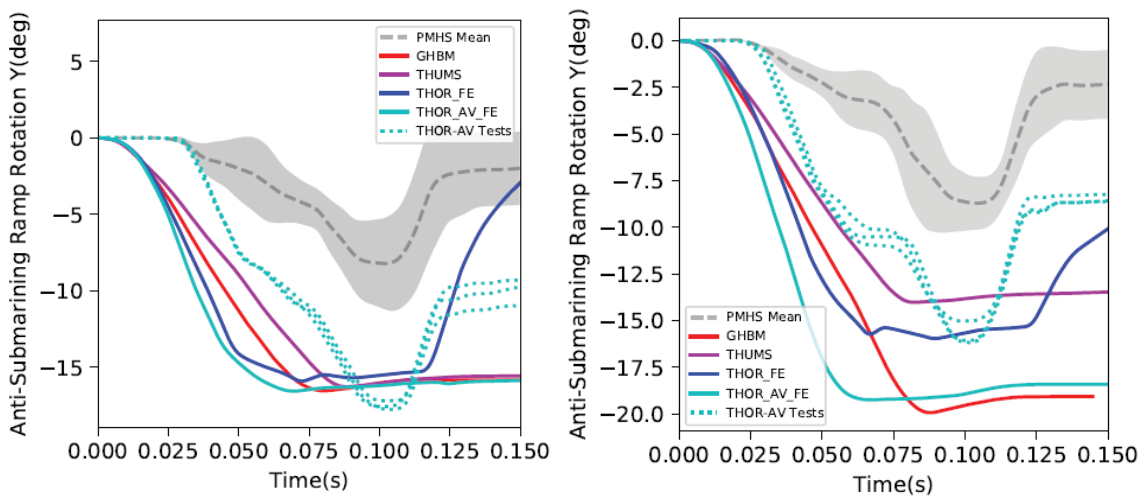


Figure A19. Anti-submarining ramp rotation in 25° (Case #3, left) and 45° (Case #4, right) seatback UMTRI test configurations.

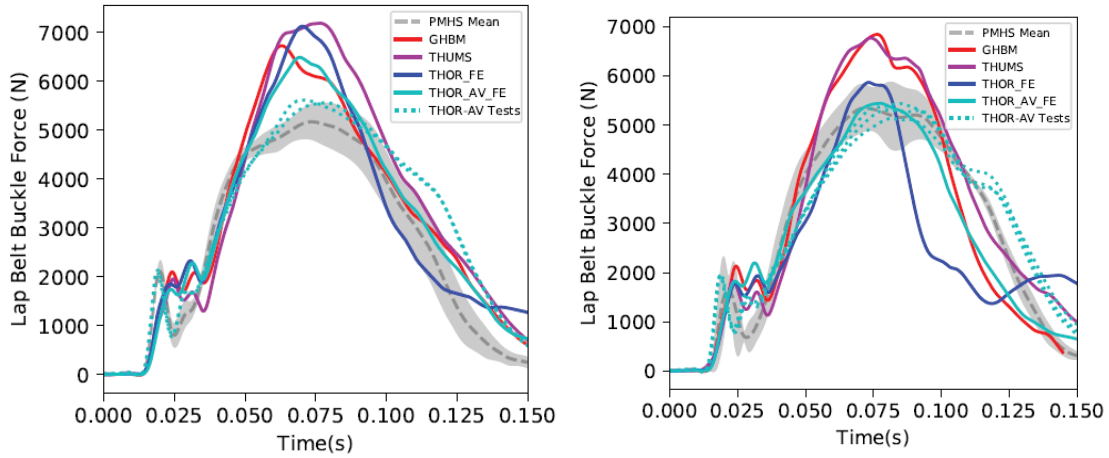


Figure A20. Buckle force in 25° (Case #3, left) and 45° (Case #4, right) seatback UMTRI test configurations.

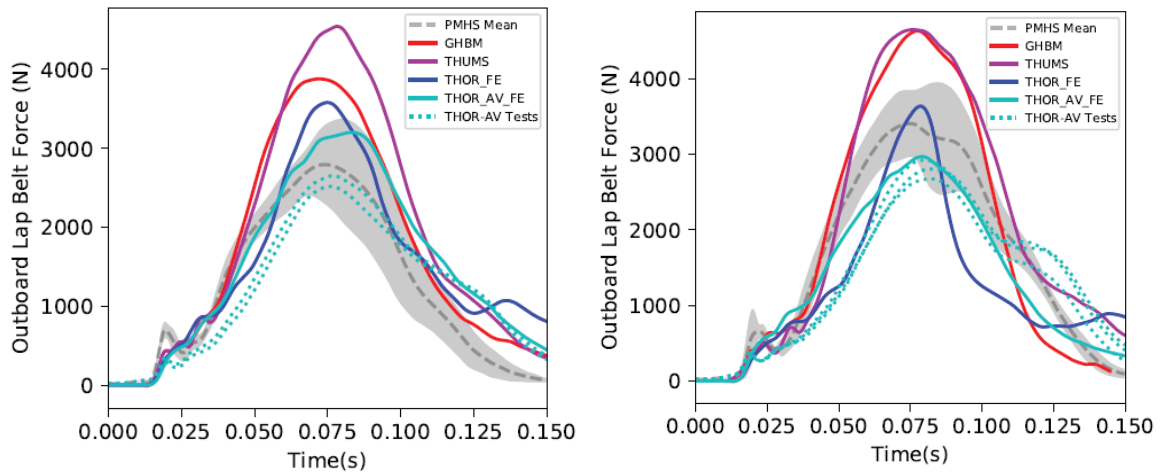


Figure A21. Outboard lap belt force in 25° (Case #3, left) and 45° (Case #4, right) seatback UMTRI test configurations.

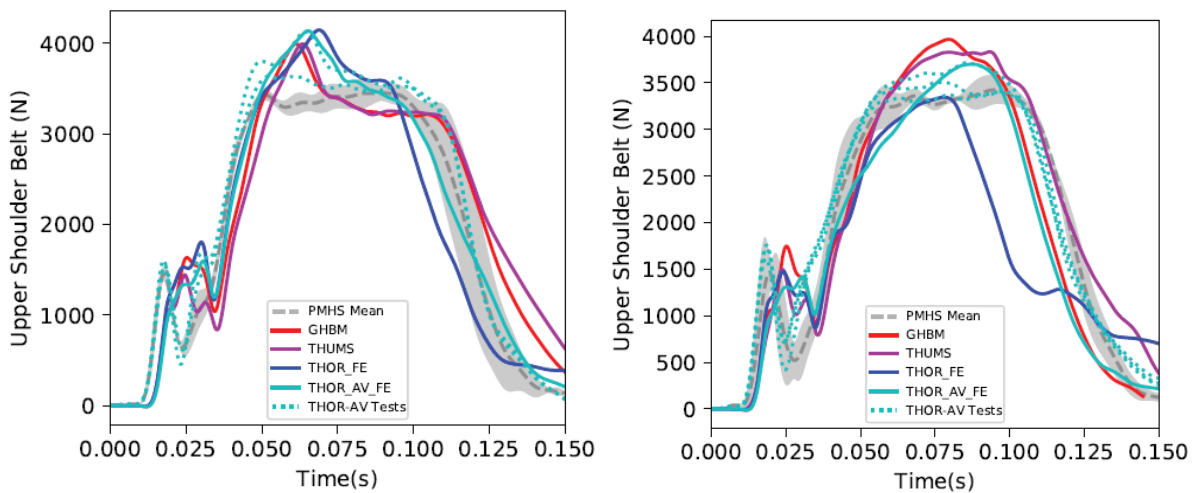


Figure A22. Upper shoulder belt force in 25° (Case #3, left) and 45° (Case #4, right) seatback UMTRI test configurations.

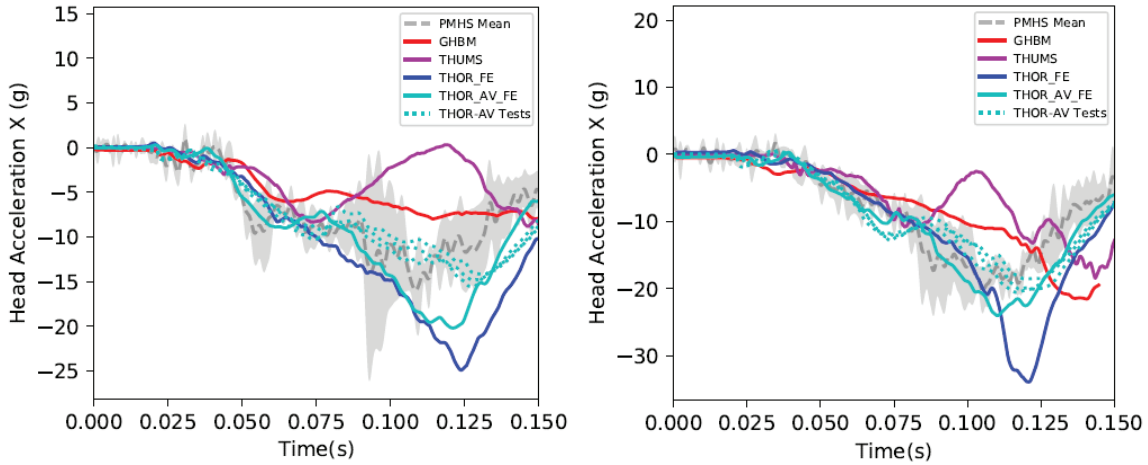


Figure A23. Head acceleration X in 25° (Case #3, left) and 45° (Case #4, right) seatback UMTRI test configurations

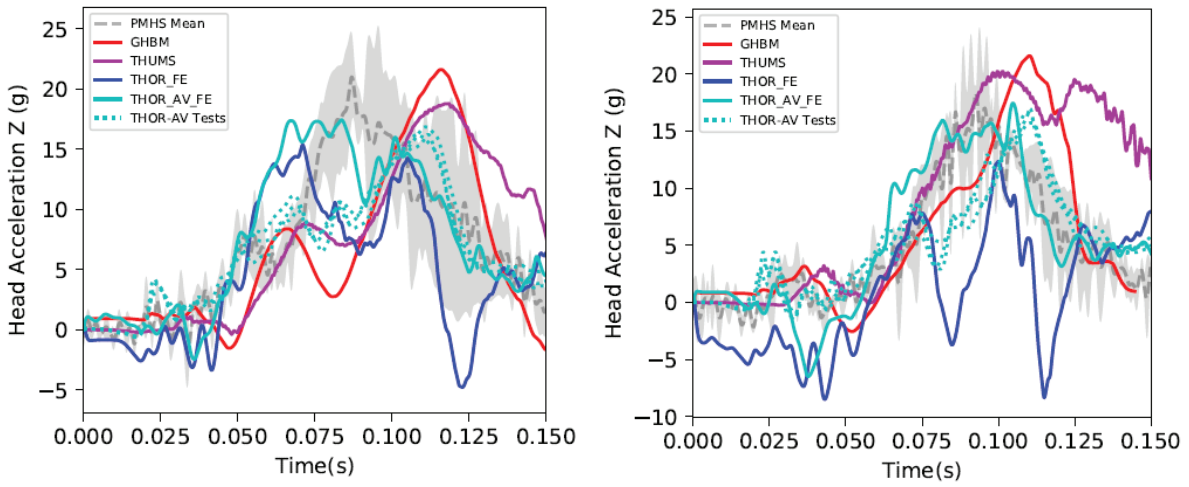


Figure A24. Head acceleration Z in 25° (Case #3, left) and 45° (Case #4, right) seatback UMTRI test configurations

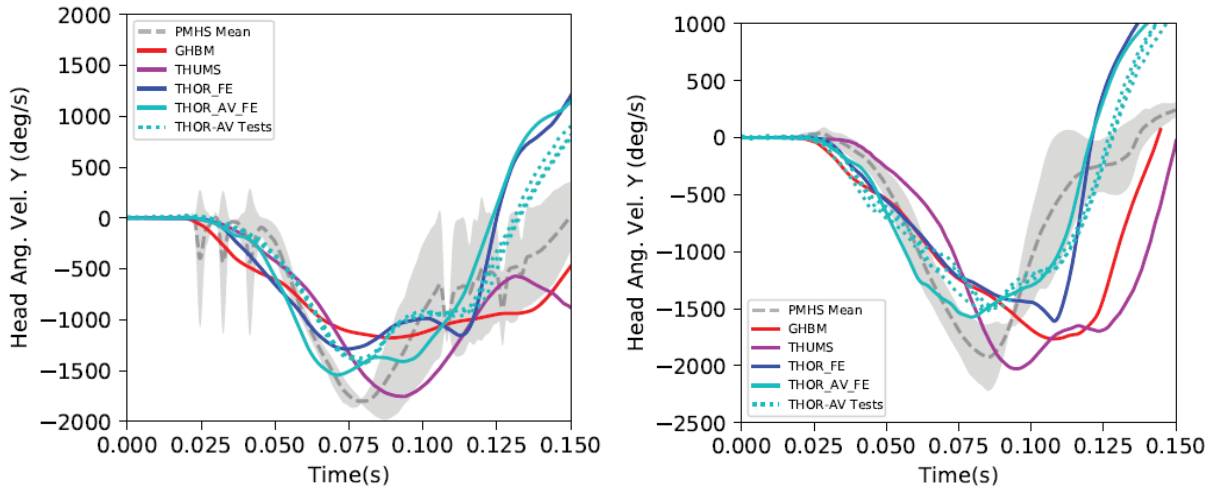


Figure A25. Head angular velocity Y in 25° (Case #3, left) and 45° (Case #4, right) seatback UMTRI test configurations

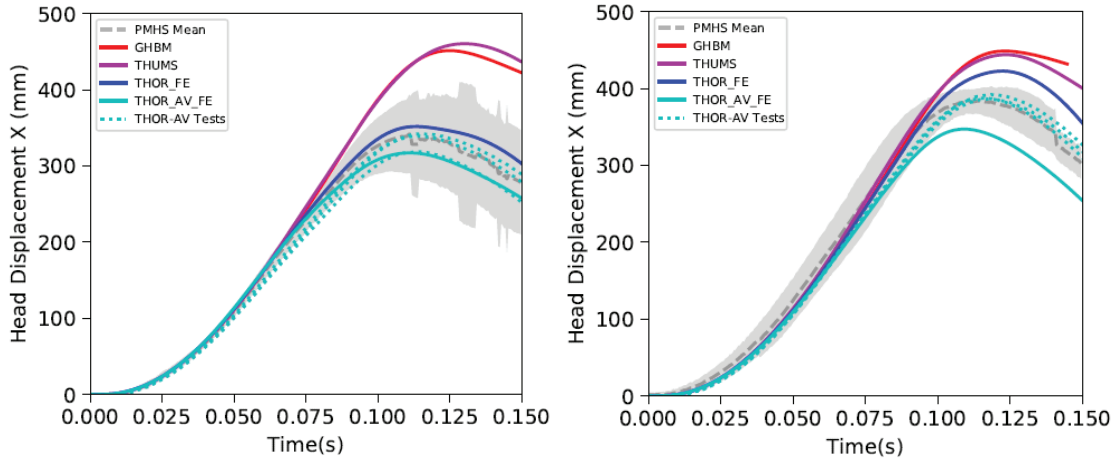


Figure A26. Head displacement X in 25° (Case #3, left) and 45° (Case #4, right) seatback UMTRI test configurations

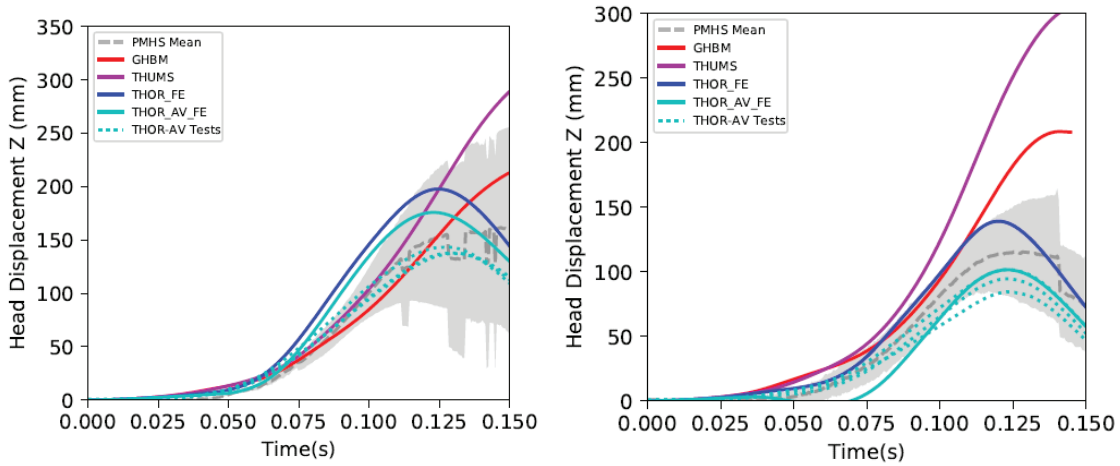


Figure A 27. Head displacement Z in 25° (Case #3, left) and 45° (Case #4, right) seatback UMTRI test configurations

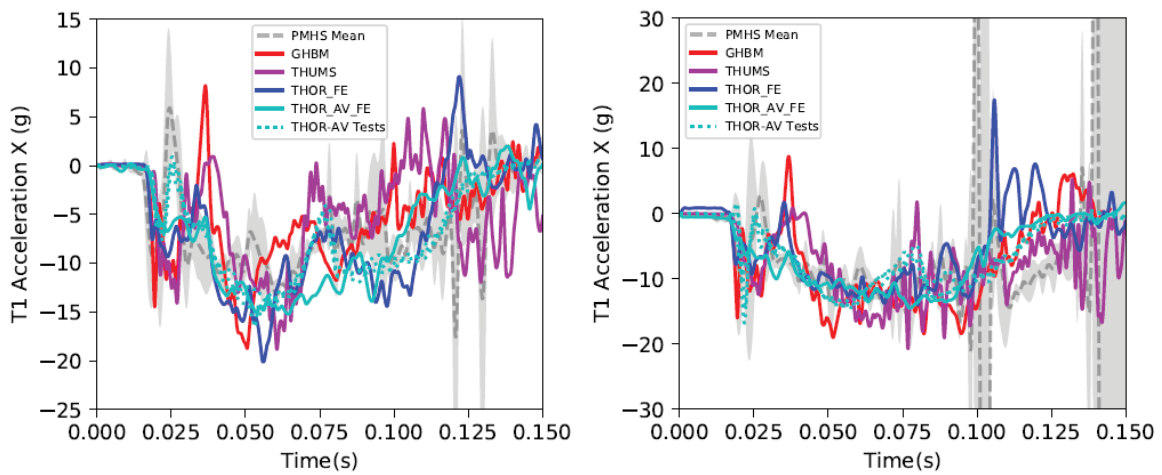


Figure A28. T1 acceleration X in 25° (Case #3, left) and 45° (Case #4, right) seatback UMTRI test configurations.

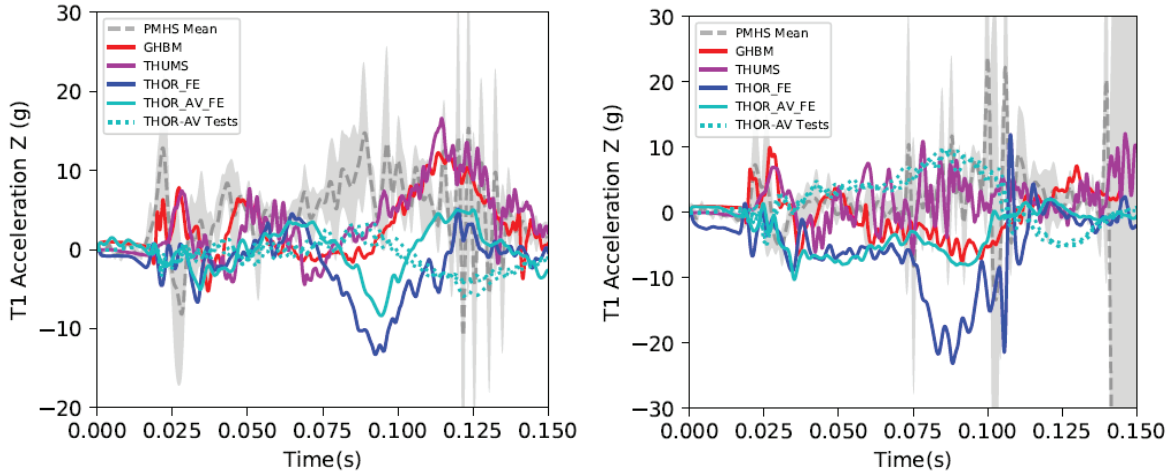


Figure A29. T1 acceleration Z in 25° (Case #3, left) and 45° (Case #4, right) seatback UMTRI test configurations.

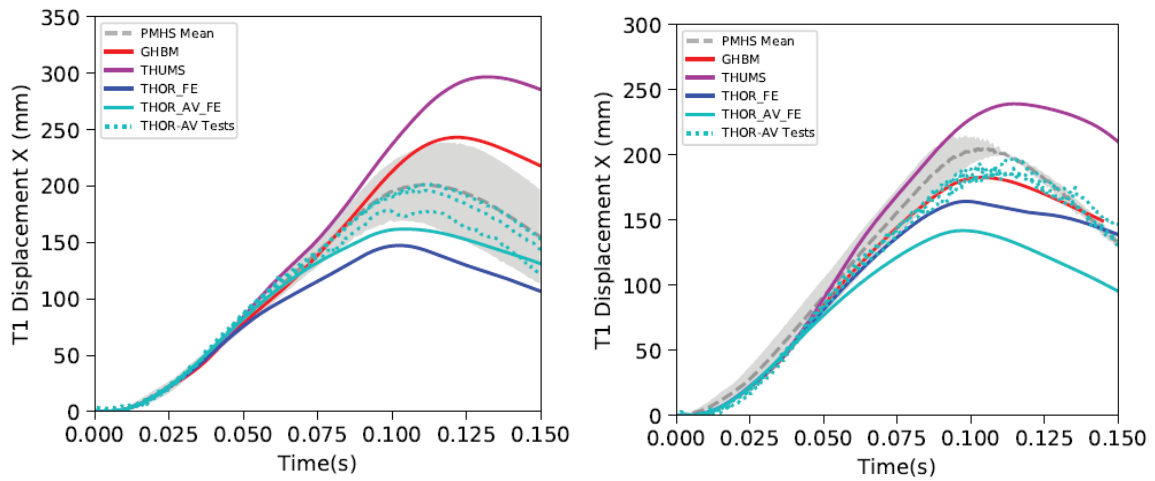


Figure A30. T1 displacement X in 25° (Case #3, left) and 45° (Case #4, right) seatback UMTRI test configurations.

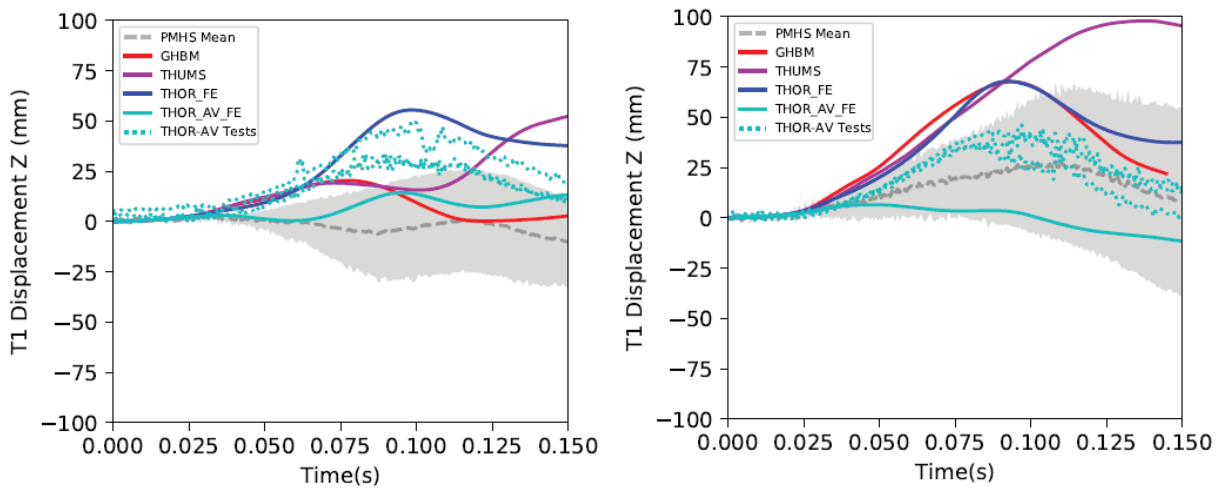


Figure A31. T1 displacement in Z in 25° (Case #3, left) and 45° (Case #4, right) seatback UMTRI test configurations

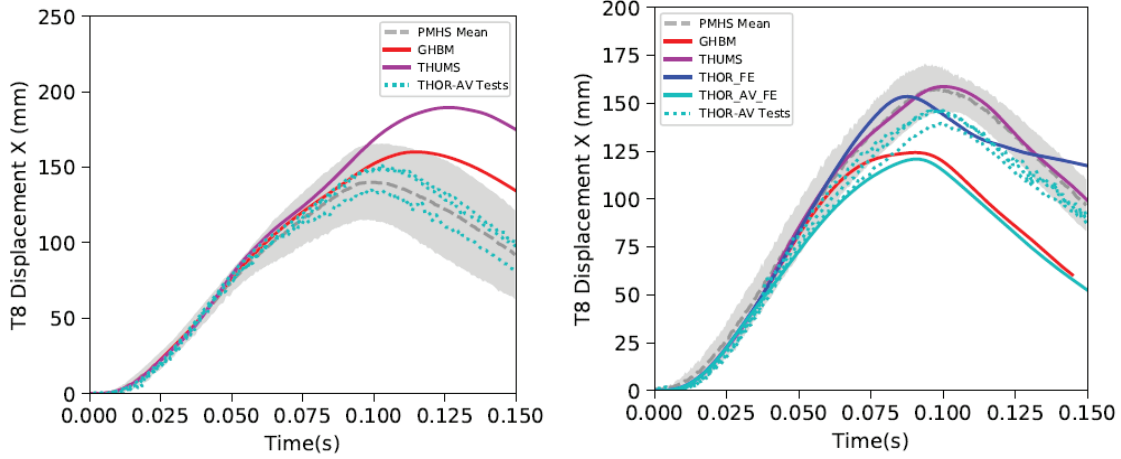


Figure A32. T8 displacement X in 25° (Case #3, left) and 45° (Case #4, right) seatback UMTRI test configurations.

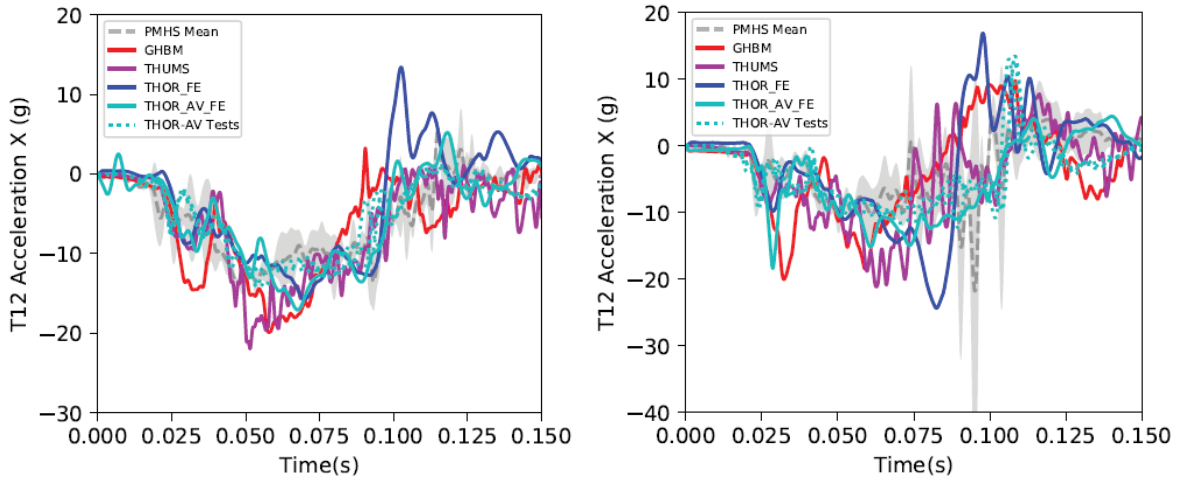


Figure A33. T12 acceleration X in 25° (Case #3, left) and 45° (Case #4, right) seatback UMTRI test configurations.

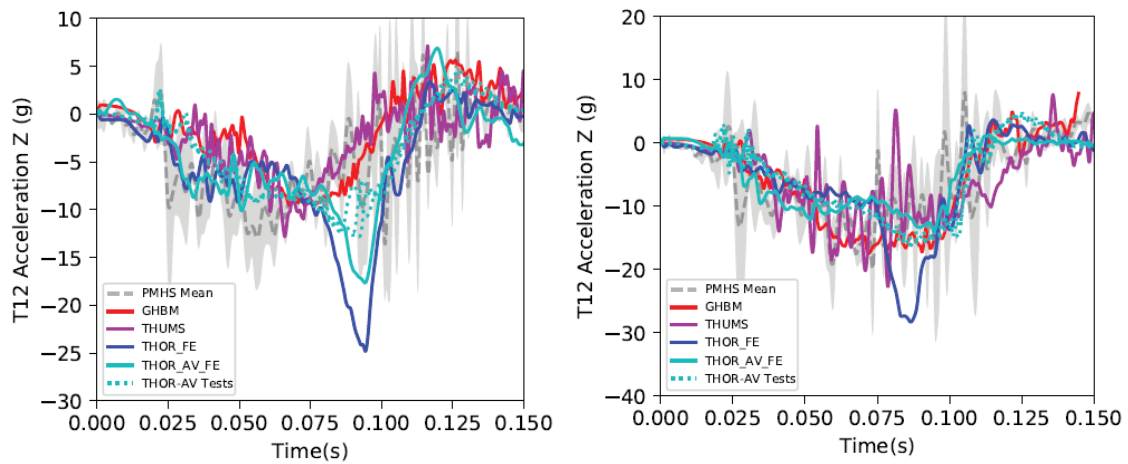


Figure A34. T12 acceleration Z in 25° (Case #3, left) and 45° (Case #4, right) seatback UMTRI test configurations

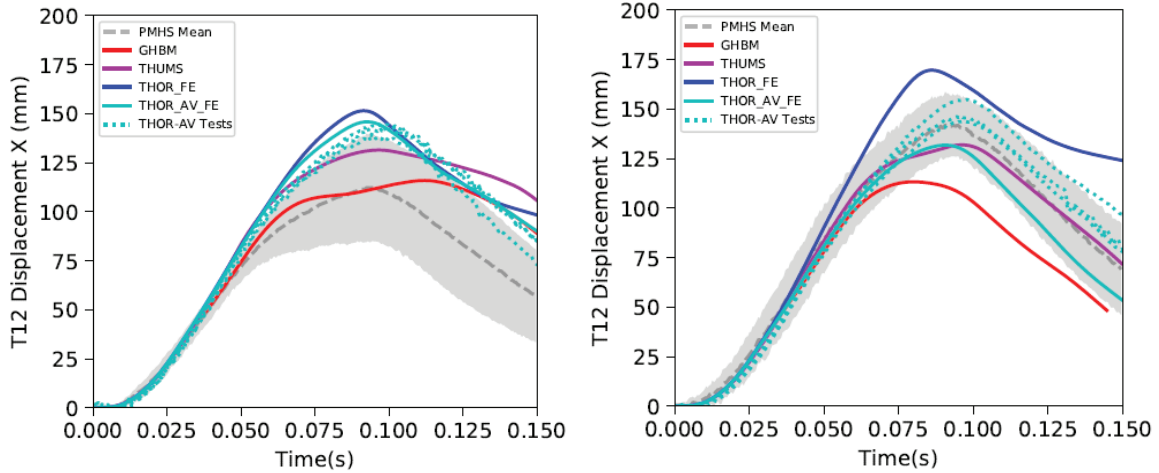


Figure A35. T12 displacement X in 25° (Case #3, left) and 45° (Case #4, right) seatback UMTRI test configurations

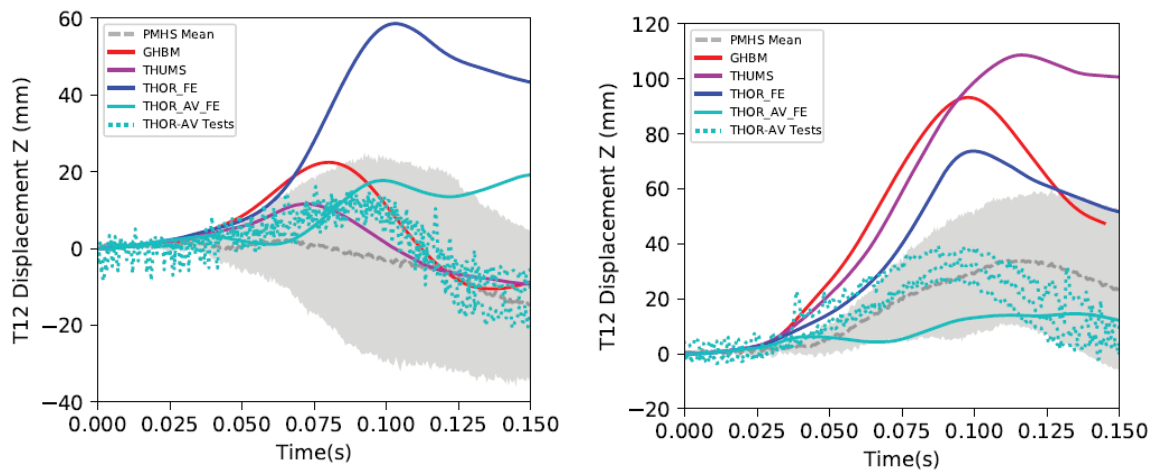


Figure A36. T12 displacement Z in 25° (Case #3, left) and 45° (Case #4, right) seatback UMTRI test configurations

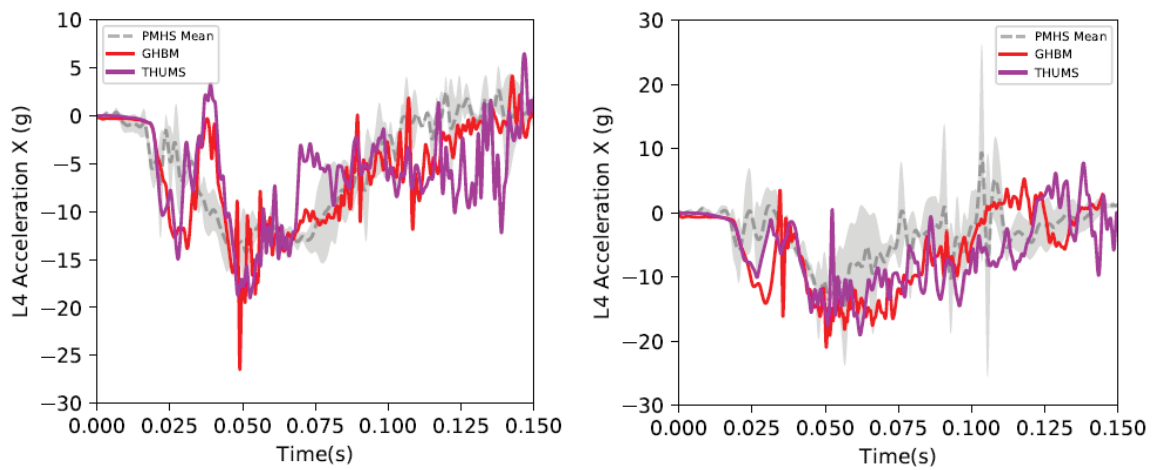


Figure A37. L4 acceleration X in 25° (Case #3, left) and 45° (Case #4, right) seatback UMTRI test configurations

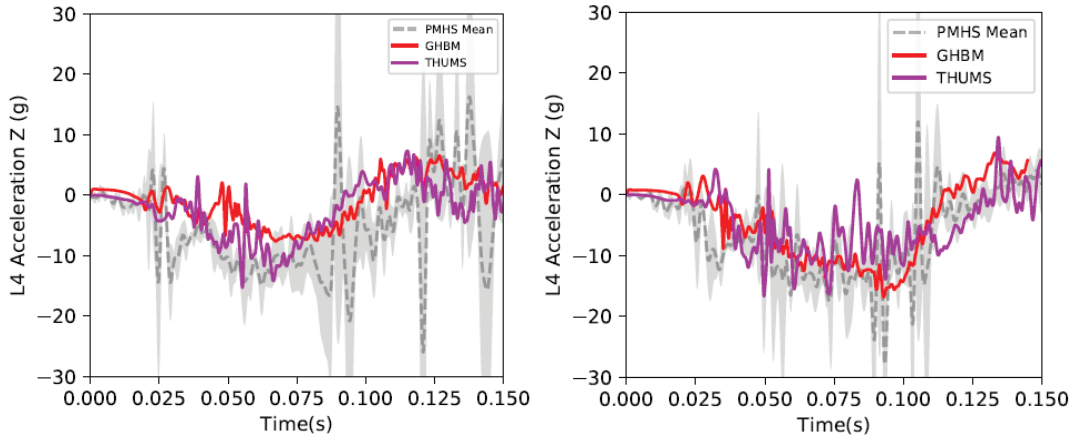


Figure A38. L4 acceleration Z in 25° (Case #3, left) and 45° (Case #4, right) seatback UMTRI test configurations

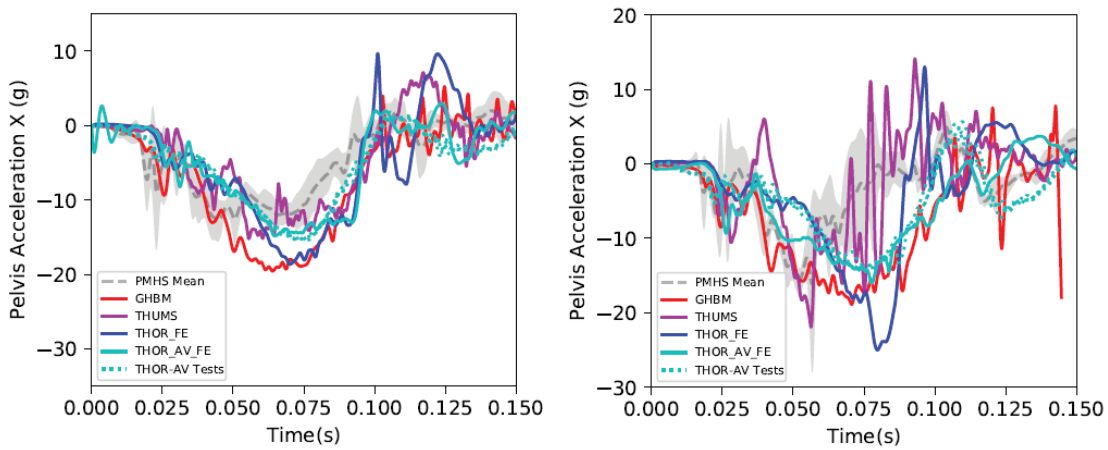


Figure A39. Pelvis acceleration X in 25° (Case #3, left) and 45° (Case #4, right) seatback UMTRI test configurations

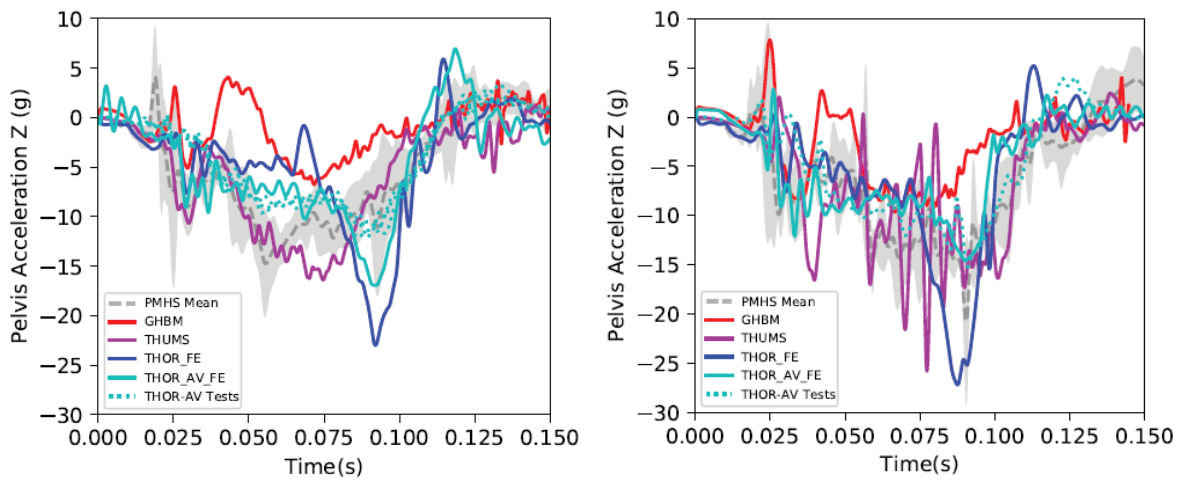


Figure A40. Pelvis acceleration Z in 25° (Case #3, left) and 45° (Case #4, right) seatback UMTRI test configurations.

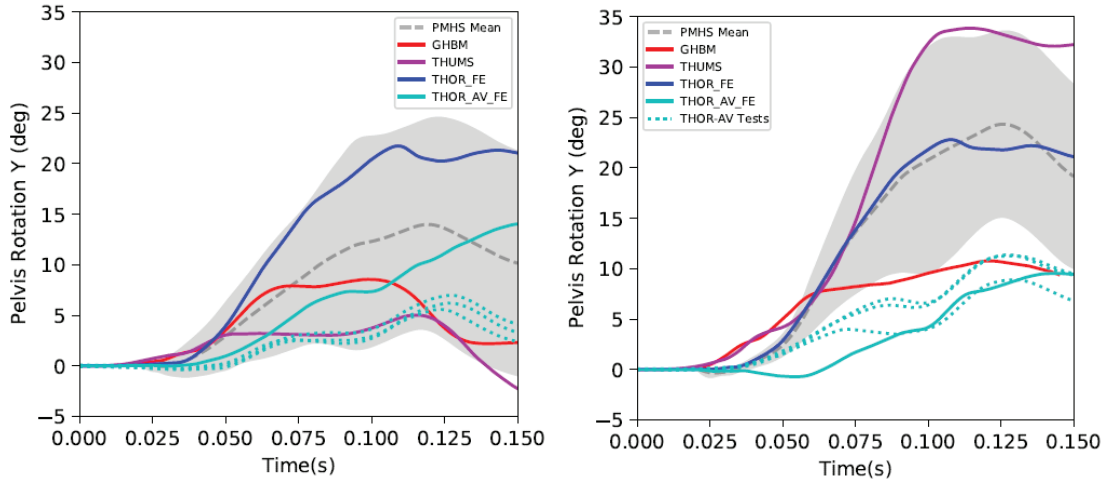


Figure A41. Pelvis rotation Y in 25° (Case #3, left) and 45° (Case #4, right) seatback UMTRI test configurations.

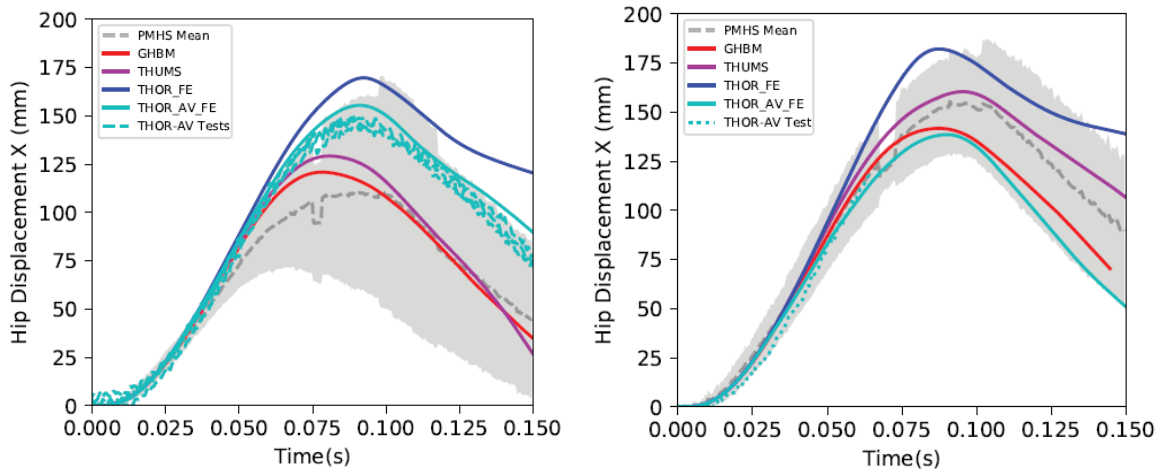


Figure A42. Hip displacement X in 25° (Case #3, left) and 45° (Case #4, right, partial data only in THOR-AV test due to the video target mounting bracket breakage) seatback UMTRI test configurations.

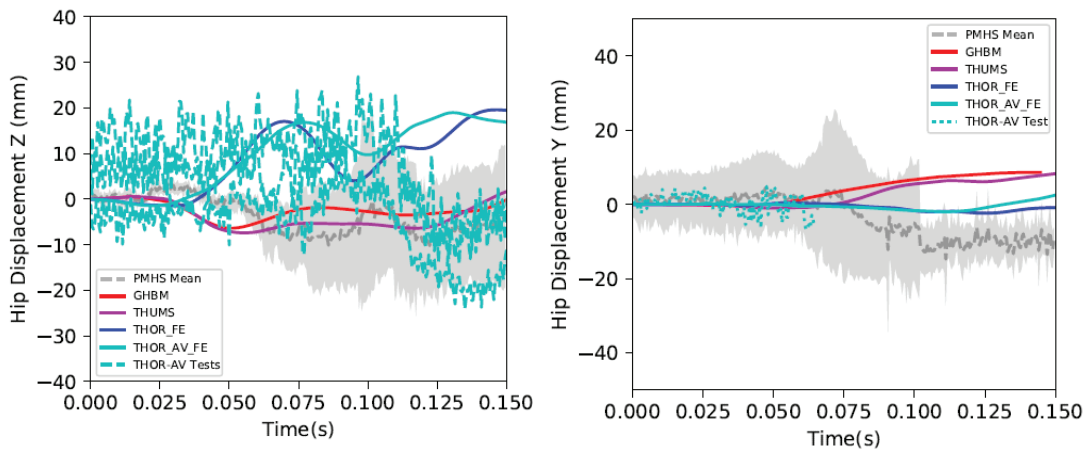


Figure A43. Hip displacement Z in 25° (Case #3, left) and 45° (Case #4, right, partial data only in THOR-AV test due to the video target mounting bracket breakage) seatback UMTRI test configurations

SENSITIVITY OF CHEST DEFLECTION MEASUREMENTS IN THOR-5F AND HYBRID III SMALL FEMALE DUMMIES TO DIFFERENT SEAT AND BELT SETTINGS

Andre Eggers, Matthias Schiebler, Julian Ott, Tobias Langner, Marcus Wisch
Federal Highway Research Institute (BAST)
Germany

Paper Number 23-0301

ABSTRACT

In frontal impact test procedures, the Hybrid III small female dummy is used to increase the protection of small car occupants. To address the increased thoracic injury risk for elderly occupants it is planned to introduce more stringent chest assessment criteria. However, previous studies raised concerns regarding the efficiency of criteria based on chest deflections measurements in the Hybrid III due to sensitivity of the measurements to variations in belt routing due to seat and D-ring settings. The seat in the most forward position and the D-ring in the highest position is mostly used in assessment tests. These settings result in a belt routing closer to the neck and reduced mid sternum chest deflection, which is not presentative of the actual peak deflection and therefore not meaningful to assess the chest injury risk.

The objective of this study was to investigate the effect of chest deflection sensitivity in the Hybrid III small female dummy in a generic sled test setup to variations of belt routings representative of contemporary vehicles. The study was complemented by sled tests with the THOR-5F in the same configurations to investigate the potential of this dummy as a future alternative. Furthermore, an analysis of field data was done to evaluate the preferred seat and D-ring settings of real small car occupants.

The results of the tests with the Hybrid III small female could confirm the findings from previous studies with shoulder belt routings representing contemporary vehicles. A routing with the belt closer to the neck showed a reduced sternal chest deflection in the Hybrid III small female. Corresponding tests with the THOR-5F showed a similar reduction of peak chest deflection at the maximum loaded IR-TRACC, but an increase at another location. Therefore, THOR-5F multi-point criteria might have the potential to address the issue of belt routing sensitivity.

The analysis of field data showed that small occupants representing the small female dummy in terms of height prefer to set the D-ring to the lowest position (driver and passenger). For the front seat passenger, the seat longitudinal and height setting mid/mid is preferred.

In conclusion the recommendations regarding seat and D-ring settings that were provided in previous studies can be confirmed. To enable an effective evaluation of chest injury risk with the Hybrid III small female the D-ring should be set to the lowest position for the driver as well as for the passenger side. For the passenger side the seat should be set to the mid/mid-position. Furthermore, these seat and D-ring settings are the most relevant preferred by small occupants based on field data.

For additional improvement of chest injury risk assessment considering the specific needs of small female occupants further research is recommended related to the THOR-5F and advanced multi-point chest injury criteria, which might be less sensitive to test parameters and resulting variation of belt routing. Repeatability and reproducibility of the chest deflection response of the THOR-5F dummy related the sensitivity of multi-point deflection measurements should be further investigated and improved if necessary.

INTRODUCTION

To increase the level of protection for all occupants involved in a frontal impact accident a frontal full-width test with a Hybrid III small female dummy in a front seat position was introduced by consumer testing organizations as well as in regulations. NHTSA (National Highway Traffic Safety Administration) introduced a full-width test to US NCAP in 2011 with a Hybrid III small female dummy on the front passenger seat. Euro NCAP introduced a 50 km/h full width rigid barrier test in 2015 with a Hybrid III small female dummy in the driver and front passenger seat as well as in the rear seat row.

Several studies have shown that elderly occupants have an increased risk of thoracic injury in frontal impact accidents. Wisch et al. 2017 identified the thorax as the most frequently injured body region for car occupants in frontal impacts with a risk of thoracic injuries at least two times greater for older car occupants. Forman et al. 2019 came to the conclusions that risk reduction in the thorax has lagged other body regions, resulting in increasing prevalence among skeletal injuries in newer vehicles especially in the elderly. Digges et al. 2013 recommended the application of older occupant risk to increase the level of protection of elderly car occupants. Age-specific injury risk functions were proposed by Laituri et al. 2005 and Prasad et al. 2010. Following those recommendations Euro NCAP will reduce the Hybrid III small female chest deflection lower performance and capping limit from the year 2023 onwards from 42 mm to 34 mm (Euro NCAP, 2022).

However, several studies have previously reported concerns related to the currently applied test tool and chest deflection instrumentation, which is the Hybrid III small female dummy with a rotational potentiometer measuring the chest deflection at one single point in the mid sternum. Therefore, to address the increased thoracic injury risk of small elderly occupants it might not be sufficient to use stricter chest deflection performance limits. Improvements to the tests tool or at least updates to the test and assessment procedure that result in reasonable chest deflection measurements are necessary.

Yamasaki et al. 2011 reported that in full-scale crash tests comparing different belt positions on the chest of a Hybrid III small female a reduction of chest deflection with the belt positioned closer to the neck was observed. Further studies investigated the effect of seat track settings and D-ring position on the belt path on the dummy chest and the resulting chest deflection measurements. Keon et al. 2016 conducted frontal impact crash tests according to the Euro NCAP test procedure with a Hybrid III small female dummy on the front passenger seat. Tests with the seat in mid track and most forward position were compared. The most forward seat position resulted in a belt routing closer to the neck and a lower chest deflection compared to the mid track seat position with a belt routing on the center of the sternum and a reductions of measured chest deflection. Digges et al. 2017 evaluated the chest deflection in the Hybrid III small female with the seat in the most forward position and the D-ring in the highest position, which is the setting preferred by vehicle manufactures and mostly used in NCAP tests. This was compared to tests with the seat in mid-track position and the D-ring in the lowest position. A significant increase in chest deflection was observed. They pointed out that is especially relevant for the protection of elderly occupants. Therefore, an improved test and assessment procedure is needed to make sure chest deflection risk is assessed in a reasonable way. Digges et al. 2019 further investigated the sensitivity of chest deflection measurements in NCAP crash tests for the Hybrid III 5% dummy to positioning of the seat and D-ring related to routing of the shoulder belt. Based on these studies the authors provided recommendations to address this issue.

One recommendation is to prescribe the seat and D-ring setting in the test procedure. The recommended setting for the passenger seat would be seat track in mid longitudinal position, mid height seat position and the D-ring set to the lowest position. This would result in a belt path closer to the center of the chest and a more meaningful chest deflection measurement.

Another recommendation from previous studies would be the use of multi-point chest deflection measurement systems like RibEye or IR-TRACC in the Hybrid III dummy (Eggers et al. 2014, Keon et al. 2015, Digges et al. 2019). In these studies, it was demonstrated in tests with multi-point chest deflection measurement in the Hybrid III that it would be possible to identify higher peak chest deflection which do not occur at the mid sternum and usually are higher for belt routings closer to the neck. However, so far, no biomechanical injury criteria are available for multi-point chest deflection measurements in the Hybrid III. Further research is needed. Meanwhile a more a biofidelic small female dummy, the THOR-5F (Wang et al. 2017), is becoming available which has multi-point chest deflection capability and could be a future alternative.

Another option proposed in the previous studies by Digges et al. is a landmark based belt routing procedure. However, after placing the belt on the mid center of the sternum with a landmark based procedure if the seat is in the most forward position and the D-ring in the highest setting the belt might move close to the neck again due to dummy movement during the deceleration pulse or already during the activation of a pretensioner.

Thus, the most effective and immediately applicable solution to achieve a more meaningful chest deflection measurement and chest injury risk assessment in the Hybrid III small female dummy would be to prescribe the seat and D-ring settings based on recommendations from previous studies in the relevant test and assessment procedure.

However, to make sure these seat and D-ring setting are not in contradiction with the preferred settings used by real car occupants field data should be analyzed understand how small occupant are using the seat and belt.

Furthermore, before recommending the test settings to be implemented by Euro NCAP or other worldwide consumer or regulatory test procedures the relevance of the findings observed in previous studies to other contemporary vehicles should be confirmed in additional tests.

The objective of this study was to investigate the effect of chest deflection sensitivity in the Hybrid III small female dummy in a generic sled test setup representing characteristic variations of belt routings in contemporary vehicles. The study was complemented by sled tests with the THOR-5F in the same configurations to investigate the potential of this dummy as a future alternative test tool to address the above-mentioned issues. Furthermore, an analyses of field data was done to evaluate the preferred seat and D-ring settings of small car occupants.

METHODS

Sled tests with Hybrid III small female and THOR-5F in a generic sled setup

To investigate the sensitivity of chest deflection measurements for different belt routings resulting from different settings of the front seat and D-ring height a series of frontal impact sled tests with the dummies Hybrid III small female and THOR-5F (build level SBL-A) was conducted. The tests were done in a generic sled test setup. The test setup with the THOR-5F is shown in Figure 1. It consisted of a rigid seat with a seat pan angle of 10°. The seat was covered with 40 mm Neopolen® foam. The seat back angle was 23°. The feet of the dummy were placed on a footrest covered with carpet. A production 3-point belt system was used with a 3.5 kN shoulder belt load limiter and a shoulder belt retractor pretensioner. The pretensioner was activated at 16ms. In all tests a 50 km/h full-width deceleration pulse was used (Figure 2).



Figure 1. Sled test setup: Rigid seat, 3-point belt system with shoulder belt pretensioner and load limiter

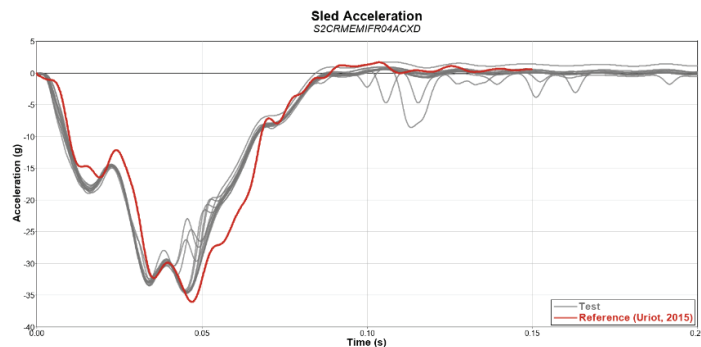


Figure 2. 50 km/h Full-Width Pulse (Reference Pulse Uriot, et al. 2015)

The belt anchorage points of the D-ring, buckle and anchor were adjustable to simulate different positions and settings of the D-ring, different longitudinal seat track positions and different seat height adjustments representing different vehicle geometries. Two different combinations of the belt anchorage points were used. The purpose of the two belt anchorage point settings was chosen to represent possible combinations and resulting belt routing of contemporary vehicles currently available on the European market.

To define the combinations of belt anchorage points the respective points were measured in three real vehicles. The chosen vehicles were Volkswagen Golf 7, Tesla Model 3 and Renault Zoe. An H-point tool was positioned

in the driver seat according to the Euro NCAP Full-Width-Frontal-Impact-Test-Protocol Version 1.2.1 (Euro NCAP, 2021). The seat was varied in longitudinal direction between the two settings “most forward” and “25% travel from most forward”. The variation of the seat height was done between the two settings “fully upward” and “75% downward” as defined in the Euro NCAP protocol. Additionally in combination with seat variations the D-ring was varied between the two settings “highest” and “lowest”. The combination of the different settings resulted in a maximum of eight different relative positions of the D-ring for the Golf and Tesla, which are shown in Figure 3. For the Zoe only four variations are shown as the seat was not adjustable in height. For the buckle only two different settings are shown in Figure 3 resulting from the two possible height settings for the seat of the Golf and Tesla. The fore-aft variation in longitudinal direction did not affect the related position to the H-point as the buckle was attached to the seat and therefore moving with the H-point in all of the three vehicles. The small variation of the buckle position in longitudinal (x-)direction results from the movement of the seat in x-direction related to the height adjustment.

Two characteristic combinations of anchorage points for the buckle and D-ring position relative to the H-point were chosen which are close to the possible variations representing the three vehicles. D1 is representing a belt routing more outboard on the shoulder of the occupant whereas D2 is representing a belt routing close to the neck. The location of the buckle and D-ring attachment points in relation to the possible coordinates measured in the three vehicles are shown in Figure 3.

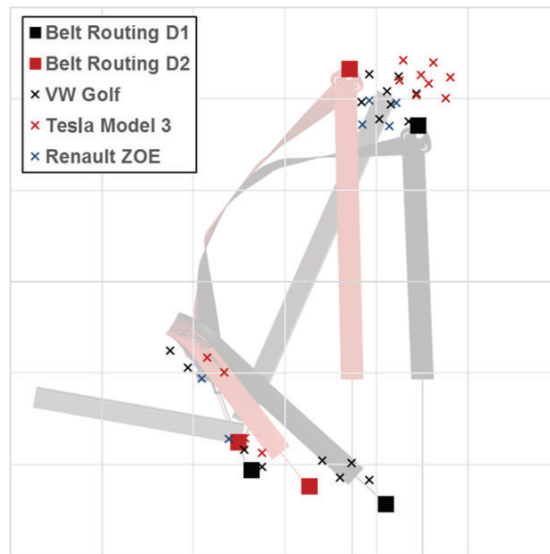


Figure 3. Buckle and D-ring anchorage points D1 and D2 chosen for the tests in the generic test setup relative to the possible points measured in three real vehicles.

The location of the buckle and D-ring attachment points for D1 and D2 were transferred to the generic test setup. The resulting belt routing with the two dummies Hybrid III small female and THOR-5F in the generic test setup are shown in Figure 4 and Figure 5.

Figure 4 shows the belt routing D1 with a chin to belt webbing distance of 125 mm for the Hybrid III and 100 mm for the THOR-5F. The belt routing is more outboard on the shoulder and covers the center of the chest. Figure 5 shows belt routing D2 with a chin to webbing distance of 105 mm for the Hybrid III and 65 mm for the THOR-5F closer to the neck. Three repeated tests were done with the Hybrid III small female and THOR-5F dummy for each of the belt routing configurations.

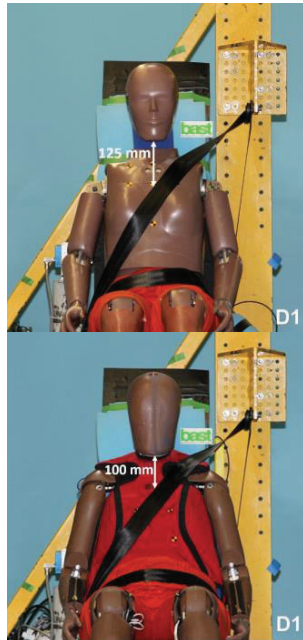


Figure 4. Belt routing D1 (shoulder belt more outboard on the clavicle)

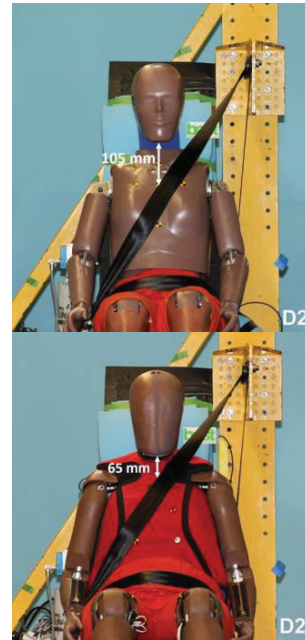


Figure 5. Belt routing D2 (shoulder belt close to the neck)

Field data study - seat adjustments and D-ring position

To evaluate how small occupants are represented by the small female dummy in terms of body height (Small female dummy reference standing height: 151 cm) field data from GIDAS (German In-Depth Accident Study, www.gidas.org) was considered. The database was not analyzed with the purpose to relate injury outcome to seat and belt settings, but only to evaluate the seat and belt settings of small car occupants.

The analysis was based on a GIDAS data set from June 2022 including passenger vehicles with first year of registration after 2004. Only accidents between passenger cars and cyclists were selected in this preliminary study as a high number of those cases exists in the database and to make sure the occupant of the vehicle of interest was almost never (even slightly) injured thus no modification of the seat and belt setting were expected during rescue after the accident. The selection criterion for the car occupant was a standing body height between 145 and 155 cm. The age of the occupant was not of further interest. For each driver or passenger fulfilling the above-mentioned criteria the settings of the D-ring (highest, mid or lowest) and the setting of the seat in longitudinal fore/aft position (most forward, mid or most rearward) and the seat height adjustment (highest, mid or lowest) was evaluated.

RESULTS

Dummy kinematics

Hybrid III small female D1 vs. D2

Upper body kinematics of the Hybrid III small female dummy are primarily influenced by the position of the D-ring with respect to the neck / clavicle (see Figure 4 and Figure 5). For belt routing D1 the belt is further away from the neck (more outboard on the shoulder), hence the belt force is applied further away from the spine and the leverage about the vertical axis of the dummy is consequently larger. Belt routing D2 is closer to the neck and the leverage accordingly smaller. Figure 6 shows the dummy kinematics at 75 ms and 100 ms. As a result of the different belt routings, rotation of the dummy's upper body about the vertical axis begins at approx. 60 ms for belt routing D1, while the dummy-to-belt interaction for belt routing D2 is more stable with no significant rotation of the upper body. The larger leverage for belt routing D1 does not only result in an earlier rotation of the dummy, also the overall rotation of the upper body is larger and the belt is close to slipping from shoulder.

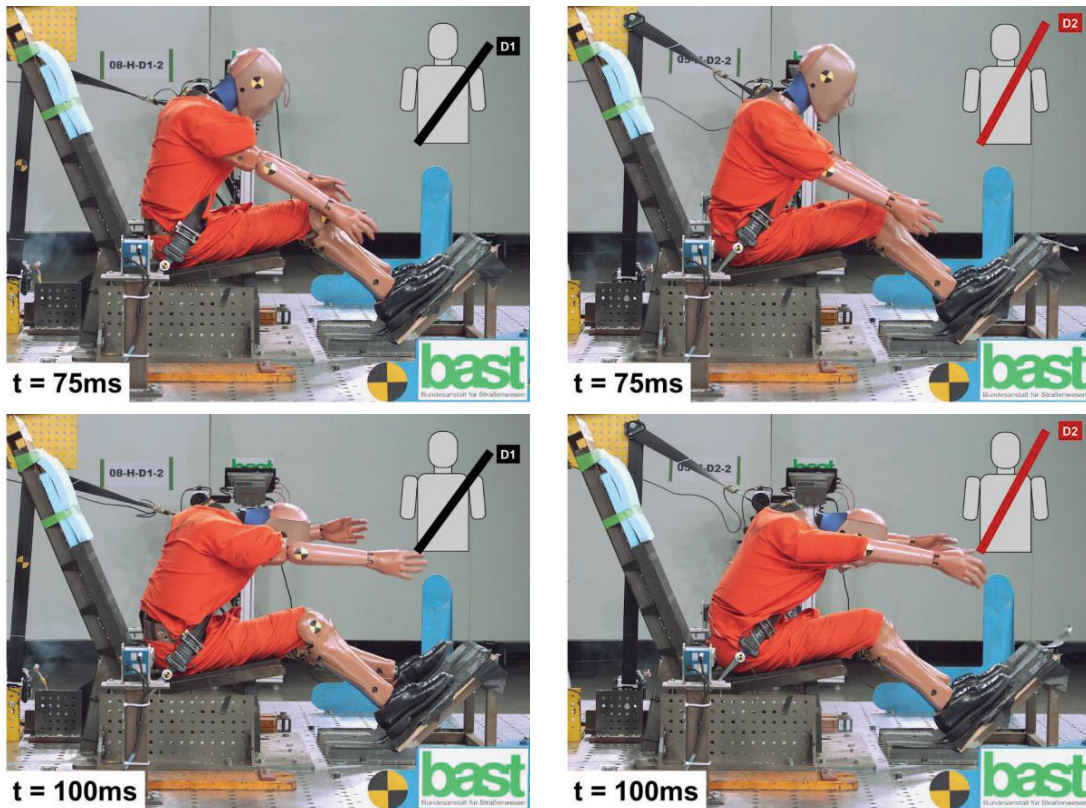


Figure 6. Hybrid III kinematics for belt routing D1 and D2 at 75ms and 100ms.

THOR-5F D1 vs. D2

As for the Hybrid III small female dummy, upper body kinematics of the THOR-5F are primarily influenced by the position of the D-ring with respect to the neck / clavicle and thus the leverage of the belt force (see Figure 4 and Figure 5). Figure 7 shows the dummy kinematics at 75 ms and 100 ms for both belt routings. As a result of the different belt routings, rotation of the dummy's upper body about the vertical axis begins at approx. 50 ms for belt routing D1 and results in an overall larger rotation of the upper body. For belt routing D2 the dummy-to-belt interaction is more stable, while the rotation of the upper body is delayed and reduced. The earlier rotation of the upper body for belt routing D1 reduces the head forward displacement while the risk that the belt slips off the shoulder is increased.

Hybrid III small female vs THOR-5F

Similar observations can be made with respect to the influence of the belt routing, however, the second flex-joint in the THOR-5F dummy increases the overall flexibility of the spine and thus the rotation of the upper body begins earlier and the overall rotation is greater. Furthermore, the bending of the spine and the forward displacement of the head is larger with the head almost contacting the femur or knees.

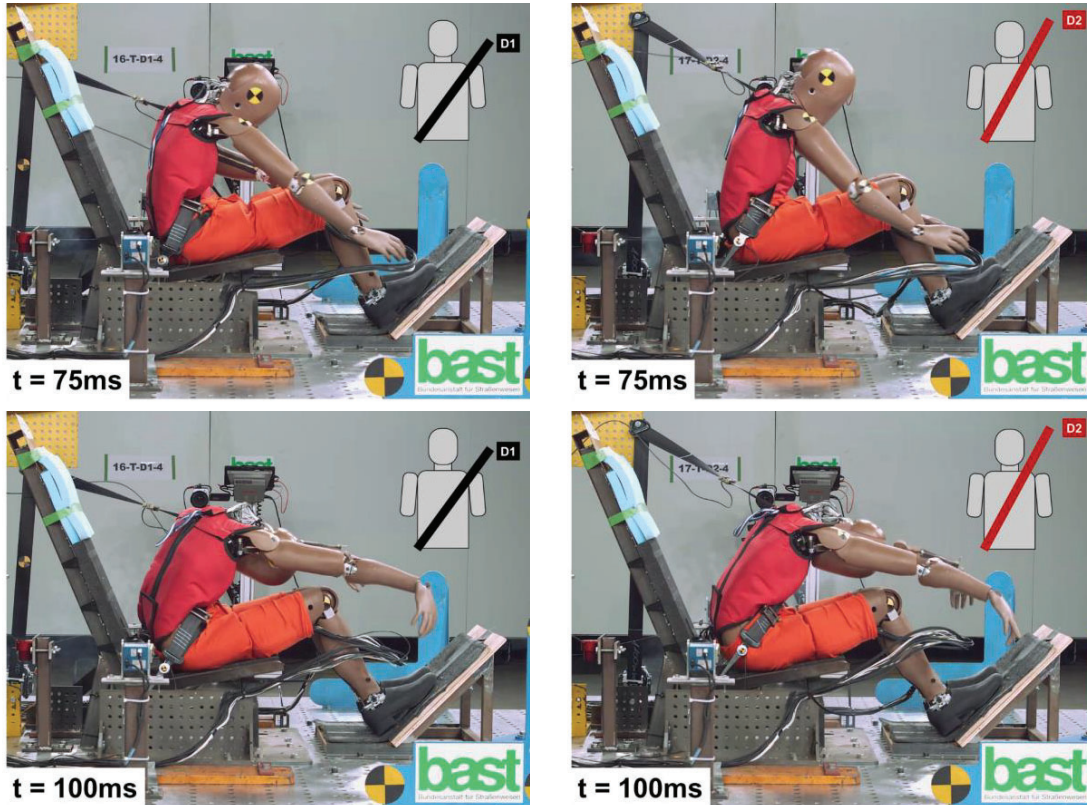


Figure 7. THOR-5F kinematics for belt routing D1 and D2 at 75ms and 100ms.

Chest deflection

The chest deflection measurements of the Hybrid III small female chest potentiometer are shown in Figure 8 for the belt routing configurations D1 and D2. Three repeated tests were done in each configuration. In Table 1 the chest deflection peak values, mean values from three tests and coefficient of variation are shown. In

Table 2 the chest deflection values for D2 are shown respectively. The repeatability is excellent. The chest deflection mean value decreases from the belt routing configuration D1 to D2 by 22 % from 22 to 18 mm.

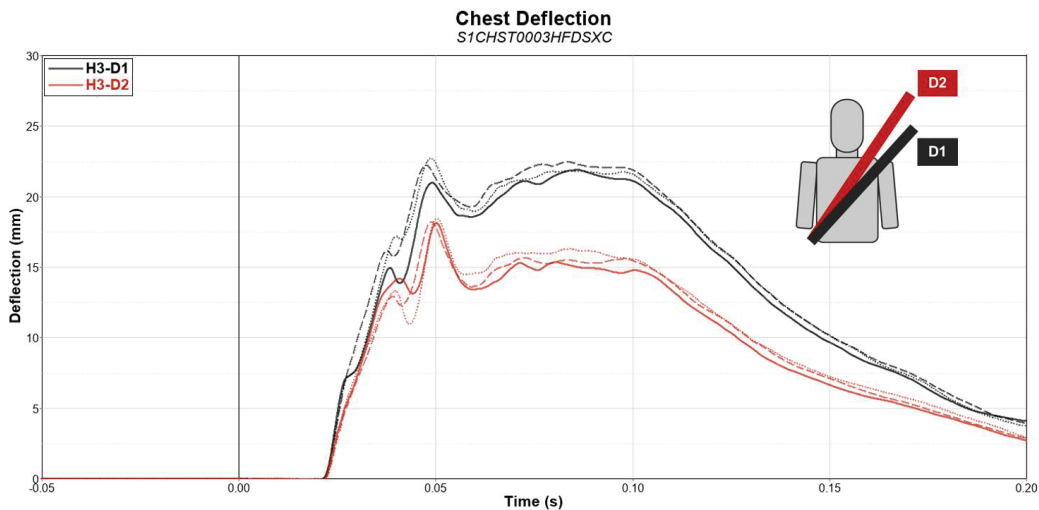


Figure 8. Hybrid III small female chest deflection for belt routing configurations D1 vs. D2.

Table 1. Hybrid III small female chest deflection measurements for belt routing configuration D1.

Test number	Displacement	Mean	Coefficient of Variation
07-H-D1-1	22 mm	22 mm	3%
08-H-D1-2	22 mm		
09-H-D1-3	23 mm		

Table 2. Hybrid III small female chest deflection measurements for belt routing configurations D2.

Test number	Displacement	Mean	Coefficient of Variation
04-H-D2-1	18 mm	18 mm	0 %
05-H-D2-2	18 mm		
06-H-D2-3	18 mm		

Figure 9 shows the resultant IR-TRACC deflections measured at the four locations at the chest of the THOR-5F. The peak values from three repeated tests, mean values and coefficients of variation are shown in Table 3 for belt routing configuration D1 and in Table 4 for D2 respectively.

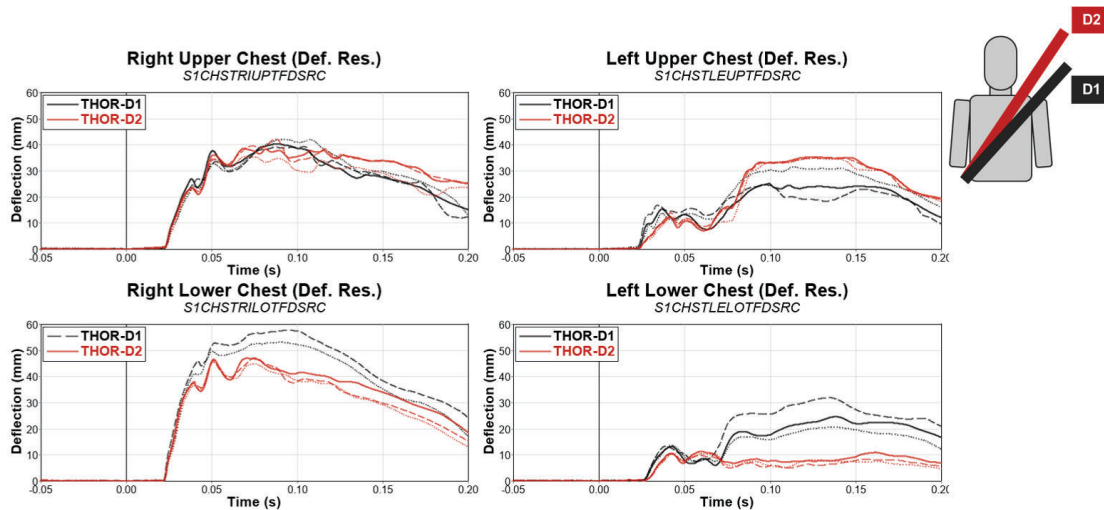


Figure 9. THOR-5F resultant IR-TRACC deflections for belt routing configurations D1 vs. D2.

For the configuration D1 with the belt more outboard on the shoulder the repeatability of chest deflection measurements is good at the right side of the chest. At the left side of the chest the variation is higher (14% to 22%). For D-ring configuration D2 the repeatability is higher at all four measurements location (between 0% and 9%).

The IR-TRACC resultant deflection are higher at the right side of the chest due to the higher loadings by the shoulder belt to this side of the dummy. The maximum resultant deflection of the four IR-TRACCs (R_{max}) can be observed at the right lower IR-TRACC for both belt routing configurations D1 ($R_{max} = 55$ mm) and D2 ($R_{max} = 47$ mm). In comparison to the peak deflections measured with the Hybrid III small female the maximum deflection R_{max} measured in THOR-5F is about 2.5 times higher for both belt routings.

Comparing D1 and D2 the mean values of R_{max} is reduced by 16% from 55 mm to 47 mm. The mean value of the maximum resultant deflection at the left upper IR-TRACC increases by 30% from D1 (27 mm) to D2 (35 mm). The deflections at the other two locations also decrease comparing D1 and D2 (right upper by 5% from 41 mm to 39 mm, left lower by 58% from 26 mm to 11 mm).

Table 3. IR-TRACC resultant chest deflection for belt routing configuration D1.

Test number	10-T-D1-1	11-T-D1-2	16-T-D1-4
Right Upper [mm]	40	39	42
Mean	41		
Coefficient of Variation	3%		
Right Lower [mm]	No data	58	53
Mean	55		
Coefficient of Variation	6%		
Left Upper [mm]	25	25	31
Mean	27		
Coefficient of Variation	14%		
Left Lower [mm]	25	32	21
Mean	26		
Coefficient of Variation	22%		

Table 4. IR-TRACC resultant chest deflection for belt routing configuration D2.

Test number	14-T-D2-2	15-T-D2-3	17-T-D2-4
Right Upper [mm]	39	42	36
Mean	39		
Coefficient of Variation	9%		
Right Lower [mm]	47	47	46
Mean	47		
Coefficient of Variation	2%		
Left Upper [mm]	35	35	35
Mean	35		
Coefficient of Variation	0%		
Left Lower [mm]	11	10	11
Mean	11		
Coefficient of Variation	5%		

Field data study - seat adjustments and D-ring position

In Table 5 and Table 6 the settings of the seat longitudinal and height adjustments for car occupant representing a small person in terms of standing height (145-155 cm) are shown. In Table 7 the height adjustments of the D-ring are provided. The majority of the drivers in the data set had the seat set to the most forward position (60%). In 40% of the cases it was set to mid position. The height adjustment was set to mid for 57% of the cases. For the small front passenger occupants, the preferred seat setting is the mid/mid position. The most often observed setting of the D-ring height adjustment is the lowest setting for both the driver (59%) and the passenger (65%).

Table 5. Seat longitudinal adjustment

	most forward	mid	most rearward
Driver	60%	40%	0%
Front Passenger	3%	97%	0%

Table 6. Seat height adjustment

	highest	mid	lowest
Driver	30%	57%	13%
Front Passenger	13%	74%	13%

Table 7. D-ring height adjustment

	highest	mid	lowest
Driver	16%	25%	59%
Front Passenger	6%	29%	65%

DISCUSSION AND LIMITATIONS

The results of the sled tests with the Hybrid III small female dummy could confirm the findings from previous studies in a generic environment with belt anchorage location representing possible shoulder belt routings of contemporary vehicles. The observation from Digges et al. 2019, Digges et al. 2017, Keon et al. 2015 and Yamasaki et al. 2011 regarding the effect of belt routing on reduction of mid sternum chest deflection were also seen in this study. The belt routing of test configuration D1 with a belt position more outboard on the shoulder also resulted in a higher chest deflection in the Hybrid III small female. The belt routing of test configuration D2 with a belt position close to the neck resulted in a reduction of chest deflection in the Hybrid III small female. Therefore, the recommendations regarding test settings of the seat and D-ring adjustments for a more meaningful effective chest deflection assessment with the Hybrid III small female dummy can be confirmed based on the results of this sled test study.

THOR chest measurements are also sensitive to belt routing. The maximum peak deflection R_{max} measured at the right lower IR-TRACC was also reduced between D2 to D1. However, the left lower IR-TRACC is nearly unloaded for D-Ring position 2, while in D-Ring position 1 approx. 25 mm chest deflection are observed, which indicates increased coupling between left and right thorax for D-Ring position 1.

R_{max} means the highest peak resultant deflection values of the of the four IR-TRACC. R_{max} is currently used as chest injury criterion for the THOR-50M dummy. If a similar criterion would be used for the THOR-5F there might occur a similar issue with this dummy regarding non-biofidelic reduction of chest deflection with a belt

routing close to the neck. However, if a multi-point chest injury criterion would be used which considers not only the peak value of one IR-TRACC but several IR-TRACCs measurements on both sides of the chest it could be a more robust criterion, which would not be sensitive to belt routing resulting from variations in D-ring and seat settings. Therefore, to give conclusions regarding the potential of THOR-5F as an alternative test tool advanced multi-point injury criterion are needed.

For a reasonable development and application of multi-point deflection-based injury criteria a good repeatability and reproducibility of these dummy measurements is a pre-requisite. The reproducibility was not assessed in this study as only one THOR-5F dummy was available. The repeatability of R_{max} based on the IR-TRACC deflection of the right lower was good (between 2% and 6%). However, the repeatability of IR-TRACC measurement at other locations which would be needed for a multi-point criterion was not good especially for configuration D1. However, in this configuration it might not be an issue of variability in the dummy chest itself or the deflection measurement system, but due to variations in belt sliding on the shoulder in this configuration with the belt more outboard on the clavicle. This needs to be further investigated.

A preliminary field data analysis of the seat setting preferred by small drivers indicate that the most forward position and the mid height setting is preferred. However, in some cases small drivers might change the seat setting before they exit the car to be able to get out more comfortable with more space. Therefore, these figures might be biased for the driver. The setting most forward in longitudinal direction in more cases would be more reasonable as the drivers need to reach the pedals. Also, the seat height setting “highest” would be expected in more cases as the drivers need to be able to look over the steering wheel. Therefore, no specific recommendation of a seat setting for the driver can be made based on this data.

The preferred seat for-aft and height setting in the field data for small passengers is the mid/mid setting, which seems to be reasonable. There is also no concern that the data is biased by change of the seat setting after the accident. Therefore, this setting is recommended as standard test position of the front passenger seat for an updated test procedure with a dummy respecting a small occupant.

The preferred adjustment of the D-ring by small car occupants based on field data is the setting “fully down” for both driver and passenger. Therefore, this setting could be recommended as a standard setting in tests with a small dummy in the driver as well as in the passenger seat.

Limitations

The sled tests with Hybrid III small female and THOR-5F were done in a simplified generic test setup. The generic test configuration can only reproduce the boundary conditions of a real vehicle to a limited extent. In this study a rigid seat was used. No airbag or knee support was used. Depending on the fore-aft adjustment of the seat, the feet-to-footrest contact and resulting feet support might change. The study should be repeated or complemented by investigations using full-scale tests or tests in a more realistic generic seat environment including other components like an airbag. In addition, the analysis of respective field data should be extended.

CONCLUSIONS AND RECOMMENDATIONS

The objective of this study was to provide recommendations to be considered in possible future updates to procedures, e.g. consumer testing like Euro NCAP for an improved safety assessment of chest injury risk with special focus on small (female) elderly occupants in frontal impact.

In conclusion the recommendations regarding seat and D-ring settings that were provided in previous studies can be confirmed. To enable a meaningful evaluation of chest injury risk with the Hybrid III small female dummy the D-ring should be set to the lowest position for the driver as well the passenger side. Furthermore, for the passenger side the seat should be set to the midtrack position. The height of the seat should also be set to the mid-position. These settings will result in a more meaningful belt routing on the dummy chest. Sled test with the Hybrid III small female dummy have shown that these setting results in a more meaningful dummy chest deflection measurement. Furthermore, these seat and D-ring settings are the most relevant preferred by small occupants based on field data.

For additional improvement of a chest injury risk assessment procedure considering the specific needs of small female occupants and further enhancement of the occupant protection level it is recommended to consider improved ATDs like the THOR-5F with advanced multi-point chest injury criteria. The THOR-5F chest

measurement have shown the potential for improved chest injury risk assessment as they might be less sensitive to test parameters and resulting variation of belt routing.

However, to evaluate the potential of the THOR-5F to address the mentioned issues advanced multi-point deflection-based chest injury criteria are necessary. Further research related to this is needed. A pre-requisite for the development and reliable application of advanced multi-point chest deflection criteria is a sufficiently repeatable and reproducible chest deflection response of the dummy. The repeatability of chest deflection measurements in this test series looked promising. Repeatability and reproducibility of the chest deflection response of the THOR-5F dummy related to the sensitivity of multi-point deflection measurements should be further investigated and improved if necessary.

REFERENCES

Carroll, J, Smith, S, Adolph, T, Eggers, A. (2009) Deliverable 1.1 - A comparison between crash test results and real-world accident outcomes in terms of injury mechanisms and occupant characteristics, EC FP7 THORAX, GA No 218516, Brussel

Digges K, Dalmotas D, Prasad P and Mueller B (2017). The need to control belt routing for silver NCAP ratings. Proceedings of the 25th International Technical Conference on the Enhanced Safety of Vehicles (ESV), Detroit Michigan, United States. Paper Number 17-0403, 2017

Digges, K., Dalmotas, D., and Prasad, P.; An NCAP star rating system for older occupants, Proceedings of the 23rd ESV Conference, Paper No. 13-0064, 2013

Digges, Kennerly; Dalmotas, Dainius; Prasad, Priya (2019). Application of Multiple Rib Gages to Improve Chest Injury Measurements. Proceedings of the 26th International Technical Conference on the Enhanced Safety of Vehicles (ESV), Eindhoven, The Netherlands. Paper Number: 19-0266-O.

Eggers A, Eikhoff B, Dobberstein J, Zellmer H, and Adolph T; Effects of Variations in Belt Geometry, Double Pretensioning and Adaptive Load Limiting on Advanced Chest Measurements of THOR and Hybrid III, IRC 14-40, 2014 IRCOBI Conference, Berlin, Germany.

Euro NCAP Adult Occupant Protection Assessment Protocol Version 9.2.1, 2022. Euro NCAP Adult Occupant Protection Assessment Protocol-V9.2.1

Euro NCAP Full-Width-Frontal-Impact-Test-Protocol Version 1.0.2, 2015. Full-Width-Frontal-Impact-Test-Protocol-V102

Euro NCAP Full-Width-Frontal-Impact-Test-Protocol Version 1.2.1, 2021. Euro NCAP Full-Width-Frontal-Impact-Test-Protocol-V1.2.1

Forman J, Poplin GS, Shaw CG, McMurry TL, Schmidt K, Ash J, Sunnevang C. Automobile injury trends in the contemporary fleet: Belted occupants in frontal collisions. *Traffic Inj Prev.* 2019;20(6):607-612. doi: 10.1080/15389588.2019.1630825. Epub 2019 Jul 8. PMID: 31283362.

Keon, T. (2016). Alternative Approaches to Occupant Response Evaluation in Frontal Impact Crash Testing, *SAE Int. J. Trans. Safety* 4(1):202-217, 2016, <https://doi.org/10.4271/2016-01-1540>.

Laituri, T., Prasad, P., Sullivan, K., Frankstein, M., Thomas, R. (2005), Derivation and Evaluation of a Provisional, Age Dependent AIS 3+ Thoracic Risk Curve for Belted Adults in Frontal Impacts, SAE Paper No. 2005-01-0297. Based on these curves, a political decision was made to choose 50% risk AIS3+ (FI-17-07)

Prasad P, Mertz HJ, Dalmotas DJ, Augenstein JS, Diggs K. Evaluation of the field relevance of several injury risk functions. *Stapp Car Crash J.* 2010 Nov; 54:49-72. doi: 10.4271/2010-22-0004. PMID: 21512903

Uriot Wang, Z., McInnis, J., Benfant, L., Feng, Z., and Lee, E., (2017). THOR 5th Percentile Female ATD Design," in 25th International Technical Conference on the Enhanced Safety of Vehicles (ESV) Paper Number 17-0295.

Wisch, M.; Lerner, M.; Vukovic, E.; Hynd, D.; Fiorentino, A.; Fornells A. (2017). Injury Patterns of Older Car Occupants, Older Pedestrians or Cyclists in Road Traffic Crashes with Passenger Cars in Europe – Results from SENIORS. IRCOBI Conference. Antwerp, Belgium.

Passenger Cars in Europe – Results from SENIORS

Yamasaki, T. and Uesaka, K. Rear occupant protection JNCAP test—Test results and findings. Proceedings of 22nd International Technical Conference on the Enhanced Safety of Vehicles (ESV), 2011. Washington, DC

ACKNOWLEDGEMENTS

The authors would like to thank Autoliv for providing seatbelts for the test series. The dummy THOR-5F used in this study was provided by Humanetics Innovative Solutions.

THOR-50M FITNESS ASSESSMENT IN FMVSS NO. 208 UNBELTED CRASH TESTS

James Saunders
Dan Parent
Peter Martin
NHTSA
USA

Paper Number 23-0339

ABSTRACT

Research Question/Objective: A prerequisite for entering a dummy design into CFR Title 49, Part 572 is to demonstrate that the specifications yield ATD units capable of implementation in a regulatory environment. Specifications for the THOR-50M have produced units that are repeatable, reproducible, and durable in many test conditions, including belted sled tests and qualification testing. Herein, two THOR-50M units are implemented in a series of unbelted vehicle crash tests run in accordance with FMVSS No. 208 procedures, and evaluated based on usability, durability, and the successful collection of sensor data for use in injury risk prediction.

Methods and Data Sources: Two THOR-50M units, both conforming to NHTSA's 2018 THOR-50M design and qualification specifications, were run in a series of unbelted crash tests. Nineteen tests were run with four 2020-21 vehicle models: Honda Accord, Mazda CX-5, Chevy Equinox, Ford Escape. Four were run against a full-frontal barrier and fourteen against an angled barrier in accordance with FMVSS No. 208 procedures, with the exception of using NHTSA's THOR 50th Percentile Male Dummy Seating Procedure instead of using FMVSS No. 208 seating. Dummy qualifications were performed periodically throughout the test series following NHTSA's THOR-50M Qualification Procedures.

Results: The two units held up well to the rigors of the crash tests. Both were fully instrumented, one of which included an internal DAS system. Sensor anomalies and failures during tests were traced to cable damage, which was repaired between tests. The parts and assemblies within both units did not sustain any damage beyond scuffs and cuts to exterior vinyl components. There were no parts that needed to be replaced. Dummy qualifications posed no issues. The test lab was able to maintain a testing schedule typical of other regulatory tests with other types of dummies.

Discussion and Limitations: This test series demonstrated that the THOR-50M could be implemented in vehicle crash testing consistent with regulatory compliance testing in that the ATDs showed sufficient usability and durability. Both units successfully collected sensor data for use in injury risk prediction. The minor sensor anomalies that did occur were mostly isolated to the ATD without the internal DAS system. A limitation of this study was that only four vehicle models were tested and all tests were run at a single lab.

Conclusions and Relevance to Session Submitted: In a series of FMVSS No. 208 unbelted frontal rigid barrier crash tests, two THOR-50M units were implemented and successfully completed the test series. Scripted procedures for dummy assembly, qualification, and handling were followed without issue, and the seating procedures resulted in highly uniform positioning. Sensor anomalies observed over the course of testing were consistent with those common in dummies already in Part 572. There were no broken parts or part replacements throughout testing. Based on the experiences of this testing series, the THOR-50M appears fit for use in standardized testing.

INTRODUCTION

NHTSA has performed many types of research tests using the Test Device for Human Occupant Restraint 50th percentile male (THOR-50M) anthropomorphic test device (ATD). These include belted THOR-50M in the front and rear seat in both full vehicle and sled tests and different types of frontal research crash testing to develop new test procedures [1][2]. This included vehicle-to-vehicle with overlaps from 20 percent to 100 percent overlap and at different impact angles [3]. It also included tests involving moving deformable barriers into the front of a vehicle in

overlap and oblique conditions [4]. In addition, the durability of the THOR-50M has been observed in a wide array of component, sled, and vehicle crash test conditions [5][6].

More recently, NHTSA used the THOR-50M in crash tests in a new series of tests that were very similar to those specified in FMVSS No. 208, Occupant Crash Protection. The most recent series included unbelted THOR-50M positioned in the front seat of a vehicle into a rigid barrier. The THOR-50M had been tested previously in the driver seat in the frontal rigid barrier test procedure and in unbelted sled test conditions. But until the new test series discussed herein, the dummy had not been included in unbelted vehicle crash tests following the FMVSS No. 208 test procedures.

An objective of the unbelted test series was to evaluate the fitness of the THOR-50M in a standardized testing environment for codification within CFR Title 49, Part 572, Anthropomorphic Test Devices. This paper summarizes the THOR-50M testing experience under conditions similar to the way Part 572 ATDs are used by NHTSA to carry out regulatory tests. This includes how the THOR-50M qualified before and after testing, any damage to the THOR-50M, instrumentation performance, and any issues with performing the tests.

METHODOLOGY

Overview

Two THOR-50M units, both conforming to NHTSA's 2018 THOR-50M design specifications [7][8], were run in a series of unbelted crash tests. Nineteen full-scale vehicle crash tests were run with four 2020-21 models: Honda Accord, Mazda CX-5, Chevy Equinox, Ford Escape. Four were run against a full-frontal rigid barrier and the others were run against an angled, rigid barrier. Details of the tests are discussed below.

Unbelted Rigid Barrier Tests

The nineteen tests were run by following FMVSS No. 208 procedures for the unbelted driver and right front passenger seating positions [9]. For reference, the FMVSS No. 208 unbelted crash configurations are shown in Figure 1.

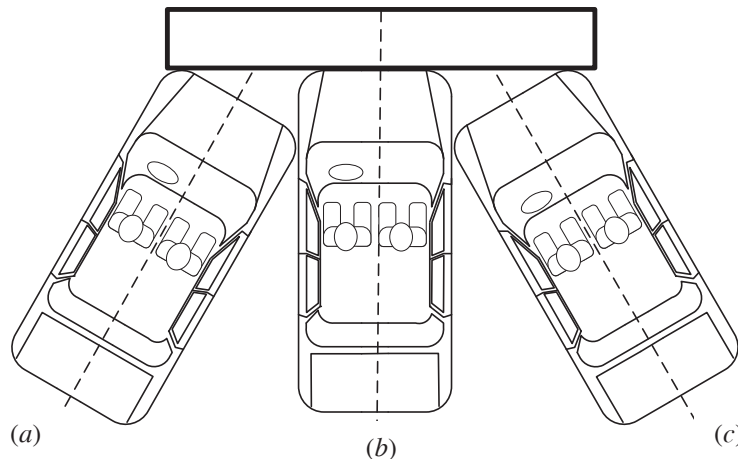


Figure 1. FMVSS No. 208, unbelted crash test configurations:

- a) Left side impact with the rigid barrier angle set at 30°.
 - b) Full frontal impact with the rigid barrier angle set at 0°.
 - c) Right side impact with the rigid barrier angle set at 30°.
- Impact speed: 32-40 km/hr for all three configurations

Each crash test was performed following the test procedure specified in FMVSS No. 208, with the following exceptions:

- THOR-50M units were used in the driver and front passenger seating positions, and they were positioned according to the Revised THOR 50th Percentile Male Dummy Seating Procedure [10].
- In FMVSS No. 208, the vehicle impact speed specified for these tests is 32-40 km/hr (20-25 mph), but all tests run in this test series described herein were run at either 40 km/hr or 48 km/hr. Although 48 km/hr is above the maximum regulatory speed, six tests were run at the higher speed to assess the integrity of the THOR-50M when exposed to energy levels above and beyond those prescribed by the standard.

Table A-1 in the Appendix provides a list of summary information for each of the nineteen crash tests.

THOR-50M Units Tested

During this test series, two different THOR-50M ATDs were used, identified by their serial numbers: DO9799 and EG2595. Both were manufactured by Humanetics in accordance with NHTSA's Parts List and Drawings [7]. After EG2595 was delivered to NHTSA in 2018, the dummy was sent to Diversified Technical Systems, Inc. (DTS) for installation of an in-dummy data acquisition system (DAS) based on the SLICE6 DAS modules.

Both dummies were instrumented and assembled at NHTSA's Dummy Management Laboratory (DML) at the Vehicle Research and Test Center (VRTC) in Ohio prior to delivery to the crash test lab, Applus-Idiada-Karco Engineering, Adelanto, CA. Final assembly (including joint torque settings), wire harness routing, and instrumentation polarity checks were fulfilled at Applus-Idiada-Karco by following NHTSA's THOR-50M Procedures for Assembly, Disassembly, and Inspection (PADI) [11]. For EG2595, NHTSA provided a DTS Mini Distributor with cables and PSU to facilitate download and storage of test data by Applus-Idiada-Karco.

The instrumentation included head accelerometers, head angular rate sensors, upper and lower neck load cells, T1 and T6 accelerometers, chest and abdomen 3D IR-TRACC assemblies, thoracic spine load cell, ASIS load cells, acetabulum load cells, and femur load cells (about 130 channels in all). All of these instruments are specified within the drawing package, with installation instructions included in the PADI. Additionally, both units were instrumented with sensors to measure the internal temperature before, during, and after testing. The full list of instrumentation is provided in the individual vehicle test reports.

THOR-50M Qualification and Inspection

Prior to the initial vehicle crash test at Applus-Idiada-Karco, a full set of qualification tests was conducted on each THOR-50M at NHTSA's DML. Thereafter, a partial qualification test series was conducted after each vehicle crash test by Applus-Idiada-Karco on the THOR-50M unit(s) that were used in the crash.

The partial set included most of the full-body test modes as shown in Table 1. A full qualification test series was also conducted on each THOR-50M halfway through the test series at Applus-Idiada-Karco. All qualification tests were carried out in accordance with NHTSA's THOR-50M Qualification Procedures [8]. Also, before every test, a full polarity check was performed to assure that all sensors were working properly.

After every crash test, the THOR-50M unit(s) underwent a physical inspection at Applus-Idiada-Karco. Each body region was examined by partially disassembling the dummy. An approximate 60-point visual inspection was carried out. Photographic images of any and all damage are documented in each test report.

As part of the inspection, each sensor was scrutinized for its overall condition and functionality. This was determined by examining crash test signal data channels for any sensor anomalies, such as clipping, unexpected drops, or flat signals. Instruments were also inspected for any physical evidence of damage. If any damage or sensor anomalies were found, the instruments were closely inspected to determine the source of the anomaly (typically, a loose wire) and repaired where possible.

Table 1. THOR-50M Qualification Tests and Requirements.

Dummy test assembly	Body region	No. of qualif. requirements
Full dummy	Face	2
Full dummy	Head*	2
Full dummy	Upper thorax*	4
Full dummy	Lower thorax*	2
Full dummy	Lower abdomen*	3
Full dummy	Upper leg (R and L)*	3
Head/neck sub-assembly	Neck extension	4
Head/neck sub-assembly	Neck flexion	4
Head/neck sub-assembly	Neck lateral flexion (R, L)	3
Neck assembly only	Neck torsion (R and L)	3
Knee assembly only	Knee (R and L)	2
Lower leg only (no shoe)	Ankle eversion (R and L)	3
Lower leg only (no shoe)	Ankle inversion (R and L)	3
Lower leg only (incl. shoe)	Heel (R and L)	1
Lower leg only (incl. shoe)	Ball of foot (R and L)	3

**Included in Partial set of qualifications*

THOR-50M Crash Test Exposures

For the three FMVSS No. 208 unbelted test configurations (right 30° angle, left 30° angle, frontal 0°), the two THOR-50M units were subjected to multiple crash exposure modes – near-side, 0° full, and far-side – as shown in Table 2. Each configuration exposed the dummy to a different loading condition. Multiple tests were run in each condition to assure that the dummy was thoroughly exercised in each exposure mode. Each set of exposures represents a test with a different vehicle. For example, the three 30° Near Driver exposures represents three left 30° angle tests with three different vehicle models. Also, both THOR-50M units are respresented in each exposure set.

Additionally, the near side and far side modes were exposed to a limited number of 48 km/hr tests. At the regulatory speed of 40 km/hr, the longitudinal acceleration of a vehicle in the angled test is typically less than that of the 0° impact. The added 48 km/hr crashes allowed the THOR-50M units to be exercised more thoroughly in the 30° angled mode.

Table 2. THOR-50M test exposures (19 total tests).

Seat position, THOR-50M Exposure	Tests at 40 km/hr	Tests at 48 km/hr
30° Near Driver	3	2
0° Full Driver	4	0
30° Far Driver	2	1
30° Near Passenger	2	2
0° Full Passenger	4	0
30° Far Passenger	2	1

THOR-50M injury risk: baseline comparative values

Injury Assessment Reference Values (IARVs) typically refer to the limits for a given injury criterion calculated based on crash test results. For regulatory purposes, IARVs are defined in the regulation that describes the crash test modes, such as FMVSS No. 208. As the THOR-50M is not currently included in FMVSS No. 208, a set of baseline comparative values were selected for the purposes of the current study (Table 3).

To guide the selection of baseline values, we referred to injury criteria specific to the THOR-50M [12]. Generally, we selected reference values that represent a 50% risk of either Abbreviated Injury Scale (AIS) 2+ or 3+ injury severity, depending on the body region. When metrics were used that correspond to risk levels other than 50%, we selected values with risk levels that correspond to IARVs defined for the Hybrid III 50th percentile male in FMVSS No. 208.¹

Table 3. THOR-50M baseline comparative reference values

Body Region	Measurement or criterion	Units	Baseline Comparative Ref.	Injury severity, risk level
Head	HIC15	none	700*	AIS 2+, 11%
	BriC	none	0.96	AIS 3+, 50%
Neck	Nij	none	0.88*	AIS 2+, 30%
Chest	3ms Clip	g	60*	Unreported
	Deflection	mm	51.4	AIS 3+, 50%
Pelvic	Acetabulum Force	N	3381	AIS 2+, 50%
Femur	Peak Compression	N	9450*	AIS 2+, 30%
Lower Leg	Revised Tibia Index	none	1.23	AIS 2+, 50%

*The reference value for THOR-50M corresponds to the same risk level as specified in FMVSS No. 208 for the HIII-50M

Test Schedule

Table 4 summarizes the schedule of testing. All crash tests were run at the same lab, Applus-Idiada-Karco. The nineteen tests were run between September 2020 and September 2021, with a four-month gap between mid-January to mid-May 2021 in which no testing was performed due to other NHTSA priorities. A NHTSA test number is denoted for each test, from which test reports, photos, videos, and instrumentation data may be found by searching within NHTSA's Crash Test Database². Each report provides all test signals from the crash tests, pre- and post-test measurements of the vehicle, pre-test measurements of the occupant positions, qualification testing results performed before the crash test on each of the THOR-50M unit(s), and post-test inspection of the THOR-50M unit(s).

The one-year, nineteen-test schedule is typical of the schedule at a given test lab that supports NHTSA's regulatory and consumer information programs. For comparison purposes, consider a recent timeline NHTSA followed to support the New Car Assessment Program (NCAP). From January 2020 through September 2021, Applus-Idiada-Karco ran fourteen frontal crash tests to support NCAP. The NCAP tests were run at 56 km/hr using belted Hybrid III dummies in which a similar schedule was followed. That is, between full vehicle tests, the ATDs underwent qualification testing, partial tear-down for inspection purposes, and other handlings and delays similar to those

¹ Values reported in Table 3 have been chosen for comparative purposes only, as reported herein. Table 3 should not be interpreted as a NHTSA determination of injury assessment reference values for a future regulatory implementation of the THOR-50M.

² NHTSA's Vehicle Crash Test Database, <https://www.nhtsa.gov/research-data/research-testing-databases#/vehicle>.

experienced in the THOR-50M test series described herein. (During this time period, Applus-Idiada-Karco did not run any FMVSS No. 208 tests under NHTSA's compliance program.)

Table 4. Testing Schedule

Crash test date	Test no.	EG2595 Pre-test qualif start/stop dates	DO9799 Pre-test qualif start/stop dates
9/9/2020	v11284	n/a	7/16 - 7/23 Full ¹
9/25/2020	v11285	7/14 - 7/22 Full ¹	n/a
10/1/2020	v11286	n/a	9/15 - 9/16 Partial
10/9/2020	v11287	10/6 - 10/8 Partial	n/a
10/21/2020	v11245	n/a	10/9 - 10/12 Partial
12/7/2020	v11246	10/14 - 11/24 Full	n/a
12/15/2020	v11362	n/a	10/28 - 11/17 Full
12/18/2020	v11363	12/16 - 12/17 Partial	n/a
1/8/2021	v11361	12/23 - 1/6 Partial	12/23 - 1/5 Partial
1/15/2021	v11364	1/12 - 1/14 Partial	1/12 - 1/13 Parial ²
----- BREAK IN TESTING -----			
5/21/2021	v11630	5/13 - 5/19 Full	n/a
6/7/2021	v11637	5/28 - 6/1 Partial	n/a
6/24/2021	v11629	6/14 - 6/15 Partial	n/a
7/2/2021	v11628	6/30 - 6/30 Partial	n/a
7/30/2021	v11635	7/12 - 7/29 Partial	n/a
8/13/2021	v11636	8/12 - 8/12 Partial	n/a
9/17/2021	v11639	8/20 - 8/26 Partial	6/24 - 7/22 Partial ¹
9/22/2021	v11665	no pre-test qualif	no pre-test qualif
9/24/2021	v11638	10/11 - 10/21 Full ³	10/12 - 10/20 Full ³

¹ Qualification tests performed by NHTSA at DML

² DO9799 temporarily returned to DML for other NHTSA purposes.

³ Post-test qualifications performed after test v11638.

RESULTS

Qualification tests

Throughout the test series, there were six sets of full qualification tests carried out, and fifteen partial sets. In all but one instance, every qualification target was met. The one instance occurred with the neck of DO9799. After a break in testing from January-May 2021 (during which time NHTSA employed DO9799 for other research investigations), the dummy was shipped back to Applus-Idiada-Karco without a fully qualified neck. Specifically, neck axial force in the neck extension test was slightly above the target. Nonetheless, we proceeded with the final two vehicle tests with the neck because we had no qualified spares to swap into the dummy.

Aside from loose cables and connectors on instrumentation on the non-DAS unit, DO9799 (discussed in the next section), neither of the two units had any parts replaced. Only routine adjustments were needed in order to meet all the qualification criteria during crash testing.

Moreover, post-test qualifications performed at Applus-Ididia-Karco were consistent with the pre-test qualifications performed at NHTSA's DML. That is, all tests met the qualification requirements with the exception of neck axial force in the extension test. There were no instances in which either of the THOR-50M units fell out of compliance after being subjected to any of the nineteen crash tests, despite being subjected to fairly high crash forces (as judged by proximity to injury references seen later on in Figs. 6 and 7). Even in the one instance in which the qualification target was not met (axial force in the neck extension test on DO9799), the Applus-Ididia-Karco result was very consistent with the DML: the axial force was over the 3210 N limit by about 200 N at both labs.

In summary, the qualification schedule followed in this series is typical of how an ATD is used in NHTSA's FMVSS compliance program. That is, between qualifications, the ATD undergoes a full vehicle test, partial tear-down for inspection purposes, and other handlings and delays.

Seating procedure

The THOR-50M seating procedure, cited earlier, was followed in all tests. There were tests with four different vehicles and two seating positions. Among the tests, a 2020 Honda Accord was used more often than the other three models. For the Accord tests, there were five in which a THOR-50M unit was seated in the driver seat. Below is a diagram derived from the Accord vehicle reports that indicates the relative uniformity of the dummy positioning. It shows the x- and z- coordinates relative to the door lock striker on the driver side of the vehicle. Coordinates of high interest are shown in the figure, including the outboard H-point. Both of the THOR-50M units are represented in this figure: three with EG2595, two with DO9799.

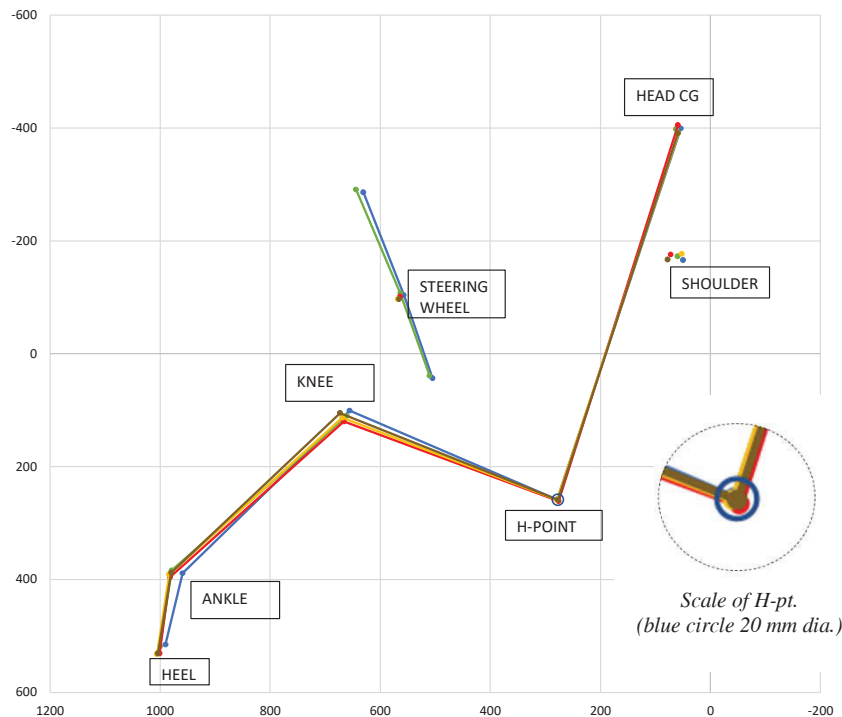


Figure 2. THOR-50M Driver: Seated coordinates in five Honda Accord tests

For comparative purposes, a circle with a diameter of 20 mm is drawn around the average H-point, and shows that all H-points are enclosed by the circle. This corresponds to the positioning requirement for the THOR-50M (and

HIII-50M as specified in FMVSS No. 208) wherein the H-point of the dummy must lie within +/- 10 mm of the H-point determined by the SAE J826 manikin in the x- and z-directions. Other measurements, such as pelvis angle and tilt sensor readings were all within the target tolerances specified by the seating procedure.

The steering wheel is provided as a reference on the relative variability seen from one vehicle to another, independent of any variability associated with THOR-50M units. Other sources of variability among the five THOR-50M positioning observations included the seat back angle (varied by 2°), head restraint post angle (also varied by 2°), and seat track position (varied by 10 mm).

Temperature control.

According to NHTSA's Qualification Procedures, the temperature of the dummy must be soaked in a controlled environment that is 20.5° to 22.2° C (69° to 72° F) and has a relative humidity from 10 to 70% for at least 4 hours prior to a test. This requirement has been put in place because the dummy response is temperature dependent. The damping material that covers the ribs is particularly sensitive to temperature.

For the DAS-equipped unit, EG2595, the heat generated by the DAS battery pack will warm the internal ribs once it is switched "ON." During full-dummy qualification testing, an added step was taken to assure that the actual rib surface temperature was between 20.6° to 22.2° C at the time of the pendulum impacts. This was accomplished by applying a thermocouple to monitor the temperature of rib number 2 while using a portable fume extractor³ to maintain the temperature range. This device provides air movement, forcing the hot air out of the ATD via a suction hose that is easily inserted into the jacket. Subsequently, cool ambient air is pulled through existing openings in the jacket around the neck and arms, over the spine box, DAS battery pack, and thorax ribs.

For FMVSS No. 208 crash testing, the ATD soak requirement is also 20.5° to 22.2° C. In tests with the EG2595, we were routinely able to maintain this range without the need for a fume extractor by limiting the "ON" time of the DAS unit. The thermocouple remained in place on rib number 2 to ensure that temperature was maintained at 20.5° to 22.2° C at the time of the crash.

There were, however, exceptions in which the rib temperature was slightly elevated at the time of the crash. One such test occurred on September 24, 2021 (Figure 3). This was the very last test in the entire test series. Both THOR-50M units were seated in the vehicle: EG2595 (with the internal DAS) and DO9799 (no internal DAS). The rib temperature of DO9799 may be treated as a benchmark. At approximately 0740 hours, DO9799 was removed from the dummy calibration lab, which was set to a slightly lower temperature, and brought into the vehicle bay. EG2595, on the other hand, had been brought into the vehicle bay the day before.

For EG2595, the rib temperature at the time of the crash was over the limit by 0.1 degrees C. Two factors contributed to this: 1) a slightly longer than usual time lapse between the final switching "ON" of the DAS unit (just over 30 minutes); and 2) the outside air temperature. At the lab where the tests occurred (Applis Idiada Karco), bay doors to the lab are opened just prior to the test, the vehicle is released, and the actual crash occurs outdoors. During this test, the slightly longer than usual delay between the bay door opening and the barrier impact allowed the hot outside air temperature (32.8° C, 91° F) to warm the dummy.

This exercise demonstrates the need for diligence on maintaining the temperature when using any DAS-equipped dummy. It is not a situation that is unique to the THOR-50M. In another recent NHTSA test series using the WorldSID-50M dummy (which also has an internal DAS) [13], we used the fume extractor during the immediate pre-crash exercises to ensure that the rib temperatures are maintained within the specified range.

³ Weller Tools, <https://www.weller-tools.com>.

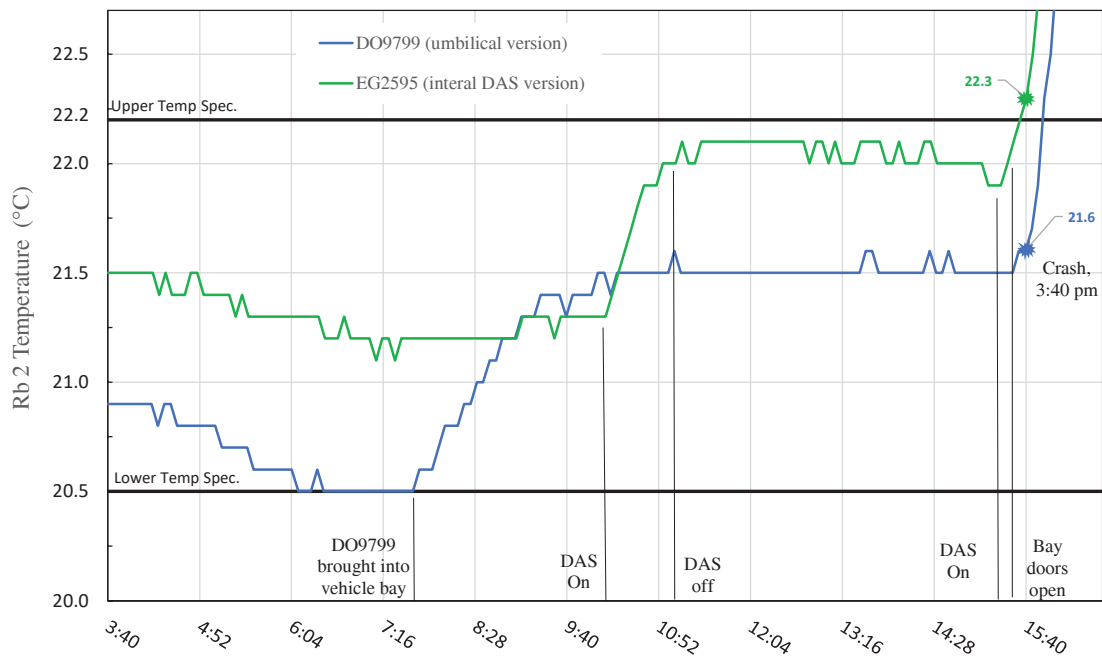


Figure 3. THOR-50M Rib No. 2 Temperature Timeline Prior to Crash Test v11638.

Crash Tests - General rigor

To assess the degree to which the THOR-50M units were exposed to a harsh testing environment, we examined various dummy metrics. Figures 4 and 5 indicate the proximity to baseline comparative values (Table 3) for the driver and passenger exposures, respectively. The colors in the plots indicate the ratio of the respective THOR-50M metric to the comparative value:

Dark green:	<= 40%	
Light green:	> 40 and <= 60%	
Yellow:	> 60 and <= 80%	
Brown:	> 80 and <= 100%	
Red:	> 100%	

For example, in Figure 4 there were five crashes for 30° near-side driver exposures, three at 40 km/hr (involving an Accord, a CX-5, and an Equinox), two at 48 km/hr (involving a CX-5 and an Accord). Two of the 40 km/hr crashes produced a BrIC score between 80-100% (brown) of the baseline reference of 0.96. The other crash was between 60-80% (yellow), as were the two 48 km/hr tests.

Figures 4 and 5 help show the degree to which the various body regions of the dummy were exposed to injurious conditions. In the majority of crash configurations, each body region had at least one high-risk exposure for both the driver and passenger positions. Nonetheless, neither of the THOR-50M units sustained damage, with the exception of sensor connector and cable problems in DO9799. Notably, the DAS unit, EG2595, did not sustain any connector or cable breaks.

In summary, the crash test series demonstrated how the dummy stood up to the rigors of crash testing. Additionally, the following observations were made:

* The 30° near-side crashes were generally more injurious for neck injuries.

* The 48 km/hr tests were more rigorous for all injury metrics and for all crash configurations.

* The Head Injury Criterion (HIC) has comparatively low injury values for all conditions.

* Abdominal deflections were universally low and are not included in Figs. 4 and 5 (all well below 63 mm, which corresponds to 10% risk of AIS 3+ injury). This was not surprising, as there was no lap belt loading to the abdomen in these unbelted tests, and the frontal airbags distributed the restraint force over the entire torso.

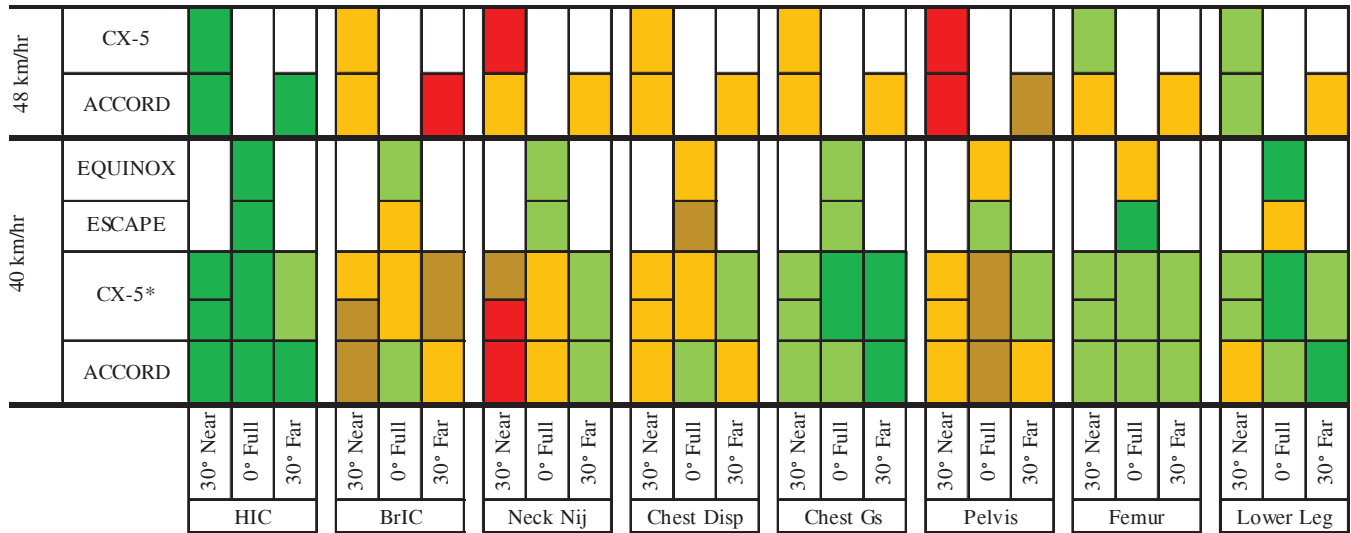


Figure 4. THOR-50M Driver: Comparative injury metrics by exposure. (*CX-5 was used in two duplicate 30° near side crash tests.)

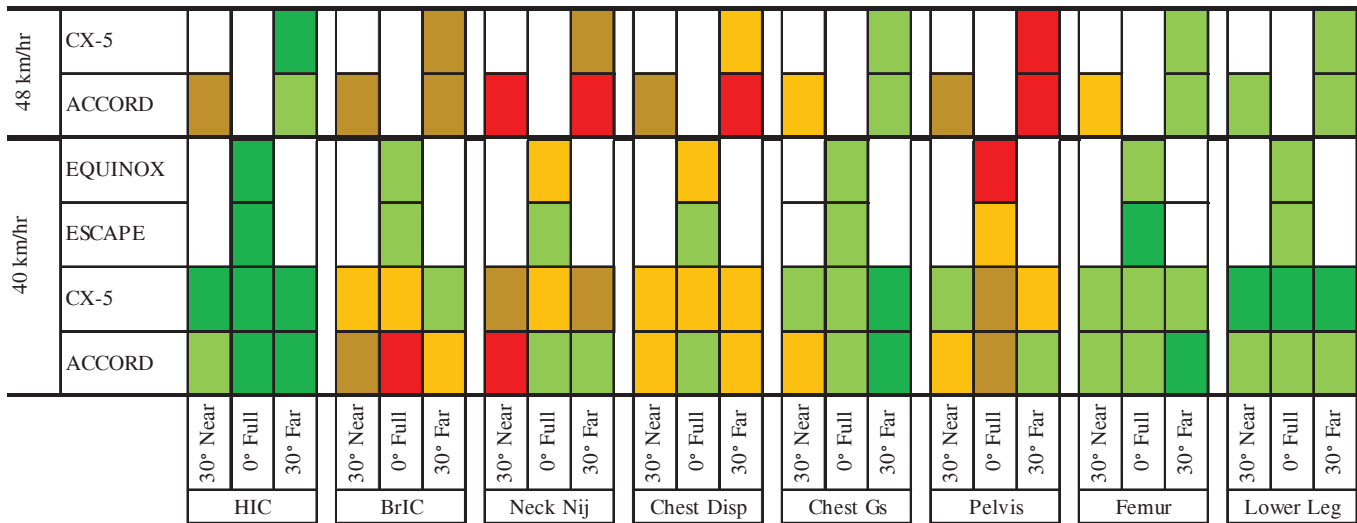


Figure 5. THOR-50M Passenger: Comparative injury metrics by exposure.

Note: In Figs. 4 and 5, for Pelvis, Femur, and Lower Leg, the maximum of the right and left measurement is represented in the charts. Additionally, for Lower Leg, the maximum of the upper and lower tibia index is represented.

Dummy kinematics

NHTSA had not previously exercised the THOR-50M in unbelted vehicle crash tests, and in this series we observed body motions that were not seen in the previous studies cited in the Introduction. The most noteworthy observation occurred in several cases where vaulting over the airbag caused head contact with the windshield and header. An example of this occurred in test v11287 on the passenger side head of a right 30° angled (near side), 48 km/hr crash test with EG2595. The contact is shown in Figure 6. This resulted in fairly high compressive loads in the upper neck load cell (4808 N), which yielded an N_{ij} value of 1.56 (red bar in Fig. 5) in the compression-extension mode. Additionally, HIC15 (629) and BrIC (0.84) were elevated (brown bars in Fig. 5). This was the worst-case test for passenger-side compressive neck loading, though other tests showed similar dummy kinematics for both the driver and the passenger. Nonetheless, the post-test inspection of the dummy revealed no unusual damage. Subsequently, the dummy underwent a full series of qualification tests; all qualification targets were attained without issue.



Figure 6. Passenger-side head impact with the windshield in test v11287, right 30° angled (near side), 48 km/hr.

Dummy inspections

The two THOR-50M ATDs were inspected throughout the test series. Other than instrumentation, no parts were found to have become damaged and in need of replacement. Aside from minor wear and tear such as head skin abrasions, there was no damage to either THOR-50M unit. Sensor anomalies and damage to the THOR-50M ATDs are summarized in the Appendix. Note that some instrumentation (for example, the right acetabulum X-axis force channel) was not functioning prior to the beginning of this test series.

DISCUSSION

Availability of replacement parts

The test series served as a "dry run" for the THOR-50M as it would be used in a regulatory environment using two serialized dummies, EG2595 and DO9799. During the test series, there were no part replacements in either of the units. However, this is not necessarily how the dummy will be used. NHTSA treats each of our THOR-50M units not so much as a serialized dummy, but as a set of serialized parts and sub-assemblies that are disassembled and reassembled at regular intervals. These sub-assemblies undergo routine maintenance on separate schedules, unlike what was done in the test series described herein.

When a THOR-50M unit is returned to NHTSA's DML after testing, it undergoes a routine breakdown and inspection. When the dummy is reassembled, a different set of parts may be introduced. Pre-qualified sub-assemblies may also be introduced. For example, a head and neck assembly may be taken out of service at regular intervals and set aside to await preventative maintenance. At a later time, a full inspection and re-qualification takes place. This process may or may not include the replacement of bumpers (also serialized), cables, or other components. However, it takes place under a separate schedule. Once cleared for use, the sub-assembly may end up in another serialized dummy. Thus, a serialized dummy does not typically define the dummy well because different parts are constantly being swapped in and out in regular intervals.

However, for the test series described herein, there were no spare parts or sub-assemblies available, so there were no part swaps. For this reason, EG2595 was delivered by the DML to Applus-Idiada-Karco – and the entire tests series was run – without a fully functioning acetabulum load cell (right X-force was not operating) and with a non-functioning occipital condyle potentiometer. Also, during a break in testing from January-May 2021, NHTSA employed DO9799 for other research investigations. When the dummy was being prepared for shipment back to Applus-Idiada-Karco, the DML discovered that the neck did not fully pass the qualification tests. We knowingly proceeded with the final two vehicles tests with the neck because we had no qualified spares to swap into the dummy.

Once the THOR-50M design is adopted in 49 CFR Part 572 and the dummy begins use in FMVSS compliance testing, an investment by NHTSA into an inventory of dummies with a full supply of spare parts may become a higher priority.

Qualification frequency

For the same reasons as stated above, we chose to run the full set of qualification tests on the THOR-50M after each crash test. This was confirmed midway through the series by a second set of full qualification tests. This, however, did not compromise the crash test results, as all qualification targets were met, with the exception of the neck tension on DO9799 in the neck extension test (upon return from the DML, as noted earlier). Nonetheless, in our future regulatory program, NHTSA may exercise added vigilance and opt to run a full set of qualification tests before every crash test. If crash tests are scheduled within a few days (with both tests preceded by a full set of qualification tests), sub-assembly swaps (or swapping out of the complete dummy) may be needed.

It is also notable that Applus-Idiada-Karco did not have substantial experience with THOR-50M qualification testing before this test series. They were **not** one of the laboratories included in the original lab-to-lab qualification testing used to develop the qualification specifications. Additionally, EG2595, a relatively new unit, was not included in the original ATD-to-ATD or lab-to-lab qualification test series. Thus, Applus-Idiada-Karco's experience has provided NHTSA with additional evidence that the qualification tests are reproducible and that NHTSA's THOR-50M design specifications have produced highly uniform and durable units.

Channel counts

During the test series describe herein, both dummies were fully instrumented with over 130 channels, including 40 channels in the lower legs alone. For future regulatory use, the channel count will likely be reduced. Many of the signal problems identified during this test series would probably be among channels that would be omitted from regulatory use: accelerometers on the pelvis, tibia shaft, and anterior superior iliac spine; femur moment channels. Thus, the time we devoted to repairing or replacing these instruments would not be experienced in future regulatory testing. NHTSA also recorded other data during this test series that are not typically gathered in regulatory tests. These include toepan intrusion measurements and 6-axis vehicle vs dummy measurements that are needed to track head kinematics.

Vehicle assessment

With regard to vehicle safety and how the four vehicle models compare with one another, no firm conclusions can be drawn due to the small sample size and the lack of repeat tests under identical conditions. Injury metrics are

reported herein in order to demonstrate that the THOR-50M was exposed to rigorous testing, not to evaluate or compare the safety of the vehicles tested.

LIMITATIONS

A limitation of this study was that only four vehicle models were tested and all tests were run at a single lab. The usability experience at other labs may vary. It may also vary with other vehicle models.

CONCLUSIONS

In a series of 19 FMVSS No. 208 unbelted frontal rigid barrier crash tests, two THOR-50M units were implemented and successfully completed the test series. Scripted procedures for dummy assembly, qualification, and handling were followed without issue, and the seating procedures resulted in highly uniform positioning. Sensor anomalies observed over the course of testing were consistent with those common in dummies already in Part 572. Aside from minor abrasions on the head skin of one of the units, there were no broken parts or part replacements throughout testing. Based on the experiences of this testing series, the THOR-50M appears fit for use in standardized testing.

REFERENCES

- [1] Summers S, Hall I, Keon T, Parent, D (2020). Occupant response evaluation in flat, full-frontal rigid barrier impact testing, Report No. DOT HS 813 014, National Highway Traffic Safety Administration, October 2020, *available at:* <https://rosap.ntl.bts.gov/view/dot/56343>
- [2] Hu J, Reed MP, Rupp JD, Fischer K, Lange P, Adler A (2017). Optimizing seat belt and airbag designs for rear seat occupant protection in frontal crashes (No. 2017-22-0004). SAE Technical Paper No. 2017-22-0004, SAE International, Warrendale PA, 2017.
- [3] Saunders J, Craig MJ, Suway J (2011). NHTSA's Test Procedure Evaluations For Small Overlap/Oblique Crashes, Paper No. 11-0343, 22nd International Technical Conference on the Enhanced Safety of Vehicles, 2011.
- [4] Saunders J, Parent D (2018). Repeatability and reproducibility of oblique moving deformable barrier test procedure, SAE Technical Paper No. 2018-01-1055, SAE International, Warrendale PA, 2018, *available at:* <https://www.regulations.gov/document/NHTSA-2019-0106-0005>.
- [5] Parent D, Craig M, Moorhouse K (2017). Biofidelity Evaluation of the THOR and Hybrid III 50th Percentile Male Frontal Impact Anthropomorphic Test Devices. Stapp Car Crash Journal, 61, 227-276, *available at:* <https://www.regulations.gov/document/NHTSA-2019-0106-0004>.
- [6] National Highway Traffic Safety Administration (2019). THOR-50M Durability Report, October 2019, Regulations.gov Docket ID NHTSA-2019-0106-0003, *available at:* <https://www.regulations.gov/document/NHTSA-2019-0106-0003>.
- [7] National Highway Traffic Safety Administration (2018). Parts List and Drawings, THOR-50M Advanced Frontal Crash Test Dummy, August 2018. Regulations.gov Docket ID NHTSA-2019-0106-0002, *available at:* <https://www.regulations.gov/document/NHTSA-2019-0106-0002>.
- [8] National Highway Traffic Safety Administration (2023). THOR 50th Percentile Male (THOR-50M) Qualification Procedures, Washington, DC: *Undergoing final document proofing; publication scheduled for 2023.*
- [9] National Highway Traffic Safety Administration (2008). Laboratory Test Procedure for FMVSS No. 208, Occupant Crash Protection, NHTSA Test Procedure 208-14, April 16, 2008, *available at:* https://www.nhtsa.gov/sites/nhtsa.gov/files/documents/tp-208-14_tag.pdf

[10] Louden AE (2019). Revised THOR 50th percentile male dummy seating procedure, Report No. DOT HS 812 746. Washington, DC: National Highway Traffic Safety Administration, *available at*:
https://rosap.nhtsa.gov/view/dot/40786/dot_40786_DS1.pdf

[11] National Highway Traffic Safety Administration (2020). THOR-50M Procedures for Assembly, Disassembly, and Inspection (PADI), August 2018 *available at*:
<https://www.regulations.gov/document/NHTSA-2019-0106-0007>

[12] Craig M, Parent D, Lee E, Rudd R, Takhounts E, Hasija V (2020). Injury Criteria for the THOR 50th Male ATD, *Regulations.gov* Docket ID NHTSA-2019-0106-0008, *available at*:
<https://www.regulations.gov/document/NHTSA-2019-0106-0008>.

[13] Tatem WM, Louden A (2023). WorldSID-50M fitness assessment in FMVSS No. 214 moving deformable barrier and pole crash tests, Paper No. 23-0340, 27th International Technical Conference on the Enhanced Safety of Vehicles, Yokohama, Japan, April 2023.

APPENDIX

Table A-1. Summary information of unbelted tests series

Test Date	Make and Model	Crash Config	Speed (km/hr)	Driver	RF Pass	Test No.
9/9/2020	2020 Honda Accord	30° L	48	DO9799	<i>HIII-50M</i>	v11284
9/25/2020	2020 Honda Accord	30° R	48	EG2595	<i>HIII-50M</i>	v11285
10/1/2020	2020 Honda Accord	30° L	48	<i>HIII-50M</i>	DO9799	v11286
10/9/2020	2020 Honda Accord	30° R	48	<i>HIII-50M</i>	EG2595	v11287
10/21/2020	2020 Mazda CX-5	30° L	48	DO9799	<i>HIII-50M</i>	v11345
12/7/2020	2020 Mazda CX-5	30° R	40	EG2595	<i>HIII-50M</i>	v11346
12/15/2020	2020 Mazda CX-5	30° L	48	<i>HIII-50M</i>	DO9799	v11362
12/18/2020	2020 Mazda CX-5	30° R	40	<i>HIII-50M</i>	EG2595	v11363
1/8/2021	2020 Honda Accord	0°	40	DO9799	EG2595	v11361
1/15/2021	2020 Mazda CX-5	0°	40	DO9799	EG2595	v11364
5/21/2021	2020 Mazda CX-5	30° L	40	EG2595	<i>HIII-50M</i>	v11630
6/7/2021	2020 Mazda CX-5	30° L	40	<i>HIII-50M</i>	EG2595	v11637
6/24/2021	2020 Honda Accord	30° L	40	EG2595	<i>HIII-50M</i>	v11629
7/2/2021	2020 Honda Accord	30° R	40	EG2595	<i>HIII-50M</i>	v11628
7/30/2021	2020 Honda Accord	30° L	40	<i>HIII-50M</i>	EG2595	v11635
8/13/2021	2020 Honda Accord	30° R	40	<i>HIII-50M</i>	EG2595	v11636
9/17/2021	2021 Chevrolet Equinox	0°	40	EG2595	DO9799	v11639
9/22/2021	2021 Ford Escape	0°	40	EG2595	DO9799	v11665
9/24/2021	2020 Mazda CX-5	30° L	40	DO9799	EG2595	v11638

Table A-2. EG2595 inspection: instrumentation anomalies and damage

Date	Test No.	Sensor Anomaly	Description	Repaired
9/25/2020	v11285	Acetabulum LC, Right, X-force	The channel was found to be inoperable upon receipt of the dummy from the DML. Cause of malfunction was unknown. A replacement load cell was not available and a timely repair was not feasible. All crash testing conducted without this signal.	NA
<i>Before 1st test</i>		Occipital Condyle, Rotary Potentiometer	Dummy arrived from DML with OC unwired. A special connector needed for the SLICE6 system was not readily available. All crash testing conducted without this signal.	NA

Table A-3. DO9799 inspection: instrumentation anomalies and damage

Date	Test No.	Sensor Anomaly	Description	Repaired
9/9/2020 <i>1st test</i>	v11284	Tibia, Left, Mid-shaft, X-acceleration	The channel was found to be inoperable upon receipt of the dummy from the DML. Cable damage at accelerometer was found, too close to accelerometer to fix. All crash testing conducted without this signal.	No
		Tears in face foam	THOR-50M was delivered by DML with tears in the face foam. All face qualification tests passed nonetheless. All crash testing conducted with foam in this condition.	No
		Abdomen, Right, DGIR, X-displacement	This channel recorded an intermittent signal. The cause was undetermined. The intermittent signal did not occur in the rest of the qualification and vehicle testing.	NA
		Upper Chest, Left, DGIR, Z-rotation	No data recorded due to damage to cable despite operability during qualification and pre-test polarity checks. It was determined that a wire was damaged. Cause of damage was unknown; may have occurred pre-test since there was no data at time t=0. The wire was repaired after the test.	Yes
10/1/2020 <i>2nd test</i>	v11286	Scrapes on top of head skin	Abrasions to head covering were presumed to have occurred during testing.	No
		Femur, Left, Y-moment	No data recorded due to damage to cable despite operability during pre-test polarity checks. Cause of damage was unknown; may have occurred pre-test. The wire was repaired after the test.	Yes
		Tibia, Right, Mid-shaft, X-acceleration	No data recorded due to damage to cable despite operability during pre-test polarity checks. Cause of damage was unknown; may have occurred pre-test since there was no data at time t=0. The wire was repaired after the test.	Yes
12/15/2020 <i>4th test</i>	v11362	T1, X-acceleration	Intermittent signal recorded. Cause was not readily obvious. Continued testing without further investigation.	NA
		Pelvis, Z-acceleration	No data recorded due to damage to cable despite operability during pre-test polarity checks. Cause of damage was unknown; may have occurred pre-test since there was no data at time t=0. The wire was repaired after the test.	Yes
9/22/2021 <i>8th test</i>	v11665	A.S.I.S., Left, Y-Moment	The channel failed during the crash tests, with an intermittent signal due to a broken cable. The connector was resoldered to repair.	Yes
		Femur, Right, Z-moment	The channel failed during the crash tests when the signal dropped off due to a broken cable. The connector was resoldered to repair.	Yes
		Upper Tibia, Left, X-Force	Sensor failed between 68.3 to 76.9 ms. Channel was inspected; cause of the failure is unknown. Channel was retested without issue. Continued testing without further investigation.	NA
9/24/2021 <i>9th (last) test</i>	v11638	A.S.I.S., Left, Y-Moment	No data recorded despite operability during pre-test polarity checks. Cable problem found in post-test inspection; cause of damage was unknown; may have occurred pre-test since there was no data at time t=0. The wire was repaired after the test.	Yes
		Acetabulum, Right Y-Force.	The channel failed at 78 ms during the last crash test.	Yes
		Femur, Right, Y-Force	No data recorded despite operability during pre-test polarity checks. Cause of damage was unknown; may have occurred pre-test since there was no data at time t=0. The wire was repaired after the test.	Yes

WORLD SID-50M FITNESS ASSESSMENT IN FMVSS NO. 214 MOVING DEFORMABLE BARRIER AND OBLIQUE POLE CRASH TESTS

Whitney Tatem
Allison Louden
NHTSA
USA

Paper Number 23-0340

ABSTRACT

A prerequisite for entering an anthropometric test device (ATD) design into the Code of Federal Regulations (CFR) Title 49, Part 572 is to demonstrate that the specifications yield units capable of implementation in a regulatory environment. Specifications for the WorldSID 50th percentile male (WorldSID-50M) ATD have produced units that are repeatable, reproducible, and durable in many test conditions, including qualification, sled, and crash testing. Herein, three WorldSID-50M units are implemented in a series of vehicle crash tests run in accordance with the Federal Motor Vehicle Safety Standard (FMVSS) No. 214 procedures, and evaluated based on usability, durability, and the successful collection of sensor data for use in injury risk prediction.

Methods and Data Sources: The National Highway Traffic Safety Administration (NHTSA) investigated WorldSID-50M performance in FMVSS No. 214 moving deformable barrier (MDB) and oblique pole tests. Performance metrics assessed included uniformity in periodic qualification testing during the crash test series, the durability of the ATD, successful collection of sensor data, and general usability. All qualification and crash tests were run at one lab with three WorldSID-50M units. Each ATD was the standard build level F with an in-dummy data acquisition system (IDDAS) setup (DTS G5 units), a RibEye Multi-Point Deflection Measurement System, thorax pads, modified shoulder pads, and a sleeveless suit. Before the test series, each ATD was fully qualified per NHTSA's WorldSID 50th Percentile Male Qualification Procedures Manual, and additional qualification tests were conducted throughout the crash series. Eighteen crash tests (seven MDB and eleven oblique pole) with model year 2019 and 2020 vehicles were ultimately conducted.

Results: The three WorldSID-50M units met qualification test requirements throughout the crash test series with minimal issues. Results were within performance specifications after tightening loose bolts in the upper and lumbar spine prior to being used in the crash tests. The WorldSID-50M Dummy Seating Procedure was followed and resulted in repeatable and reproducible seating positions. In crash tests, the WorldSID-50M ATDs were durable and successfully collected sensor data. Apart from a broken ankle in one test, no permanent damage was seen on any ATD. One pole test resulted in loss of the maximum thorax rib deflection due to a RibEye LED blockage by another rib. The issue was resolved by relocating the rib's LEDs. The WorldSID-50M posed no other difficulties in performing the crash tests.

Conclusion and Limitations: This controlled study of the WorldSID-50M in FMVSS No. 214 testing showed that the ATD is durable and successfully collects sensor data in both qualification and crash testing. There were few sensor anomalies throughout the test series, and any instrumentation issues were quickly resolved. Collectively, this series of crash tests demonstrates that the design of the WorldSID-50M appears robust and provides a tool suitable for use in standardized side impact testing. A limitation of this study is that all tests were conducted at a single lab. Further, few small, compact, and sub-compact size vehicles were included in this test series. Additional analysis of data from ongoing crash tests encompassing a more comprehensive vehicle fleet will yield more holistic results assessing the WorldSID-50M.

INTRODUCTION

NHTSA has performed research tests using an advanced side impact ATD, the WorldSID-50M, since 2005. This ATD is an alternative to the ES2re, where the WorldSID provides better biofidelity (quantitatively shown using NHTSA's Biofidelity Ranking System) and enhanced injury assessment capability [1]. To date, the WorldSID-50M has been assessed in over 70 crash tests and 1,800 component-level tests to refine the ATD design.

For an ATD design to be entered into CFR Title 49, Part 572¹, the specifications must yield units capable of implementation in a regulatory environment. In December 2015, NHTSA issued a Request for Comments (RFC) that included implementing the WorldSID-50M into current New Car Assessment Program (NCAP) side test protocols [2]. Subsequently in 2016, NHTSA conducted a series of research crash tests including nine NCAP MDB tests and nine FMVSS No. 214 oblique pole tests using the then current version of the WorldSID-50M². Further, in 2019, NHTSA conducted repeatability and reproducibility (R&R) tests at three crash labs including both NCAP MDB and FMVSS No. 214 oblique pole tests with a 2018 Honda Accord and the WorldSID-50M³. The WorldSID-50M has additionally been utilized in qualification and sled testing environments to evaluate R&R [3] and durability [4]. RibEye performance was evaluated in linear impactor, sled, and crash conditions [5]. During all series of testing, the WorldSID-50M seating procedures, test procedures incorporating the IDDAS, and the RibEye were evaluated and updated, among others, as appropriate.

NHTSA recently announced its intent to enter the WorldSID-50M into CFR Title 49, Part 572 (RIN: 2127-AM22) and subsequently into FMVSS No. 214 as an ATD option (RIN: 2127-AM23). Considering that updates to the WorldSID-50M design and associated procedures have been made since the RFC in 2015, the objective of this research was to evaluate the latest version of the WorldSID-50M based on usability, durability, and the successful collection of sensor data when exposed to qualification tests and FMVSS No. 214 MDB and oblique pole crash tests.

METHODOLOGY

Overview

NHTSA conducted a series of eighteen full-scale vehicle crash tests from September 2020 through June 2022 that epitomizes the WorldSID-50M envisioned use in a regulatory setting – a crash test series of FMVSS No. 214 MDB and oblique pole tests including qualification tests. Ten distinct 2019-2020 model year vehicles were used in testing: the Chevrolet Malibu, Ford Ranger, GMC Terrain, Hyundai Santa Fe, Hyundai Veloster, Kia Soul, Mini Cooper S convertible, Nissan Rogue, Ram 1500, and Toyota Tacoma. Details of the tests are discussed below.

FMVSS No. 214 Tests

The eighteen crash tests were run by following FMVSS No. 214 procedures for either the driver (for left-side vehicle impacts) or the front passenger (for right-side vehicle impacts). For reference, the FMVSS No. 214 crash configurations are depicted in Figure 1. Eleven pole tests were conducted in accordance with the latest FMVSS No. 214 test procedure, TP-214P-01, dated September 2012. The first test of the series was conducted with a higher NCAP target test speed of 32.2 ± 0.8 km/h. Following this test, all the remaining ten pole tests were run at the compliance target test speed of 31.0 ± 0.9 km/h. Seven MDB tests were conducted in accordance with the latest FMVSS No. 214 test procedure, TP-214D-09, dated September 2012, and all run at the compliance target test speed of 52.9 ± 0.8 km/h⁴.

¹<https://www.ecfr.gov/current/title-49/subtitle-B/chapter-V/part-572?toc=1>

²<https://www.nhtsa.gov/research-data/research-testing-databases#/vehicle> [Test Numbers 9780-9791, 10051-10056]

³https://www.nhtsa.gov/sites/nhtsa.gov/files/documents/nhtsas_rr_evaluation_of_the_wordsid_50th_male_atd_tag.pdf

⁴ <https://www.nhtsa.gov/vehicle-manufacturers/test-procedures>

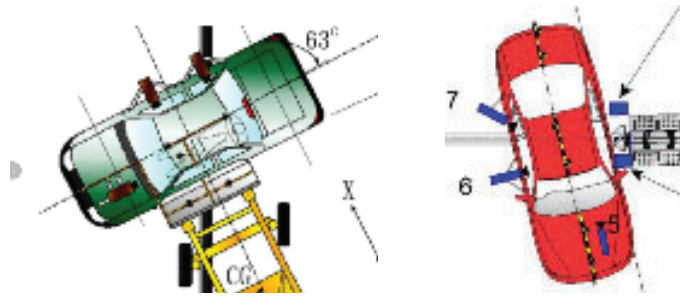


Figure 1. (L) Impact by the MDB, and (R) oblique impact with the rigid pole.

In all tests, the WorldSID-50M was positioned per the WorldSID 50th Percentile Male Dummy Seating Procedure Evaluation and Revision [6]. Performance metrics assessed included uniformity in periodic qualification testing during the crash test series, the durability of the ATD, successful collection of sensor data, and general usability.

WorldSID-50M Units Tested

During this test series, three different WorldSID-50M ATDs were used, all conforming to NHTSA's WorldSID-50M design specifications. Each unit was manufactured by Humanetics in accordance with NHTSA's Parts List and Drawings [7]. The WorldSID-50Ms were also notably equipped with a Diversified Technical Systems, Inc. (DTS) G5 IDDAS, a RibEye Multi-Point Deflection Measurement System, thorax pads, modified shoulder pads, and a sleeveless suit.

All ATDs were instrumented and assembled (including wire harness routing and instrumentation polarity checks) at NHTSA's Dummy Management Laboratory (DML) at the Vehicle Research and Test Center (VRTC) in Ohio prior to delivery to the crash test lab, Transportation Research Center, Inc. (TRC). Final inspections, setup (including joint torque settings), and qualification tests [8] were fulfilled at TRC by following NHTSA's WorldSID-50M Procedures for Assembly, Disassembly, and Inspection (PADI) [7].

Two WorldSID-50M units were configured for left side impacts while the third was configured for right side impacts. They will henceforth be referred to as WS-L1, WS-L2, and WS-R, respectively. Each ATD was instrumented with head accelerometers, head angular rate sensors, upper and lower neck load cells, shoulder load cells, T1/T4/T12 accelerometers, lumbar load cells, pelvic accelerometers, pubic load cells, left and right sacroilia load cells, and femur/femoral neck load cells. All these instruments are specified within the drawing package, with installation instructions included in the PADI [7]. Additionally, all units were instrumented with sensors to measure the internal ATD temperature before, during, and after testing.

WorldSID-50M Configurations

DTS G5 In-Dummy Data Acquisition System (IDDAS)

The WorldSID-50M contains provisions for IDDAS up to 128 channels depending on the specific configuration, and the DAS units can be installed in a variety of locations throughout the ATD thorax, pelvis, or upper legs. The design used in this test series utilizes the two 32-channel DTS G5 IDDAS installed in the thorax/spine for a quantity of 64 channels. In addition, the ATDs are also equipped with a separate IDDAS controller for the RibEye system that is installed on the non-struck side of the spine box.

RibEye Multipoint Deflection Measurement System

RibEye, manufactured by Boxboro Systems⁵, is a multipoint optical measurement system that is capable of measuring 3D rib deflection at multiple points on each of the six independent ribs of the WorldSID-50M. The RibEye consists of two groups of three sensors (receivers) mounted on the impact-side of the spine box, one at each rib level, as depicted in Figure 2(a). On the opposite side at each rib level are three LEDs per rib, mounted on the

⁵ <https://www.boxborosystems.com/ribeye.html>

inner surface of the inner rib, as shown in Figure 2(b). The LEDs are mounted at front, middle, and rear locations on each rib, spaced at 35 mm apart, as determined by an optimization study [9] (Figure 3). Further, each LED has a specific mounting method, vertical position, orientation, and an angle for positioning on the ribs [7]. This combination of optical sensors and LEDs makes RibEye capable of measuring both lateral and oblique rib deflections, a distinct advantage over other systems such as the IR-TRACC, when the ATD is subjected to the oblique loading that sometimes occurs in side impacts.

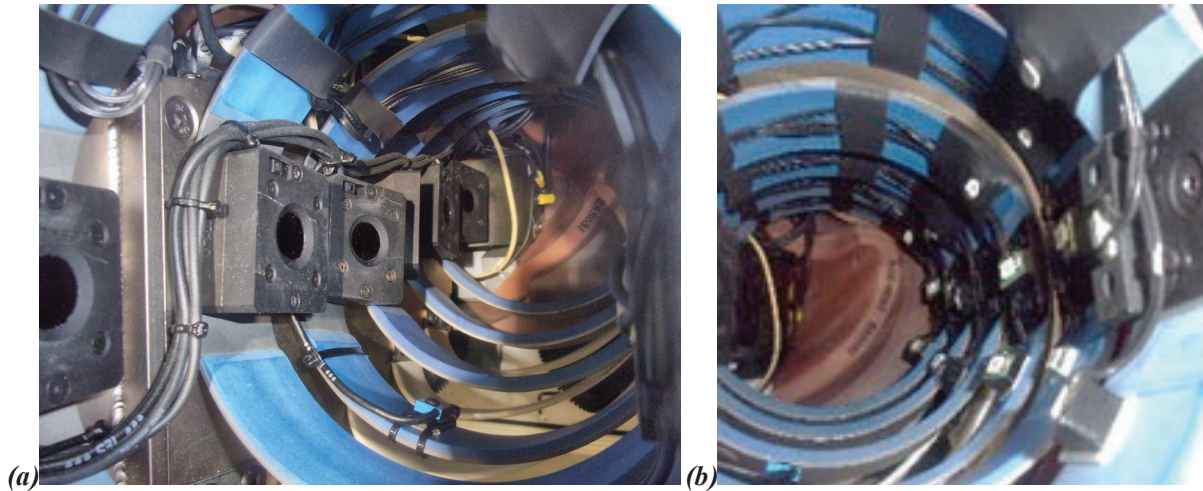


Figure 2. RibEye sensors (a) and LEDs (b) installed in a WorldSID-50M.

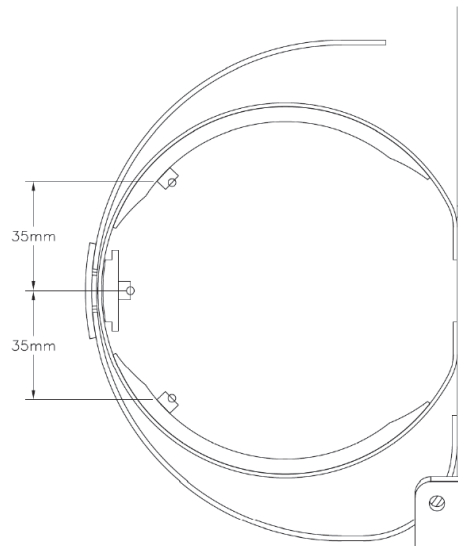


Figure 3. Schematic showing front, middle, and rear RibEye LED locations on a WorldSID-50M rib.

Given that RibEye is a novel optical measurement system, there are some distinct and notable traits when compared to other systems. Each sensor on the RibEye has a finite measurement range, so if an LED moves outside the detectable range, its position cannot be measured. When this occurs, the RibEye system produces an ‘error code’ indicating as such. From previous tests conducted by NHTSA, LEDs going out of range are often inconsequential if at least one LED on a rib does not exceed the range of the sensor. An error code is also produced when one or more sensors are blocked from the LEDs or if too much ambient light is detected by a sensor. An example of this is when one rib deflects more than an adjacent rib, blocking the path from an LED to a sensor. When this situation occurs, the rib with the most deflection is often measured, rendering the blocked LED insignificant.

Thorax Pads

The original WorldSID-50M build has a single thorax pad between the outside of the ribs and jacket. Because NHTSA witnessed these pads tearing during evaluation testing, it was thought that it would be beneficial to split the single pad into pads for each individual rib as depicted in Figure 4(a). The split pad design was used in the first sixteen crash tests of this series. In parallel, a new probe face was developed within the ISO WorldSID 50th Task Group for qualification testing. This development proved to significantly reduce the risk for tearing of the single thorax pad during qualification tests, which had been impetus for developing the split pad concept. With the new probe face greatly alleviating pad durability concerns, NHTSA chose to revert to the original one-piece thorax pad as depicted in Figure 4(b), harmonizing with the ISO group. The last two tests of the series were conducted with this single pad design.

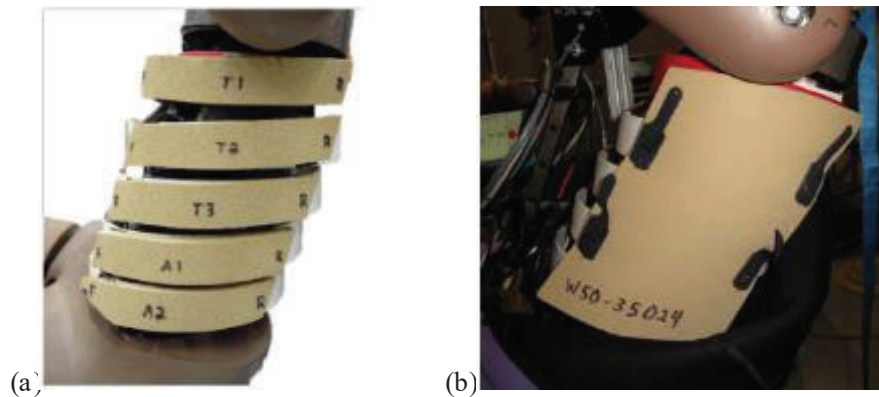


Figure 4. WorldSID-50M (a) split and (b) single thorax pads.

Shoulder Pads

The original design of the WorldSID-50M shoulder pad by Humanetics was a soft vinyl and foam pad. During testing in 2016 with the original foam shoulder pad and RibEye, it was observed that the shoulder pad would protrude into the shoulder rib cavity during impact causing shoulder LED blockages. Therefore, prior to this series of testing, a new shoulder pad designed by VRTC (Figure 5) with a similar footprint but hollowed-out underside, with stiffening qualities that prevent it from being pushed into the shoulder rib cavity of the ATD was developed, tested, and evaluated by NHTSA in the 2018-2019 R&R crash test series.

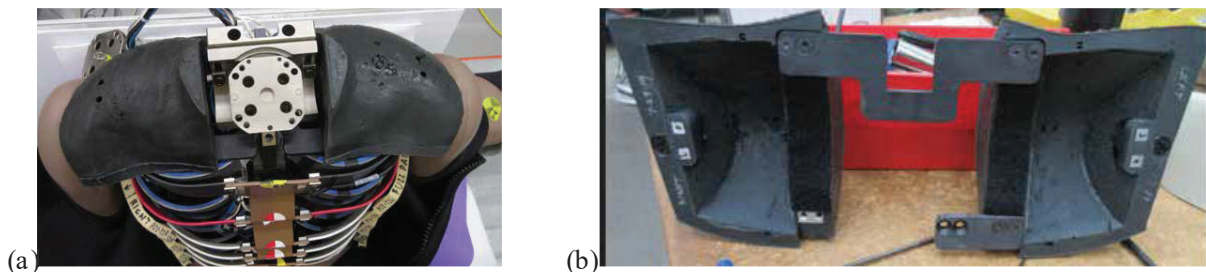


Figure 5. Top (a) and bottom (b) view of VRTC's prototype WorldSID-50M shoulder pad design.

For this crash test series, in the first few crash tests, VRTC's prototype design was used with a screw attachment at the shoulder rib. However, during the test series, it was noted that the aluminum screw mounting blocks molded into the shoulder pads were tearing out of the pads during testing. Therefore, the design was modified mid-series with a minor change where the screw was replaced by a single pin at the shoulder rib clamp. This new design was implemented to improve the ease of use of the shoulder pads, along with improving the durability of the shoulder pads.

Sleeveless Suit

The original WorldSID-50M skinsuit included sleeves for the arms and contained a sizeable hole under the arm to facilitate arm motion. However, in this configuration, the sleeve fabric could bunch together during shoulder flexion and the hole provided a path for external light to enter the thoracic cavity, potentially interfering with the RibEye functionality. Therefore, a sleeveless skinsuit design has been adopted by NHTSA as depicted in Figure 6. The sleeveless suit provides improved freedom of arm motion without bunching and eliminates the potential light path under the arm.



Figure 6. WorldSID-50M dressed in its sleeveless skinsuit.

WorldSID50-M Qualifications and Inspections

Prior to the initial vehicle crash test for each WorldSID-50M, a full set of qualification tests was conducted at NHTSA's DML at VRTC or at TRC (Appendix A details the qualification location). Thereafter, a full set of qualification tests were conducted at TRC after every third crash test. Partial qualification tests were conducted after some vehicle crash tests on the WorldSID-50M units if there were instrumentation issues or dummy damage at both VRTC DML and TRC DML. All qualification tests were carried out in accordance with NHTSA's draft WorldSID-50M Qualification Procedures [8]. Additionally, before every qualification test, a polarity check and sensor checkout were performed to assure that all sensors were oriented and working properly.

After every crash test, the tested WorldSID-50M unit underwent a physical inspection. Each body region was examined by partially disassembling the ATD, and a visual inspection was carried out. Photographic images of any damage are documented in each test report.

As part of the inspection, each ATD sensor was scrutinized for its overall condition and functionality. This was determined by examining crash test signal data channels for any sensor anomalies, such as clipping, unexpected drops, or flat signals. Instruments were also inspected for any physical evidence of damage. If damage was found, the instruments were closely inspected to determine the source of the anomaly and repaired where possible.

Crash Test Exposures and Schedule

For the two FMVSS No. 214 test modes (MDB and oblique pole), the three WorldSID-50M units were subjected to multiple crash exposures as shown in Table 1. Each test type exposed the ATD to a different loading condition. Multiple tests were run in each condition to assure the ATD was thoroughly exercised in each exposure mode.

Table 1. WorldSID-50M crash test exposures (n = 18).

NHTSA Test #	Test Date	Vehicle Model Year	Vehicle Make	Vehicle Model	Test Type	WorldSID-50M Unit
Primary Testing Series						
11600	9/25/2020	2019	Chevrolet	Malibu	L Pole	WS-L1
11601	10/22/2020	2020	Nissan	Rogue	L Pole	WS-L1
11603	12/15/2020	2020	Hyundai	Santa Fe	L Pole	WS-L1
11604	1/14/2021	2020	Hyundai	Veloster	L Pole	WS-L1
11605	1/28/2021	2020	Hyundai	Santa Fe	L MDB	WS-L1
11606	2/4/2021	2020	GMC	Terrain	L MDB	WS-L1
11607	2/11/2021	2020	Hyundai	Veloster	L MDB	WS-L1
11608	3/11/2021	2020	Nissan	Rogue	L MDB	WS-L1
11609	3/18/2021	2020	Ford	Ranger	L MDB	WS-L1
11610	3/23/2021	2019	Chevrolet	Malibu	L MDB	WS-L1
11611	4/1/2021	2020	GMC	Terrain	L Pole	WS-L1
11612	4/8/2021	2020	Ford	Ranger	L Pole	WS-L1
11613	4/15/2021	2019	Ram	1500	R Pole	WS-R
11614	4/22/2021	2019	Mini	Cooper S Con.	R Pole	WS-R
11615	4/29/2021	2020	Mini	Cooper S Con.	R MDB	WS-R
Secondary Testing Series						
11656	9/15/2021	2019	Mini	Cooper S Con.	R Pole	WS-R
14356	6/8/2022	2020	Toyota	Tacoma	L Pole	WS-L2
14355	6/15/2022	2020	Kia	Soul	L Pole	WS-L2

All crash tests were run at TRC per the schedule of testing summarized in Table 1. The eighteen tests were run between September 2020 and June 2022, with five- and nine-month gaps between April to September 2021 and September 2021 to June 2022, respectively, in which no testing was performed due to RibEye LED enhancement efforts, which are discussed subsequently.

A NHTSA test number is denoted for each test, from which test reports may be found by searching within NHTSA’s Crash Test Database⁶. Each report provides all test signals from the crash tests. It also includes the pre- and post-test qualification testing results performed on each of the WorldSID-50M units, as well as a post-test inspection of the ATD. NHTSA Test numbers 11600–11615 are henceforth referred to as ‘the primary testing series,’ while numbers 11656, 14356, and 14355 are referred to as ‘the secondary testing series.’

WorldSID-50M Injury Assessment

Injury Assessment Reference Values (IARVs) typically refer to the limits for a given injury criterion calculated based on crash test results. For regulatory purposes, IARVs are defined in the regulation that describes the crash test modes, such as FMVSS No. 214. The WorldSID-50M does not currently have specified IARVs. Therefore, for the purpose of this research paper, a set of baseline comparative values were selected for the purposes of the current study.

To guide the selection of baseline values, existing injury criteria specific to the WorldSID-50M were referenced. Generally, reference values were selected based on current European NCAP metrics with the addition of BrIC, as displayed in Table 2.

⁶ <https://www.nhtsa.gov/research-data/research-testing-databases#/vehicle>

Table 2. WorldSID-50M EuroNCAP reference values for injury assessment.

Body Region	Criterion / Measurement	Units	EuroNCAP Reference Value
Head	HIC15	none	700
	BrIC	none	0.96
Chest	Shoulder Force	N	3,000
	Thoracic Rib Deflection	mm	50
Abdomen	Abdominal Rib Deflection	mm	65
Pelvis	Pubic Force	N	2,800

RESULTS AND DISCUSSION

Qualification Tests

Each WorldSID-50M was fully qualified before the test series, and additional qualifications (some full, some partial) were conducted throughout the test series as described below (see Appendix for a full test summary). All qualifications were performed and processed according to the Draft NHTSA WorldSID-50M Qualification Manual [8], and the corridors contained therein.

WS-L1

From September 2020 to April 2021, WS-L1 went through six full qualifications. In five of the six full qualification tests, the WorldSID-50M passed in its entirety. During the fourth qualification, which occurred after test 11607, the WorldSID-50M did not initially pass the thorax with a arm test. After some troubleshooting, an inspection revealed loose bolts on top of the spine box which were simply tightened to remedy the failure. It is unclear at what point these bolts began coming loose since full qualification tests were only being performed after every third crash test. The bolts were tightened and the thorax with a arm test was conducted again resulting in a passing test.

WS-R

From January 2021 to April 2021, WS-R went through two full qualifications. During the first full qualification test, the WorldSID-50M did not pass the thorax with a arm test in its initial impacts. After several additional attempted thorax with arm tests, inspection revealed there were loose bolts that connect the lumbar mounting wedge to the rubber lumbar spine. Again here, simply tightening the bolts remedied the failure. It is unclear when the bolts began to loosen due to different troubleshooting methods executed by VRTC and TRC (e.g., replacing ribs and additional qualifications).

The post-primary-test-series qualification (the second full qualification), which occurred after test 11615, passed all test modes except for the pelvis. The lateral sacroiliac force result was low (1812 N) compared to the draft specification of 1860-2280 N. Because this was a post-series qualification, the test result was documented and accepted.

However, during the secondary test series pre-test qualifications (the third full qualification), there were additional difficulties in attaining passing results on the pelvis qualification test mode. After four attempts, the pelvis results not meeting the proposed criterion were accepted due to this being a newly proposed criterion. While a high impactor force was encountered in one of the attempts, the primary failing parameter was the sacroiliac lateral force, which was consistently low. This result was like the result in the second full qualification.

Following crash test 11656, the fourth full qualification was performed. WS-R underwent troubleshooting and additional testing to resolve the pelvis issues. Prior to any tests being performed, the rubber lumbar component was replaced as a first attempt to remedy the problem. The tests that followed no longer exhibited any abnormalities with the sacroiliac force; however, the new issue became low pubic force responses. Multiple parts were swapped out and tested to identify the cause of these issues. At the time of manuscript preparation, these issues are still unresolved, and investigation is ongoing.

WS-L2

Due to the pelvis issues discussed in WS-R, a third WorldSID-50M unit was introduced, WS-L2. In May 2022, a full qualification was performed with passing results prior to the last two oblique pole crash tests (14355 and 14356). A full post-test qualification was conducted in July 2022, and the ATD passed all test modes.

Seating Procedure

The WorldSID-50M seating procedure was followed to position the ATD in each crash test. The procedure places the seat pan at mid-angle, at the lowest height position, and typically at midtrack, barring any lower body interference with the trim panels of the vehicle dashboard. Among the vehicles used in the test series, a 2019 Mini Cooper S convertible was used more often than the other vehicle models. A WorldSID-50M unit was seated in the front passenger seat in three Mini Cooper tests. Figure 7 displays a stick figure derived from the Mini Cooper vehicle reports that indicates the relative uniformity of the ATD positioning (WorldSID-50M unit WS-R in all cases). It shows the x- and z-coordinates relative to the door lock striker on the passenger side of the vehicle. Coordinates of high interest are shown in the figure, including the outboard H-point.

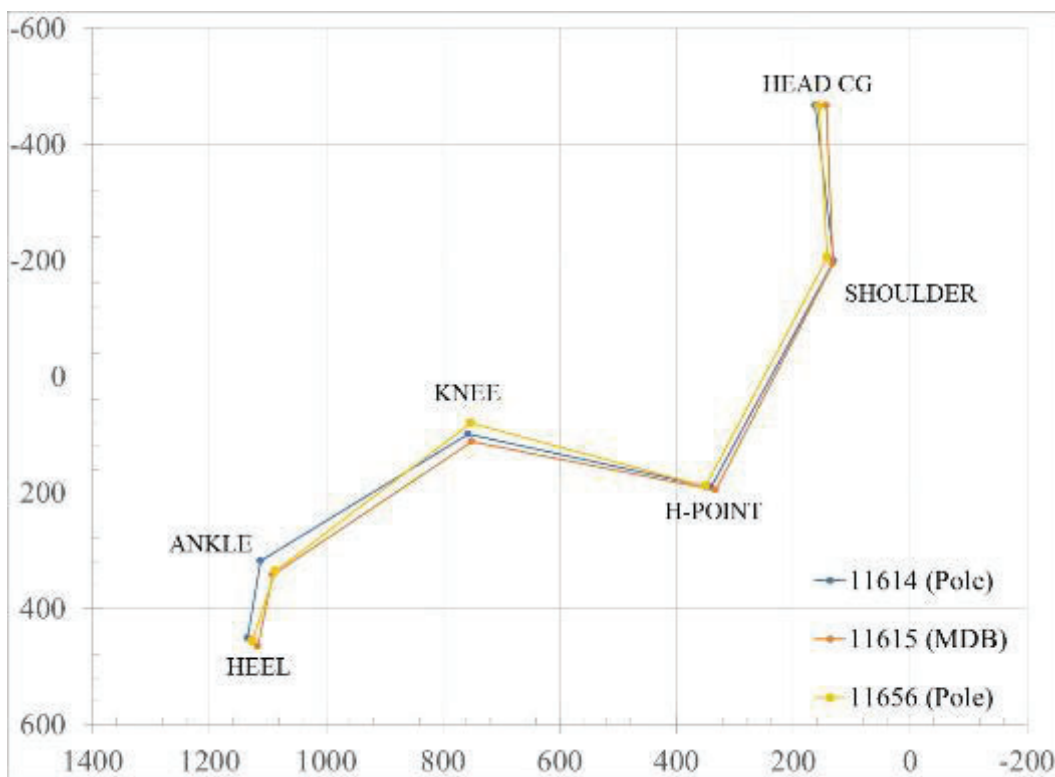


Figure 7. WorldSID-50M Front Passenger: Seated coordinates in three Mini Cooper S convertible tests.

Oblique Pole Tests

All the seats were able to be positioned at midtrack without any interference with the vehicle interior in all eleven oblique pole tests. The seating procedure specifies tilt sensor ranges (± 2.5 degrees) for both the pelvis and head position along with an H-Point target location range of ± 10 mm. The Ford Ranger driver test position was the only test where the neck was adjusted out of the zero-degree position. In this test, the neck was adjusted 3 notches, rotating the chin upward. On average, in the oblique pole tests, the measured position of the H-point was -0.2 mm rearward and 5.4 mm below the projected H-point. There were no major issues with seating the ATDs in the pole tests, though there were a few deviations or noteworthy observations that are detailed in the sections below.

MDB Tests

The seats were able to be positioned at midtrack without any interference with the vehicle interior in six of the seven MDB tests. On the Nissan Rogue MDB test, the knees of WS-L1 were meeting the underside of the dash, leading to the seat being placed rearward of midtrack – this is discussed in further detail below. The GMC Terrain MDB test was the only test where the neck was adjusted out of the zero-degree position – on this test, the neck was adjusted 1 notch, rotating the chin upward. On average, in the MDB tests, the measured position of the H-point was 0.2 mm rearward and 5.7 mm below the projected H-point. There were no major issues with seating the ATDs in the MDB tests, though there were a few deviations or noteworthy observations that are detailed in the sections below.

Foot Placement

The seating procedure was developed to help place the WorldSID-50M feet in a similar manner in a variety of vehicles, with the right foot placement based on pedal type and the left foot dependent on the presence of a footrest and if it elevated the heel.

Right Foot

Throughout the test series, the heel point was marked at 200 mm from the pedal center point depending on the type of pedal (hinged or hanging). For many tests, the right foot was within the range established of +/-10mm in the fore/aft position. It was not always clear if the heel point was taken based on the center of the shoe. When comparing right foot placement in the GMC Terrain MDB and pole tests, it was noted that the right heel point for the MDB test was incorrectly established using 250 mm from the pedal center point instead of the 200 mm distance specified in the seating procedure. Because of this, the right heel was positioned roughly 40 mm rearward from where the right heel was positioned in the GMC Terrain pole test.

Left Foot

Throughout the test series, the left foot was often positioned in such that it was only partially on the footrest. On two (Chevrolet Malibu and Hyundai Veloster) of the six left-side pole tests and on three (Hyundai Santa Fe, Chevrolet Malibu, and Ford Ranger) of the six left-side MDB tests, the left foot was placed so that the foot was partially on the footrest.

In discussing this with the test lab, their interpretation of the seating procedure was that the foot did not need to be positioned so that it was completely on the footrest. They either misinterpreted the equidistant spacing marking based on the centerline of the seat and the right foot placement, which would make the foot sit partially on the footrest, or the ATD ankle structure prevented the foot from fully engaging with the footrest. Because of these scenarios, NHTSA is investigating the section of the seating procedure dealing with the placement of the left foot.

Temperature Control

According to NHTSA's Qualification Procedures and for FMVSS No. 214 crash testing, the temperature of the WorldSID-50M must be soaked in a controlled environment that is 20.5-22.2 C (69-72°F) and has a relative humidity from 10-70% for at least four hours prior to a test. The IDDAS, RibEye, and trigger systems all produce heat when active and thus can increase the internal temperature of an ATD, especially when operating simultaneously. The damping material that covers the ribs is particularly sensitive to temperature, so the internal temperature of the WorldSID-50M ATDs were monitored on test day. Per the Qualification Procedures, the ribs shall not reach a temperature higher than 23.9 C (75° F) [8]. The WorldSID-50M ATDs had temperature sensors installed on top of the RibEye controller (non-struck side) and on the thorax rib 2 damping material near the spine box (impact side).

Indeed, elevated rib temperatures were observed in the first three crash tests of this series. There were a few instances where the rib temperature was close to exceeding or did exceed the established upper temperature threshold of 23.9 C. One such test, 11601, in which the rib temperature was slightly elevated at the time of the crash is shown in Figure 8. The black solid line is the ambient temperature of the lab, the solid blue line is the temperature on the RibEye DAS, and the blue dashed line is the temperature of the second thorax rib (impact side). The final

switching 'ON' of the DAS unit in this test occurred ~2:15pm, and the RibEye controller and rib temperatures began to rise. At the lab where the tests occurred, the doors to the setup lab were opened prior to the test, which occurred just after 3:00pm. The colder external air temperature slightly cooled the ATD between bay door opening and firing of the test, but overall temperatures remained elevated due to the DAS. The WorldSID-50M rib temperature at the time of the crash was over the limit by 0.4°C.

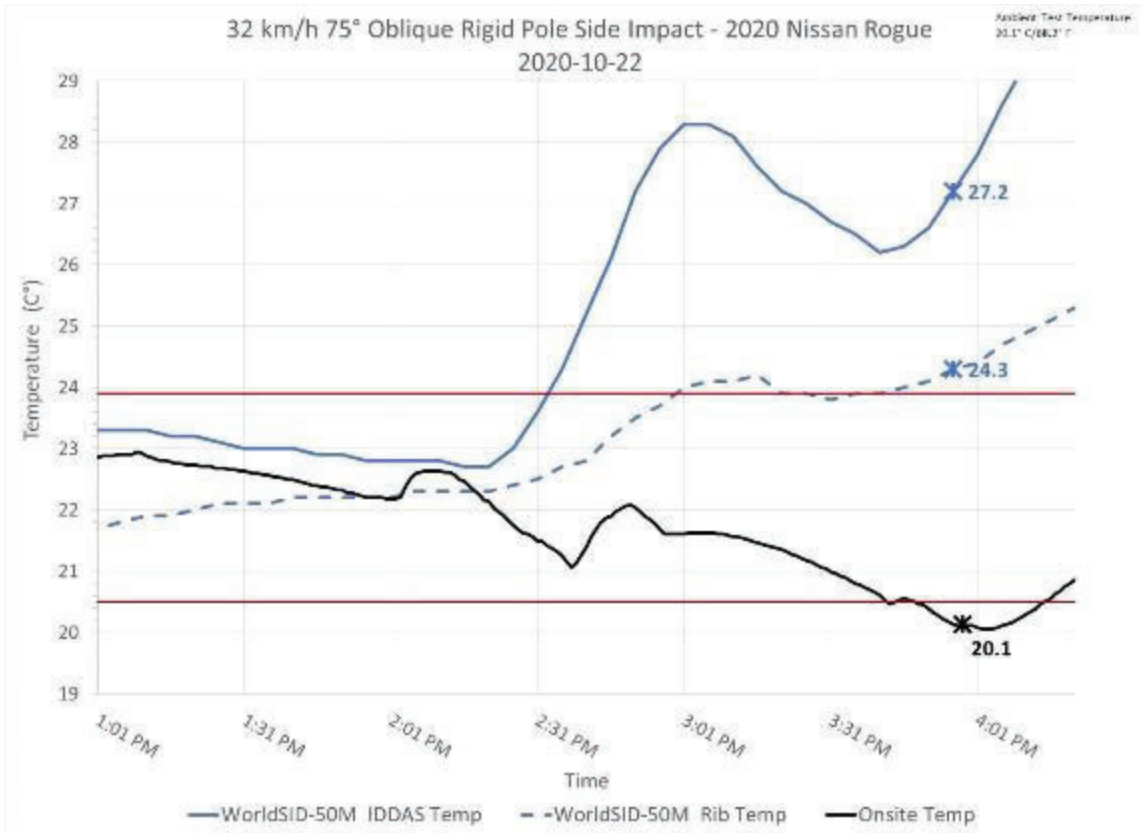


Figure 8. WorldSID-50M Rib Temperature Timeline for Crash Test 11601.

Without any countmeasures, when the temperature exceeds the limit, it is advisable to delay the test until the temperature drops back below the threshold, if feasible. To reduce the amount of time needed for the WorldSID-50M to cool down, and to prevent it from overheating in the first place, a fume extractor⁷ was used in many of the remaining crash tests to cool and maintain the internal ATD temperature pre-crash, as depicted in Figure 9. This device provides air movement, forcing the hot air out of the ATD via a suction hose that is easily inserted into the suit opening below the abdomen ribs. Subsequently, cool ambient air is pulled through existing openings in the suit around the neck and arms, over the spine box, RibEye controller, and ribs.

⁷ Weller Fume Extractor

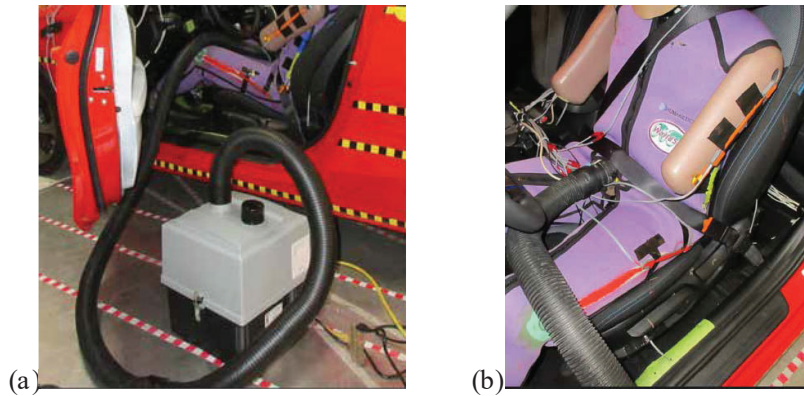


Figure 9. The implemented ATD fume extractor, shown (a) outside of a test vehicle and (b) with its connection to the WorldSID-50M.

The Hyundai Veloster pole test, 11604, was the first test that the fume extractor was used in to cool down the WorldSID-50M following trigger check. It was extremely effective in cutting down the time required for the ATD to cool down. On subsequent tests, including 11606 as seen in Figure 10, the fume extractor was implemented whenever there was any sort of delay with the ATD DAS turned on. As displayed in Figure 10, the final switching ‘ON’ of the DAS unit occurred ~3:37pm, and the fume extractor was activated ~4:00pm. This prevented the rib temperature (dashed blue line) from exceeding the limit, also preventing any additional temperature related delays. Throughout the remainder of the test series, this device demonstrated good effectiveness at reducing the WorldSID-50M internal temperature in a short period of time.

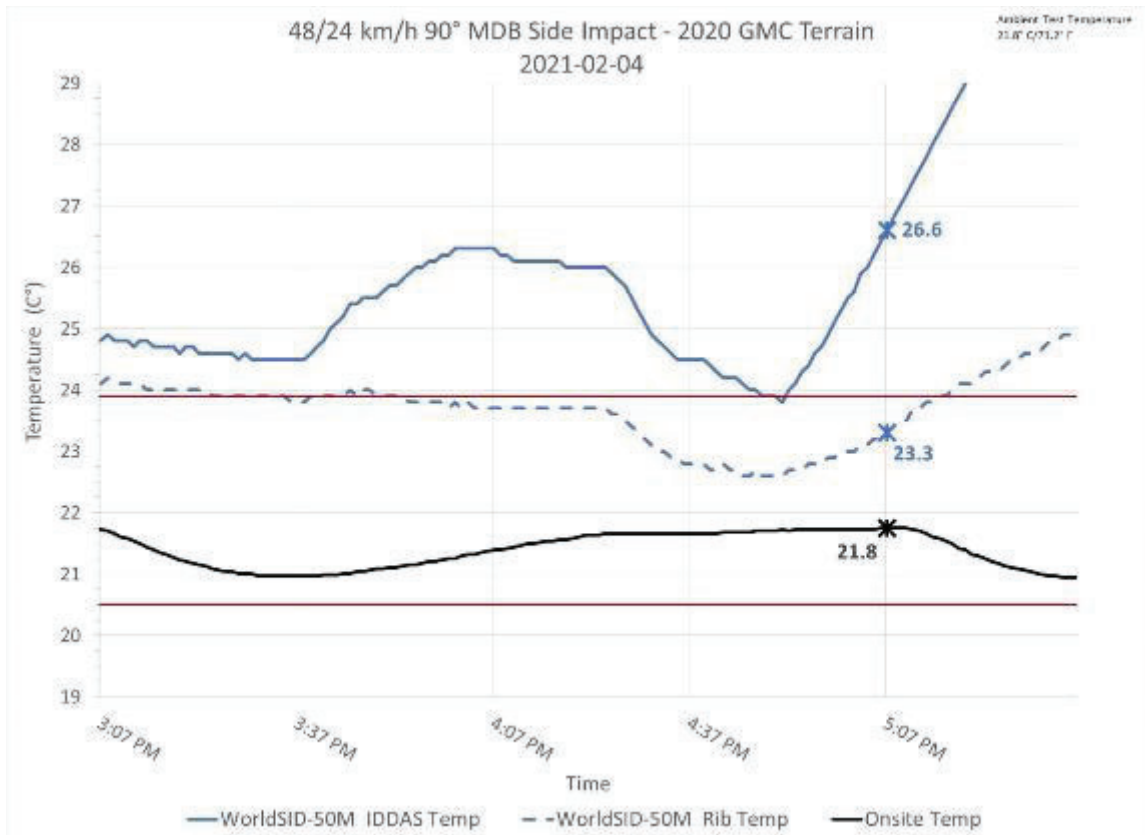


Figure 10. WorldSID-50M Rib Temperature Timeline for Crash Test 11606.

It is notable that if the IDDAS, RibEye, and trigger systems are tested the day before a crash test and there are no system issues the day of the test, the WorldSID-50M can generally be kept within the target temperature range without the use of a fume extractor. The test lab was routinely able to maintain the appropriate WorldSID-50M temperature range without the need for a fume extractor by limiting the "ON" time of the IDDAS units.

Durability

The WorldSID-50M was inspected after each crash test for damage. Throughout the crash test series and qualifications, none of the WorldSID-50M units sustained irreparable breakage. There were a few part repairs and/or replacements as enumerated below.

RibEye Multipoint Deflection Measurement System

During the first few crash tests (11600-11603 and 11605), there were some intermittent LED signals, which could have stemmed from how the wiring harness was installed and manufactured. While WS-L1 was undergoing its fourth set of qualification tests, which occurred after eight crash tests (when the loose bolts on top of the spine box were identified), loose LED connector pins were found. Following inspection of all RibEye connectors and discussion, all the LEDs and their connector pins were ultimately replaced in a new manufactured wiring harness. Additionally, a partial qualification was conducted on the body to verify that changing the LEDs resulted in similar responses prior to the swap. It was also noted that the shrink wrap around the LEDs may need to be checked periodically to identify loose or broken connections at the LED.

During the final post-test inspection of WS-L1 (after the thirteenth crash test, 11612), it was found that the rear LED on the left abdomen 2 rib had become detached from its mount. This was fixed by simply gluing it back in place.

Shoulder Rib Stiffeners

After the first crash test, the WorldSID-50M shoulder rib stiffeners were found to be bent. This damage had also been observed during a previous WorldSID-50M R&R crash test series in 2019. New, undeformed stiffeners lay flush against the outer shoulder rib band, but post-test there was a gap between the rib band and stiffeners. Despite this deformation, the WorldSID-50M passed shoulder and thorax with arm qualification tests, so the next crash test proceeded with the bent stiffeners. The stiffeners were however replaced during the next set of qualification tests after crash test 11601. Following the replacement, it was decided that if the ATD continued passing qualifications, the rib stiffeners would not continue to be replaced unless there was significant damage.

Ankle Z-Axis Radial Limit Screw

In both GMC Terrain tests, 11606 and 11611, the right foot of WS-L1 was found after the test to have rotated significantly about its Z-axis as depicted in Figure 11(a). Upon closer inspection, it was found that the z-axis radial limit screw had been sheared as shown in Figure 11(b). Visually inspecting the footwell, there were no unusual characteristics that stood out as possible causes of the damage. A high-speed camera was placed in the footwell on the GMC Terrain pole test (11611), and subsequently on the Ford Ranger pole test to gain a better understanding of the foot interaction through the impact event. It appears that the foot engages the brake pedal of the GMC Terrain a bit more behind the face of the pedal compared to how it engages with the Ford Ranger's brake pedal. It is possible that this allows the foot to roll off the Ranger's brake pedal before enough force builds up to shear the bolt, whereas the Terrain's brake pedal does not allow for a similar motion to occur.

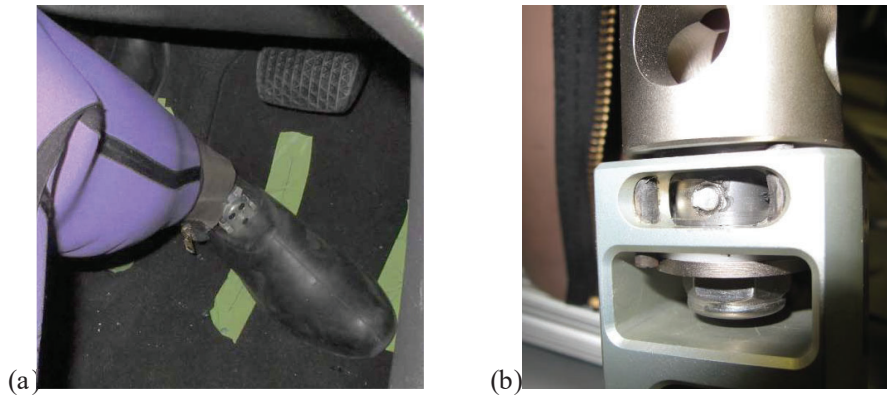


Figure 11. WorldSID-50M ankle damage as observed in both GMC Terrain tests, 11606 and 11611. (a) Right foot rotation about the z-axis, and (b) the sheared z-axis radial limit screw.

Loose Bolts

Difficulties encountered during qualification of both WorldSID-50M led to additional troubleshooting and inspection. In both instances, the primary difficulty was performing a passing thorax with arm test.

On WS-L1, the five bolts at the top of the spine box that secure the Upper Bracket Weldment – Spine Box to the spine box side plates were found to be loose. Tightening these bolts alleviated the issues preventing a passing qualification.

On WS-R, the bolts attaching the rubber lumbar spine to the lumbar mounting wedge were loose when the ATD was inspected following the initial qualification attempts. After tightening these bolts, the ATD was able to be qualified successfully.

Debris in Pelvis

There were multiple instances later in the test series where bits of glass and other debris were noted down inside of the pelvis of the WorldSID-50M. This debris was removed from the pelvis using a shop vacuum to prevent the debris from flying up and obstructing the LEDs and sensors of the RibEye System in subsequent tests.






Arm Flesh

Following the Ford Ranger pole test (test 11612), inspection of WS-L1 revealed that the flesh of the right arm had pulled away from the internal plastic structure at the top of the arm. It is unclear if this damage occurred during the impact event or during removal of the ATD from the vehicle following the test. Since this was the last planned test of the series with WS-L1, this was simply noted, and no further action was taken.

Crash Tests – General Rigor

To assess the degree to which the WorldSID-50M units were exposed to a rigorous testing series, ATD injury metrics were assessed after crash testing. Figure 12 indicates the proximity of observed injury metrics to baseline comparative values (Table 2). The coloration of the figure indicates the ratio of the respective WorldSID-50M injury metrics observed in this crash test series to EuroNCAP values:

Table 3. Coloration indicating the ratio of metrics to their comparative values.

Dark green:	$\leq 40\%$	
Light green:	> 40 and $\leq 60\%$	
Yellow:	> 60 and $\leq 80\%$	
Brown:	> 80 and $\leq 100\%$	
Red:	$> 100\%$	

For example, of the nine pole tests, the HIC in four crashes was less than 40% (dark green) of the EuroNCAP reference value of 700. Four of the pole tests produced a HIC score between 41 – 60% (light green) of the EuroNCAP value, and the remaining pole tests produced a HIC score between 61 – 80% (gold) of the reference value.

Figure 12 displays the degree to which the various body regions of the WorldSID-50M were exposed to injurious conditions. In both crash configurations, each body region had at least a couple moderate-risk exposures. By considering Figure 12, it can be concluded that the pole tests were universally more injurious. While maximum thoracic rib deflection was the greatest injury metric in pole tests, the maximum lateral shoulder force was greatest in the MDB tests. In both crash configurations, the pubic symphysis lateral force yields a comparatively low injury metric to all others.

Despite numerous moderate- to high-risk crash test exposures, none of the WorldSID-50M sustained irreparable damage. Therefore, this crash test series demonstrates how the WorldSID-50M can sustain the rigors of current FMVSS No. 214 crash testing.

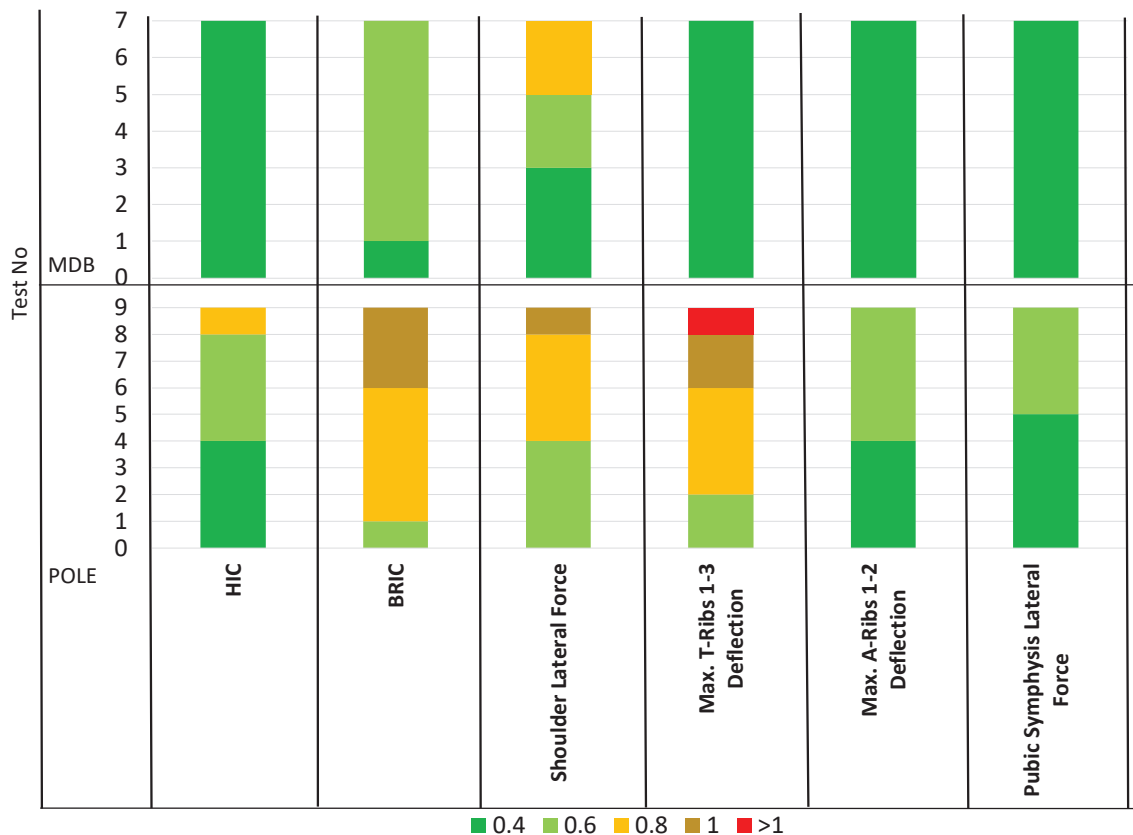


Figure 12. WorldSID-50M: Comparative injury metrics by exposure.

Crash Tests – RibEye Response

RibEye software measures the position of LEDs over time throughout a crash test event and computes rib deflections. It also displays error codes in the data when the sensors exhibit blockages, or an LED has moved out of range. Although most error codes observed in crash tests have been inconsequential and have not affected the ability of RibEye to measure maximum thorax and abdomen deflections, the error codes aid in understanding what might have caused sensor blockages if they occur.

MDB

Of the seven MDB tests performed in this series only two tests resulted in error codes - the Hyundai Santa Fe (11605) and the Mini Cooper S Convertible (11615). After analyzing the data, the error codes on these two tests were determined to be insignificant and neither affected the ability of RibEye to measure the maximum deflection of the thorax or abdomen ribs. Therefore, the maximum deflection of the thorax and abdomen ribs was successfully captured in all the MDB tests performed. The subsections below detail each of the scenarios causing the error codes that occurred in these MDB tests.

LED Traveled Out of Range

The front LED of the shoulder rib traveled out of range during the Mini Cooper S Convertible MDB test. Because the maximum shoulder rib deflection was able to be measured by the rear LED, the front LED going out of range was inconsequential.

Intermittent LED Power Connection

During the Hyundai Santa Fe MDB test, the middle LED on thorax rib 1 displayed an error code indicating this LED was blocked from all three sensors. Upon reviewing the data and inspecting the ATD, faulty connector pins were discovered in the connectors of the individual LED power circuits. Once the power connector and wire harness were replaced, there were no additional issues stemming from these power connections. Because the front LED on thorax rib 1 measured the maximum deflection on that rib (and for the thorax body region), the intermittent signal from the middle LED on thorax rib 1 was inconsequential.

Oblique Pole

There were two oblique pole tests where the RibEye system did not record any error codes, the Hyundai Veloster and the GMC Terrain. Of the nine tests where the RibEye system recorded error codes, the Mini Cooper S Convertible (11614) was the only test where measurement of the maximum deflection of the thorax and abdomen body regions was not obtained. Additionally, there was one test that resulted in a maximum shoulder deflection that could not be captured due to excessive shoulder rib movement. The subsections below detail each of the scenarios causing the error codes that occurred in these pole tests.

LED Traveled Out of Range

There were seven instances of LEDs travelling out of range during the pole tests. Six of these instances were recorded on the shoulder rib, which is not uncommon in the pole test condition where peak deflection is typically captured by the front or rear LED. When the front LED, for example, measures the maximum deflection of a rib, it is common for the rear LED on that rib to go out of range simply because its starting position is closer to the edge of the range toward which the rib is moving (Figure 13).

Of the six instances where an LED traveled out of range, only one resulted in the maximum shoulder deflection of the test not being captured. In the Chevrolet Malibu test (11600), the front LED of the shoulder rib went out of range. This location on the rib would have measured the maximum shoulder deflection. It is notable that the front LED had already measured 53 mm of deflection before it went out of range, so the shoulder was loaded substantially. The instance of a non-shoulder rib LED travelling out of range occurred in the Nissan Rogue test (11601). In this test, the front LED of thorax rib 1 travelled outside of the calibrated range, but the rear LED successfully captured maximum deflection, so this was inconsequential.

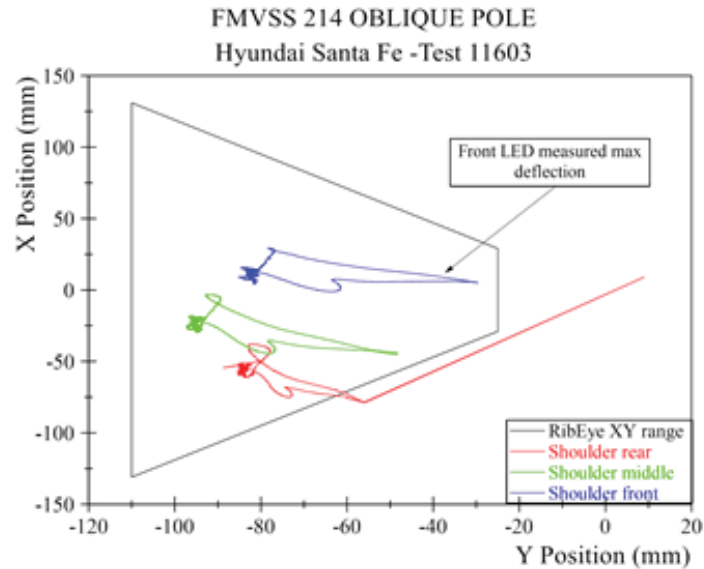


Figure 13. RibEye range plot for the Hyundai Santa Fe oblique pole crash test, 11603.

Intermittent LED Power Connection

Each of the first three pole tests recorded error codes indicating the thorax rib 2 front LED was blocked from all three sensors. Upon reviewing the data and inspecting the ATD, faulty connector pins were discovered in the connector of the LED power circuit. Once the LED and wire harness were replaced, there were no additional issues stemming from this power connection.

Thorax Rib 2 Blocked by Thorax Rib 1

There were five tests that recorded error codes indicating at least one LED on thorax rib 2 was blocked from the top sensor. These blockages were all caused by thorax rib 1 deflecting between the LED and the top sensor. This blockage is somewhat common but is inconsequential since this is an indication of thorax rib 1 having higher rib deflection than thorax rib 2 which rules out thorax rib 2 as a possibly having the maximum overall rib deflection.

Thorax Rib 3 Blocked by Abdomen Rib 1

There were two tests that recorded error codes indicating an LED on thorax rib 3 was blocked from the bottom sensor. These blockages were both caused by abdomen rib 1 deflecting between the LED and the bottom sensor. Unlike thorax rib 1 blocking thorax rib 2, these blockages include ribs from both the thorax and abdomen body regions. In these two tests, thorax rib 3 would not have measured the maximum thorax deflection, so these blockages were inconsequential. However, if blocked LEDs on thorax rib 3 would have measured the maximum thorax deflection, then these blockages would have been consequential. In this test series, the maximum thorax and abdomen body region deflections were successfully captured regardless of these blockages.

Thorax Rib 1 Blocked by the Shoulder

During the Mini Cooper S Convertible pole test (11614), the shoulder rib traveled inward and downward a significant amount due to airbag and intrusion interactions. A still image from the crash test close to the point of maximum shoulder deflection is depicted in Figure 14. The shoulder rib displaced to the extent that it fully blocked the rear LED and partially blocked the middle LED of thorax rib 1 from the top sensor as shown via a CAD model rendering in Figure 15. If the thorax rib 1 LEDs had not been blocked, it would have measured the maximum thorax deflection. Therefore, this blockage prevented the maximum thorax deflection from being recorded. This is the only test, including all past NHTSA WorldSID-50M crash tests, where the maximum thorax body region deflection was not captured.



Figure 14. Still image of the WorldSID-50M from the 2019 Mini Cooper Convertible crash test (11614) showing ATD interaction with the combination head/torso airbag and intrusion which caused the arm, shoulder rib, and thorax ribs to experience similar loading.

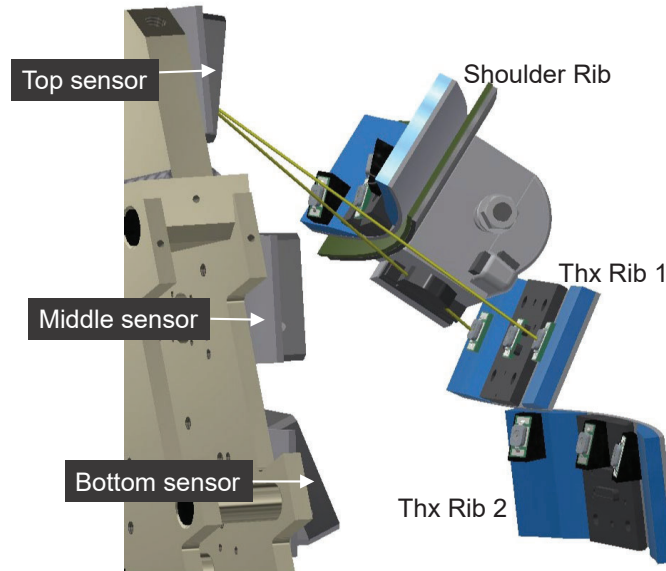


Figure 15. 3D CAD model of the rib motion during crash test 11614 in which the rear LED on thorax rib 1 is blocked by the shoulder rib. NOTE: Model is shown as a left side impact, but, the test was a right-side impact.

Relocation of RibEye LEDs

Relative to the other tests in this series, the Mini Cooper pole test (11614) yielded high shoulder rib deflection (60 mm), and it was this shoulder rib deflection that blocked the thorax rib 1 LEDs from the top sensor. With the LEDs of thorax rib 1 being blocked by the shoulder rib, it marks the first test where the maximum thorax deflection was not captured by the RibEye system, which raised concern regarding the possibility of this to occur in future crash testing.

In response, the 2019 Mini Cooper S convertible was retested in a pole condition with a WorldSID-50M that had updated LED locations. To allow more clearance from the rib above, and potentially prevent future LED blockages,

the LEDs on thorax rib 1 were relocated from the centerline of the rib to the bottom edge of the rib, and the middle LED was rotated to be oriented horizontally (Figure 16).

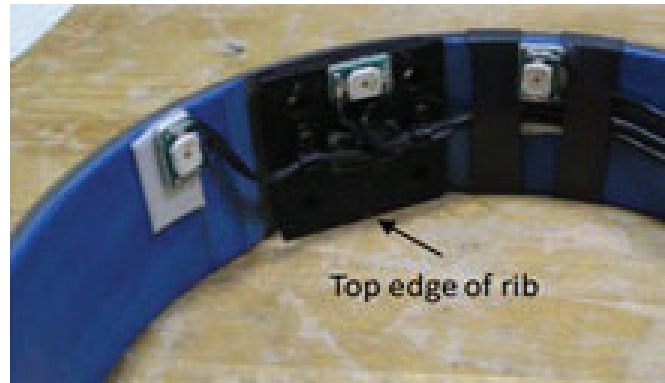


Figure 16. LEDs on thorax rib 1 of the WorldSID-50M after relocation from the centerline to the bottom edge where only the center LED is horizontally oriented.

Once this adjustment was made, test 11656 was conducted as a repeat of the right-side pole test on a 2019 Mini Cooper S convertible with the updated LED locations. An identical 2019 Mini Cooper Convertible was used with all the test setup parameters matching the previous test as closely as possible. Thorax rib 1 did not record any error codes in the repeat pole test, and the thorax rib 1 LEDs were clearly visible to the top sensor, as depicted in the below rendering (Figure 17). By overlaying the rib deflection data of these two tests, it was confirmed that the rib response was nearly identical. Therefore, it can be concluded that the relocation of the thorax rib 1 LEDs resolved the blockage that occurred in the first Mini Cooper test, and the maximum thorax deflection was successfully recorded in the repeat test.

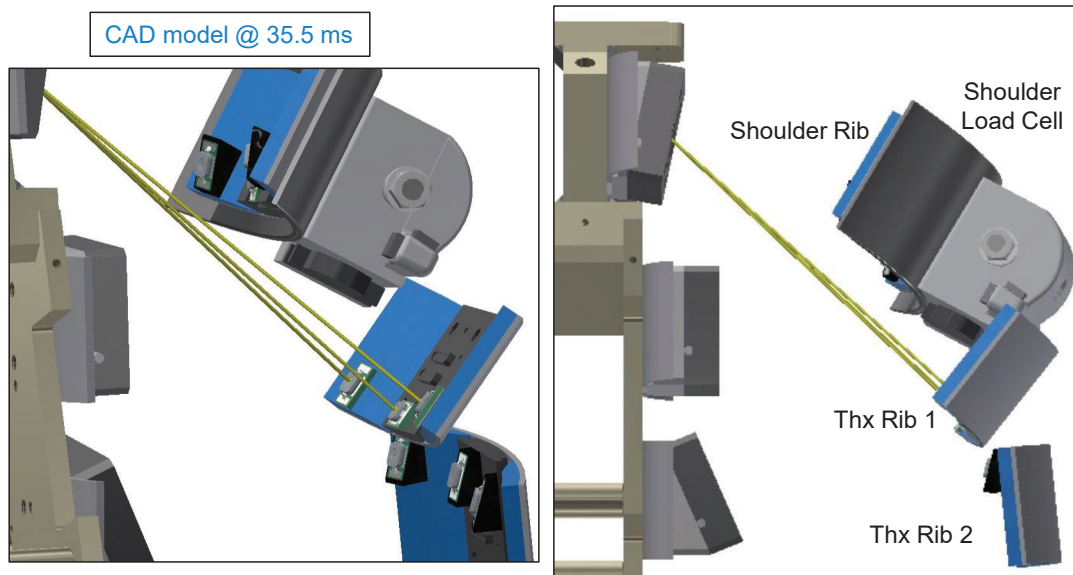


Figure 17. 3D CAD model of the rib motion during crash test 11656 in which the LEDs on thorax rib 1 are visible to the top sensor at maximum deflection.

After this test, the RibEye LED locations were further refined to allow for more deflection of the adjacent ribs where blockages might occur. In this iteration, the LEDs on both thorax rib 1 and abdomen rib 1 were moved to the bottom of the rib from center as depicted in Figure 18. The LEDs were also all rotated to be oriented horizontally rather than vertically. To evaluate these LED location adjustments, the 2020 Toyota Tacoma and 2020 Kia Soul were selected

as subsequent test vehicles based on their previous NCAP pole crash test performance. NCAP results on these vehicle models using the Side Impact Dummy (SID)-IIs showed elevated rib deflections and iliac forces.



Figure 18. LEDs on thorax rib 1 of the WorldSID-50M after relocation from the centerline to the bottom edge where all the LEDs are horizontally oriented (view is looking down onto the top of the rib).

In the tests of these vehicles – 14356 and 14355, respectively – the maximum deflection of the thorax and abdomen body regions were recorded successfully. Relocation of the LEDs on thorax rib 1 and abdomen rib 1 allowed for more clearance and movement of the shoulder rib and thorax rib 3 to prevent LED blockages. These results serve as preliminary validation of the RibEye LED relocations. More RibEye evaluation is underway to further support these updates.

LIMITATIONS

This study had minor limitations in that the vehicle fleet was limited. Few small, compact, and sub-compact size vehicles were included in this test series. Further, crash tests were only conducted at one lab. The updated RibEye LED placement was only utilized in three vehicle tests. In addition, the current IDDAS being evaluated is the DTS G5 which is older technology, and the older mini distributor yielded minor issues throughout this crash test series. A more up-to-date mini distributor model would allow for lower battery input voltage. Further, the TDAS Control software used in this test series has been superseded by DTS DataPro software.

CONCLUSIONS

In this crash series of FMVSS No. 214 MDB and oblique pole tests, the WorldSID-50M successfully completed the crash test series and was durable. Scripted procedures for WorldSID-50M assembly, qualification, and handling were followed without issue, and the seating procedures resulted in highly uniform positioning. The WorldSID-50M passed many qualification tests without an issue regarding the test setup or response specifications. The pelvis qualification test is an ongoing exception, due to evolving proposed specifications. The thorax with arm test yielded failures, but the results were in specification after tightening loose bolts in the upper and lumbar spine. Throughout the eighteen crash tests, the WorldSID-50M exhibited few sensor anomalies, all of which could be attributed to identifiable causes and were inconsequential. No major damage was observed in WorldSID-50M aside from a broken ankle rotation stop yielded from a single vehicle model. RibEye was durable and worked well, achieving maximum thorax and abdomen deflections in all but one test, which was subsequently remedied.

REFERENCES

- [1] Rhule, H., Moorhouse, K., Donnelly, B., & Stricklin, J. (2009). Comparison of WorldSID and ES-2re biofidelity using an updated biofidelity ranking system. Proceedings of the 19th International Technical Conference on the Enhanced Safety of Vehicles, Washington, DC, Paper Number 09-0563.
- [2] National Highway Traffic Safety Administration (2015). NCAP RFC, December 16, 2015, Regulations.gov Docket ID NHTSA-2015-0119-0001, available at: <https://www.regulations.gov/document/NHTSA-2015-0119-0001>
- [3] Rhule, D. A., & Stricklin, J. L. (2022, July). Evaluation of the WorldSID 50th percentile male side impact dummy – Qualification and sled test repeatability and reproducibility (Report No. DOT HS 813 214). National Highway Traffic Safety Administration.
- [4] Rhule, D., Millis, W., & Stricklin, J. (2022, January). WorldSID 50th percentile male durability assessment (Report No. DOT HS 813 212). Washington, DC: National Highway Traffic Safety Administration.
- [5] National Highway Traffic Safety Administration (2023). Evaluation of RibEye Installed in the WorldSID 50th Percentile Male Dummy. Washington, DC: *Undergoing final document proofing; publication scheduled for 2023.*
- [6] Loudon, A. E. (2019, April). WorldSID 50th percentile male dummy seating procedure evaluation and revision (Report No. DOT HS 812 694). Washington, DC: National Highway Traffic Safety Administration.
- [7] National Highway Traffic Safety Administration (2023). WorldSID-50M Procedures for Assembly, Disassembly, and Inspection (PADI), Washington, DC: *Undergoing final document proofing; publication scheduled for 2023.*
- [8] National Highway Traffic Safety Administration (2023). WorldSID-50M Procedures for Qualification. Washington, DC: *Undergoing final document proofing; publication scheduled for 2023.*
- [9] Rhule, H., Millis, W., Mallory, A., & Stricklin, J. (2019, July). Determination of optimal RibEye LED locations in the WorldSID 50th percentile male dummy (Report No. DOT HS 812 758). Washington, DC: National Highway Traffic Safety Administration.

APPENDIX

Table A-4 Qualification Summary of WS-L1.

Qualification Number	ATD Qualified	Start/End Dates	VRTC or TRC	Full or Partial	Additional Info
1	WS-L1	9/1/20-9/10/20	VRTC	Full Qual	No Issues
2	WS-L1	10/26/20-11/6/20	TRC	Full Qual	Noted shoulder rib stiffeners were deformed following previous crash test. Shoulder rib possibly deformed as well.
2a	WS-L1	10/29/20-11/10/20	TRC	Partial Qual Shldr, Thrx w/Arm	These tests were performed due to replacement of shoulder rib stiffeners and shoulder rib.
3	WS-L1	1/15/21-1/21/21	TRC	Full Qual	No Issues
4	WS-L1	2/23/21-2/25/21	TRC	Full Qual	Following this qual, it was determined to replace the LED set due to intermittent connections – ATD transferred to VRTC for LED swap (no tests performed at VRTC).
4a	WS-L1	3/8/21-3/10/21	TRC	Partial Qual Shldr, Thrx w/Arm, Thrx w/o Arm, Abdomen	Partial qual performed to verify LED replacements didn't affect ATD performance; had issues passing Thorax w/ Arm - after inspecting, it was determined that the plate that attaches to the top of the spine box was loose, tightened bolts and passed qualification
5	WS-L1	3/25/21-3/29/21	TRC	Full Qual	No Issues
6	WS-L1	4/14/21-4/20/21	TRC	Full Qual	No Issues

Table A-2 Qualification Summary of WS-L2.

Qualification Number	ATD Qualified	Start/End Dates	VRTC or TRC	Full or Partial	Additional Info
1	WS-L2	4/19/22-5/4/22	VRTC	Full Qual	No Issues
2	WS-L2	7/18/22-7/21/22	VRTC	Full Qual	No Issues

Table A-3 Qualification Summary of WS-R.

Qualification Number	ATD Qualified	Start/End Dates	VRTC or TRC	Full or Partial	Additional Info
1	WS-R	1/26/21-2/12/21	TRC	Full Qual	Thorax w/ and w/o Arm were failing. Suspected stiff ribs, returned to VRTC for investigation.
1a	WS-R	2/25/2021	VRTC	Thorax w/o Arm Only	Attempted 2 Thorax w/o Arm to confirm failing results from TRC. Following this, the 3 thorax ribs were replaced due to a suspicion of stiff thorax ribs.
1b	WS-R	3/11/21-3/15/21	TRC	Partial Qual Shldr, Thrx w/ Arm, Thrx w/o Arm	After replacing the 3 thorax ribs, ATD returned to TRC to get partial qual, validating results of the rib replacement. Thorax w/ Arm still wouldn't pass. ATD returned to VRTC for further investigation.
1c	WS-R	3/25/21-3/31/21	VRTC	Partial Qual Shldr, Thrx w/ Arm, Thrx w/o Arm, Abdomen	Further investigation: 4 screws that connect the lumbar mounting wedge to the rubber lumbar spine were found to be loose. After tightening and reassembly, this qual was performed to verify fix.
2	WS-R	5/4/21-5/10/21	TRC	Full Qual	After 3 attempts, could not get the pelvis test to pass. Accepted the results as is since this is a post-test qualification.
3	WS-R	8/3/21-9/9/21	VRTC	Full Qual	All body hits were performed due to the ATD being stripped down for instrumentation calibration. Pelvis impacts were performed while attempting to troubleshoot the pelvis issues. These tests were performed with a variety of lower body components swapped out. The pelvis was ultimately accepted as is with the failing qualifications to prevent significant delays with the crash test.
4	WS-R	9/29/21-10/5/21	TRC	Full Qual	Because this was a post-test qual, the lab only needed to perform 1 hit with passing inputs. Both lateral neck tests had low headform angular rate. Thorax with arm had low rib 2 def., and pelvis had both low pelvis accel and low pubic force.